Polymeric Coatings for Targeted Nanoparticle Delivery to Subsurface Contaminants

by

Stuart Andrew Linley

A thesis
Presented to the University of Waterloo
In fulfillment of the
Thesis requirement for the degree of
Doctor of Philosophy
In
Chemical Engineering

Waterloo, Ontario, Canada
© Stuart Linley 2019

Examining Committee Membership

The following members served on the Examining Committee for this thesis. The decision of the Examining Committee is by majority vote.

Supervisor	Frank Gu Professor	University of Toronto Dept. Chemical Engineering & Applied Chemistry
Internal Examiner	William A. Anderson Professor	University of Waterloo Dept. Chemical Engineering
Internal Examiner	Raymond Legge Professor	University of Waterloo Dept. Chemical Engineering
Internal/External Examiner	Neil R. Thomson Professor	University of Waterloo Dept. Civil & Environmental Engineering
External Examiner	Subhasis Ghoshal Professor	McGill University Dept. Civil Engineering

Author's Declaration

This thesis consists of material all of which I authored or co-authored: see Statement of Contributions included in the thesis. This is a true copy of the thesis, including any required final revisions, as accepted by my examiners.

I understand that my thesis may be made electronically available to the public.

Statement of Contributions

Chapter 2 of this thesis is partially adapted from my comprehensive examination research proposal as well as a report from the CHE 765 reading course taken with Prof. Frank Gu. S. Linley is the sole author of all content in Chapter 2.

Chapter 3 of this thesis is adapted from a previously published article co-authored by myself; a PhD student, Dr. Timothy Leshuk; a PhD student, Mr. Andrew B. Holmes; a masters student, Mr. Wanis Nafo; Professor Neil R. Thomson and Professor Adil Al-Mayah of the University of Waterloo's Civil and Environmental Engineering department; Dr. Kevin McVey and Dr. Kanwartej Sra of Chevron Environmental Technology Company; and my supervisor, Professor Frank Gu. S.L. conceived, designed, and performed the majority of the experiments; A.B.H. and W.N. performed the X-Ray CT experiments and prepared the X-Ray CT figures; S.L. analyzed the data, prepared the figures, and wrote the paper with input from A.B.H. on the text for the X-Ray CT section. T.L. performed some early proof-of-concept experiments and contributed to the drawn schematic. N.R.T. and A.A.M. contributed analytical equipment, materials, and critically reviewed the paper. K.M. and K.S. provided project support and evaluation, and critically reviewed the paper. F.G. supervised the project, contributed reagents, materials, analysis tools, and critically reviewed the paper.

Chapter 4 of this thesis is adapted from a previously submitted article co-authored by myself, Professor Neil R. Thomson of the University of Waterloo's Civil and Environmental Engineering department; Dr. Kevin McVey and Dr. Kanwartej Sra of Chevron Environmental Technology Company; and my supervisor, Professor Frank Gu. S.L. conceived, designed, and performed all experiments, analyzed all data, prepared all figures, and wrote the paper. N.R.T. provided materials and critically reviewed the paper. K.S. and K.M. provided project support and evaluation, and critically reviewed the paper. F.G. supervised the project, contributed reagents, materials, analysis tools, and critically reviewed the paper.

Chapter 5 of this thesis is adapted from a previously submitted article co-authored by myself, Professor Neil R. Thomson of the University of Waterloo's Civil and Environmental Engineering department; Dr. Kevin McVey and Dr. Kanwartej Sra of Chevron Environmental Technology Company; and my supervisor, Professor Frank Gu. S.L. conceived, designed, and performed all experiments, analyzed all data, prepared all figures, and wrote the paper. N.R.T. provided materials, analytical tools, modelling software, and contributed manuscript text on the modelling experimental method as well as providing critical review. K.S. and K.M. provided project support and evaluation, and critically reviewed

the paper. F.G. supervised the project, contributed reagents, materials, analysis tools, and critically reviewed the paper.

Chapter 6 of this thesis is adapted from a previously submitted article co-authored by myself, a co-op undergraduate student, Mr. Darron Phann; Professor Neil R. Thomson of the University of Waterloo's Civil and Environmental Engineering department; Dr. Kevin McVey and Dr. Kanwartej Sra of Chevron Environmental Technology Company; and my supervisor, Professor Frank Gu. S.L. conceived and designed all experiments. D.L. contributed in adapting the cobalt ferrite nanoparticle synthesis procedure from the literature. S.L. and D.L. performed all experimental work. S.L. analyzed the data, prepared the figures, and wrote the paper with input from D.L. in the experimental section detailing cobalt ferrite nanoparticle synthesis. N.R.T. provided materials, analytical tools, modelling software, and contributed manuscript text on the modelling experimental method as well as providing critical review. K.S. and K.M. provided project support and evaluation, and critically reviewed the paper. F.G. supervised the project, contributed reagents, materials, analysis tools, and critically reviewed the paper.

Abstract

Terrestrial oil spills account for the majority of oil spills world wide and present a challenging remediation problem owing to the inaccessibility of subsurface petroleum hydrocarbons (PHC). Contaminants such as crude oil demonstrate acute and chronic toxicity, necessitating remediation activity which is applied in the form of *ex situ* and *in situ* treatments. Among *in situ* remediation techniques, nanomaterial-based treatment strategies have been developed over the past decade to take advantage of improved subsurface mobility and reaction kinetics due to particle size. Increased use of nanoremediation has led to development of coating strategies to improve efficiency of use, and such techniques have raised concerns over the release of mobile nanoparticles into the wider environment.

This thesis focuses on the development of a nanoparticle coating to facilitate nanoparticle (NP) aqueous stability, mobility in porous media, and preferential adsorption to target contaminants in porous media. The concept of targeted delivery is borrowed from nano-medicine, where chemotherapeutic drugs are encapsulated by nanomaterials which target accumulation in diseased material through active or passive means. In this thesis, an amphiphilic polymer coating allows NP binding to a hydrophobic interface to localize the NP at the site of contamination and reduce NP migration past contaminated zones. The targeted binding, realized through hydrophobic interactions between the nanoparticle coating and the crude oil model contaminant, is an example of an active targeting technique.

The NP surface was modified by oleic acid and Pluronic deposited in layers to produce an externally amphiphilic coating capable of stabilizing the NP in water and interacting with crude oil. By modifying the Pluronic coating concentration and Pluronic molecule hydrophobicity, we were able to tune the recovery of NP transport through clean porous media and NP binding to oil-impacted porous media. It was also found that Pluronic coating concentration influenced the morphology of the NP, producing larger aggregates of nanoparticles or individually stabilized nanoparticles.

The effect of environmental factors such as oil concentration in porous media, oil type, temperature, and pH on nanoparticle transport and binding in flow-through sand packed columns was investigated. It was found that higher oil concentrations, longer crude oil molecules, and higher temperatures resulted in higher NP binding. pH was found to have no effect on nanoparticle attachment to clean or oil-impacted sands within the pH range of 5 – 9. High temperature was used to demonstrate complete NP retention in oil-impacted natural aquifer sand packed columns flow-through experiments, and solute transport simulation software was used to model NP transport and binding using an advection-dispersion equation with single-site attachment limited by Langmuirian blocking (1D-USAT). These parameters were used to predict the NP attachment profile within sand packed columns and how it might change under different conditions such as higher flow rate or oil concentration.

NP attachment to clean sand was found to be in the range of 2 – 13 mg/kg and attachment was found to increase in the presence of oily sand in the range of 8 – 32 mg/kg, depending on the nanoparticle formulation and environmental factors selected. The attachment rate (k_{attach}) for nanoparticles in oil-impacted sand exceeded the k_{attach} for nanoparticles in clean sand by approximately one order of magnitude (10x). The attachment rates varied on the order of 10^{-5} - 10^{-4} s^{-1} in clean sand, while attachment rates varied on the order of 10^{-4} - 10^{-3} s^{-1} in oily sand. Detachment rates (k_{detach}) in clean sand flow-through were determined to be approximately equal based on 1D-USAT modelling of experimental data – approximately 10^{-6} s^{-1}.

The NP coating strategy was applied to multiple NP core materials, including iron oxide, silver, and cobalt ferrite, all produced using different synthetic methods. The coated nanoparticles all demonstrated preferential binding to crude oil-impacted sands in binding batch tests, as well as breakthrough in clean sand transport experiments and retention in oil-impacted sand transport experiments. This showed that the NP coating could be applied to various types of NPs and conferred targeted delivery behaviour on each.

Finally, potential application of targeted NP delivery to oil-impacted porous media was explored through the investigation of X-Ray computed tomography (X-Ray CT) as a sensing technique for detecting NP bound to oil-impacted sand. The oil-impacted sand exposed to Pluronic-coated NPs generated a CT signal sufficient to differentiate it from oil-impacted sand which was not exposed to NP. Conversely, clean sand exposed to Pluronic-coated NPs did not generate a substantial CT signal. This indicates that targeted NP binding to oil-impacted porous media may have use as a contrast enhancer for detecting contaminated zones at sites of concern.

This thesis summarizes the development process of a nanoparticle coating facilitating transport through porous media and targeted binding to crude oil emplaced therein. The Pluronic-coated nanoparticles demonstrated preferential attachment to oil-impacted sediments, transport through clean sand packed columns, and retention in oil-impacted sand packed columns. This nanoparticle coating-strategy shows promise as a versatile technique for enhancing nanoparticle accumulation in contaminated subsurface areas which may enable contaminant detection and enhanced remediation, as well as reduce uncertain nanoparticle environmental fate in future applications.

Acknowledgements

I would first and foremost like to offer my thanks to the various co-op students employed by the Frank Gu Lab at this University of Waterloo who assisted me in performing the many experiments which make up the bulk of this thesis. The students I would like to recognize, in order of term hired, are as follows: Cullen Tielemans, Ye (Anny) Huang, Shuyu (Rosa) Chen, Caleb Jefferies, Karyn Sun, Ibrahim Fanek, Emma Belliveau, Zixin Zhang, Darron Phann, and Elora Deering.

I would like to offer considerable thanks to Prof. Neil R. Thomson, a member of my committee, for his guidance and assistance in the modelling aspect of this work and providing the 1D-USAT simulation software, as well as interpretation of nanoparticle transport results. Without his input and access to his laboratory resources, this project would not have been possible.

Great thanks to my remaining committee members, Prof. William Anderson and Prof. Raymond Legge for their commentary, criticism, and guidance. Thanks also to Prof. Subhasis Ghoshal for offering his time and expertise in evaluating my thesis and participating in my defence.

I would also like to recognize my supervisor, Prof. Frank Gu, for supporting my application to the Vanier Canada Graduate Scholarship as well as assistance in facilitating this project, co-ordinating with our sponsors, and providing guidance and feedback throughout my Ph.D.

Special thanks to Dr. Kammy Sra and Dr. Kevin McVey of Chevron Energy Technology Company for their advice and support of this project. Their feedback molded the direction of this project and gave me valuable opportunity to improve my presentation and project management skills. Thanks also to Dr. Gabriel Sabadell, Dr. Thomas Hoelen, Dr. Tim Buscheck Dr. John Wilson, and Dr. Robert Hinchee for their advice and support.

I would like to express my gratitude to other research groups and services which helped produce the data presented herein: Wayne Noble, Shirley Chatten, and Mark Merlau from the Department of Civil & Environmental Engineering at the University of Waterloo for chromatography work. Ralph Dickhout from the Department of Chemical Engineering for assisting with ICP-MS. The Canadian Centre for Electron Microscopy at McMaster University for performing TEM, SEM, and HR-TEM analyses. Prof. Adil Al-Mayah and Wanis Nafo for performing X-Ray CT characterization. Prof. Tong Leung and Dr. Anisur Rahman of the Quantum Nano Centre Metrology Facility for assistance with VSM.

Thanks also to the administrators and staff of WIN and the Chemical Engineering Department for facilitating my work and co-ordinating various aspects of my PhD studies from courses, TAships, and finance to equipment and laboratory maintenance: Chris Kleven, Caroline Brookes, Ji Su Kwon, Judy Caron, Liz Bevan, Rose Guderian, Ingrid Sherrer, and Pauline Ferfolja. Special thanks to WIN Director Arthur Carty for his commitment to support my Vanier Graduate Scholarship application.

Thanks to the members of my research group for their support over the years, particularly to Dr. Tim Leshuk who helped with proof-of-concept experiments in the first months of this project and prospective Dr. Andrew Holmes who collaborated with me on X-Ray CT data interpretation and implementation of the nanoparticles from this work for Spectral Induced Polarization (SIP) spectroscopy (not discussed here). Thanks to Dr. Sandy Liu for help with materials procurement and the occasional piece of valuable advice.

I would like to gratefully acknowledge the financial support I have received throughout my Ph.D. which have enabled me to pursue this opportunity: the Natural Sciences and Engineering Research Council of Canada (NSERC) Vanier Graduate Scholarship, the Waterloo Institute for Nanotechnology (WIN) Nanofellowship, the Ontario Graduate Scholarship (OGS), the G.A. Paper Scholarship, and the UW Graduate Studentship.

Finally, I would like to thank my parents who constantly stood by me throughout this experience, offering encouragement and a support network I always knew I could rely on in any event. The road to completing this PhD has been rocky and challenging, and it has been the steadfast support of my parents that have made it seem possible to reach the end.

Dedication

For my parents, Mr. Andrew Linley and Mrs. Susan Linley

and

In memory of my grandfather, Mr. James C. McMaster

Table of Contents

Examining Committee Membership ii
Author's Declaration iii
Statement of Contributions iv
Abstract iv
Acknowledgements viii
Dedication x
Table of Contents xi
List of Figures xv
List of Tables xx
Chapter 1: Introduction 1
1.1 Overview 1
1.2 Research Objectives 2
1.3 Thesis Outline 3
Chapter 2: Literature Review 6
2.1 Heavy Hydrocarbon Impacted Soils & Remediation Technologies 6
2.2 Nanoparticles in Soil Remediation 8
2.2.1 Contaminants Addressed by nZVI 8
2.2.2 Recent Advances: Catalyst Improvement 10
2.2.3 Recent Advances: nZVI Dispersibility 11
2.3 Other Nanomaterials for Adsorptive Contaminant Removal 13
2.3.1 Iron Sulfide Nanoparticles 13
2.3.2 Iron Oxide and Metal Ferrite Nanoparticles 14
2.3 Factors Affecting Nanoparticle Transport in Porous Media 15
2.4 Nanoparticle Synthesis & Coating Strategies 17
2.5 Nanoparticle Targeted Binding & Application to Soil Remediation 19
2.6 Conclusion 20

Chapter 3: Targeted Nanoparticle Binding & Detection in Petroleum Hydrocarbon Impacted Porous Media 21
3.1 Summary 21
3.2 Introduction 22
3.3 Materials and Methods 24
3.3.1 Materials 24
3.3.2 Nanoparticle Synthesis 25
3.3.3 Nanoparticle Phase Transfer 25
3.3.4 Nanoparticle Binding Studies 25
3.3.5 Analyses 26
3.4 Results and Discussion 27
3.4.1 Nanoparticle Design 27
3.4.2 Nanoparticle Characterization 28
3.4.3 Nanoparticle Binding 30
3.4.4 X-Ray CT Visualization of Nanoparticle Binding 34
3.5 Conclusions 36
Chapter 4: Nanoparticle Targeted Delivery to Petroleum Hydrocarbon Impacted Porous Media 38
4.1 Summary 38
4.2 Introduction 39
4.3 Experimental 40
4.3.1 Materials 40
4.3.2 Nanoparticle Synthesis 41
4.3.3 Nanoparticle Phase Transfer 41
4.3.4 Column Flow-through Experiments 41
4.3.4 Analyses 42
4.4 Results and Discussion 42
4.4.1 Effect of Nanoparticle Coating on Morphology and Transport Efficiency 42
4.4.2 Nanoparticle Transport and Binding in Clean and Oil-Impacted Porous Media 47

4.5 Conclusions 50
Chapter 5: Factors Affecting Nanoparticle Targeted Binding to PHC-Impacted Sediments 51
5.1 Summary 51
5.2 Introduction 52
5.3 Materials & Methods 53
5.3.1 Materials 53
5.3.2 Nanoparticle Synthesis 54
5.3.3 Nanoparticle Binding Batch Tests 54
5.3.4 Nanoparticle Transport and Binding Tests 55
5.3.5 Analysis 55
5.3.6 Nanoparticle Transport Modelling 56
5.4 Results and Discussion 57
5.4.1 Effect of NP Pluronic Coating Concentration 57
5.4.2 Effect of Oil Concentration and Oil Type 60
5.4.3 Effect of Temperature and pH 63
5.4.4 Nanoparticle Transport and Binding in Stop-Flow Systems 65
5.5 Conclusions 71
Chapter 6: Pluronic as a Universal Nanoparticle Coating for Targeted Delivery of Nanoparticles to PHC-Impacted Porous Media 73
6.1 Summary 73
6.2 Introduction 74
6.3 Materials and Methods 75
6.3.1 Materials 75
6.3.2 Nanoparticle Synthesis 76
6.3.3 Binding Batch Studies 77
6.3.4 Column Transport and Binding Studies 78
6.3.5 Analyses 78
6.3.6 Nanoparticle Transport Modelling 79

6.4.1 Silver Nanoparticle Synthesis 79
6.4.2 Nanoparticle Characterization 80
6.4.3 Effect of Temperature on Nanoparticle Binding 82
6.4.4 Nanoparticle Transport and Binding in Column Tests 85
6.5 Conclusions 92
Chapter 7: Conclusions and Future Work 94
7.1 Summary 94
7.2 Conclusions 94
7.3 Recommendations for Future Work 96
7.5 Preparations for Field Deployment 98
Appendix A: Description of Variables in Advection/Dispersion Equation 100
Appendix B: Borden Sand Soil Characterization 101
Appendix C: Silver Nanoparticle Synthesis Optimization 103
Appendix D: Quartz Crystal Microbalance (QCM) Preliminary Investigation 107
D.1 Purpose & Introduction 107
D.2 Materials & Methods 107
D.2.1 Materials 107
D.2.2 QCM Experiments 107
D.3 Results & Discussion 108
D.4 Conclusions and Next Steps 113
Bibliography 114

List of Figures

Figure 1. Engineered nanoparticles preferentially attach to NAPL PHC over soil grains. This is observed through higher X-ray CT signal when NP are exposed to oil-impacted sand (right) compared to clean sand (left). 21

Figure 2. Schematic illustrating nanoparticles with an amphiphilic polymer coating (Pluronic) avoiding adsorption to sand grains and specifically adsorbing to NAPL PHC through hydrophobic interactions. Polyethylene Oxide (PEO; red) blocks of the coating extend into the aqueous phase and contract in the NAPL PHC. Polypropylene Oxide (PPO; blue) blocks of the coating extend into the NAPL PHC and contract in the aqueous phase. Oleic acid (black) binds the coating to the nanoparticle surface and interacts favourably with the NAPL PHC when at the interface. 27

Figure 3. HR-TEM image of sample A-100: **A** Iron oxide nanoparticles prior to Pluronic coating, **B** Clusters of iron oxide nanoparticles after Pluronic coating, **C** Iron oxide nanoparticle prior to Pluronic coating, and **D** Edge of a Pluronic coated nanoparticle aggregate demonstrating crystalline nanoparticles within an amorphous polymer coating. 29

Figure 4. Nanoparticle sizing in suspension by Dynamic Light Scattering (DLS). Uncoated particles in hexane were found to be 8.4 nm in diameter with a polydispersity index (PDI) of 0.260. Coated particle aggregates in water were found to be 89.8 nm in diameter with a PDI of 0.138. 29

Figure 5. ICP-OES results demonstrating preferential binding of nanoparticle Formulation A to OSS when compared to SS. Iron concentration in suspension was measured directly using ICP-OES. NP bound to sand was calculated indirectly using the observed decrease of iron in the suspension. Error bars represent ± one standard error. 30

Figure 6. NP binding batch test using nanoparticles phase-transferred in the absence of Pluronic (using only oleic acid). Aqueous phase iron concentration indicated some targeting behaviour when comparing SS to OSS, but the effect is mild compared to binding observed using Formulation A nanoparticles. Estimated NP deposition is 0.39 ± 0.30 μg/g in SS and 2.71 ± 0.28 μg/g in OSS. 31

Figure 7. Magnetic hysteresis curve for freeze-dried Formulation A nanoparticles. The saturation magnetization for Formulation A nanoparticles was found to be 59.76 emu/g with negligible error; error on the order of 10-5 emu/g. 32

Figure 8. Magnetic hysteresis curves for OSS before (OSS Control) and after exposure to Formulation A nanoparticle solution (OSS + NP). The saturation magnetization was 1.037 ± 0.016 x 10-3 emu/g for the OSS Control sample, and 1.523 ± 0.016 x 10-3 emu/g for the OSS+NP sample. 33

Figure 9. Indirectly calculated nanoparticle (NP) binding increases as nanoparticle coating formulation becomes more hydrophobic. The nomenclature X-# identifies nanoparticle samples (Table 1). 33

Figure 10. Images A, B, and C show the top, left, and right projections of CT X-Ray absorbance through the centre of a cuvette containing nanoparticle-spiked silica sand at a concentration of 1 mg/kg (NP/SS). Image D shows a 3-D projection of the X-ray absorbance throughout the cuvette. The blue regions indicate areas of higher X-ray absorbance which correspond to the upper portion of the cuvette which contains nanoparticle spiked sand. The green regions indicate areas of lower X-ray absorbance which correspond to the lower portion of the cuvette which contains clean, reference sand. This figure demonstrates the limited identification of nanoparticles at concentrations ~1 mg/kg in silica sand. 35
Figure 11. X-ray Computed Tomography of Oil-impacted Silica Sand (OSS; A, B, and C) and Silica Sand (SS; D, E, and F) samples. In each cuvette, the top portion contains sand contacted with Formulation A nanoparticles for 48 h, filtered, washed, and dried while the bottom portion contains the respective control (CTRL) sand, as indicated in B and E. A and D show the top view of each cuvette packed with OSS and SS, respectively. B and E show the side view of each cuvette packed with OSS and SS, respectively. C and F show a 3-D volumetric reconstruction of each cuvette for OSS and SS, respectively. 36
Figure 12. Engineered nanoparticles with a Pluronic coating are transported through a clean sandy loam and preferentially retained in an artificially PHC-impacted sandy loam. 38
Figure 13. TEM composite image of 6 nanoparticle samples coated with different Pluronic polymers. A) F127, B) F108, C) P105, D) P104, E) P103, F) P123. 43
Figure 14. Nanoparticle elution curves resulting from transport through 15 cm saturated packed columns for particles coated with various Pluronic polymers. A) F127, B) F108, C) P105, D) P104, E) P103, F) P123. 45
Figure 15. TEM Composite showing nanoparticle morphology at different Pluronic coating concentrations. A) 1 g/L, B) 2.5 g/L, C) 5 g/L, D) 10 g/L 46
Figure 16. Nanoparticle elution curves resulting from transport through 15 cm saturated packed columns for particles coated with L62-P104 Pluronic in a 4:1 ratio at various concentrations: A) 1 g/L, B) 5 g/L, C) 10 g/L. 47
Figure 17. Nanoparticle elution profiles for SPIONs coated with 1 g/L 4:1 L62:P104 Pluronic. Panels show recovery through **A)** clean Borden sand and **B)** oily Borden sand (1.5% m/m). 48
Figure 18. Nanoparticle elution profiles for SPIONs coated with 2.5 g/L 4:1 L62:P104 Pluronic. Panels show recovery through A) clean Borden sand and B) oily Borden sand (1.5% m/m). 49
Figure 19. Schematic illustrating conditions under which preferential NP binding occurs. NP binding to PHC-impacted sediments decreases with increasing NP Pluronic coating concentration, increases with increasing PHC concentration and PHC chain length, and is unaffected by pH conditions. 51

Figure 20. TEM composite showing nanoparticles synthesized with different Pluronic coating concentrations: **A)** 1g/L, **B)** 2.5 g/L, **C)** 5 g/L, **D)** 7.5 g/L, **E)** 10 g/L. At lower Pluronic coating concentrations, nanoparticles agglomerate into larger, spherical aggregates (panels **A,B**). At higher coating concentrations, nanoparticles are individually stabilized and there is an absence of aggregates (panels **D,E**). 57
Figure 21. Effect of Pluronic NP coating concentration on binding to PHC-impacted sediments: **A)** concentration of iron in NP suspension initially, and after contact with clean sand or crude oil-impacted sand; **B)** normalized concentration of iron in NP suspension after contact with clean sand or crude oil-impacted sand; **C)** estimated mass of NP bound to sand after contact with clean sand or crude oil-impacted sand..... 58
Figure 22. Influence of oil concentration **(A, B)** and type **(C)** on nanoparticle binding. **A)** NP binding to oil-impacted sand increases as oil concentration in the sand increases. **B)** Estimated NP binding normalized by mass of sand or mass of oil. As the oil concentration in the sand increases, NP increases but reaches a threshold point. This is also demonstrated by the decreasing mass of NP bound per mass of oil present in the sand. **C)** NP binding increases as the gravity and hydrocarbon chain length of the oil increases. 60
Figure 23. Surface response plot showing how NP binding is influenced by crude oil concentration and oil type. At high oil concentrations, binding significantly increases as oils increase in gravity and hydrocarbon chain length. For high gravity oils, binding significantly increases as oil concentration increases. The horizontal plane at the bottom of the figure represents nanoparticle binding to clean Borden Sand under identical test conditions..... 62
Figure 24. Effect of temperature **(A)** and pH **(B)** on NP binding to oil-impacted sand. As temperature increases, approaching the LCST of Pluronic, binding of NP to oil-impacted sand increases. Over the pH range of 5 to 9, pH was not found to significantly influence NP binding to oil-impacted sand. 64
Figure 25. Observed (symbols) and simulated (black line) nanoparticle BTCs in clean (left panels) and oil-impacted (right panels) Borden Sand packed columns. For comparison, the tracer BTCs (red line) are shown for simulations using the column specific porosity, dispersivity and stop-flow conditions. 66
Figure 26. Comparison of observed (symbols) and simulated (lines) bromide breakthrough curves for the columns packed with clean Borden sand (left panels) and oil-impacted Borden sand (right panels). Each experimental system was performed in triplicate (vertically descending from trial 1 to 3). 67
Figure 27. 1D-USAT simulations of NP attached mass profiles over a 15 cm column under **A)** different flow rates and **B)** different $Mattachmax$. Different $Mattachmax$ values are representative of how NP binding changes with different oil type and concentration. 69

Figure 28. 1D-USAT simulations of NP attached mass profiles in a 1 m column containing an impacted zone under continuous flow conditions. The column geometry consists, from top to bottom, of a 50 cm zone of BS, a 30 cm zone of OBS, and a final 20 cm zone of BS. $Mattachmax$ and k_{attach}/k_{detach} values were selected for each zone according to the average values from **Table 10**. Panel **A)** shows how attached mass profile changes with flow rate (constant injection concentration = 400 mg/L) and panel **B)** shows how attached mass profile changes with input concentration (constant flow rate = 4 x 10^{-6} m/s)..... 70
Figure 29. Schematic illustrating Pluronic self-assembly onto various oleic acid-coated nanoparticles and subsequent targeted binding behaviour toward PHC-impacted porous media; NP attach to crude oil coated sand and transport through clean sand. 73
Figure 30. TEM characterization of nanoparticle samples composed of different materials (**Top Row:** iron oxide, **Middle Row:** silver, **Bottom Row:** cobalt ferrite) and different coatings (**Left Column:** oleic acid, **Middle Column:** 1 g/L Pluronic solution, **Right Column:** 10 g/L Pluronic solution). Nanoparticle morphology was strongly dependent on coating rather than material composition. 81
Figure 31. Batch binding trials demonstrating 1g/L Pluronic-coated nanoparticles preferentially binding to 1.5% m/m crude oil-coated Borden sand (OBS) at room temperature and at 50 ºC. **A)** ion concentration in the aqueous phase as measured by ICP, **B)** estimated solid-phase NP concentration from $[ion]_{aq}$ measurements. Increased temperature increases nanoparticle attachment to both clean and oily sand. 82
Figure 32. Measurement of NP binding to clean (BS) or 1.5% crude oil-coated Borden Sand (OBS) at room temperature (RT; ~22 ºC) or 50 ºC. Two analytical methods are being compared – indirect (aq) and direct (s) measurement of NP solid-phase concentration. All corresponding measurements (e.g. RT BS (aq) and RT BS (s)) are equal within one standard deviation except RT OBS. 83
Figure 33. Effect of Pluronic coating concentration on Iron Oxide (Fe) and Silver (Ag) nanoparticle binding to clean (BS) and 1.5% crude oil-coated (OBS) Borden Sand at 50 ºC. It appeared that binding of iron oxide particles to both BS and OBS increased with coating concentration while binding of silver particles was completely unaffected. Overall, it appeared that coating concentration had little influence on nanoparticle binding at 50 ºC. 84
Figure 34. Elution profiles displaying the transport and binding of 10 g/L Pluronic coated iron oxide nanoparticles through clean and oily Borden Sand. L = 15 cm, Q = 0.3 mL/min, stop flow from 95 min to 2740 min. Nanoparticle elution is clearly observed in all clean sand columns, while nanoparticle retention is observed in all oily sand columns. 85
Figure 35. Elution profiles displaying the transport and binding of 10 g/L Pluronic coated silver nanoparticles through clean and oily Borden Sand. L = 15 cm, Q = 0.3 mL/min, stop flow from 95 min to 2740 min. Nanoparticle elution is clearly observed in all clean sand columns, while nanoparticle retention is observed in all oily sand columns. 86

Figure 36. Elution profiles displaying the transport and binding of 10 g/L Pluronic coated cobalt ferrite nanoparticles through clean and oily Borden Sand. L = 15 cm, Q = 0.3 mL/min, stop flow from 95 min to 2763 min. Nanoparticle elution is clearly observed in all clean sand columns, and some nanoparticle elution from aqueous cobalt recovery is observed in all oily columns. 87
Figure 37. Comparison of observed (symbols) and simulated (lines) bromide breakthrough curves for the columns packed with clean Borden sand (left panels) and oil-impacted Borden sand (right panels) used for transport and binding experiments using iron oxide nanoparticles. Each experimental system was performed in triplicate (vertically descending from trial 1 to 3). 88
Figure 38. Comparison of observed (symbols) and simulated (lines) bromide breakthrough curves for the columns packed with clean Borden sand (left panels) and oil-impacted Borden sand (right panels) used for transport and binding experiments using silver nanoparticles. Each experimental system was performed in triplicate (vertically descending from trial 1 to 3). 89
Figure 39. Comparison of observed (symbols) and simulated (lines) bromide breakthrough curves for the columns packed with clean Borden sand (left panels) and oil-impacted Borden sand (right panels) used for transport and binding experiments using cobalt ferrite nanoparticles. The clean sand experimental system was performed in duplicate owing to a leak in one of the columns (vertically descending from trial 1 to 2). The oily sand experimental system was performed in triplicate (vertically descending from trial 1 to 3). 90

List of Tables

Table 1. Soil remediation *in situ* and *ex situ* technologies 6
Table 2. Metals removal by nZVI reduction 9
Table 3. Summary of nanoparticle formulations explored in Chapter 3 26
Table 4. Properties of Pluronic polymers used for amphiphilic nanoparticle coating in Chapter 3 28
Table 5. Properties of Pluronic coating polymers discussed in Chapter 4. 42
Table 6. Nanoparticle Sizes from TEM and DLS sizing. TEM diameter is the average of 100 particle measurements from the corresponding panel in **Figure 13**. 43
Table 7. Properties of pluronic co-polymers used in Chapter 5. 54
Table 8. Selection of variables for surface response plot showing effect of oil concentration and oil type on Nanoparticle binding to Borden Sand. 61
Table 9. Calibrated effective porosity and dispersivity values for each column trial. 66
Table 10. Estimated attachment-detachment kinetic model parameters from equation (23). $Mattachmax$ values were adopted from the binding batch tests (**Figure 24**, 50°C). Minimum k_{attach} values were estimated for the OBS packed columns. 68
Table 11. Column physical parameters for all transport & binding experiments 90
Table 12. Attachment parameters estimated from 1D-USAT/DDS fitting of experimental data for various nanoparticle samples to clean Borden Sand (BS). 91
Table 13. Attachment parameters estimated from 1D-USAT/DDS fitting of experimental data for various nanoparticle samples to oily Borden Sand (OBS) 91

Chapter 1

Introduction

1.1 Overview

Terrestrial contamination of soils by petroleum hydrocarbons (PHC) is a global environmental issue which is severe and widespread, resulting from petroleum industry activities such as exploration, extraction, refining, and transportation. PHC contamination, including crude oil, is an issue of environmental concern due to the acute and chronic toxic effects of such compounds, as well as their environmental persistence, necessitating human intervention for the cleanup of such sites. Remediation of PHC-impacted soils is a challenging problem, however, because of the nature of PHC contaminants, how they interact with porous media, and their relative inaccessibility in subsurface environments.

Traditional remediation of PHC-impacted soil makes use of primarily *ex-situ* treatments, requiring the contaminated material to be excavated which imposes large costs and is ultimately environmentally disruptive and unsustainable. In response, more cost-efficient, less disruptive technologies have been introduced which do not require excavation and are known as *in-situ* treatments. Such treatments include bioremediation, chemical oxidation, thermal desorption, and injection of reactive nanoparticles.

Nanoremediation, mostly consisting of nano zero valent iron (nZVI) for the treatment of chlorinated hydrocarbons, makes use of nanoscale material properties such as small particle diameter to avoid filtration in porous media and high surface area to allow fast reaction kinetics toward contaminants. One of the greatest challenges facing field application of nanoscale treatment agents is subsurface mobility of the particles which is limited by aggregation and gravimetric settling, as well as adsorption to porous media material. Consequently, nanoparticle stabilization through surface functionalization with polymeric materials has been the focus of significant research over the past two decades. This has led to significant improvements in nanoparticle mobility, but also introduced concerns regarding the unknown fate and environmental toxicity of released nanoparticles. Furthermore, PHC-impacted porous media typically exhibits heterogenous contaminant distribution and relying on a homogenously distributed nanomaterial from point-source injection may result in inefficient use of the treatment agent.

This thesis explores the use of polymeric nanoparticle coatings which facilitate nanoparticle stability in aqueous suspension, mobility through porous media, and preferential adsorption to PHC molecules distributed in a porous medium. This targeted binding approach seeks to mitigate concerns regarding unknown nanoparticle fate and inefficient use of treatment agent by accumulating injected nanoparticles at the subsurface site of contamination. By promoting adsorptive interactions between the

nanoparticle and the contaminant-water interface, particles can be concentrated at the contaminant interface, enabling more efficient treatment, and fewer particles may mobilize beyond the encountered zones of PHC-impacted porous media, reducing the amount of nanoparticles distributed to the wider environment.

Targeted nanoparticle binding to crude oil, the selected PHC contaminant of concern, was achieved through a two-step functionalization process whereby the nanoparticle is first coated with oleic acid, which attaches directly to the surface, then the hydrophobic nanoparticle is coated with a blend of amphiphilic Pluronic block co-polymers to provide aqueous stability and favourable interactions with the crude oil interface. The mobility and binding performance of the coated particles was assessed through binding batch studies as well as packed column flowthrough studies where the particles were exposed to crude oil-impacted or unmodified natural sediment acting as a model porous medium. Various factors influencing nanoparticle mobility and binding were investigated, such as Pluronic molecular structure, Pluronic coating concentration, crude oil type, crude oil concentration, temperature, and pH. A solute transport simulation, 1D-USAT, was implemented to extract kinetic parameters defining nanoparticle transport in clean vs. oil-impacted porous media from experimental data. Use of Pluronic-coated nanoparticles with targeted binding toward crude oil-impacted porous media as contrast agent for subsurface detection and sensing via X-Ray computed tomography (CT) was explored as a potential application for this technology. Finally, the nanoparticle coatings were applied to a variety of nanoparticle core materials, all produced through different synthetic methods to evaluate the versatility of this coating strategy and its applicability to various nanomaterials which may be employed in a subsurface environment. Some pathways of interesting future work to explore include investigating the role that flow rate and temperature play in a continuous-flow transport and binding environment, investigating nanoparticle transport and binding in heterogeneously impacted higher dimension experimental environments, applying this nanoparticle coating technology to commonly used nanoremediation agents such as nZVI, and further investigating the role that targeted binding nanoparticles can play in enhancing subsurface sensing and detection technologies such as spectral induced polarization (SIP) and X-Ray CT.

1.2 Research Objectives

The overall objective of this research project was to develop a nanoparticle coating which would enable targeted binding behaviour of a nanoparticle to crude oil in subsurface porous media environments. The colloid transport and targeted binding behaviour of coated nanoparticles was first established. The influence of nanoparticle coating formulation as well as environmental factors on nanoparticle transport and binding were then investigated and used to demonstrate nanoparticle transport and binding in model soil systems. A colloid transport model was used to describe the transport behaviour of the coated nanoparticles in oil-impacted and clean systems. Finally, the coating was applied to various

nanoparticles produced using different synthetic methods, demonstrating the versatile application of the developed coating.

The specific objectives of this study are as follows:

1. Demonstrate the ability of Pluronic-coated nanoparticles to bind to crude-oil impacted porous media
   - Investigate nanoparticle preferential attachment to crude oil-impacted sediments in binding batch tests by assessing metals concentration in aqueous suspension
   - Determine the effect of coating formulation on binding
   - Confirm ICP aqueous-phase binding with solid-phase analysis

2. Demonstrate the ability of Pluronic-coated nanoparticles to transport through real aquifer porous media material
   - Investigate nanoparticle transport in natural sand packed columns
   - Determine the effect of nanoparticle coating formulation on morphology and transport behaviour
   - Demonstrate nanoparticle transport and preferential binding in an oil-impacted packed column

3. Determine the effect of key coating and environmental parameters on nanoparticle binding
   - Determine the effect of coating concentration on binding behaviour
   - Determine how oil type, oil concentration, temperature, and pH influence binding in batch conditions
   - Demonstrate nanoparticle binding and transport under favourable conditions in packed columns containing natural aquifer porous media
   - Describe nanoparticle transport behaviour using a modified advection dispersion equation; use generated parameters to predict transport behaviour under various conditions

4. Demonstrate applicability and performance of coating when applied to different types of nanoparticles
   - Develop coating strategy suitable for various nanoparticles produced using different syntheses
   - Demonstrate nanoparticle transport and binding for all coated materials in sand packed columns

1.3 Thesis Outline

This thesis is comprised of seven chapters; an introduction, a literature review, four experimental research-based chapters, and a final chapter discussing conclusions and recommendations for future work. This chapter, the first, introduces the problems addressed herein, the hypothesis for this work, and the specific research objectives pursued to test this hypothesis.

Chapter 2 reviews the current state-of-the-art in the field of nanoremediation, including nanoparticle treatment agents, colloid filtration theory (CFT), nanoparticle coating materials, and previous research on targeted delivery of nanoremediation agents to subsurface environments. A brief summary of findings and directions for future research are presented.

Chapter 3 describes the synthesis of iron oxide nanoparticles and subsequent functionalization with a Pluronic coating to endow the particles with aqueous stability and adsorptive interaction with crude oil-impacted porous media. The nanoparticles display preferential binding to oil-impacted sand in binding batch tests and are used as a contrast agent for an X-Ray CT scan, where oil-impacted sands exposed to nanoparticles could be distinguished from clean sands exposed to nanoparticles by virtue of a higher concentration of nanoparticles retained in the oil-impacted sand.

Chapter 4 describes nanoparticle application in transport experiments and investigates how the polymer coating formulation influences mobility and retention in packed sand columns. Different Pluronic molecules and coating concentrations were found to alter transport behaviour, and transport & binding in a column packed with crude oil-impacted natural sediment was demonstrated using two nanoparticle coating formulations. This work indicates that coating formulation may be tuned to target specific degrees of mobility or binding in porous media.

Chapter 5 investigates the effect of coating properties and porous medium environmental factors on nanoparticle binding to crude oil-impacted porous media. The factors investigated include nanoparticle coating concentration, crude oil type, crude oil concentration, ambient temperature, and pH. These parameters, particularly temperature, were used to demonstrate significant nanoparticle attachment to oil-impacted natural sediment in packed columns. These flowthrough experiments were used in conjunction with a solute transport simulation, 1D-USAT, to extract kinetic parameters describing nanoparticle transport and attachment.

Chapter 6 demonstrates the application of the nanoparticle coating strategy to different types of nanoparticles produced using various synthetic methods. Binding behaviour was assessed using binding batch experiments at multiple temperatures as well as flow-through transport and binding experiments in columns packed with natural sediments. A solute transport simulation, 1D-USAT, was used to extract kinetic parameters describing nanoparticle transport and attachment which match closely with batch experiment results. Binding and transport behaviour was attributed to the functional coating and targeted binding was achieved using the same coating on different nanoparticles.

Chapter 7 summarizes the findings of the research discussed in chapters 3 to 6 and draws conclusions based on this work. Overall, it was found that a nanoparticle functional coating designed to facilitate mobility through clean porous media and targeted attachment to oil-impacted porous media under flow-through conditions was successfully developed. Furthermore, the coating could be applied to

multiple types of nanoparticles and tuned to improve mobility or binding by altering the polymer coating formulation. Important next research steps are highlighted, such as examining the effect of flow rate, temperature, and oil concentration in nanoparticle transport and binding experiments with continuous flow, applying this nanoparticle coating to common nanoremediation agents such as nZVI, and exploring application of targeted nanoparticle binding in subsurface sensing technologies such as X-Ray CT and SIP.

Chapter 2

Literature Review

2.1 Heavy Hydrocarbon Impacted Soils & Remediation Technologies

The petroleum industry is the largest and one of the most important industries in the modern world. Global dependence on petroleum has fueled vast economic development and technological advancement, supporting society as we currently know it. While the benefits of petroleum technology are extensive, this powerful energy source is not without its downsides. Contamination of water and land by Petroleum Hydrocarbons (PHCs) is a major source of environmental concern. While major ocean-based oil spills experience the most press coverage, terrestrial oil spills actually make up the majority of global oil spills[1]. PHC contamination during exploration, extraction, refining, and transportation have resulted in over 3,000 officially registered contaminated soil sites in Canada alone[2].

Heavy hydrocarbon contamination, such as spills of crude oil, are of particular concern since heavy crude often contains a complex mixture of organic compounds including long chain alkanes, aromatics, and polycyclic aromatic hydrocarbons (PAHs) which may have chronic or acute toxic effects on a variety of organisms[3–5]. Furthermore, the penetration of crude oil into sediments affects its water and air transport properties, impacting biological processes of microbes and plants[3,5]. Due to the chemical nature of heavy hydrocarbons and their interaction with porous media, the challenge of PHC-impacted soil remediation is a complex and difficult problem. Penetration of PHCs into sediments and adsorption to soil matter make accessing the pollutant non-trivial, and further complicates remediation techniques.

PHC contaminated soil remediation strategies can be broadly divided into two categories, *in situ* and *ex situ*. *In situ* technology performs remediation work by applying the treatment to the contaminated soil site without disrupting the surrounding environment while *ex situ* treatment excavates contaminated soil to enable improved access to contaminants and easier treatment application. These categories can each be further divided into thermal, chemical, physical and biological treatments as shown in **Table 1**.

Table 1. Soil remediation *in situ* and *ex situ* technologies

Category	***In situ***	***Ex situ***
Thermal	Thermal desorption Microwave assisted steam	Thermal desorption Incineration
Chemical	Oxidation	Oxidation
Physical	Capping Soil washing	Excavation and disposal Soil washing
Biological	Biostimulation Bioaugmentation	Land farming

The most commonly employed remediation strategies are *ex situ* excavation and disposal or excavation and incineration due to the simplicity and minimization of uncertainty that these techniques provide[6,7]. While easily controllable and effective, excavation techniques are costly, disruptive to the environment, and unsustainable due to disposal of treated sediments in landfills[8]. Similar *ex situ* techniques such as chemical oxidation and soil washing pose additional disadvantages due to higher treatment costs and increased risk of residual contamination. Even *ex situ* land farming, which saves operational costs due to its low energy and additive inputs, still has to address the initial cost of excavation and risk associated with transport of contaminated sediments. In contrast, *in situ* remediation techniques offer the possibility of a less expensive, more sustainable solution[8].

While *in situ* techniques are promising in terms of cost, environmental impact, and long-term sustainability, they are not without disadvantages. The most widely employed *in situ* remediation technique is bioremediation, which is the use of naturally occurring microbes to metabolize the contaminants. This technique has minimal environmental impact but limited applicability to heavy oils due to the presence of biorefractory compounds. Furthermore, bioremediation is a slow process and somewhat temperature dependent making it best suited to warmer climates[9]. *In situ* chemical oxidation (ISCO) is quick and effective with less selectivity compared to bioremediation, but is very sensitive to the geochemistry of the application area and can require multiple injections of consumable chemicals, increasing its cost and limiting its sustainability[9]. Finally, *in situ* thermal desorption strategies employ steam generation to desorb and vaporize oils from sediments, enabling them to be pumped out using vapour extraction techniques. Traditional thermal desorption techniques can be prohibitively expensive due to poor heat transfer from outside the sediment to the site of the contaminant and the large area to which heat must be applied[9]. More recent research into microwave (MW) assisted steam generation and radio frequency (RF) soil heating have revealed a much more energy efficient heating process due to uniform heating of the mass rather than radiative heating layer-by-layer[10]. These techniques are limited by poor penetration depth of radiation at higher frequencies and the moisture content requirement of soil in order for heating to occur.

Each of the techniques discussed has the potential to be improved through the application of various amendments, for example, stimulation of microbes by adding nutrients in the case of bioremediation. ISCO techniques such as persulfate oxidation can be 'activated' by the presence of a Fenton catalyst such as Fe^{2+} or a metal oxide[9,11]. In the case of microwave/RF assisted thermal desorption, the addition of an amendment that improves EM radiation absorption, localized heating, and generation of oxidative species has the potential to improve the energy efficiency of treatment as well as total treatment

time[12]. In each of these cases, delivery of nanoparticles to contaminated sites has the potential to enhance *in situ* remediation. As well as acting as amendments for existing remediation techniques, nanoparticle delivery has been investigated as its own remediation strategy with promising results in recent years.

2.2 Nanoparticles in Soil Remediation

The most commonly applied nanomaterial for soil remediation is Zero Valent Iron (ZVI). It is a redox active material capable of degrading a wide range of organic compounds as well as immobilizing toxic heavy metals[13]. ZVI got its start applied as a bulk material in permeable reactive barrier technology to control and contain contaminants which would otherwise be dispersed by groundwater[14–16]. Nano Zero Valent Iron is an extension of this technology tailored more towards targeted remediation of source zones rather than controlling and containing contamination. The more reactive, mobile nZVI particles may be injected at the site of contamination for express reaction with the contaminant of concern[13].

2.2.1 Contaminants Addressed by nZVI

The principal contaminants addressed by nZVI are chlorinated hydrocarbons and toxic heavy metals. nZVI reacts with chlorinated hydrocarbons via a reductive pathway (1) - (3).

$$Fe^0 \rightarrow Fe^{2+} + 2e^- \quad (1)$$

$$H_2O \rightarrow H^+ + OH^- \quad (2)$$

$$R\text{-}Cl + H^+ + 2e^- \rightarrow R\text{-}H + Cl^- \quad (3)$$

Where R represents a generic hydrocarbon. Fast reductive dichlorination with standard redox potential E_h = -0.44 V represents a niche use-case in which nZVI has found significant application, however, by-products from the dechlorination reaction such as acetylene, ethene, and ethane are not efficient oxidants for nZVI and are not fully degraded[17]. For example, in the case of trichloroethylene (TCE), a common example chlorinated hydrocarbon (4).

$$C_2HCl_3 + 3Fe^0 + 3H^+ \rightarrow C_2H_4 + 3Fe^{2+} + 3Cl^- \quad (4)$$

To achieve complete mineralization of contaminants such as TCE, nZVI may be employed as a source of Fe^{2+} ions and act as an activator of persulfate or peroxide[18–20]. In particular, persulfate has enjoyed significant popularity as an oxidant due to its high oxidation potential compared to other oxidants (E_h = 2.01 V) which can be further enhanced through activation to produce sulfate free radical species (E_h = 2.6 V). nZVI activation of persulfate for the degradation of TCE follows reaction scheme (5) & (6)[19,21].

$$Fe^{2+} + S_2O_8^{2-} \rightarrow Fe^{3+} + SO_4^{2-} + SO_4^{-}\cdot \quad (5)$$

$$6SO_4^{-\cdot} + C_2HCl_3 + 4H_2O \rightarrow 2CO_2 + 9H^+ + 3Cl^- + 6SO_4^{2-} \quad (6)$$

Consequently, nZVI may be used in conjunction with persulfate to achieve complete mineralization of a wide range of hydrocarbon contaminants[22–24]. A major drawback of the nZVI-activated persulfate system is surface passivation due to buildup of iron sulfate on the surface of the particles. Recent research has found that passivation may be slowed by adding chelating agents such as EDTA to the reaction system[24].

In the case of inorganic contaminants such as heavy metals, removal is dependent on both reduction by nZVI and adsorption to the iron oxide or iron oxyhydroxide shell that forms around the surface of the nZVI particle[25]. Various reactions between produced iron ions, the zero valent iron, oxygen, and water lead to the generation of these oxide and oxyhydroxide shells (7) - (11)[19,25].

$$Fe^{3+} + 3OH^- \rightarrow Fe(OH)_3 \quad (7)$$

$$Fe(OH)_3 \rightarrow FeOOH + H_2O \quad (8)$$

$$2Fe^0 + O_2 \rightarrow 2FeO \quad (9)$$

$$6FeO + O_2 \rightarrow 2Fe_3O_4 \quad (10)$$

$$4Fe_3O_4 + O_2 \rightarrow 6Fe_2O_3 \quad (11)$$

These oxidation reactions occur immediately in oxygen rich environments, often during nZVI synthesis, meaning typical nZVI particles always exhibit an oxide shell[25,26]. Furthermore, this process limits the overall particle size of nZVI. The typical oxide layer thickness is ~3 nm on all nZVI particles and particles smaller than 8 nm in diameter cannot support an iron oxide shell – in this case the particle is fully oxidized and no zero valent iron is present[25]. nZVI-mediated metals removal proceeds through a reduction and adsorption mechanism if the redox potential of the metal cation in question is more positive than the standard redox potential of nZVI (E_h = -0.44 V). If the redox potential of the metal cation is more negative than this value, removal proceeds through an adsorption only mechanism. The standard reduction potential of common metal cation contaminants is provided in **Table 2**.

Table 2. Metals removal by nZVI reduction

Metal Contaminant	**Reduction**	E_h^0 **(V)**	**Removal Mechanism**
Chromium	$Cr^{(VI)}_2O_7^{2-}$ / Cr^{3+}	1.33	Reduction, Adsorption, Coprecipitation
Mercury	Hg^{2+} / Hg^0	0.85	Reduction, Adsorption

Selenium	$Se^{(VI)}O_4^{2-}$ / $Se^{(IV)}O_3^{2-}$	0.82	Reduction, Adsorption
Arsenic	$As^{(V)}O_4^{3-}$ / $As^{(III)}O_3^{3-}$	0.57	Reduction, Adsorption, Complexation, Oxidation
Uranium	$U^{(VI)}O_2^{2+}$ / $U^{(IV)}O_2$	0.41	Reduction, Adsorption
Copper	Cu^{2+} / Cu^0	0.34	Reduction, Adsorption
Lead	Pb^{2+} / Pb^0	-0.13	Reduction, Adsorption
Nickel	Ni^{2+} / Ni^0	-0.25	Reduction, Adsorption
Cobalt	Co^{2+} / Co^0	-0.28	Reduction, Adsorption, Coprecipitation
Cadmium	Cd^{2+} / Cd^0	-0.40	Adsorption, Coprecipitation
Zinc	Zn^{2+} / Zn^0	-0.76	Adsorption, Coprecipitation
Barium	Ba^{2+} / Ba^0	-2.91	Adsorption, Coprecipitation

The corresponding removal mechanisms have some exceptions. While most metals capable of being reduced by nZVI end up as zero valent metals adsorbed on the surface of the iron particle, multi valent ions such as selenium, chromium, and arsenic experience varied an more complex pathways. Selenium is removed through a step-by-step reduction where $Se^{(VI)}$ is reduced to $Se^{(IV)}$ which can adsorb onto the nZVI surface. From here, the selenium may stay as selenite or be further reduced to Se^0 [27]. In the case of chromium, $Cr^{(VI)}$ is first reduced to $Cr^{(III)}$ which adsorbs to the nZVI surface and eventually precipitates with hydroxyl groups to form Cr_2O_3 or coprecipitates with Fe^{2+} to form Cr_2FeO_4 [28]. Arsenic presents a complicated removal mechanism whereby reduced $As^{(III)}$ diffuses through the iron oxide/oxyhydroxide shell of the particle and adsorbs directly to the nZVI surface through an inner-sphere complexation route. This $As^{(III)}$ may be simultaneously reduced by the Fe^0 core and oxidized by reacting with the oxide shell, eventually depositing as As^0 between the nZVI core and oxide shell[29]. Metals unable to be reduced by nZVI are typically precipitated or co-precipitated as metal hydroxides on the surface of the nZVI, increasing their removal capacity beyond what would be predicted for ion adsorption alone.

2.2.2 Recent Advances: Catalyst Improvement

Nano-scale engineering of nZVI particles is primarily focused on improving two attributes of the material; 1) improving reaction kinetics and treatment efficiency, and 2) improving dispersibility in porous media environments. Improving the treatment efficiency of nZVI is typically done by engineering the surface of the material to either incorporate sorbents or chelating agents to draw contaminants close to the reaction or sorption site, or by functionalizing the particle with conducting materials which catalyze reduction. Treatment efficiency can also be improved through protecting the nZVI surface from passivation in the activated persulfate reaction by using chelating agents.

Toward improving the treatment efficiency of nZVI nanoparticles, recent work by Gu et al. incorporates several modifications to improve different aspects of the reduction mechanism, using a reduced graphene oxide (rGO) sheet as a platform to support polydopamine functionalized nZVI particles[30,31]. The polydopamine blocks oxygen access to the nZVI particles and chelates Fe^{2+} ions, slowing passivation by iron sulfate while the rGO sheet prevents nZVI aggregation, adsorbs polyaromatic contaminants through π-π interactions, and facilitates electron transfer from the nZVI to adsorbed contaminants[30,31]. In a similar manner, compositing nZVI with adsorptive materials such as activated carbon, graphene, or biochar is a common strategy to achieve faster contaminant removal by making use of the support material to adsorb the contaminant quickly, then rely on the nZVI component to reduce and detoxify it over the long term[32–37]. Incorporating catalytic metals has long been understood to enhance reductive dechlorination by changing the mechanism to dehalogenation via hydrogen reduction rather than direct electron transfer[38]. These bimetallic particles typically use Pd or Ni as the catalyst to improve selectivity and rate of reduction[38–40], however the economics of particle production using these more expensive materials prohibits large scale implementation of this technology. Recently, a great deal of research attention has been devoted to sulfidized nZVI (S-nZVI), which produces enhanced reactivity and selectivity for reductive dechlorination and metal ion removal using lower cost sulfur instead of expensive metallic elements[41–44]. The dechlorination mechanism for S-nZVI particles differs from bimetallic catalysts in that it has been identified as electron transfer at FeS surface sites rather than hydrogen reduction[45], however the full mechanism has not yet been elucidated. Other recent work by Bhattacharjee and Ghoshal has found that S-nZVI can reach similar degradation efficiencies at Pd-nZVI by controlling the structure of FeS deposition on the particles through co-precipitation during synthesis, offering a particle with highly efficient reductive dechlorination at costs 70% lower than Pd-nZVI[46]. S-nZVI synthesis and application is a rapidly developing research area with highly promising results for improving nZVI remediation technology in all soil remediation areas.

2.2.3 Recent Advances: nZVI Dispersibility

Improvement of nZVI dispersibility addresses one of the primary drawbacks of nZVI for soil remediation – emplacement of the remediation agent at the treatment site. Uncoated nZVI is extremely prone to aggregation and filtration within the porous medium, leading to transport distances of less than 10 cm under typical conditions[47,48]. To address this problem, polymeric coating molecules are used to reduce aggregation, enhance aqueous stability, and improve the mobility of the particles. Commonly applied polymeric coatings include carboxymethyl cellulose (CMC)[36,49–52], polyacrylic acid (PAA)[50,53], polystyrene sulfonate[54], and xanthan gum[50,55,56] which rely on electrostatic and steric stabilization mechanisms to prevent nanoparticle aggregation and prevent attachment to porous media material.

Coating of nZVI particles is performed through favourable intermolecular interactions between the iron oxide/oxyhydroxide surface of the nZVI particle and carboxylate groups present in the polymeric coating. The carboxylate group performs a monodentate complexation of surface iron atoms which anchors the polymer in place[52] with an interaction energy of 770 – 788 kcal/mol, producing extremely stable attachments[57].

Other mobility enhancement strategies involve nZVI particles supported on mobile support materials, such as mesoporous silica[58–60] or carbonaceous particles[36,37,61]. These strategies rely on the support material to immobilize the nZVI particles, preventing them from aggregating and preventing mobility loss due to sedimentation. The reduced aggregation also has the side effect of maintaining nZVI reductive activity for longer periods of time as the surface area is maintained due to limited aggregation[58]. In a similar vein, silica coating strategies can prevent nZVI aggregation while allowing smaller mobile particle sizes and maintaining contaminant access to the reductive iron surface[62].

A major concern in the world of soil remediation is the fate of engineered nanomaterials released to the environment. Many reviews have pointed out the environmental risks associated with uncontrolled nanoparticle release, a concern which grows in relevance as the mobility of nanoparticles is enhanced by using composites and coatings[63–66]. Nanoparticles functionalized to exhibit controlled mobility are therefore interesting and relevant for addressing this challenge. One approach towards controlled mobility is the application of nanoparticle coatings with targeted interactions toward contaminants of interest. This concept has been demonstrated in various ways using nanoparticles with aliphatic coatings to provide aqueous stability and favourable interaction with contaminants[67–70]. nZVI particular examples have demonstrated this capability by using a triblock copolymer in which each block provides a specific functionality – a carboxylate-rich block facilitates attachment to the nZVI particle, a hydrophilic block enables aqueous stability, and a hydrophobic block enables interaction with a contaminant of concern[68]. Thus far, contaminants including trichloroethylene[68], dodecane[54], and crude oil[71], as well as model aliphatic compounds such as octadecylichlorosilane[69] have been successfully targeted using functional surfactant coatings. Such functional coatings limit nanoparticle fate by immobilizing nanoparticles at the site of contamination and this has potential to enhance cost-effectiveness and efficiency of *in situ* soil remediation, as well as enable subsurface detection of contaminants by acting as a contrast agent. Other approaches to controlling nanoparticle fate involve time-mediated mobility of particles where the coating preventing nZVI aggregation dissolves or wears off, rendering the particles immobile shortly after application. This has been achieved recently by using nZVI coated with $Mg(OH)_2$ which dissolves in water as it transports through porous media[72].

2.3 Other Nanomaterials for Adsorptive Contaminant Removal

Aside from nZVI, there are a variety of inorganic nanoparticles which facilitate toxic metals removal in subsurface environment through adsorption, inclusion, and precipitation. The major contaminants of concern in this context include toxic heavy metal ions, such as Cd^{2+}, Hg^{2+}, and Pb^{2+}, and toxic oxyanions or metalloids such as selenate (SeO_4^{2-}) and arsenate (AsO_4^{3-}). The adsorptive properties of mineral materials toward these toxic metal species has long been understood, but application in subsurface environments has remained a challenge due to their limited mobility through porous media and tendency to aggregate. Synthesis and stabilization of mineral nanoparticles overcomes this barrier by addressing the mobility and aggregation issues associated with bulk scale materials. Use of nanoscale materials also has the significant benefit of providing more surface area and sorption sites, thereby increasing metals removal efficiency per mass of sorbent.

Nanoparticle stabilization is achieved through the use of polymeric coatings which impart electrosteric or steric stabilization. Most of the nanomaterials used in this application are iron based, so the attachment mechanism anchoring the coating to the particles is typically monodentate or bidentate complexation with surface ions, similar to the coating methods used for nZVI. To this end, most of the coating materials are rich in carboxylate functional groups – prominent examples include carboxymethyl cellulose (CMC) and polyacrylic acid (PAA). Commonly applied nanoparticle adsorptive agents include FeS, iron oxides (Fe_2O_3, Fe_3O_4, and FeOOH), $Fe_3(PO_4)_2$, and metal ferrites ($MnFe_2O_4$, Fe_2O_3/MnO_2, Fe_2AlO_4, etc.).

Sorbent selection is a contaminant-specific concern. In the case of metal ion contamination, inorganic nanoparticles make excellent sorbent materials, but in the case of soil contamination by organic compounds such as Petroleum Hydrocarbons (PHCs), different sorbent materials are required. In particular, biochar nanocomposites have proven to be versatile platforms for incorporating a variety of modifications which increase the material's surface area or porosity, change its surface charge, or provide functional groups which promote specific interactions.

2.3.1 Iron Sulfide Nanoparticles

Iron sulfide is an effective sorbent for most divalent cations which are removed through adsorption and coprecipitation, but is especially effective at removing Hg^{2+} which can interact with the sulfide surface and oxidized areas of the nanoparticle through ion exchange, precipitation, and surface complexation[73,74]. Mercury's efficient adsorption to iron sulfide is in part to do with its complimentary Lewis acid-base interaction whereby Hg^{2+} can form a strong bond with sulfur[75]. Iron sulfide can exist in two forms, pyrite (FeS_2) and mackinawite (FeS). The latter has a disordered tetragonal crystal structure which affords it a high specific surface area which contributes to its superior Hg^{2+} affinity. Hg^{2+} removal

via precipitation (12), ion exchange (13), and adsorption (14) is shown briefly in the following reaction schemes:

$$FeS + Hg^{2+} \rightarrow HgS + Fe^{2+} \quad (12)$$

$$FeS + xHg^{2+} \rightarrow Fe_{(1-x)}Hg_xS + xFe^{2+} \ (x < 1) \quad (13)$$

$$FeS + Hg^{2+} \rightarrow Fe\text{-}S\text{-}Hg^{2+} \quad (14)$$

Where precipitation is preceded by partial dissolution of FeS. Effective application of FeS nanoparticles relies on its ability to be transported to the contaminated zone and maintain its high sorption surface area, both problems which are solved through the application of stabilizer coatings such as Carboxymethyl Cellulose (CMC)[73,75], starch[76], and chitosan[77]. Adding such coatings during nanoparticle synthesis greatly improves the particles' Hg^{2+} sorption capacity through two methods – first, the electrosteric interactions of the coating prevent aggregation and preserve FeS surface area, and second, the presence of CMC or starch during synthesis disrupts crystallization, causing a higher surface area, disordered FeS to precipitate[73,76].

2.3.2 Iron Oxide and Metal Ferrite Nanoparticles

Iron oxides demonstrate high scavenging affinity for heavy metal ions due to their large specific surface area and abundant surface hydroxyl groups[78,79]. In particular, iron oxides have a niche application in arsenic removal from groundwater due to their low cost and selectivity toward arsenic, a common and highly toxic contaminant. The adsorption kinetics and capacities of iron-based oxides may be improved by the incorporation of rare earth ions into the iron oxide structure, producing metal ferrites[80]. These metal ferrites exhibit improved adsorption due to the embedded rare earth ion breaking up the iron oxide crystal structure, forcing greater hydroxylation of iron and rare earth atoms which then serve as sites for arsenate complexation (15)[80,81].

$$Fe\text{-}OH + H_3AsO_4 \rightarrow Fe\text{-}O\text{-}AsO(OH)_2 + H_2O \quad (15)$$

Cerium[82,83] and manganese[80,84] are commonly applied as rare earth elements in such metal ferrites, and studies investigating their transport properties in porous media have confirmed increased penetration into small-scale porosity zones when modified by stabilizers such as starch[85]. Further enhancement to arsenic adsorption may be achieved through combining metal ferrites with carbonaceous adsorbents such as biochar and graphene[86,87]. Despite frequent investigation of metal ferrite materials in arsenic and other metal ions' removal from water[88–91], relatively few studies have focused on the *in situ* immobilization of metal species in complex soil environments[92] and investigated viable coating strategies

to support this application. Considering high-concentration arsenic contamination is mainly found in groundwaters[93], this appears to be an underdeveloped research niche.

2.3 Factors Affecting Nanoparticle Transport in Porous Media

Ability for nanoparticles to transport through porous media to access a contaminated site for treatment is a critical step for *in situ* remediation. The most commonly applied strategy for nanoparticle delivery is in the form of injection and flow in aqueous suspension by which nanoparticle transport pathways should mirror the movement of water through porous media. Groundwater flow in its simplest form can be described by Darcy's Law (equation (16), an empirical model in which flow rate is found to be proportional to the pressure differential across the transport region as well as the hydraulic conductivity of the porous medium (**k**) and the viscosity of the fluid (**μ**).

$$q = -\frac{k}{\mu}(\nabla p - \rho g) \tag{16}$$

This model is favoured for its simplicity and allows estimation of single phase flows in porous media by tuning the parameter **k**. Hydraulic conductivity is a measure of the degree to which a medium facilitates fluid transport; a medium with a high hydraulic conductivity, for example gravel ($k = 1 - 10^{-2}$ m/s), allows easy flow of water, while a medium with a low hydraulic conductivity such as clay ($k = 10^{-9} - 10^{-12}$ m/s) restricts water flow or may be impermeable. Hydraulic conductivity of porous media is typically related to the pore size; smaller pores result in lower k values. In real soil sites, heterogeneity and a wide range of hydraulic conductivities contribute to complex groundwater flow patterns and inhibit transport through some regions. This can create difficulties for remediation as forcing injected aqueous suspensions to reach contaminants in low-k zones is a challenge. In these cases, suspended colloids or dissolved species must rely on diffusion to enter saturated pores of low-k media which is a much slower process. For these reasons, significant effort has been devoted to investigating alternative delivery strategies such as hydraulic fracturing and foam-based injection[94–97].

Ideally, the suspended nanoparticles behave like a dissolved species in water and travel directly with groundwater flow experiencing some diffusion and dispersion but total mass conservation, allowing estimation of their transport using an advection/dispersion differential equation (equation (17)

$$\frac{\partial(\phi c)}{\partial t} + \frac{\partial(qc)}{\partial x} - \frac{\partial}{\partial x}\left[\phi D \frac{\partial c}{\partial x}\right] = 0 \tag{17}$$

where φ is porosity, c is nanoparticle concentration, q is Darcy flux, and D is a dispersion constant. This model accounts for the movement and change of the nanoparticle front and profile over time due to Darcyan flow (q) as well as mechanical dispersion and Fickian diffusion (D). Realistically, nanoparticles are significantly affected by three primary mechanisms which hinder their transport: physical filtration,

stability in suspension, and adsorption to porous media[98,99]. Secondary effects such as changes in solution viscosity and medium hydraulic conductivity due to adsorption of nanoparticles further complicate the system and make prediction using simple models unreliable[100–102].

Physical filtration is the simplest mechanism affecting nanoparticle transport in porous media. Interception of a suspended colloid by a collector, for example a pore, is directly dependent on the size of the colloid and the collector[103]. When the size of a nanoparticle exceeds the dimension of a pore, it may not pass through, resulting in retention of the nanoparticle within the medium. Although nanoparticles are very small, this factor can still affect even well-dispersed nanoparticles in low-permeability media[98]. This problem is compounded by aggregation, meaning that care must be taken to ensure good nanoparticle stability. Consideration must also be given to nanoparticle size distribution to allow for good nanoparticle recovery.

Colloidal stability of nanoparticle suspensions is perhaps the most critical factor for nanoparticle stability in porous media, dictating transport potential as well as environmental fate and ecotoxological impact[104]. Nanoparticle aggregation results in larger particles that can be physically filtered in porous media, or settled out of solution. The forces causing nanoparticle aggregation can be electrostatic, magnetic, hydrophobic, or Van der Waals attractions, all of which can be heavily influenced by solution properties such as pH or salinity. Stability of nanoparticle suspensions can largely be described by Derjaguin, Landau, Verwey, and Overbeek (DLVO) theory in which the sum of attractive (-) and repulsive (+) forces should be net positive. In DLVO theory, the repulsive force is supplied by electrostatic repulsion due to surface charge of the particles while attractive force is provided by Van der Waals interactions. Outside of DLVO theory, repulsive force can also be generated by steric interactions of molecules on the surface of the nanoparticle. Briefly, deformation of molecules attached to the surfaces of two interacting particles results in an increase of free energy for volume interactions, producing a repulsion[105]. The most widely employed nanoparticle stabilization tactic is surface modification by polymeric coatings which can employ both of these mechanisms[104,106]. For electrostatic stabilization, polyelectrolytes with high molecular weight and high densities of functional groups such as CMC, Polyacrylic Acid (PAA), or Polystyrene Sulfonate (PSS) are commonly used due to their strong, permanent charges which provide strong repulsive force. This technique could make use of cationic or anionic polymers, however only anionic polymers are useful for stabilization of nanoparticles in porous media due to the tendency for positive charges to adsorb to the negatively charged surfaces of minerals[106]. Electrostatic stabilization of nanoparticles can still be compromised by certain groundwater conditions[107,108]. For example, environments containing high concentrations of Ca^{2+} can destabilize nanoparticles through the formation of a Ca^{2+} layer which neutralizes its surface charge and weakens the

repulsive force. Similarly, different pH conditions can affect the protonation state of the polyelectrolyte, weakening the surface charge and allowing aggregation[109]. Non-ionic polymer stabilization is also commonly used for nanoparticles, relying on steric repulsion to counteract Van der Waals aggregation[99,104,106].

Adsorption of nanoparticles to the surface of minerals present in porous media is also a significant challenge affecting nanoparticle transport[98]. Adsorption is typically due to electrostatic attraction or hydrophobic forces, however specific adsorption of nanoparticles or polymers due to structural properties is also possible. Particle interaction with the porous medium results deposition and release phenomena which can cause the medium to act as a source or sink for particles, affecting transport properties.

Filtration and deposition/release behaviour of nanoparticles in porous media can be accounted for by the inclusion of a source/sink term in equation 5. Recent work by Tosco & Sethi has produced a comprehensive model for the transport of iron nanoparticles in porous media in which they describe the formulation of these source/sink terms (equations (18(20)[101,102].

$$\begin{cases} \dfrac{\partial(\phi c)}{\partial t} + \dfrac{\partial(qc)}{\partial x} - \dfrac{\partial}{\partial x}\left[\phi D \dfrac{\partial c}{\partial x}\right] = -\left[\dfrac{\partial(\rho_b s_1)}{\partial t} + \dfrac{\partial(\rho_b s_2)}{\partial t}\right] & (18) \\ \dfrac{\partial(\rho_b s_1)}{\partial t} = \phi k_{a,1}\left(1 + A_1 s^{\beta 1}\right)c - \rho_b k_{d,1} s_1 & (19) \\ \dfrac{\partial(\rho_b s_2)}{\partial t} = \phi k_{a,2}\left(1 + \dfrac{x}{d_{50}}\right)^{\beta_2} c - \rho_b k_{d,2} s_2 & (20) \end{cases}$$

Equation 6a describes nanoparticle deposition/release behaviour due to adsorption while equation 6b describes nanoparticle physical filtration. Please see Appendix A for a description of each of the variables used in this set of equations. In summary, to facilitate optimal nanoparticle mobility in porous media, filtration, aggregation, and adsorption should be avoided by tuning the nanoparticle surface properties as can be achieved through polymer functionalization.

2.4 Nanoparticle Synthesis & Coating Strategies

Methods for manufacturing iron-based nanoparticles can be divided into two categories: "top-down" and "bottom-up". The first category involves re-structuring of bulk materials through processes such as laser ablation, thermal reduction of pre-existing oxides, or hydration of metallic complexes. The second category refers to the construction of nanomaterials from even more basic building blocks (atoms or molecules) and includes techniques such as chemical vapour deposition and aqueous reduction or co-precipitation of salts[99]. Previously, large-scale application of nanoparticle-based soil remediation strategies have been held back by prohibitive costs of nanoparticle production[110]. The large masses of nanomaterials required for remediation of contaminated sites mandates that nanoparticle synthesis be both

cost effective and amenable to large scale manufacturing. While scalable techniques of nZVI production have been developed, as of a couple of years ago the cost of nZVI is still 10x – 100x more expensive than its bulk granular scale counterpart due to the high energy intensiveness of the synthesis processes[99]. These produced nanoparticles still suffer significant stability issues and additional expense is required for surface modification to enable stability and transport under injection conditions. Furthermore, nZVI coating materials have a detrimental affect on the ability of the nanoparticles to perform direct oxidation or reduction of contaminants by blocking contaminant access to reactive sites. While nZVI has demonstrated interesting applicability to a number of soil remediation challenges, expense of production and detrimental effects of surface coatings still pose a significant barrier for entry into the mainstream *in situ* remediation market.

Iron oxide, on the other hand, does not support the direct oxidation/reduction remediation strategy focused on by nZVI, but it does present less expensive, scalable synthesis techniques and is less impacted by the passivation effects of polymer coatings. One of the most common synthesis techniques for iron oxide nanoparticles produces Fe_3O_4 using the co-precipitation of Fe^{2+} and Fe^{3+} salts in the presence of a base. Briefly, intermediate iron hydroxide species are formed by the salt precursors at high pH, followed by condensation and aging of oxide species[111–113]. The reaction process is described in equation (21.

$$Fe^{2+} + 2Fe^{3+} + 8OH^- \rightarrow Fe_3O_4 + 4H_2O \quad (21)$$

Nanoparticle size distribution produced by this method can be carefully controlled by the inclusion of a surfactant (such as oleic acid) during preparation[113]. This wet chemical method is easily scalable, makes use of inexpensive, ubiquitous reactants, and does not require intensive energy input making widely used for large-scale synthesis[114].

Application of Fe_3O_4 nanoparticles in the environmental remediation field has not been nearly as extensive as nZVI, but thanks to the interest of the medical community for the use of Fe_3O_4 in therapeutic and imaging applications, a large amount of research into stabilizing iron oxide nanoparticles in physiological media has been conducted which should be directly applicable to stabilizing nanoparticles in porous media environments. The most common polymer stabilizers for Fe_3O_4 are dextran, polyethylene oxide (PEO), and poly(D,L-lactic-co-glycolic acid) (PLGA)[111]. These polymers are non-ionic, giving them stability in saline solutions[115], and principally stabilize nanoparticles through steric interactions. Fe_3O_4 stability using poly(ethylene oxide)-block-poly(propylene oxide)-block-poly(ethylene oxide) (PEO-PPO-PEO; Pluronics) copolymers and oleic acid has also been reported, producing a nanoparticle highly stable in water with a strongly hydrophobic core[116,117]. With an abundance of coating materials to consider, it is important to remember that when selecting stabilizing agents, non-toxic, inexpensive polymers should be the top candidates to minimize environmental impact and cost[100]. The capability for

iron oxide to be produced cost effectively at scale, effectively stabilized by inexpensive polymers, and behave as an amendment for a variety of *in situ* remediation techniques including ISCO and MW heating makes it a very attractive candidate as an *in situ* soil remediation technology.

2.5 Nanoparticle Targeted Binding & Application to Soil Remediation

A principal concern associated with the use of nanoparticles for environmental remediation is their environmental fate and ecotoxicity. While much research has been devoted to increasing the transport distances of nanoparticles in porous media, it has been noted that indefinite flow of nanoparticles could result in uncontrollable dispersion in the environment resulting in unseen toxicological consequences[100]. Efficiency of nanoparticle use is another important consideration with respect to improving nanoparticle transport distance. Mobilization of nanoparticles away from the contaminated zone would result in no contribution to remediation and wasted material. To best exploit the remediation properties of engineered nanoparticles, it is most desirable to enhance attachment to entrapped contaminants of interest[118,119].

Targeted nanoparticle delivery is a concept already widely employed in medical research. For example, targeted delivery of chemotherapeutic drugs to cancerous cells serves to greatly improve the efficacy of the drug[120]. Targeted delivery strategies can be divided into two broad categories: passive and active. Passive techniques rely on non-selective properties of the target zone, for example, accumulation of nanoparticles in a tumor due to enhanced permeability of tumor vasculature[121]. Active techniques, in addition to making use of passive targeting effects, rely on design of the nanoparticle to bind directly to a zone of interest. In targeted drug delivery applications, this is typically achieved by coupling a specific ligand to the nanoparticles' surface that will be recognized by a receptor on the target cell[121]. Targeted delivery for soil remediation applications is similar to active targeting in nanoparticle drug delivery, but instead of making use of biospecific ligands, contaminant targeting must be achieved through non-specific thermodynamic interactions[119]. Such non-specific active targeting has been demonstrated for chlorinated hydrocarbon NAPLs in a number of works[118,119,122]. Recently, Wang & Acosta demonstrated that a combination of a high ionic strength environment using Ca^{2+} with a benzethonium chloride/oleic acid nanoparticle coating promoted significant partitioning of iron nanoparticles into a tetrachloroethylene (TCE) phase from aqueous suspension. Earlier literature cites the use of a specifically formulated PMAA-PMMA-PSS block co-polymer to impart similar affinity for NAPL phases. In this example, the PMAA segment of the polymer facilitates attachment to the iron nanoparticle, the hydrophobic PMMA block supports favourable thermodynamic interaction with the NAPL, and the PSS block promotes aqueous stability[118,119]. Despite these successes, as a whole, research into targeted delivery of nanoparticles to contaminated soils is sparse and underdeveloped. Extension of these targeted delivery properties from

chlorinated hydrocarbons to heavy PHCs has the potential to make impactful improvements to nanoparticle based soil remediation techniques.

2.6 Conclusion

Remediation of PHC contaminated soil is an issue of pressing concern in the environmental community due to detrimental health effects on plant and animal communities in impacted zones. Currently, the most widely implemented technologies are expensive, energy intensive, and unsustainable long term. These negative consequences are primarily the result of excavation associated with current *ex situ* treatment methods, leading to the development of *in situ* techniques. While *in situ* methods are fundamentally more sustainable than their *ex situ* counterparts, remediation success is often uncertain and there is great room for improvement in terms of remediation time or cost. Nanoparticles offer the possibility for acting as a direct remediation platform or as an amendment to existing *in situ* strategies to improve their speed or cost. The majority of nanoparticle focused remediation work has been done on nano-Zero Valent Iron which has strong reactive potential with regards to reduction and oxidation of contaminants. There are a number of drawbacks to nZVI, however, including production cost and scalability, transport in porous media, and passivation over short time periods. Improvements have been made to nZVI transport properties over the past decade, but these improvements have come at the expense of nanoparticle reactivity. Iron oxide nanoparticles also offer promising application in soil remediation, serving as a source of a Fenton catalyst for various oxidation, or acting as an energy absorber for thermal strategies. Delivery of nanoparticles to contaminated sites is a challenging problem which could be improved through the adoption of targeted binding approaches already used in nanomedicine. To date, several demonstrations of nanoparticles with affinity for DNAPLs have been shown, but large opportunity for improvements and novel research exists in this field. Overall, nanoparticle based remediation is a promising field with wide potential impact that could benefit strongly from improved delivery techniques and targeted binding that could be applied to a variety of active nanomaterials

Chapter 3

Targeted Nanoparticle Binding & Detection in Petroleum Hydrocarbon Impacted Porous Media†

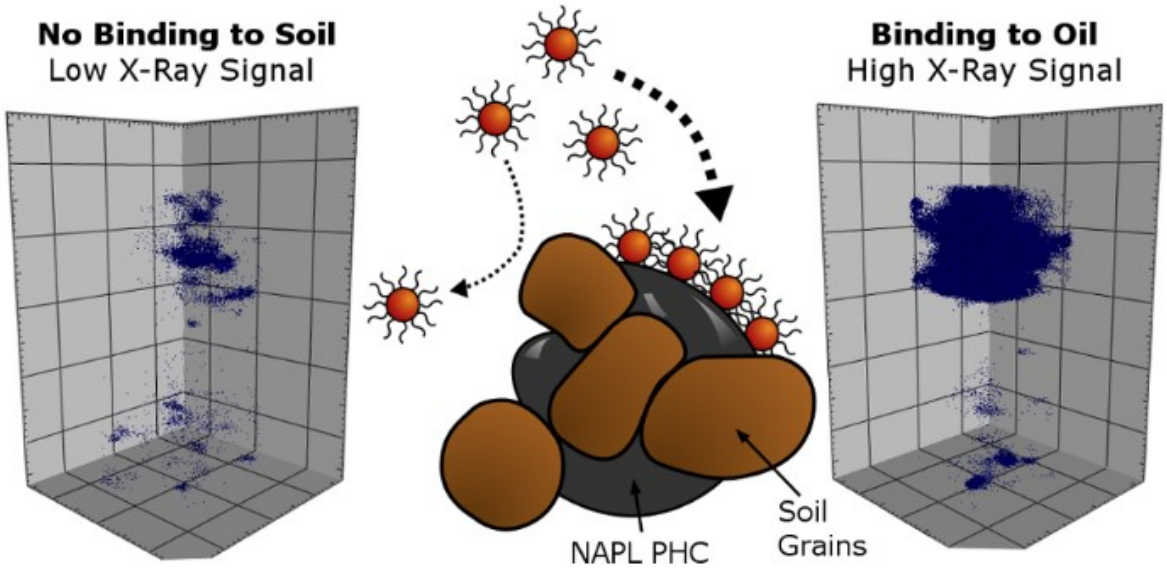

Figure 1. Engineered nanoparticles preferentially attach to NAPL PHC over soil grains. This is observed through higher X-ray CT signal when NP are exposed to oil-impacted sand (right) compared to clean sand (left).

3.1 Summary

Targeted nanoparticle binding has become a core feature of experimental pharmaceutical product design which enables more efficient payload delivery and enhances medical imaging by accumulating nanoparticles in specific tissues. Environmental remediation and geophysical monitoring encounter similar challenges which may be addressed in part by the adoption of targeted nanoparticle binding strategies. This study illustrates that engineered nanoparticles can bind to crude oil-impacted silica sand, a selective adsorption driven by active targeting based on an amphiphilic polymer coating. This coating strategy resulted in 2 mg/kg attachment to clean silica sand compared to 8 mg/kg attachment to oil-impacted silica sand. It was also shown that modifying the surface coating influenced the binding behaviour of the engineered nanoparticles – more hydrophobic polymers resulted in increased binding (**Figure 1**). Successful targeting of Pluronic-coated iron oxide nanoparticles to a crude oil and silica sand mixture was demonstrated through a combined quantitative Orbital Emission Spectroscopy mass analysis

† This chapter is adapted from a previously published article: Linley, S.; Holmes, A.; Leshuk, T.; Nafo, W.; Thomson, N. R.; Al-Mayah, A.; McVey, K.; Sra, K.; Gu, F. X. Targeted Nanoparticle Binding & Detection in Petroleum Hydrocarbon Impacted Porous Media. Chemosphere 2019, 215, 353–361.

supported by Vibrating Scanning Magnetometer magnetometry, and a qualitative X-ray micro-computed tomography (CT) visualization approach. These non-destructive characterization techniques facilitated efficient analysis of nanoparticles in porous medium samples with minimal sample preparation, and in the case of X-Ray CT, illustrated how targeted nanoparticle binding may be used to produce 3-D images of contaminated porous media. This work demonstrated successful implementation of nanoparticle targeted binding toward viscous LNAPL such as crude oil in the presence of a porous medium, a step which opens the door to successful application of targeted delivery technology in environmental remediation and monitoring.

3.2 Introduction

Targeted binding is a familiar concept in the field of healthcare which typically refers to specific analytes preferentially binding to specific receptors on cells and tissues[123]. This observation has driven innovation in nanomedicine over the past two decades and resulted in functionalized nanoparticles specifically modified to target diseased tissues and release therapeutic payloads[120,124]. Implementation of a targeted nanoparticle binding platform provides direct enhancement to therapeutic efficiency and reduces side effects by minimizing drug action on healthy tissue. Targeted binding can also drive accumulation of nanoparticles in tissue with specific physical or chemical characteristics which can then be detected using medical imaging technologies and provide an image of target areas[116,125,126]. Soil contamination and its remediation bears many similar challenges to diseased tissue and its treatment; the impacted site is often not easily accessible, *in situ* treatment wishes to avoid delivering a payload to clean soil, and the contaminated region has different chemical and physical characteristics from the surrounding material. By taking advantage of the unique physical and chemical properties of the impacted region, nanoparticles can be designed to preferentially accumulate there, allowing for targeted treatment or enhanced imaging. Soil remediation using materials designed for targeted removal of specific contaminants has been a subject well studied in the area of toxic metals removal wherein the mobile contaminant species is adsorbed to a high-surface area nanostructure such as titanate nanotubes or modified graphene oxide[127–130]. Some graphene oxide-based strategies introduce the possibility of target contaminant immobilization by forming graphene oxide-metal ion complexes with enhanced adsorption to mineral material[131–133]. Treatment strategies pursuing elimination of fixed contaminants, such as in the case of viscous non-aqueous phase liquids (NAPLs), require the treatment agent to be emplaced in the contaminated region rather than adsorb the contaminant to its surface, and a knowledge gap exists in this regard. Soil contamination by NAPL petroleum hydrocarbons (PHCs) often requires some type of remedial activity to address potential impacts on ecosystems or human health. While conventional *in situ* remediation technologies utilizing direct delivery of reagents have been successful in treating some types of PHCs[134–

[136], options are limited for viscous hydrocarbons such as heavy crude oils, for which no effective *in situ* treatment strategy exists. Advancements in nanotechnology have led to the emergence of nanoremediation which utilizes the higher specific surface area of nanoparticles to achieve faster treatment, but applications are still limited by other drawbacks such as particle self-aggregation and aggregation with mineral material[137,138]. Nanoremediation treatment of a contaminant may occur directly as a result of nanoparticle contact, as in the case of nZVI[139], or indirectly through Fenton-like catalysis of a persulfate reaction where the nanoparticle supplies leached iron ions[140]. The challenge of delivering nanoparticles to a treatment zone has spurred significant investigation of coating materials to improve their transport properties[141–145]; however, these improvements do not guarantee nanoparticle delivery directly to the NAPL interface, and have led to serious discussion regarding the toxicity risks of releasing mobile nanoparticles into an unrestricted environment[100,138,146]. Based on similarities to nanomedicine, *in situ* nanoremediation may be improved by the adoption of targeted binding. To this end, a successful targeted nanoparticle delivery system must be capable of: (1) using nanoparticles that can be tuned to stick or bind to target NAPL mass that they contact, (2) transporting functional nanoparticles in various geologic media over significant distances (i.e., > 1 m), and (3) allowing the bound nanoparticles to be triggered either actively or passively to enable treatment.

In general, targeted delivery is divided into two broad categories: passive and active which rely on physical and chemical surface properties of the target zone, respectively[121,147,148]. The targeting mechanism for NAPL PHCs presented in this paper is similar to active targeting seen in drug delivery and achieved by tailoring the nanoparticle surface to interact with the NAPL PHC interface[119]. Such an 'active targeting' technique has been previously demonstrated for chlorinated hydrocarbon NAPLs using a block co-polymer nanoparticle surface coating capable of stabilizing nanoparticles in aqueous suspension and promoting hydrophobic interactions[118,119,122]. Targeted delivery of nanoparticles has the potential to further increase the impact and efficiency of nanoremediation techniques by concentrating the reagent in direct contact with the NAPL.

In this paper, we report on the selective binding of functional nanoparticles to one class of NAPL PHCs. Specifically, we focussed on the ability of an inexpensive, non-toxic[149], amphiphilic block co-polymer coating (Pluronic) applied to iron oxide nanoparticles to promote aqueous stability and hydrophobic interactions with viscous hydrocarbons. Iron oxide nanoparticles were selected as the core material due to their simple synthesis, possible application as an iron catalyst for various chemical oxidation processes [150], and capability to act as an energy absorber for thermal treatment strategies [151–154]. Nanoparticle targeted binding behaviour was assessed using a batch experimental design and quantified indirectly using aqueous-phase concentration measurements. This indirect approach was supported by

direct quantification of bound nanoparticles using VSM magnetometry, and binding was further visualized using a qualitative X-ray Computed Tomography (CT) technique.

Nanotechnology-enabled sensing techniques are a subject of significant research for detecting contaminants. Through interaction of the nanoparticle with an analyte of interest, a detectable signal can be generated to confirm or measure the presence of the analyte[155,156]. Using nanoparticles adsorbed to target contaminants in porous media as a contrast agent is a nano-enabled sensing technique analogous to X-Ray CT medical imaging. In the context of geosciences, X-Ray CT relies on identifying areas of varying radiological density which can vary with mineral type[157], for example, Fe_3O_4 absorbs X-Rays more strongly than SiO_2. The possibility and threshold of detection for nanoparticles in porous media is a key question that must be addressed in the context of X-Ray CT detection of nanoparticles in geologic media. Typical characterization of nanoparticles or trace metals embedded in soil relies on tedious, destructive techniques such as acid digestion and subsequent ICP-MS or ICP-OES analysis[158,159], prompting research into new analysis techniques which avoid lengthy sample preparation[160–162]. 3-D mapping of nanoparticle accumulation would require performing this type of lengthy analysis multiple times in order to construct a model. With the X-Ray CT technique introduced here, non-destructive 3-D analysis of relatively large samples is achieved with a single, quick, high-resolution scan and minimal sample preparation. This research effort investigates one of the critical features of a potential targeted nanoparticle delivery system, i.e., ability to bind to a target NAPL mass, and demonstrates what a possible end-use of nanoparticle targeted binding might look like through the application of X-Ray CT to detect contaminated sands containing bound nanoparticles. Research that addresses the other two features of a robust targeted delivery platform (transport in various porous media, and activation options for treatment) is ongoing.

3.3 Materials and Methods

3.3.1 Materials

Iron (II) sulfate heptahydrate ($FeSO_4 \cdot 7H_2O$, > 99%), iron (III) chloride hexahydrate ($FeCl_3 \cdot 6H_2O$, > 99%), ammonium hydroxide (NH_4OH, 28-30% in water), dichloromethane (DCM, > 99%), and oleic acid (> 90%) were purchased from Sigma Aldrich (St. Louis, MO, USA). Hydrochloric acid (37%) and ethanol (ACS grade, 99%) were purchased from Fisher Scientific (Hampton, NH, USA). Pluronic co-polymers P104, L62, and L121 (Table 1) were gifted by Brenntag (Essen, Germany) and BASF (Ludwigshafen, Germany). Silica sand (99.7% SiO_2, d_{50} = 0.2 mm) was purchased from Opta Minerals, Inc. (Hamilton, ON, Canada). Crude oil (heavy, sour crude, API gravity 13.3 (ρ = 0.977 g/cm^3), kinematic viscosity 4.745 x 10^{-4} m^2/s @ 40 °C) was provided by Chevron Energy Technology Company (Houston, TX, USA). All materials were used as received.

3.3.2 Nanoparticle Synthesis

Nanoparticle synthesis was adapted from several methods previously reported[163–165]. $FeSO_4 \cdot 7H_2O$ and $FeCl_3 \cdot 6H_2O$ were added to deoxygenated water at a molar ratio of 2:3 ($FeSO_4$:$FeCl_3$). Sufficient NH_4OH and oleic acid were added to achieve final concentrations of 4 and 0.22 mol/L, respectively. This solution was stirred at 70 °C for 1 h, then stirred at 90 °C under flowing N_2 for 1 h to purge evolved NH_3 gas. After cooling to room temperature, the black, magnetic precipitate was recovered by magnetic decantation and washed 3x by deoxygenated Millipore DI water (Millipore Elix 5), and then 3x by ethanol before being dried under flowing N_2.

3.3.3 Nanoparticle Phase Transfer

A mixture of oleic acid in hexane (1% v/v) was prepared to which dried nanoparticles were added at a concentration of 90 g/L and sonicated for 10 min (VWR "Symphony" 1.9 L Ultrasonic Cleaner). The resulting suspension was added to various aqueous solutions of Pluronic co-polymer(s) at a concentration of 10 % v/v and probe sonicated for 30 min to emulsify the water and hexane phases (Fisher Scientific FB505 Sonic Dismembrator, 200 W). The emulsified nanoparticle sample was transferred to a separatory funnel and separated over 48 h. The resulting aqueous nanoparticle suspension (~3 g/L) was stored until used.

3.3.4 Nanoparticle Binding Studies

Oil-impacted silica sand (OSS) was prepared by dissolving crude oil in DCM at a concentration of 60 g/L, mixing it with dry silica sand, and evaporating the DCM such that the final concentration of crude oil in sand was 1.5% (m/m). 15 g of OSS was then added to a 20-mL cylindrical glass vial, followed by 10 mL of nanoparticle suspension diluted with Millipore DI water to either 1:100 or 1:10 of its concentration after phase-transfer. The glass vials were then loaded onto an orbital shaker (Stovall Life Sciences "Belly Dancer") for 48 h. Following mixing, the nanoparticle solution was recovered by filtration (1.5 µm glass fiber, Whatman). The retentate was washed with 100 mL Millipore DI water and dried by vacuum desiccation for 96 h before CT, scanning electron microscopy (SEM)/energy dispersive X-ray spectroscopy (EDS), or Vibrating Scanning Magnetometer/ Superconducting Quantum Interference Device (VSM/SQUID) analysis. For control, a "clean" silica sand (SS) sample was prepared identically as above except the DCM/crude oil mixture was not added. Three replicates of each sample were prepared to capture variability. The composition of the different nanoparticle formulations investigated are listed in **Table 3**. All batch experiments were performed in triplicate.

Table 3. Summary of nanoparticle formulations explored in Chapter 3

Formulation ID[a]	Pluronic L62 (g/L)[b]	Pluronic L121 (g/L)[b]	Pluronic P104 (g/L)[b]	Dynamic Light Scattering diameter (nm)
A (A-100)	10	-	-	89.80
B-40	4	-	6	64.42
B-60	6	-	4	57.60
B-80	8	-	2	61.60
C-40	2	2	6	75.61
C-60	3	3	4	82.68
C-80	4	4	2	81.16

3.3.5 Analyses

Aqueous nanoparticle samples were acid digested in 6 mol/L HCl and then diluted by a factor of 10 with 1 mol/L HCl prior to analysis by ICP-OES (Prodigy) to quantify total iron (method detection limit (MDL) of 4 µg/L). Nanoparticle mass bound on the OSS or the SS (µg of NP/dry g of sand) was estimated from the difference between the initial and final (after 48 h of exposure) nanoparticle concentration.

High Resolution Transmission Electron Microscopy (HR-TEM) analysis was performed using a JEOL 2010F with an acceleration voltage of 200 keV. The nanoparticles were dispersed in ethanol, sonicated, and a droplet placed on a holey carbon coated Cu grid, which was allowed to air dry before being analysed.

Dynamic Light Scattering (DLS) was used to characterize nanoparticle hydrodynamic size and uniformity. A subsample (3 mL) of the nanoparticle suspension in hexane (prior to Pluronic coating) or in water (after Pluronic coating) was placed into a polypropylene cuvette and analyzed by DLS (Brookhaven 90Plus Particle Size Analyzer).

Sample magnetization was measured using a Vibrating Scanning Magnetometer (VSM; Quantum Design MPMS 3). Sand samples (as described above) were packed into polycarbonate VSM sample holders. VSM was performed at a temperature of 70 K cooled by liquid N_2 to prevent material movement within the samples and was performed with a maximum magnetic field strength of 1 T. Magnetic properties of nanoparticles required for quantitative analysis were determined using freeze-dried Formulation A particles prepared using a Labconco Freezone 2.5 freeze drier.

X-Ray CT samples (as described above) were packed into 4.5-mL polypropylene cuvettes and scanned with an open directional high-power micro-focus X-ray tube (240 kV, GE Phoenix v|tome|x m compact micro CT system) equipped with a GE DXR detector array. X-ray scan parameters (Table S1) were chosen to ensure optimal X-ray penetration and contrast. An acceleration voltage of 80 kV with a

beam current of 80 μA resulted in strong visual contrast between iron oxide and silica materials. Raw images were processed using Volume Graphics software (VGStudio Max) as two separate materials (iron oxide and silica) using beam hardening factors between 9.5 and 9.6. Both OSS and SS sample images were processed identically.

3.4 Results and Discussion

3.4.1 Nanoparticle Design

Engineered nanoparticles were designed to facilitate stability in aqueous suspension and favourable interactions with a hydrophobic phase such that particles would bind to the oil-water interface while avoiding adsorption directly to mineral soil material. To achieve this behaviour, an amphiphilic polymer coating was applied to a hydrophobic nanoparticle core (**Figure 2**).

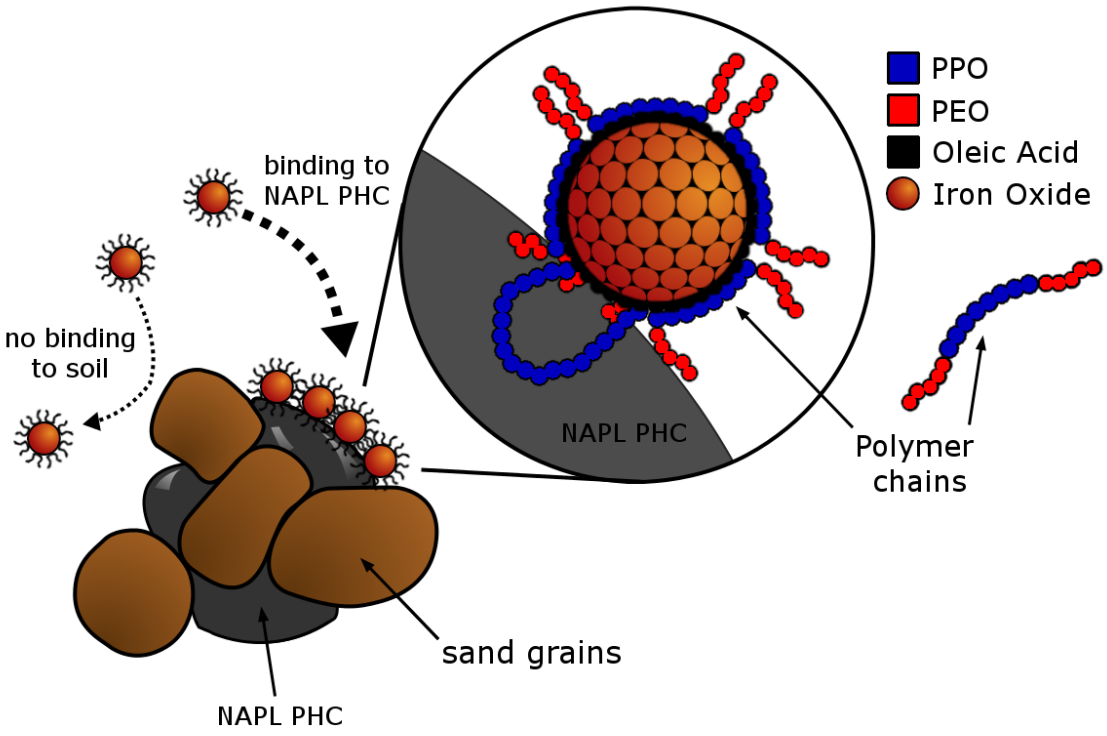

Figure 2. Schematic illustrating nanoparticles with an amphiphilic polymer coating (Pluronic) avoiding adsorption to sand grains and specifically adsorbing to NAPL PHC through hydrophobic interactions. Polyethylene Oxide (PEO; red) blocks of the coating extend into the aqueous phase and contract in the NAPL PHC. Polypropylene Oxide (PPO; blue) blocks of the coating extend into the NAPL PHC and contract in the aqueous phase. Oleic acid (black) binds the coating to the nanoparticle surface and interacts favourably with the NAPL PHC when at the interface.

The nanoparticle core was composed of iron oxide produced via a co-precipitation of iron salts, and made hydrophobic by oleic acid chemisorbed to the iron oxide surface through monodentate chelation of its carboxylate group with iron surface atoms[166]. The purpose of this oleic acid layer is twofold: first, to

provide the nanoparticle with a hydrophobic outer coating which would interact favourably with the target crude oil contaminant; and second, to provide an anchor point for the adsorption of Pluronic, the amphiphilic block co-polymer. The final particle structure allowed favourable thermodynamic interactions between hydrophobic segments of the amphiphilic polymer coating and a NAPL phase, causing nanoparticles to partition to the water/NAPL interface[118,119,122]. Pluronic, an inexpensive, commercially available polymer with highly tunable hydrophobic/hydrophilic properties, was selected as the coating material. Pluronic is a block co-polymer composed of a middle, hydrophobic segment of poly-propylene oxide (PPO) and two outer, hydrophilic segments of poly-ethylene oxide (PEO). The Pluronic coating was attached to the iron oxide core through hydrophobic interactions between the oleic acid nanoparticle capping agent and PPO segments. The PEO segments of the coating extend into the aqueous phase surrounding the nanoparticle and prevent nanoparticle aggregation through steric stabilization. Details regarding the properties of different Pluronic polymers used are given in **Table 4**. It should be noted that a similar nanoparticle structure using Pluronic F127 has been previously reported in the literature for application in promoting cellular uptake[167], however findings in this paper indicate that F127 may not be the most appropriate polymer to promote targeted binding to viscous hydrocarbons, necessitating careful selection of amphiphilic surface coating molecules based on the desired application. L62 and L121 were investigated as more hydrophobic polymers having approximate relative hydrophobic/hydrophilic mass ratios ($M_{n(PPO)}/M_{n(PEO)}$) of 4 and 9, respectively. P104 was investigated as a more hydrophilic polymer having an approximate relative hydrophobic/hydrophilic mass ratio of 1.5.

Table 4. Properties of Pluronic polymers used for amphiphilic nanoparticle coating in Chapter 3

Polymer ID	**M_n (g/mol)**	**Structure**	**M_n of PPO (g/mol)**	**M_n of PEO (g/mol)**	**$M_{n(PPO)}/M_{n(PEO)}$**
L62	2,250	PEO_5-PPO_{31}-PEO_5	1,800	450	4
L121	4,000	PEO_5-PPO_{62}-PEO_5	3,600	400	9
P104	5,000	PEO_{23}-PPO_{52}-PEO_{23}	3,000	2,000	1.5

3.4.2 Nanoparticle Characterization

HR-TEM data showed that the nanoparticle iron oxide cores were spherical with an average diameter of 6.4 ± 1.8 nm (**Figure 3 A**), consistent with DLS measurement of particle cores in hexane ─ 8.4 nm diameter with a polydispersity index (PDI) of 0.260 (**Figure 4**).

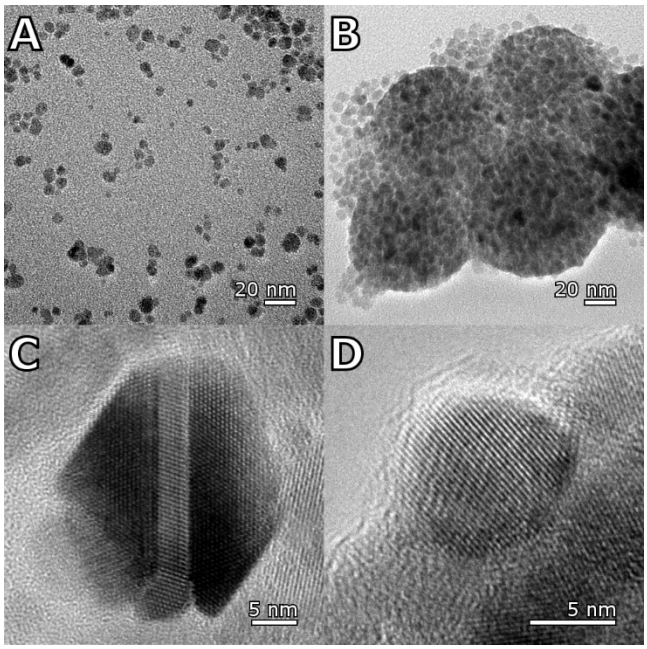

Figure 3. HR-TEM image of sample A-100: **A** Iron oxide nanoparticles prior to Pluronic coating, **B** Clusters of iron oxide nanoparticles after Pluronic coating, **C** Iron oxide nanoparticle prior to Pluronic coating, and **D** Edge of a Pluronic coated nanoparticle aggregate demonstrating crystalline nanoparticles within an amorphous polymer coating.

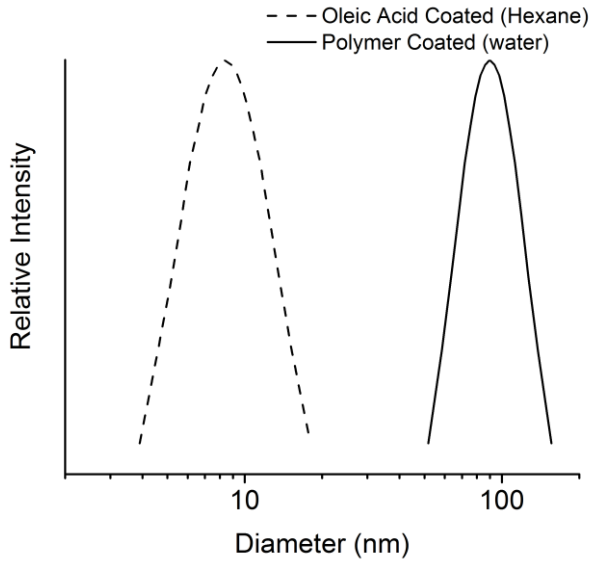

Figure 4. Nanoparticle sizing in suspension by Dynamic Light Scattering (DLS). Uncoated particles in hexane were found to be 8.4 nm in diameter with a polydispersity index (PDI) of 0.260. Coated particle aggregates in water were found to be 89.8 nm in diameter with a PDI of 0.138.

After Pluronic coating, the nanoparticle average diameter increased significantly to 120.9 ± 47 nm (**Figure 3 B**), again supported by a DLS hydrodynamic diameter of 89.8 nm with a PDI of 0.138. This increase in size is attributed to the formation of a miniemulsion of multiple iron oxide cores within a surfactant polymer coating[164,165,168]. These aggregates form due to the requirement for sufficient surface

coverage with surfactant to realize a critically-stable state; smaller particles require higher surfactant concentrations[168]. Although aggregation increased with polymer coating, the dispersity of the particles remained narrow (**Figure 4**), indicating that aggregation was limited and large aggregates (> 1 μm) were not present. HR-TEM images (**Figure 3 C, D**) demonstrated the crystallinity of the iron oxide particles individually and within an aggregate structure as indicated by the ordered rows of atoms. In contrast to the order seen within the iron oxide particles, the disordered fringe adjacent to the crystalline region of the nanoparticle observed in **Figure 3D** is interpreted as an amorphous polymer coating. The thickness of this coating was measured to be 1.1 ± 0.17 nm which compares similarly to the thickness of Pluronic species adsorbed on hydrophobic surfaces through hydrophobic interactions [169].

3.4.3 Nanoparticle Binding

The iron concentration in the filtered solution for nanoparticle Formulation A after exposure to OSS was significantly lower than the same formulation exposed to SS (**Figure 5**).

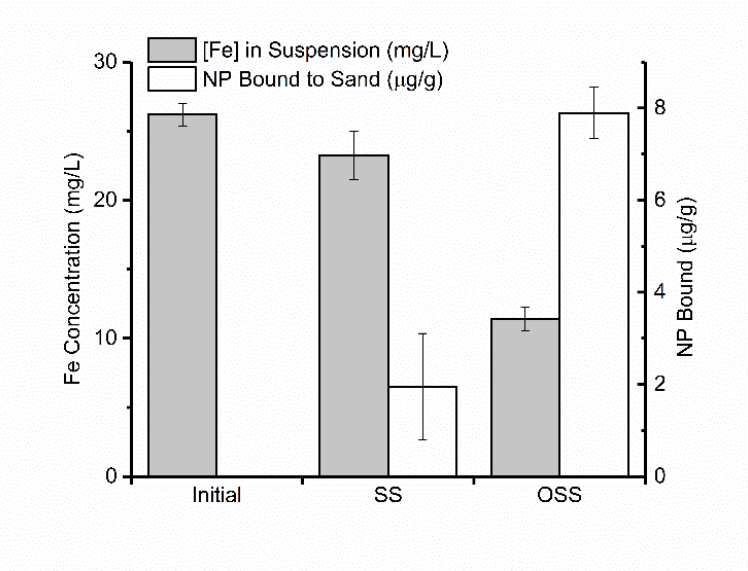

Figure 5. ICP-OES results demonstrating preferential binding of nanoparticle Formulation A to OSS when compared to SS. Iron concentration in suspension was measured directly using ICP-OES. NP bound to sand was calculated indirectly using the observed decrease of iron in the suspension. Error bars represent ± one standard error.

Compared to the iron concentration of the initial solution (26.2 ± 0.8 mg/L), a reduction of 2.9 ± 1.7 mg/L (11.2%) was observed in the SS solution, and a reduction of 14.8 ± 0.84 mg/L (56.4%) was observed in the OSS solution, indicating preferential nanoparticle adsorption to sand containing NAPL PHC. The estimated mass of nanoparticles bound to the sand after exposure was 1.95 ± 1.15 μg/g on SS, and 7.89 ± 0.56 μg/g on OSS. Nanoparticle binding using Formulation A nanoparticles also exceeded binding observed under identical conditions using oleic acid-stabilized particles in the absence of Pluronic (**Figure 6**) indicating that Pluronic coating was important to the adsorption mechanism.

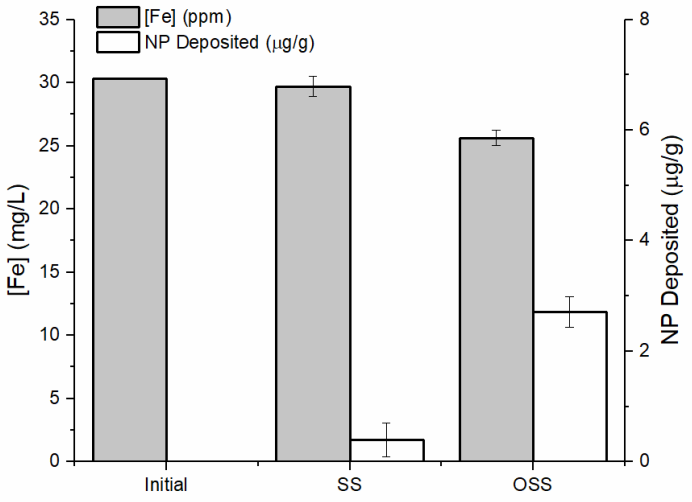

Figure 6. NP binding batch test using nanoparticles phase-transferred in the absence of Pluronic (using only oleic acid). Aqueous phase iron concentration indicated some targeting behaviour when comparing SS to OSS, but the effect is mild compared to binding observed using Formulation A nanoparticles. Estimated NP deposition is 0.39 ± 0.30 μg/g in SS and 2.71 ± 0.28 μg/g in OSS.

When the particles are stabilized using only oleic acid, a double layer of oleic acid forms around the particles, creating a hydrophilic anionic carboxylate shell preventing interaction with the NAPL PHC. Wang et al. have previously shown that addition of a cationic surfactant to an oleate nanoparticle coating system can significantly improve targeted binding to trichloroethylene by disrupting the charge of the bilayer[122]. A similar likely occurred in this system whereby Pluronic disrupts the oleate bilayer, allowing hydrophobic interaction between the oleate surface and the hydrocarbon/water interface. Furthermore, literature demonstrates that nanoparticle core properties influence particle adsorption behaviour by affecting coating conformation[170]. By layering Pluronic on top of oleic acid, we may lessen the effect of the core material on Pluronic conformation, leading to higher applicability of this coating strategy to various nanoparticle core materials. At this point, the mechanism of nanoparticle binding is not fully understood, but is hypothesized to be due to hydrophobic forces from the Pluronic coating, oleate coating, or a combination of both. Any nanoparticle binding to clean sand was attributed to van der Waals forces between the PEO segment of the Pluronic coating and the surface of the SiO_2 sand grains. Previous literature suggests hydrogen bonding occurs between the ether oxygen of PEO and the hydroxyl species on the surface of an acidic metal oxide such as SiO_2[171]. This interaction necessitates that the PEO segments of the Pluronic coating should be short to maintain a strong binding contrast between clean and oil-impacted sands.

Direct, quantitative magnetic analysis of dried OSS before and after exposure to Formulation A nanoparticle solution was assessed using VSM. The saturation magnetization of solid Formulation A

nanoparticles (required to calculate nanoparticle mass deposition in the sand sample) was measured using freeze-dried nanoparticles (**Figure 7**) and found to be 59.76 emu/g. The magnetic hysteresis curves for the magnetization of OSS samples as an applied magnetic field is cycled between polarities are shown in **Figure 8**. The saturation magnetization represents the maximum, steady-state magnetization reached by a sample under a strong magnetic field. The difference between the saturation magnetization in the OSS Control sample and the OSS+NP sample was attributed to the presence of magnetic nanoparticles. This difference was divided by the saturation magnetization of Formulation A nanoparticles to give a mass concentration estimate (g/g) for bound nanoparticles of 8.13 ± 0.27 µg/g. This VSM estimate compares closely to the estimate of 7.89 ± 0.56 µg/g determined indirectly by the decrease in iron concentration in the aqueous phase.

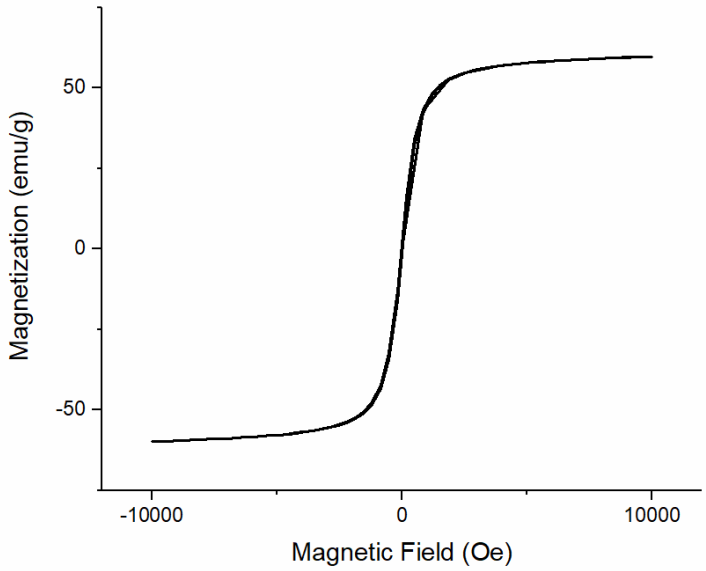

Figure 7. Magnetic hysteresis curve for freeze-dried Formulation A nanoparticles. The saturation magnetization for Formulation A nanoparticles was found to be 59.76 emu/g with negligible error; error on the order of 10-5 emu/g.

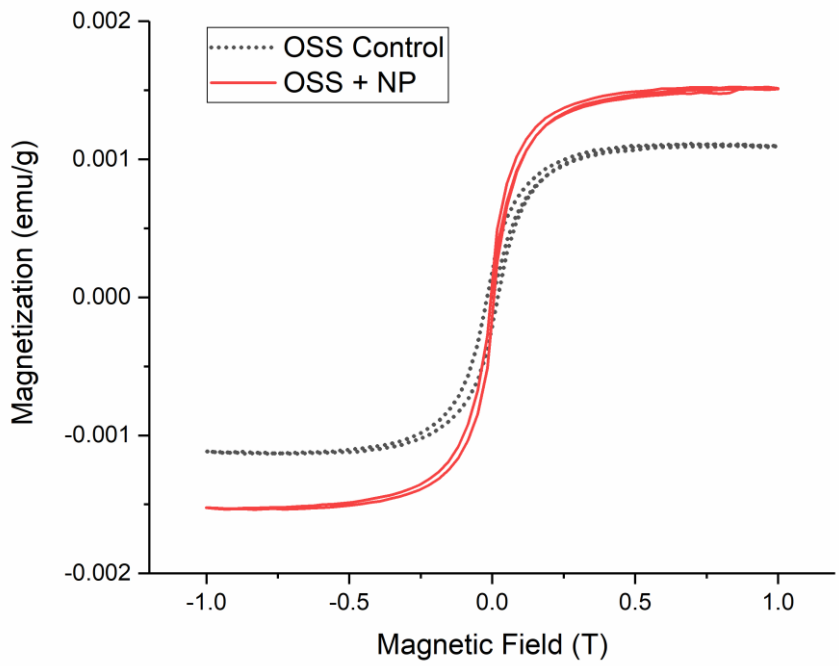

Figure 8. Magnetic hysteresis curves for OSS before (OSS Control) and after exposure to Formulation A nanoparticle solution (OSS + NP). The saturation magnetization was 1.037 ± 0.016 x 10-3 emu/g for the OSS Control sample, and 1.523 ± 0.016 x 10-3 emu/g for the OSS+NP sample.

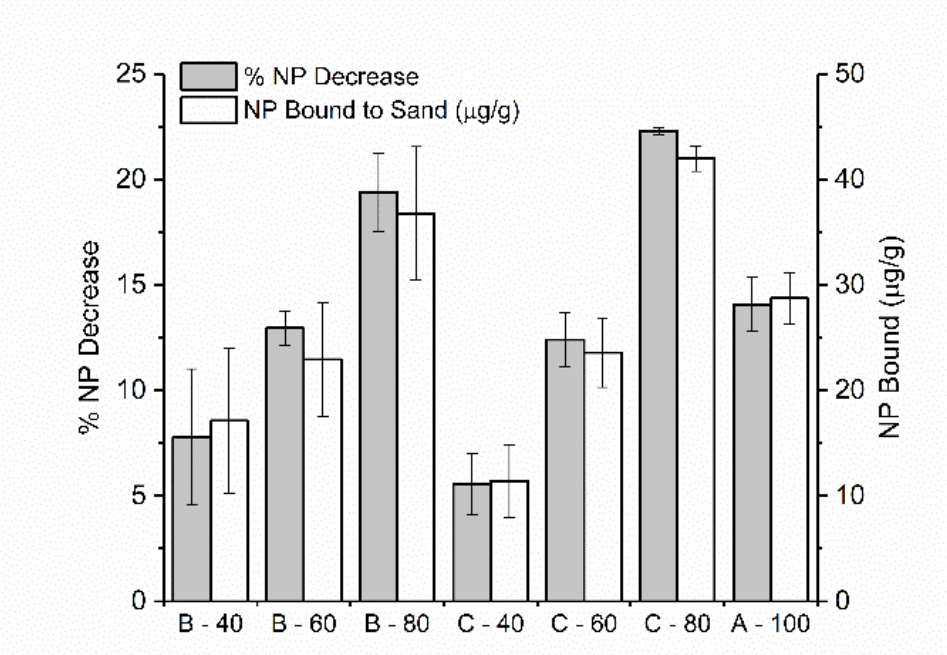

Figure 9. Indirectly calculated nanoparticle (NP) binding increases as nanoparticle coating formulation becomes more hydrophobic. The nomenclature X-# identifies nanoparticle samples (Table 1).

As the Pluronic hydrophobic/hydrophilic ratio of the nanoparticle coating increased (**Table 3**), the nanoparticle concentration in aqueous suspension decreased when exposed to OSS, implying greater nanoparticle binding (**Figure 9**). When compared to **Figure 5**, the smaller %NP decrease observed for samples in **Figure 9** is primarily due to higher initial concentrations used in this binding experiment (estimated NP binding, however, is increased). The results in **Figure 9** indicate that nanoparticle binding towards viscous hydrocarbons, specifically heavy crude oil, could be tuned by changing the surface coating formulation. These results are consistent with the behaviour of Pluronic-coated magnetite nanoparticles employed in biomedical applications - previous work using such particles as an MRI contrast agent for tumor imaging reported that Pluronic coating formulation could be adjusted to avoid adsorption to proteins and that a balance between the hydrophobic and hydrophilic characteristics of the polymer is critical to maintaining stability and dispersion[172]. The trend observed in Figure 4 relating coating hydrophobicity to nanoparticle binding supports the theory that binding is due to hydrophobic interactions as proposed by Saleh et al.[118]. While the modification of the particles in this work is different, the interactions which lead to NAPL targeting behaviour remain the same. The larger, longer hydrophobic portions of the surface coating remain contracted in water and swell in the presence of oil, resulting in a more energetically favourable configuration of the particle at the oil/water interface and facilitate targeted binding behaviour.

3.4.4 X-Ray CT Visualization of Nanoparticle Binding

X-ray micro CT was used as a qualitative tool to visualize the presence of nanoparticles bound to dried OSS and SS (as described previously). A set of 2D projection images was acquired during a full rotation of the sample, which was then used to reconstruct a 3D image consisting of volumetric pixels (voxels) using a filtering back-projection algorithm[173]. Micro-focus tubes defocus the electron beam proportionally to the electric power to prevent the sample from thermal destruction[174]. The voxel size estimated by the GE Phoenix X-ray CT machine was determined to be 27.3 μm3 for all scanned samples.

The detection of a single iron oxide nanoparticle or nanoparticle aggregate within a voxel resolution >1 μm^3 is challenging. This detection method relied on the overall X-ray absorbance of many iron oxide nanoparticles within one voxel to differentiate a response from the absorbance of silica sand, and hence there was a concentration threshold of nanoparticles for which a positive detection can be determined within a single voxel. Based on preliminary studies it was determined that the detection capabilities of the micro CT system with the X-ray scan parameters used could be as low as 1 mg/kg nanoparticles in silica sand (**Figure 10**).

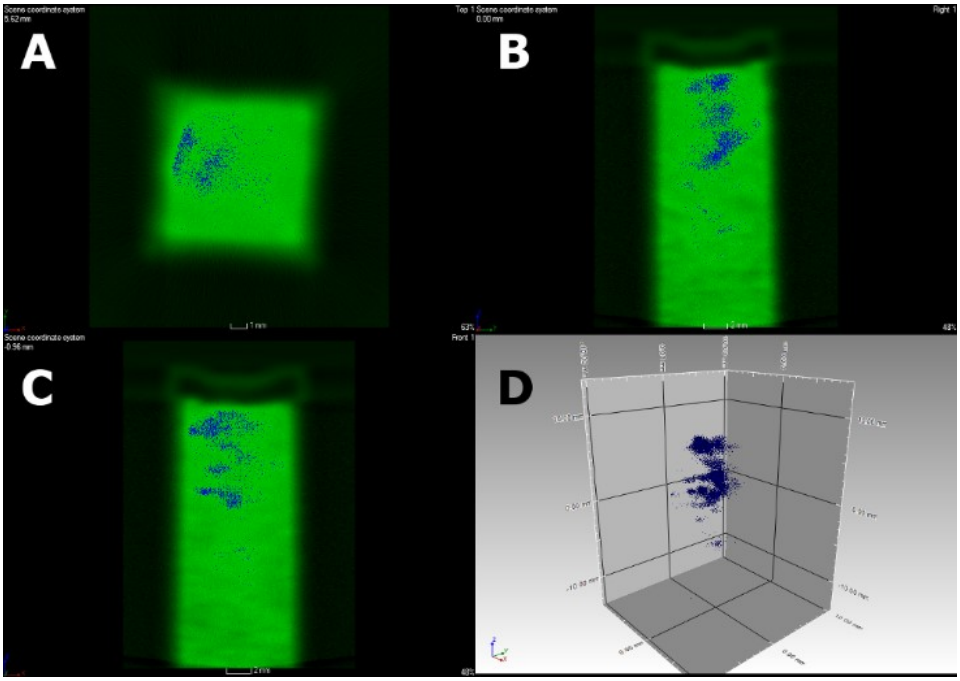

Figure 10. Images A, B, and C show the top, left, and right projections of CT X-Ray absorbance through the centre of a cuvette containing nanoparticle-spiked silica sand at a concentration of 1 mg/kg (NP/SS). Image D shows a 3-D projection of the X-ray absorbance throughout the cuvette. The blue regions indicate areas of higher X-ray absorbance which correspond to the upper portion of the cuvette which contains nanoparticle spiked sand. The green regions indicate areas of lower X-ray absorbance which correspond to the lower portion of the cuvette which contains clean, reference sand. This figure demonstrates the limited identification of nanoparticles at concentrations ~1 mg/kg in silica sand.

Formulation A nanoparticle suspension was selected for CT investigation based on the observation that binding improved with coating hydrophobicity (see **Figure 9**). The bottom-half of the cuvette shown in **Figure 11**(A-C) was packed with OSS only, while the remaining top-half of the cuvette was packed with OSS that had been exposed to the Formulation A nanoparticle suspension for 48 hours. For baseline comparison, the bottom-half of the cuvette shown in **Figure 11**(D-F) was packed with SS only, and the top-half of the cuvette was packed with SS that had been exposed to the Formulation A nanoparticle suspension for 48 hours. The packing of two materials in a single cuvette allowed for direct comparison of each sample to its relevant control.

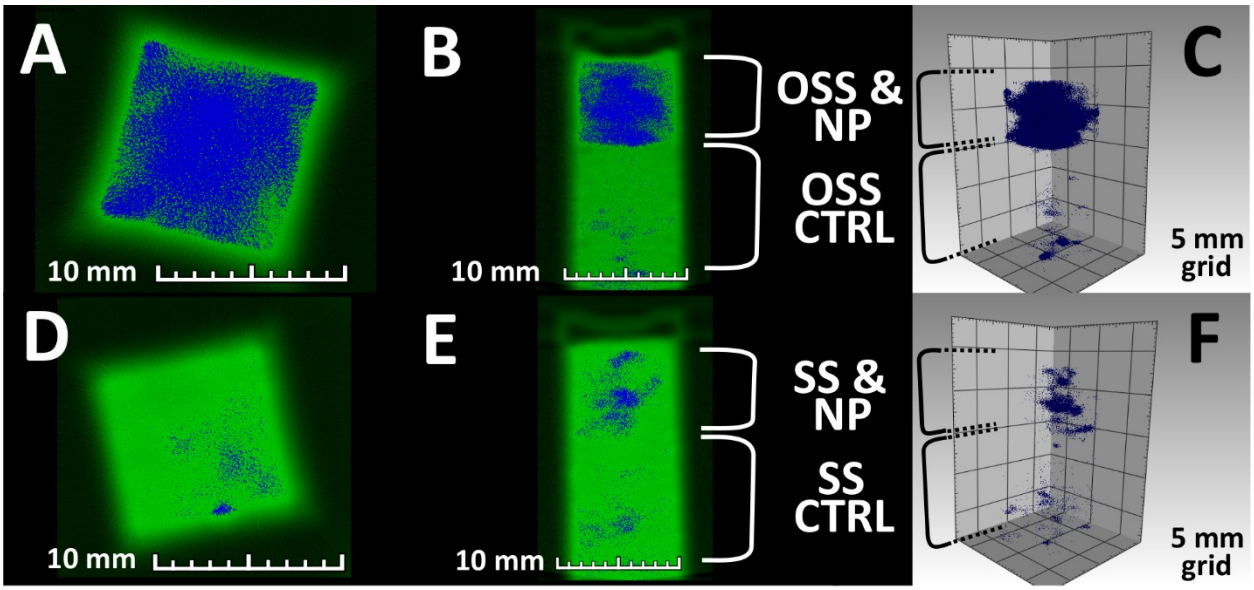

Figure 11. X-ray Computed Tomography of Oil-impacted Silica Sand (OSS; A, B, and C) and Silica Sand (SS; D, E, and F) samples. In each cuvette, the top portion contains sand contacted with Formulation A nanoparticles for 48 h, filtered, washed, and dried while the bottom portion contains the respective control (CTRL) sand, as indicated in B and E. A and D show the top view of each cuvette packed with OSS and SS, respectively. B and E show the side view of each cuvette packed with OSS and SS, respectively. C and F show a 3-D volumetric reconstruction of each cuvette for OSS and SS, respectively.

Blue colour has been used in **Figure 11** to represent regions of high X-ray absorption (higher nanoparticle density) while green has been used for regions of lower X-ray absorption (lower nanoparticle density) within each cuvette. Due to the concentrations of iron oxide nanoparticles used in the binding studies, the threshold difference (between blue and green) was very narrow. As a result, there are sparse blue regions in the lower section of each cuvette which may occur due to variations in packing density. The images in **Figure 11** do not depict absolute values of X-ray absorbance, but rather voxels which fall above (blue) and below (green) a uniform selected threshold to illustrate qualitative evidence of nanoparticle binding. All the images in **Figure 11** were obtained using identical X-ray CT operating and image processing parameters so that comparative visual contrasts between **Figure 11**(A-C) and (D-F) are possible. The increased X-ray absorbance in the top-half of the cuvette shown in **Figure 11**(A-C) suggests substantial nanoparticle binding to the OSS. In contrast, the X-ray absorbance observed in **Figure 11**(D-F) is minor for the SS that had been exposed to the nanoparticle suspension compared to **Figure 11**(A-C), thus corroborating the indirect binding data (Figure 2).

3.5 Conclusions

Demonstrating nanoparticle targeted binding to NAPL PHCs from an aqueous suspension in a porous medium matrix is one of the critical elements of a targeted nanoparticle delivery system with

potentially wide-reaching environmental implications. This work demonstrated that nanoparticle targeted binding to crude oil could be controlled as a function of surface properties determined by an amphiphilic polymer coating. Extension of this concept to the broader environmental monitoring and remediation field implies that targeted binding functionality could be applied to various nanoparticle core materials, potentially enhancing existing nanoremediation techniques and enabling the use of targeted contrast agents for advanced site characterization. Immobilization of engineered nanoparticles at the interface between the target contaminant mass and water addresses key drawbacks of current *in situ* nanoremediation strategies, namely improving efficiency and cost,[118,119] as well as limiting uncontrolled nanoparticle release[100].

The application of X-ray CT to detect nanoparticles in a porous medium has great potential for further development. In this study, there are two notable implications to be drawn from X-ray CT visualization of nanoparticle binding. First, X-ray CT is introduced as a useful, non-destructive technique for quickly analyzing 3-D sand characteristics with minimal sample preparation. Second, it implies a useful application for nanoparticle targeted binding in porous media, that is, as a contrast agent for 3-D imaging of sands impacted with viscous heavy hydrocarbons such as crude oil. Based on these findings, it is conceivable that mobile nanoparticles may be visualized by X-Ray CT in dynamic transport studies. Such experiments may generate a wealth of data to further understanding of nanoparticle transport behaviour in porous media and characterize targeted nanoparticle binding in realistic hydrogeologic conditions. One current drawback of the technique as presented here is its qualitative nature, but with careful development of a proper analysis methodology, it may be possible to extract quantitative data from this technique. In a similar vein, the use of SQUID/VSM magnetic characterization introduces quick, non-destructive, quantitative analysis techniques with minimal sample preparation which may help to overcome difficulties with characterizing nanoparticle presence in sand samples.

The work presented here limits its scope to batch investigation and novel X-ray characterization as a proof-of-concept for a targeted binding strategy, but these findings open the door to larger scale experiments under more realistic conditions. The nanoparticle coating proposed here has demonstrated limited binding to clean silica sand implying that transport through porous media should be possible, however literature has demonstrated that interactions with natural macromolecules can change the surface of engineered nanoparticles, affecting their behaviour and fate in soils[175]. To this end, research investigating the transport properties of these nanoparticles in various porous media, as well as expanded application of this novel X-ray CT nanoparticle characterization technique is ongoing in pursuit of improving and demonstrating the application of this targeted delivery platform for nanoremediation and geophysical monitoring.

Chapter 4

Nanoparticle Targeted Delivery to Petroleum Hydrocarbon Impacted Porous Media†

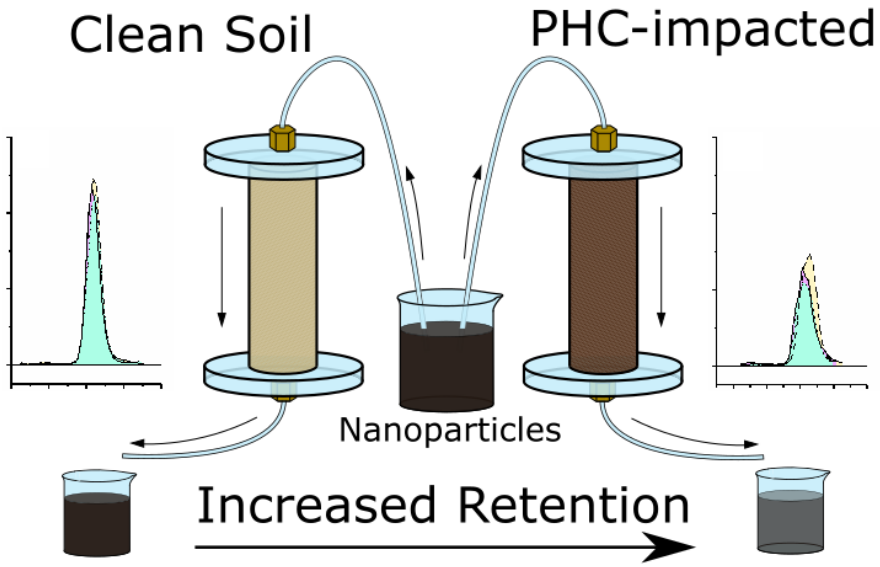

Figure 12. Engineered nanoparticles with a Pluronic coating are transported through a clean sandy loam and preferentially retained in an artificially PHC-impacted sandy loam.

4.1 Summary

Targeted delivery of nanoparticles has potential to enhance remediation and geophysical monitoring of contaminated sites by ensuring delivery of treatment or contrast agents to the contaminant/water interface. For a targeted delivery technique to be successful, nanoparticles must be capable of transporting through porous media and binding to contaminants under relevant hydrogeological conditions. In this study, successful targeted delivery of nanoparticles to sandy aquifer material mixed with crude oil was achieved using an active targeting technique based on an amphiphilic polymer coating (**Figure 12**). The effect of the polymer coating on nanoparticle transport capabilities was examined and it was found that the molecular structure and concentration of the nanoparticle coating greatly influenced nanoparticle recovery through saturated packed columns. Coatings with longer polymer molecules and lower polymer concentrations reduced recovery, and it was found that the

† This chapter is adapted from a drafted manuscript: Linley, S.; Thomson, N.R..; McVey, K.; Sra, K.; Gu, F. X. Nanoparticle Targeted Delivery to Petroleum Hydrocarbon Impacted Porous Media. Not yet submitted.

nanoparticle coating formulation could be adjusted to improve transport while maintaining targeted binding behaviour. Critically, this work demonstrated that nanoparticle retention in oil impacted sand exceeded that of clean sand in packed column flow through experiments, indicating that a nanoparticle targeted delivery strategy for soil contaminated with viscous LNAPLs such as crude oil is possible under field-relevant transport conditions.

4.2 Introduction

Soil remediation is a complex environmental challenge which often employs slow, costly, and environmentally disruptive *ex situ* treatment techniques[9]. *In situ* treatment methods offer a more sustainable and potentially more economic approach to remediation[8], and it is for these reasons that innovative nanotechnology-based remediation techniques, which make use of higher surface area to improve adsorption and reaction kinetics, have been the subject of much research over the past decade[100,176]. Nanomaterials such as nano Zero Valent Iron (nZVI)[110,140,177,178], bimetallic nanoparticles[179–181], iron oxide[182,183], and carbon nanomaterials[184–186] have been investigated as remediation agents or adjuncts for remediation of organic contaminants in soil. Typical deployment strategies for nano-based remediation technologies involve direct injection of a nanoparticle suspension to the contaminated area[178,187], and as a result, much research effort has been devoted to finding nanoparticle coating materials which facilitate efficient transport in porous media and maintain the nanomaterial's treatment capability[187]. Recent work by Bossa et al. has demonstrated the potential for Cellulose Nanocrystal (CNC) coatings to enhance both the mobility and reactivity of nZVI in packed columns and demonstrate that nanoparticle transport and remediation capability is strongly dependent on the selected nanoparticle coating material[188]. These deployment strategies rely on a blanket approach to *in situ* remediation, delivering treatment agents to all areas of a contaminated site irrespective of local heterogeneity in contaminant distribution. Since a large volume of soil can be contaminated by relatively small amounts of NAPLs, this can lead to inefficient use of remediation agent, increasing the cost and environmental impact of remediation[189].

Targeted nanoparticle delivery is a concept widely accepted and successfully deployed in nanomedicine which relies on physical and chemical properties of target cells to improve drug delivery efficiency and reduce damage to healthy cells[123,190,191]. This treatment strategy has proved particularly interesting in oncological studies wherein drug-encapsulating nanoparticles are functionalized with ligands complementary to receptors found on diseased cells, promoting uptake of the nanoparticles by cancerous tissue and ensuring the drug reaches its intended target[190]. The challenge of *in situ* soil remediation is, in many ways, similar to chemotherapy: a treatment agent must be delivered to

contaminated areas which have distinct physical and chemical properties. In both cases, the efficiency and economics of the treatment may be improved through the application of targeted delivery strategies. Targeted delivery of nanomaterials to contaminated porous media has previously been demonstrated with some success by adopting what would, in nanomedicine, be referred to as an 'active targeting' technique. That is, a nanoparticle is functionalized with a surface coating that facilitates favourable chemical interactions with the targeted substance. Previous examples of this targeted delivery concept for environmental applications has been investigated for targeting of DNAPL contaminants, often chlorinated hydrocarbons[118,119,189]. In this work, a similar targeting strategy is employed for targeting viscous LNAPLs, and nanoparticles are coated with Pluronic, an inexpensive amphiphilic block copolymer with hydrophilic poly(ethylene oxide) (PEO) segments providing stability in aqueous suspension and a hydrophobic poly(propylene oxide) (PPO) segment providing favourable hydrophobic interactions between the nanoparticle and the target contaminant, crude oil.

Successful deployment of a nanoparticle targeted delivery strategy for remediation relies on the success of three key features: 1) ability of the nanoparticle to transport through porous media to the site of the contaminant, 2) ability of the nanoparticle to preferentially attach to the target contaminant, and 3) ability of the nanoparticle to directly or indirectly effect the degradation of the target contaminant. Our previous work on feature 2) from this list has demonstrated that Pluronic-coated nanoparticles have attachment affinity for crude oil-impacted sands compared to clean sands. This work seeks to demonstrate feature 1) through successful transport of Pluronic-coated nanoparticles through real sandy aquifer porous media and determine how coating formulation influenced nanoparticle recovery. In addition to this, we establish that nanoparticle transport and binding can be achieved in column flow-through conditions, indicating the viability of nanoparticle targeted delivery strategies in soil materials under relevant hydrogeological conditions.

4.3 Experimental

4.3.1 Materials

Iron (II) sulfate heptahydrate ($FeSO_4 \cdot 7H_2O$, > 99%), iron (III) chloride hexahydrate ($FeCl_3 \cdot 6H_2O$, > 99%), ammonium hydroxide (NH_4OH, 28-30% in water), dichloromethane (DCM, > 99%), and oleic acid (> 90%) were purchased from Sigma Aldrich. Hydrochloric acid (37%) and ethanol (ACS grade, 99%) were purchased from Fisher Scientific. Pluronic co-polymers F108, P105, P104, P103, P123, and L62 were gifted by BASF Canada. Pluronic F127 was purchased through Sigma Aldrich. Crude oil (heavy, sour crude, API gravity 13.3, density 0.977 g/cm^3, viscosity 474.5 cSt @ 40 °C) was provided by Chevron Energy Technology Company. Natural aquifer material (Borden sand) was obtained from Canadian Forces Base Borden, ~100 km north of Toronto, Canada (see Appendix B for detailed soil

characteristics). Oil-impacted Borden sand (OBS) was prepared by dissolving crude oil in DCM at a concentration of ~60 g/L, mixing it with dry, disinfected Borden sand, and evaporating the DCM such that the sand was homogenously coated with oil at a concentration of 1.5% (m/m).

4.3.2 Nanoparticle Synthesis

Nanoparticle synthesis was adapted from a previously reported method[163]. $FeSO_4 \cdot 7H_2O$ and $FeCl_3 \cdot 6H_2O$ were added to deoxygenated water at a molar ratio of 2:3 ($FeSO_4$:$FeCl_3$), followed by NH_4OH and oleic acid at final concentrations of 4 and 0.22 mol/L, respectively. This solution was stirred at 70 °C for 1 h, then stirred at 90 °C under flowing N_2 for 1 h. After cooling to room temperature, the black, magnetic precipitate was recovered by magnetic decantation and washed 3x by deoxygenated Millipore DI water (Millipore Elix 5), and then 3x by ethanol before being dried under flowing N_2.

4.3.3 Nanoparticle Phase Transfer

Dried nanoparticles and oleic acid were added to hexane such that the final concentrations were 90 g/L and 1% v/v, respectively. The resulting suspension was added to various aqueous solutions of Pluronic co-polymer(s) and probe sonicated for 30 min to emulsify the water and hexane phases (Fisher Scientific FB505 Sonic Dismembrator, 200 W). The emulsified nanoparticle sample was transferred to a separatory funnel and separated over 48 h. The resulting aqueous nanoparticle suspensions were diluted by a factor of 10 and stored until used.

4.3.4 Column Flow-through Experiments

Borden sand was disinfected at 90 °C prior to use. 15 cm-long Plexiglas columns (I.D. = 3.8 cm) were packed with either clean Borden sand (CBS) or OBS by wet-packing and dry-packing, respectively. After dry-packing the OBS, the column was flushed with CO_2 gas and saturated bottom-to-top with Millipore water. Following packing, all columns were flushed with Millipore water bottom-to-top overnight to ensure full saturation prior to nanoparticle injection. Columns were inverted and as-prepared nanoparticle suspensions were injected for 30 minutes top-to-bottom at an average flow rate of 18 cm^3/h, after which Millipore water was injected at the same flow rate. Outflow samples were collected every 20 minutes from the onset of injection until 100 minutes had passed, after which outflow samples were collected every 10 minutes. For transport and binding experiments, CBS and OBS columns were prepared and nanoparticle injection was conducted identically up to 100 minutes. After 100 minutes had passed, injection was paused for 40 h such that the nanoparticle slug maintained contact with the CBS or OBS for a length of time suitable to observe nanoparticle attachment. After 40 h, outflow sampling resumed every 10 minutes for an additional 260 minutes.

4.3.4 Analyses

Transmission Electron Microscopy was performed using a Philips CM-10 electron microscope. Samples were prepared by drying 5 µL of aqueous nanoparticle suspension as prepared in the phase transfer section on a 400-mesh formvar-coated copper grid (Ted Pella).

Nanoparticle concentration in aqueous suspension was assessed using Inductively Coupled Plasma Atomic Emission Spectroscopy (ICP-AES; Teledyne Leeman Prodigy). 1 mL of collected outflow samples were acid digested using 0.2 mL 37% HCl and diluted to a total sample volume of 10 mL before quantifying iron concentration.

4.4 Results and Discussion

Various Pluronics were investigated to examine the effect of coating molecular structure on transport properties of the nanoparticles. Information regarding the selected Pluronics are provided in **Table 5**. Pluronic samples are identified by a three-part alphanumeric code which describes physical appearance, MW_{PPO} divided by 300, and % total MW_{PEO} divided by 10. For example, the identifier F127 indicates the polymer has a solid appearance at room temperature (F = flakes, P = paste, L = liquid), a MW_{PPO} of 3,600 g/mol (12 x 300 = 3,600), and that its total MW is 70% PEO (7 x 10 = 70). Pluronic synthesis can be easily altered to produce polymers with varying PPO and PEO block sizes, resulting in similar polymers with widely varying physical properties dependent on molecular weight.

Table 5. Properties of Pluronic coating polymers discussed in Chapter 4.

Polymer ID	MW (g/mol)	Structure	PPO MW (g/mol)	PEO MW (g/mol)	Hydrophilic/Hydrophobic number ratio
L62	2,250	PEO_5-PPO_{31}-PEO_5	1,800	450	0.32
P123	5,140	PEO_{17}-PPO_{62}-PEO_{17}	3,600	1,540	0.55
P103	4,290	PEO_{15}-PPO_{52}-PEO_{15}	3,000	1,290	0.58
P104	5,000	PEO_{23}-PPO_{52}-PEO_{23}	3,000	2,000	0.88
P105	6,000	PEO_{34}-PPO_{52}-PEO_{34}	3,000	3,000	1.31
F127	12,000	PEO_{95}-PPO_{62}-PEO_{95}	3,600	8,400	3.06
F108	15,000	PEO_{136}-PPO_{52}-PEO_{136}	3,000	12,000	5.23

4.4.1 Effect of Nanoparticle Coating on Morphology and Transport Efficiency

TEM images detailing particle morphology when coated by the various Pluronic polymers reveal that size and morphology is consistent between coating type when a constant coating concentration of 10 g/L is used (**Figure 13**). The average particle size for each panel is provided in Table S1 of the supplementary information, showing that there is no appreciable size difference between coating types and gives an average particle size of 8.08 nm ± 0.76 nm across all panels. DLS data supports this observation (**Table 6**), showing that the particle hydrodynamic diameters fall within the range of 25 – 50

nm with an average diameter of 33.6 nm and an average dispersity of 0.227. Although the sizes vary modestly, there is no trend relating nanoparticle hydrodynamic diameter to Pluronic coating type and no obvious morphological differences in terms of particle size, shape, or aggregation. On average, the particles are smooth, distinct, and spherical single-crystals which is consistent with the appearance of similar Pluronic-coated magnetite particles produced in previous work[192,193].

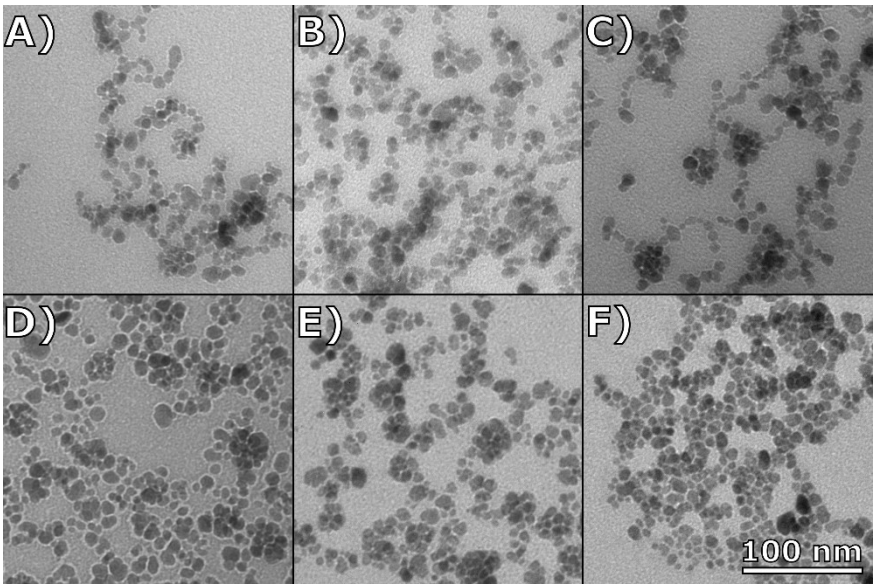

Figure 13. TEM composite image of 6 nanoparticle samples coated with different Pluronic polymers. A) F127, B) F108, C) P105, D) P104, E) P103, F) P123.

Table 6. Nanoparticle Sizes from TEM and DLS sizing. TEM diameter is the average of 100 particle measurements from the corresponding panel in **Figure 13**.

Sample	TEM Average Diameter (nm)	Standard Deviation (nm)	DLS Number Average Diameter (nm)	Dispersity
F127	7.88	1.99	26.4	0.198
F108	8.31	1.92	39.4	0.188
P105	8.37	1.90	47.1	0.149
P104	7.67	2.03	22.6	0.202
P103	8.45	1.81	30.5	0.302
P123	7.82	1.53	35.5	0.321
Average	8.08	0.76	33.6	0.227

The influence of polymer coating on nanoparticle transport and recovery was investigated through a series of transport experiments in saturated columns of packed Borden sand (**Figure 14**). Recovery was calculated as the area under the elution curve divided by the injected mass in the nanoparticle slug volume. It was found that for the same PPO centre segment (MW: 3600 g/mol in "12" Pluronics; MW: 3000 g/L in "10" Pluronics), as the size of the PEO segments increased, nanoparticle

recovery decreased. For example, F108 (the 3000 g/L PPO segment coating with the longest PEO chains) coated particles exhibit significantly lower recovery of 61.1 ± 1.0% than P103 (the 3000 g/L PPO segment coating with the shortest PEO chains) coated particles with recovery of 97.4 ± 7.2%. The most likely explanation for this behaviour relates to Pluronic adsorption on the silica surface of the Borden sand. The Pluronic polymers are held to the inner, hydrophobic SPION cores of the nanoparticles through hydrophobic forces, and as such, the binding is strong but not permanent[192,194]. Hydrogen bonding interactions between the oxygen of the PEO chains and acidic metal oxide surface groups such as silanol have been previously demonstrated in the literature[171], and this is likely occurring on the surface of the Borden sand. This may cause the Pluronic to be stripped away from the nanoparticle, resulting in destabilization, aggregation with other stripped nanoparticles, and deposition within the column. As the Pluronic coating's PEO chain length is decreased, fewer PEO segments are available for hydrogen bonding and are held closer to the core of the particle, restricting interaction with silanol groups present in the column and allowing the nanoparticles to pass through less impeded. Larger PPO segment-coatings ("12" Pluronics) appear to have lower recovery when compared to their shorter counterparts with PEO chains of similar length (F108 vs F127; P103 vs P123) implying that increased hydrophobicity facilitates destabilization of the particles once Pluronics are stripped from their surface.

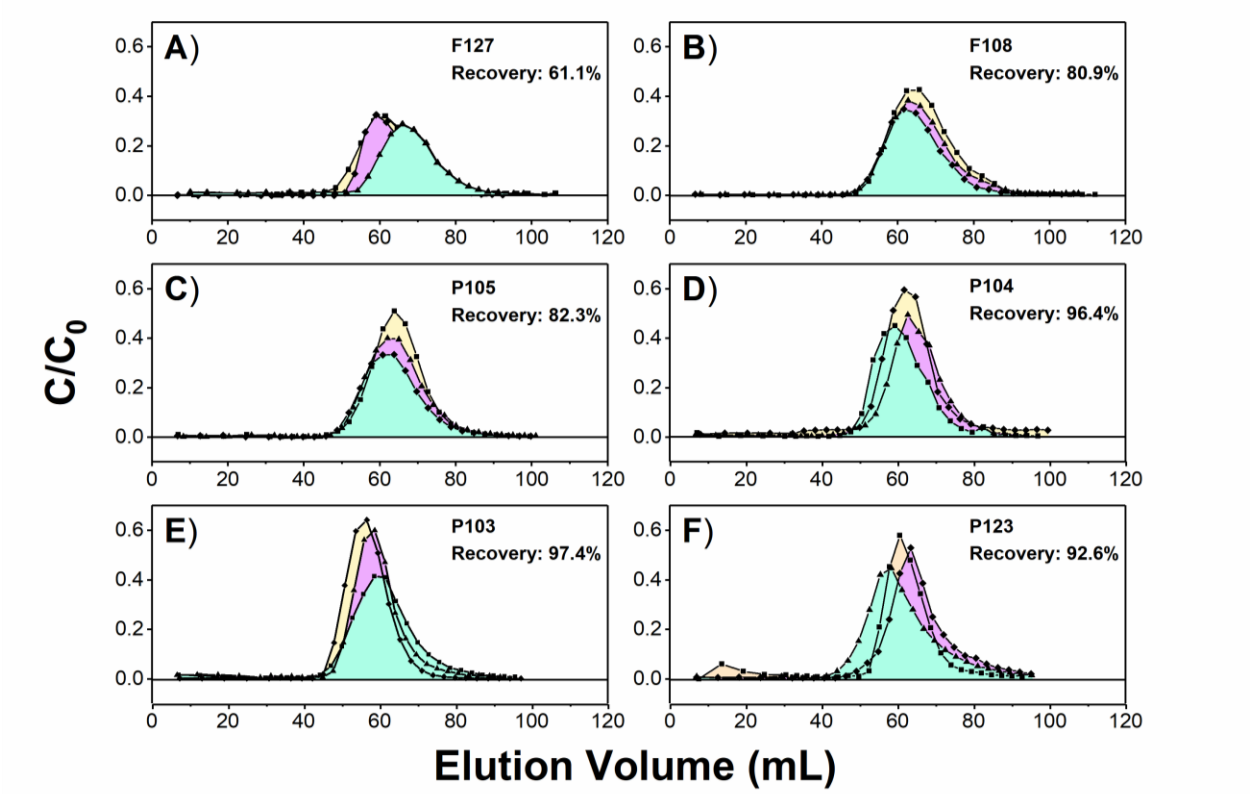

Figure 14. Nanoparticle elution curves resulting from transport through 15 cm saturated packed columns for particles coated with various Pluronic polymers. A) F127, B) F108, C) P105, D) P104, E) P103, F) P123.

In addition to the effect of various Pluronic coating types, the effect of different Pluronic coating concentrations was also investigated with respect to nanoparticle recovery through saturated soil columns. The Pluronic formulation selected for these experiments was a blend of Pluronic L62 and Pluronic P104 in a 4:1 ratio as this was found to exhibit preferential NP binding toward oil-impacted sand in previous studies[195] (see Chapter 3) and predicts good transport based on **Figure 14** (short PPO segment, short PEO segments). TEM images of nanoparticles coated with various concentrations of Pluronic can be seen in **Figure 15**, showing that a decreasing Pluronic concentration results in greater nanoparticle aggregation.

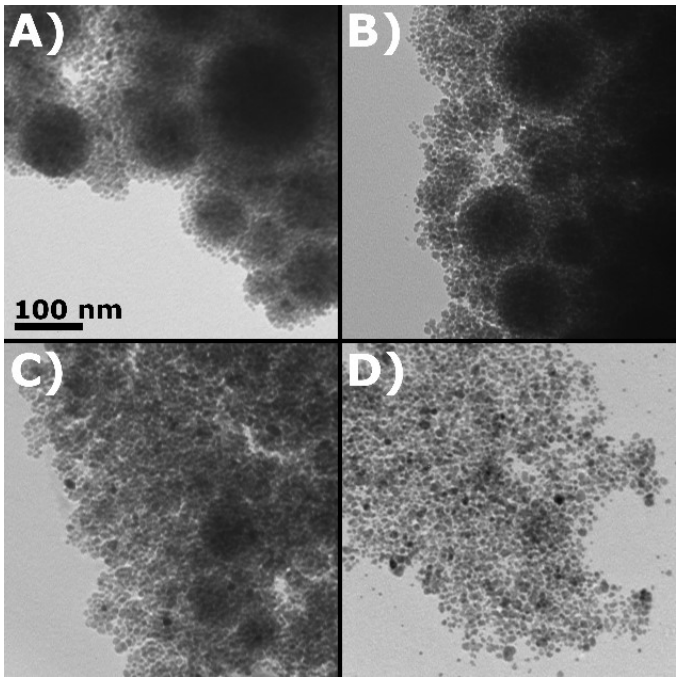

Figure 15. TEM Composite showing nanoparticle morphology at different Pluronic coating concentrations. A) 1 g/L, B) 2.5 g/L, C) 5 g/L, D) 10 g/L

The highest concentration tested, 10 g/L, is the same concentration used for producing the NP seen in **Figure 13**, and the size, morphology, and aggregation of the particles seen in **Figure 15 D**) correspond closely to those particles. At coating concentrations as low as 5 g/L, small aggregates of nanoparticles are formed (**Figure 15 C**). Further decrease in concentration to 2.5 g/L and below results in the presence of multiple large aggregates with sizes exceeding 100 nm. While the individual nanoparticles seen in **Figure 15** remain small with low dispersity, DLS sizing confirms the presence of large aggregates at lower coating concentrations by showing that the number-average hydrodynamic particle diameter increases from 43.8 nm at 10 g/L (comparable to DLS results from particles shown in **Figure 13**) to 145.0 nm at 1 g/L. The cause for this change in morphology with decreasing coating concentration is likely due to incomplete surface coverage of Pluronic on the particles. Adsorption of Pluronic on oleic acid-coated magnetite particles has previously shown to follow a Freundlich adsorption isotherm resulting in a drastic increase of adsorbed polymer over a moderate Pluronic concentration range of 0.1 to 3 mmol/L[193]. The concentration range of Pluronic in this work varies exactly within this range producing large aggregates at 1 g/L (~0.4 mmol/L) and with individually stabilized particles appearing at 5 g/L (~2 mmol/L). This incomplete coating at lower concentrations leaves areas of the hydrophobic SPION core particles exposed, driving aggregation (**Figure 15 A, B**), while at higher concentrations Pluronic adsorption increases and smaller aggregates or individual particles are stabilized (**Figure 15 C, D**).

The transport performance of nanoparticles coated with various concentrations of Pluronic was assessed in 15 cm saturated columns packed with Borden sand, and it was found that recovery followed a general trend of increasing with higher Pluronic coating concentrations (**Figure 16**).

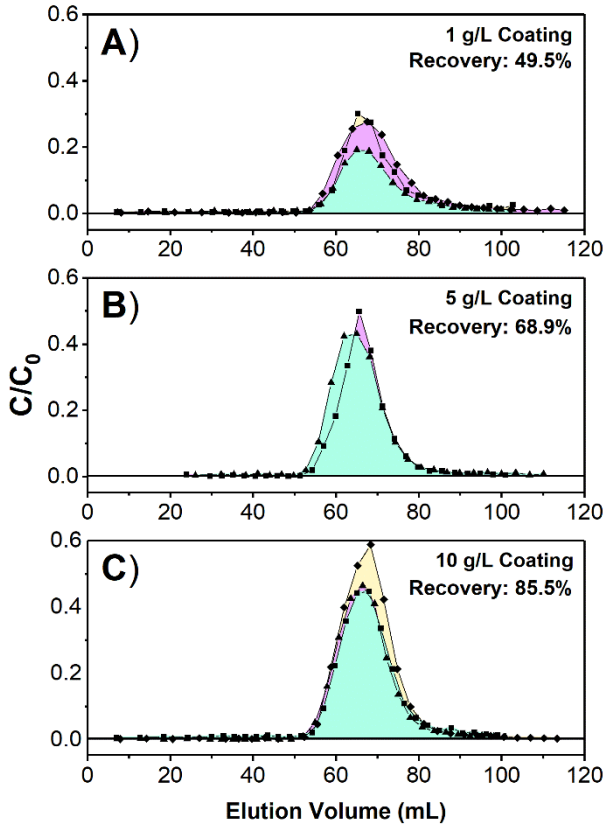

Figure 16. Nanoparticle elution curves resulting from transport through 15 cm saturated packed columns for particles coated with L62-P104 Pluronic in a 4:1 ratio at various concentrations: A) 1 g/L, B) 5 g/L, C) 10 g/L.

This trend of decreasing recovery with decreasing Pluronic concentration is likely related to both particle morphology and Pluronic adsorption to Borden sand. In the first case, when a single large nanoparticle aggregate (1 g/L coating) is deposited in the column, this represents a greater mass of iron, and a larger fraction of the total injected nanoparticle mass than when a single individual nanoparticle is deposited (10 g/L). In the second case, due to lower Pluronic adsorption on the particles, a smaller amount of Pluronic must be stripped away before they lose stability and deposit in the columns. Overall, the observed trend indicates that lower concentration coatings result in increased size, but decreased nanoparticle recovery in a transport scenario, while the opposite is true for higher concentration coatings.

4.4.2 Nanoparticle Transport and Binding in Clean and Oil-Impacted Porous Media

To demonstrate the ability of nanoparticles to transport through packed columns and bind to a contaminant of interest, the recovery of nanoparticles through clean Borden sand (BS) packed columns

was compared to nanoparticle recovery through oily Borden sand (OBS) packed columns. This was first tested using the 1 g/L 4:1 L62:P104 coating formulation (**Figure 17**).

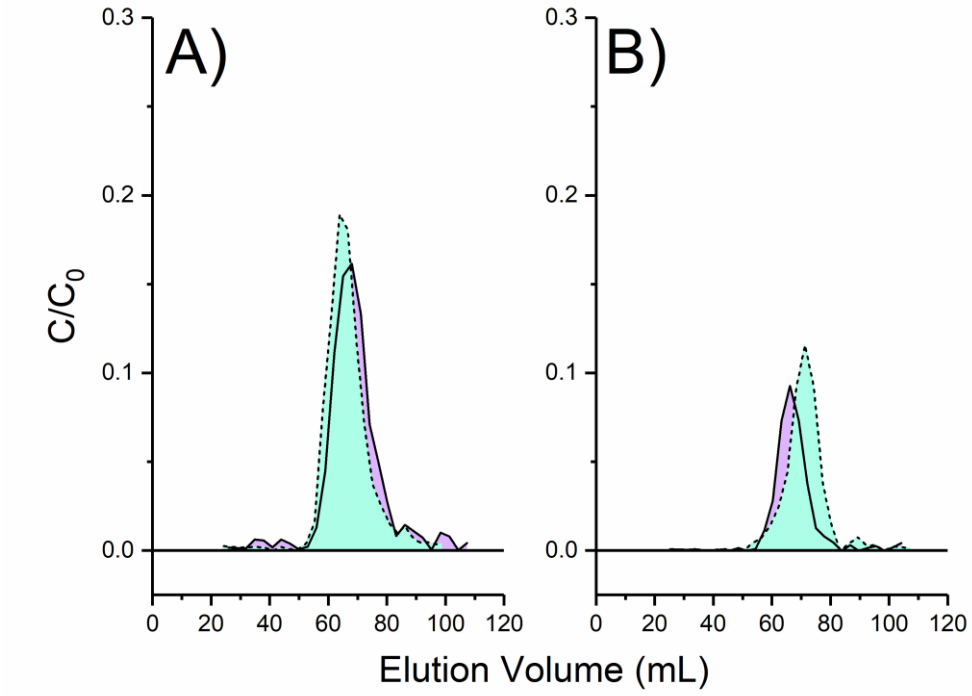

Figure 17. Nanoparticle elution profiles for SPIONs coated with 1 g/L 4:1 L62:P104 Pluronic. Panels show recovery through **A)** clean Borden sand and **B)** oily Borden sand (1.5% m/m).

The average recovery of nanoparticles passing through clean Borden sand was found to be 29.2% (**Figure 17 A**; estimated deposition of 7.6 mg/kg) while average recovery of nanoparticles passing through oily Borden sand was found to be 13.6% (**Figure 17 B**; estimated deposition of 9.8 mg/kg). The elution profiles through clean Borden sand closely match the transport data presented in **Figure 16**. In the presence of oily Borden sand, greater nanoparticle attachment due to hydrophobic interactions between the nanoparticles and the crude oil results in increased nanoparticle retention. We anticipate that the binding behaviour arises from two interactions, the first being hydrophobic forces between the PPO segments of the Pluronic coating and the crude oil, and the second being hydrophobic forces between the oleic acid inner coating and the crude oil. Previous literature suggests that binding interactions between oleic acid-coated magnetite and hydrophobic contaminants is improved through disruption of the anionic oleic-acid double layer by small molecules or polymers[122]. If the second of these two interactions is principally responsible for the targeted binding behaviour of these nanoparticles, moderate Pluronic adsorption as seen in the 1 g/L or 2.5 g/L coatings may be advantageous for allowing interaction between the oleic acid and the crude oil while still providing sufficient bilayer disruption.

Based on the results of **Figure 16**, increasing the coating concentration of the nanoparticles improved recovery through Borden sand packed columns. This transport and binding experiment comparing clean to oily packed columns was repeated using a coating formulation of 2.5 g/L 4:1 L62:P104 SPIONs (**Figure 18**) to test whether improved nanoparticle transport through clean soil could be increased while maintaining a similar degree of binding to that seen in **Figure 17**. The average recovery of 2.5 g/L 4:1 L62:P104 SPIONs passing through clean Borden sand was found to be 72.6% (**Figure 18 A**; estimated deposition of 3.4 mg/kg) while the average recovery of the same particles passing through oily Borden sand was found to be 59.4% (**Figure 18 B**; estimated deposition of 6.1 mg/kg).

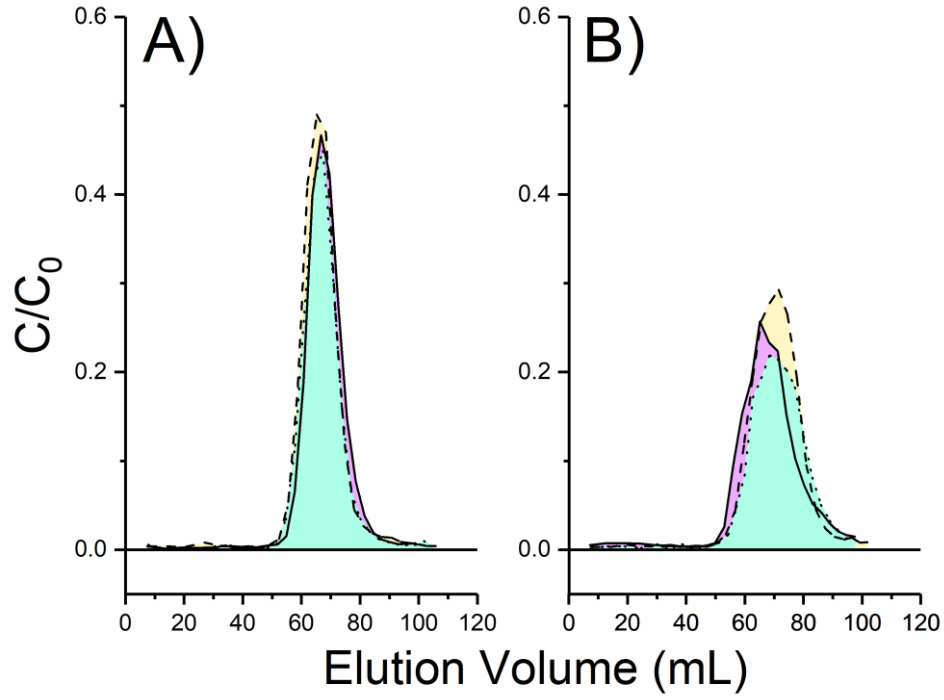

Figure 18. Nanoparticle elution profiles for SPIONs coated with 2.5 g/L 4:1 L62:P104 Pluronic. Panels show recovery through A) clean Borden sand and B) oily Borden sand (1.5% m/m).

The mass recovered through the clean Borden sand column was higher than expected considering the recovery of 5 g/L-coated SPIONs shown in **Figure 16**, but the profile appears consistent with the nanoparticle transport behaviour of other samples. Similar to the 1 g/L-coated particles tested in **Figure 17**, 2.5 g/L-coated particles experience greater attachment in the presence of oily Borden sand as opposed to clean Borden sand, a behaviour attributed to hydrophobic interactions between the nanoparticle surface coating and the crude oil in the column. These results demonstrate that targeted binding of engineered nanoparticles to hydrophobic contaminants is possible in a field-relevant model system of packed columns.

4.5 Conclusions

In summary, this work presents three key findings which support the application of nanoparticle targeted delivery to contaminated soil. Most importantly, comparison of nanoparticle retention in clean and oil-impacted saturated sandy aquifer material shows that nanoparticles are preferentially retained by the contaminated sediment under flow-through column conditions. This allows the conclusion that the implementation of nanoparticle targeted delivery may be extended to field conditions which experience similar hydrogeological behaviour. Second, it was found that nanoparticle coating formulation, both in terms of coating molecule and coating concentration, affected the recovery of nanoparticles through packed columns. As the size and relative hydrophilic content of the polymer coating increased, although particle morphology remained unchanged, recovery through packed columns decreased. As the coating concentration of the nanoparticles increased, nanoparticle morphology tended towards individually stabilized nanoparticles rather than aggregates, and recovery through packed columns increased. Finally, the findings regarding the influence of coating concentration on nanoparticle recovery through packed columns were able to be implemented to improve overall mobility of nanoparticles in a transport and binding scenario without compromising their targeted delivery behaviour.

These findings have several implications for the soil remediation and geophysical monitoring spaces. With the demonstration of nanoparticle targeted delivery in packed column scenarios, we anticipate similar application in real, field scale environments. Preferential attachment behaviour of nanoparticles to contaminated soil is provided by the Pluronic surface coating, and we anticipate that this coating may be applied to any type of nanoparticle using a similar two-step coating technique. As such, preferential accumulation of nanoparticles treatment agents or adjuncts, such as nZVI or magnetite, at the contaminant interface may serve to improve remediation effectiveness and efficiency. In a similar vein, accumulation of nanoparticles that may act as contrast agents may serve as reporters to indicate and map zones of contamination in heterogenous contaminated sites. Some of our recent work has already investigated application of the nanoparticles presented in this work as reporters for X-Ray Computed Tomography (XCT) and Spectral Induced Polarization (SIP), indicating potential for a targeted delivery geophysical monitoring technology. Nanoparticle targeted delivery has the potential to enhance various environmental remediation and monitoring techniques, and this work takes a critical step towards this goal by demonstrating its effectiveness in real soil material using packed columns.

Chapter 5

Factors Affecting Nanoparticle Targeted Binding to PHC-Impacted Sediments†

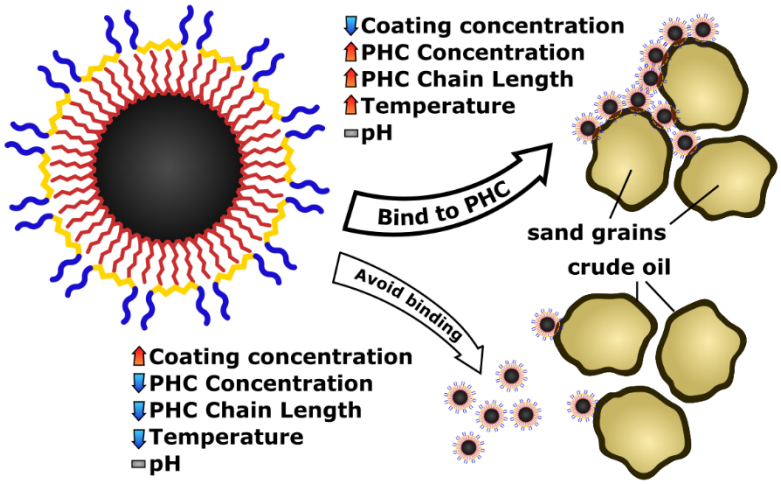

Figure 19. Schematic illustrating conditions under which preferential NP binding occurs. NP binding to PHC-impacted sediments decreases with increasing NP Pluronic coating concentration, increases with increasing PHC concentration and PHC chain length, and is unaffected by pH conditions.

5.1 Summary

Nanoparticle agents may enhance the remediation of soils and site characterization efforts, and delivery efficiency of these agents to their intended target can be improved with a targeted delivery strategy. Nanoparticles coated with Pluronic, an amphiphilic block co-polymer, demonstrate targeted binding behaviour toward viscous light non-aqueous phase liquids such as heavy crude oil. Various factors including coating concentration, oil concentration, oil type, temperature, and pH were assessed to determine their effect on nanoparticle binding to heavy crude oil-impacted sandy aquifer material. Nanoparticle binding was increased by decreasing the coating concentration, increasing oil concentration, using heavier oil types, and increasing temperature, while pH over the range of 5 to 9 was found to have no effect (**Figure 19**). Nanoparticle transport and binding in columns packed with clean and oily porous media demonstrated the ability for efficient nanoparticle targeted binding. For the conditions explored,

† This chapter is adapted from a drafted manuscript: Linley, S.; Thomson, N.R..; McVey, K.; Sra, K.; Gu, F. X. Factors Affecting Nanoparticle Targeted Binding to PHC-Impacted Sediments. Not yet submitted.

the attachment rate coefficient in clean sand was 2.10±0.66 x 10^{-4} s^{-1} for the BS columns; however, for the OBS columns a minimum attachment rate coefficient of 8.86±0.43 x 10^{-4} s^{-1}. The higher attachment rate in OBS indicates that NP may preferentially accumulate in oil-impacted sand within a heterogeneously impacted site – demonstrated with predictive modelling using 1D-USAT. This work contributes to our understanding of some of the application conditions that are required for efficient targeted binding of nanoparticles to crude-oil impacted porous media.

5.2 Introduction

As the behaviour of engineered nanomaterials are better-understood, they are being more frequently applied as agents for environmental remediation and monitoring[178,196]. With increased utilization of these nanomaterials, questions regarding environmental fate and transport efficiency have been the focus of significant research in recent years. Transport efficiency is an important consideration for nanomaterial application in porous media, as it dictates how much of the agent reaches its target destination versus unwanted deposition in non-target zones. Initially, research was focused on improving nanoparticle (NP) mobility in porous media. For example, carboxymethyl cellulose (CMC) has found application as a coating material for zero-valent iron which greatly improves mobility and dispersibility[197,198]. The concern over environmental fate of engineered nanomaterials in compounded by improvements in transport efficiency. As NPs become more mobile in porous media environments, their movement, ultimate destination, and environmental impact becomes less predictable, prompting recent investigation into how coating formulation[175,199], soil composition[200,201], organic matter[202,203], flow rate[204,205], and saturation influence NP mobility and environmental fate.

The concept of targeted delivery of NPs to contaminants present in porous media has been previously investigated with some success[119,122,206]. Targeted delivery allows particle mobility to be enhanced by using a coating material and allays some of the concern associated with environmental fate of nanomaterials. By preferentially accumulating NPs in target areas through the use of non-specific hydrophobic interactions, fewer NPs move past the zone of interest and are thus used more efficiently. Additionally, once bound to the target site, NPs have restricted mobility and their environmental fate becomes more predictable. This concept, borrowed from targeted delivery as applied in nanomedicine applications, has the potential to reduce cost and increase treatment efficiency as well as minimize unwanted side-effects due to uncontrolled release of NPs[124,147,191,207]. These design goals for medical targeted delivery present parallel solutions to the problems encountered in *in situ* nanoremediation of soils.

The NP structure investigated in this paper composes three distinct layers: 1) an iron oxide NP core coated in 2) oleic acid to impart hydrophobic characteristics, and further coated by 3) an amphiphilic polymer, Pluronic, which provides stability in aqueous media and hydrophobic interactions with target contaminants. This structure is one that has already seen successful deployment in biomedical nanotechnology as a drug delivery and targeted contrast agent for anti-cancer applications[167,172]. In such applications, targeting typically relies on a passive, size-based retention phenomena in defective tumor vasculature known as 'Enhanced Permeability and Retention', however active targeting is possible through the conjugation of specific antibodies to the surface of the particle[172]. The outer Pluronic layer has also been found to behave as an antibiofouling coating with robust attachment to the NP core, allowing good stability of the particles in physiological media[208]. In medical applications, hydrophilic Pluronics are typically selected to enhance stability, but our previous work has shown that active targeting can be achieved by selecting suitably hydrophobic Pluronic structures to improve non-specific targeting interactions[71].

Pluronic block co-polymers comprise a class of amphiphilic polymers which have been extensively investigated for their innate physical and chemical properties, as well as their application as nanomaterial coatings[167,169,172,209–211]. Their structure is given as $(EO)_x$-$(PO)_y$-$(EO)_x$, where EO represents ethylene oxide and PO represents propylene oxide. It has been previously demonstrated that the block sizes, x and y, have a significant impact on the adsorptive and micellization properties of Pluronic. For example, as the block size of propylene oxide increases, the critical micelle concentration and critical micellization temperature both decrease[209]. In addition to the structural properties of the coating itself, it is also well known that various other environmental parameters affect interfacial behaviour of molecules and NPs, for example, temperature[212], pH, and surface chemistry. In this work, we seek to elucidate the effect of various application parameters on the targeted binding of engineered NPs to a viscous light non-aqueous phase liquid (LNAPL). Understanding how these properties impact targeted binding provides the ability to predict the conditions under which targeted binding is most effective. To this end, the objectives of this study were to i) evaluate the effect of various environmental parameters on NP targeted binding in batch studies, and ii) apply these findings in a series of stop-flow NP transport and binding column trials to demonstrate the capability of targeted NP binding in a hydrodynamic porous medium system.

5.3 Materials & Methods

5.3.1 Materials

Iron (II) sulfate heptahydrate ($FeSO_4 \cdot 7H_2O$, > 99%), iron (III) chloride hexahydrate ($FeCl_3 \cdot 6H_2O$, > 99%), ammonium hydroxide (NH_4OH, 28-30% in water), dichloromethane (DCM, > 99%), oleic acid (> 90%), Sodium Bromide (NaBr, ≥99%) and acetic acid (≥99.7%) were purchased from Sigma Aldrich.

Hydrochloric acid (37%) and ethanol (ACS grade, 99%) were purchased from Fisher Scientific. Pluronic co-polymers P104 and L62 (**Table 7**) were gifted by Brenntag Canada and BASF Canada. Borden Sand (d_{10} = 0.075 mm; Cu = 2.7) was obtained from the University of Waterloo Groundwater Research Facility at the Canadian Forces Base (CFB) in Borden, ON, Canada[213] (see Appendix B for soil characterization). Crude oil (heavy, medium, and light) was provided by Chevron Energy Technology Company. All materials were used as received.

Table 7. Properties of pluronic co-polymers used in Chapter 5.

Polymer ID	M_n (g/mol)	Structure	M_n of PPO (g/mol)	M_n of PEO (g/mol)	Cloud Point in 1% aq. sol'n (°C)
L62	2,250	PEO_5-PPO_{31}-PEO_5	1,800	450	32
P104	5,000	PEO_{23}-PPO_{52}-PEO_{23}	3,000	2,000	81

5.3.2 Nanoparticle Synthesis

Iron oxide NPs were prepared as reported in our previous work[71]. Briefly, $FeSO_4 \cdot 7H_2O$ and $FeCl_3 \cdot 6H_2O$ were added to deoxygenated water at a molar ratio of 2:3 ($FeSO_4$:$FeCl_3$). Sufficient NH_4OH and oleic acid were added to achieve final concentrations of 4 and 0.22 mol/L, respectively. This solution was stirred at 70 °C for 1 h, then stirred at 90 °C under flowing N_2 for 1 h to purge evolved NH_3 gas. After cooling to room temperature, the black, magnetic precipitate was recovered by magnetic decantation and washed 3x by deoxygenated Millipore DI water (Millipore Elix 5), and then 3x by ethanol before being dried under flowing N_2.

Phase transfer of the hydrophobic nanoparticles to water was completed by using Pluronic polymer. A mixture of oleic acid in hexane (1% v/v) was prepared to which dried NPs were added at a concentration of 90 g/L and sonicated for 10 min (VWR "Symphony" 1.9 L Ultrasonic Cleaner). The resulting suspension was added to various aqueous solutions of Pluronic co-polymers at concentrations between 1 and 10 g/L, and probe sonicated for 30 min to emulsify the water and hexane phases (Fisher Scientific FB505 Sonic Dismembrator, 200 W). The emulsified NP sample was transferred to a separatory funnel and separated over 48 h. The resulting aqueous NP suspensions were stored until further use. Prior to application in binding batch tests or transport & binding column tests, the aqueous NP suspensions were diluted with Millipore DI water by a factor of 100 and 10, respectively.

5.3.3 Nanoparticle Binding Batch Tests

Oil-impacted Borden Sand (OBS) was prepared by dissolving the specified type of crude oil (light, medium, or heavy) in DCM, mixing it with dry Borden sand, and evaporating the DCM such that the final concentration of crude oil in sand reached the desired mass fraction (m/m%) for a specific trial.

This approach was used to create a homogeneous crude oil and sand mixture. 15 g of OBS was then added to a 20-mL cylindrical glass vial, followed by 10 mL of diluted NP suspension. For temperature parameter tests, vials were placed in an oil bath set to the specified temperature. For pH parameter tests, acetic acid or ammonium hydroxide was added dropwise until the desired pH was reached. NP samples were maintained under these binding conditions for 40 hours before the NP suspension was recovered by filtration (1.5 μm glass fiber, Whatman). For control, "clean" Borden Sand (BS) samples were prepared as above except no oil was present in the added DCM. Three replicates of each sample were prepared to capture variability.

5.3.4 Nanoparticle Transport and Binding Tests

Plexiglas columns (length: 15 cm, inner diameter: 3.8 cm) were wet packed with BS, or dry packed with OBS (1.5% crude oil m/m), placed in a large oven (Binder ED53) set to 50 ^{o}C (based on the NP binding batch test results), and flushed with Millipore water overnight at a flow rate of 0.1 mL/min to ensure saturation. The NP solution ([NP] ≈ 500 mg/L) was then injected at a flow rate of 0.3 mL/min for 30 minutes (9 mL injection pulse), followed by Millipore water for an additional 70 minutes. At 100 minutes, the flow was stopped (stop-flow conditions) for 44 hours (2640 minutes) to allow the NPs in this system to have the near equivalent interaction time as the binding batch tests (40 hours). At total elapsed time of 2740 minutes, the flow was resumed by injected Millipore water at a flow rate of 0.3 mL/min, and effluent samples were taken every 10 minutes until 3040 minutes. Immediately following each NP transport and binding test, a conservative tracer test was performed on each column. Each tracer test consisted of the injection of a 500 mg/L bromide (Br^-) solution for 10 minutes followed by Millipore DI water for 2 hours at a continuous flow rate of 1 mL/min. The effluent was periodically sampled.

5.3.5 Analysis

Aqueous NP samples were acid digested in 6 mol/L HCl prior to analysis by ICP-OES (Prodigy) to quantify total iron (method detection limit (MDL) of 4 μg/L). NP mass bound on the OBS or the BS (mg of NPs/dry kg of sediment) was estimated from the difference between the initial and final (after 40 h of exposure) aqueous NP concentration. In figures showing [Fe], 'initial' refers to the concentration of iron in solution prior to contact with BS or OBS. Br^- concentration in the effluent samples collected during the tracer tests was quantified using ion chromatography (Dionex ICS-1100) with a MDL of 0.5 mg/L. High Resolution Transmission Electron Microscopy (HR-TEM) analysis was performed using a JEOL 2010F with an acceleration voltage of 200 keV. The NPs were dispersed in ethanol, sonicated, and a droplet placed on a holey carbon coated Cu grid, which was allowed to air dry before being analysed.

5.3.6 Nanoparticle Transport Modelling

To determine kinetic model parameters that capture the observed binding behavior during the stop-flow column experiments, we assumed that the following single site attachment-detachment model with a nonlinear Langmuirian blocking coefficient[214] along with advective-dispersive transport of the NPs in the aqueous phase was sufficient:

$$\phi \frac{\partial C_w}{\partial t} = \frac{\partial}{\partial z}\left(D \frac{\partial C_w}{\partial z}\right) - q \frac{\partial C_w}{\partial z} - \phi \psi_c k_{attach} C_w + \rho_b k_{detach} M_{attach} \tag{22}$$

with

$$\rho_b \frac{dM_{attach}}{dt} = \phi \psi_c k_{attach} C_w - \rho_b k_{detach} M_{attach} \tag{23}$$

$$\psi_c = 1 - \frac{M_{attach}}{M_{attach}^{max}} \tag{24}$$

where C_w is the aqueous NP concentration (g m^{-3}), $D = \phi\tilde{D} = \alpha|q|$ (m^{2}s^{-1}) is the dispersion coefficient, φ is porosity (-), α is dispersivity (m), q is darcy flux (m s^{-1}), ρ_b is bulk density (kg m^{-3}), k_{attach} and k_{detach} are the NP attachment and detachment rate coefficients (s^{-1}), respectively; M_{attach} is the mass of NPs attached [g kg^{-1}], M_{attach}^{max} is the maximum mass of NPs that can be attached [g kg^{-1}], and ψ_c is the Langmuirian blocking coefficient. The unsaturated flow and solute transport model 1D-USAT[215] was used in conjunction with the dynamically dimensioned search (DDS) global search algorithm[216] within the OSTRICH toolkit[217] for parameter identification. To estimate the porosity and dispersivity for each column, equation ((23) was used without the attachment/detachment terms to simulate the Br^- tracer tests. The Br^- breakthrough curve (BTC) data were chosen as the calibration targets with the root mean square error (RMSE) as the objective function. Using column specific porosity and dispersivity values, the NP attachment and detachment rate coefficients (k_{attach} and k_{detach}) were then determined with the observed NP BTC data as the calibration targets and a RSME objective function. M_{attach}^{max} was assigned a value equivalent to the average mass of NPs bound to either the BS or OBS sand from the binding batch test performed at 50 ºC. These M_{attach}^{max} values were assumed representative of binding saturation conditions due to the nature of the well-mixed batch tests. A total mass flux boundary condition corresponding to the NP or Br^- concentration and duration of the pulse injection was specified at the inlet of the column, and a zero dispersive flux boundary condition was specified the outlet. A continuous flow rate was used in the tracer test simulations, while for the NP transport simulations, stop-flow conditions consistent with the NP column experiments were employed.

5.4 Results and Discussion

5.4.1 Effect of NP Pluronic Coating Concentration

The NPs were characterized by TEM prior to application in the binding batch experiments. It was observed that the Pluronic concentration used in the phase transfer stage of preparation (herein referred to as coating concentration) had a significant effect on the morphology of the resulting suspension (**Figure 20**).

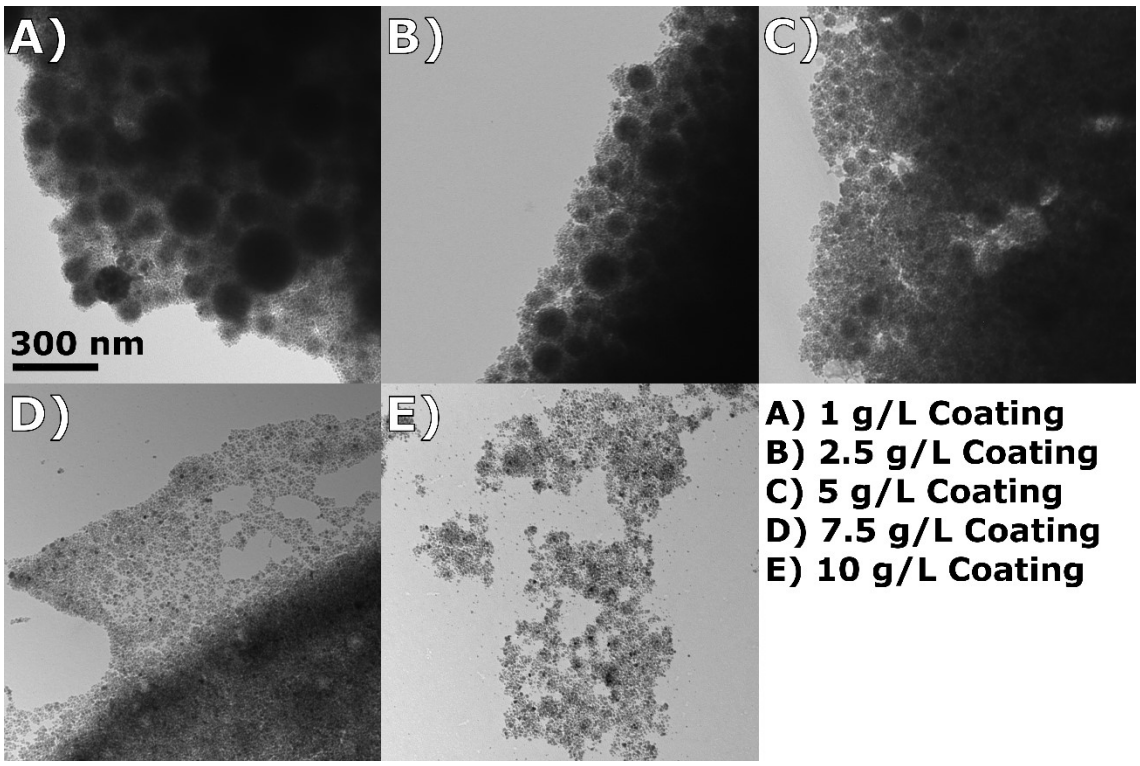

Figure 20. TEM composite showing nanoparticles synthesized with different Pluronic coating concentrations: **A)** 1g/L, **B)** 2.5 g/L, **C)** 5 g/L, **D)** 7.5 g/L, **E)** 10 g/L. At lower Pluronic coating concentrations, nanoparticles agglomerate into larger, spherical aggregates (panels **A,B**). At higher coating concentrations, nanoparticles are individually stabilized and there is an absence of aggregates (panels **D,E**).

Lower coating concentrations resulted in the presence of small, individually stabilized NPs (7 ± 2 nm) alongside spherical NP aggregates (115 ± 41 nm) as seen in **Figure 20 A**. The formation of these aggregates is thought to be due to insufficient Pluronic present to fully saturate the surface of all individual NPs. Pluronic adsorption on iron oxide surfaces follows a Freundlich adsorption isotherm[210], and previous literature has reported that a sharp increase in Pluronic surface concentration occurs in the range of 0.1-3 mmol/L[193], which corresponds closely with the concentration range used for the NPs shown on **Figure 20 A)-E)** (approximately 0.4 – 4.4 mmol/L). As the Pluronic concentration increases to 10 g/L, the amount of Pluronic adsorbed on the particle surface reaches sufficient density to stabilize

individual particles, and the presence of large aggregates diminishes (**Figure 20 C**) and disappears (**Figure 20 D & E**).

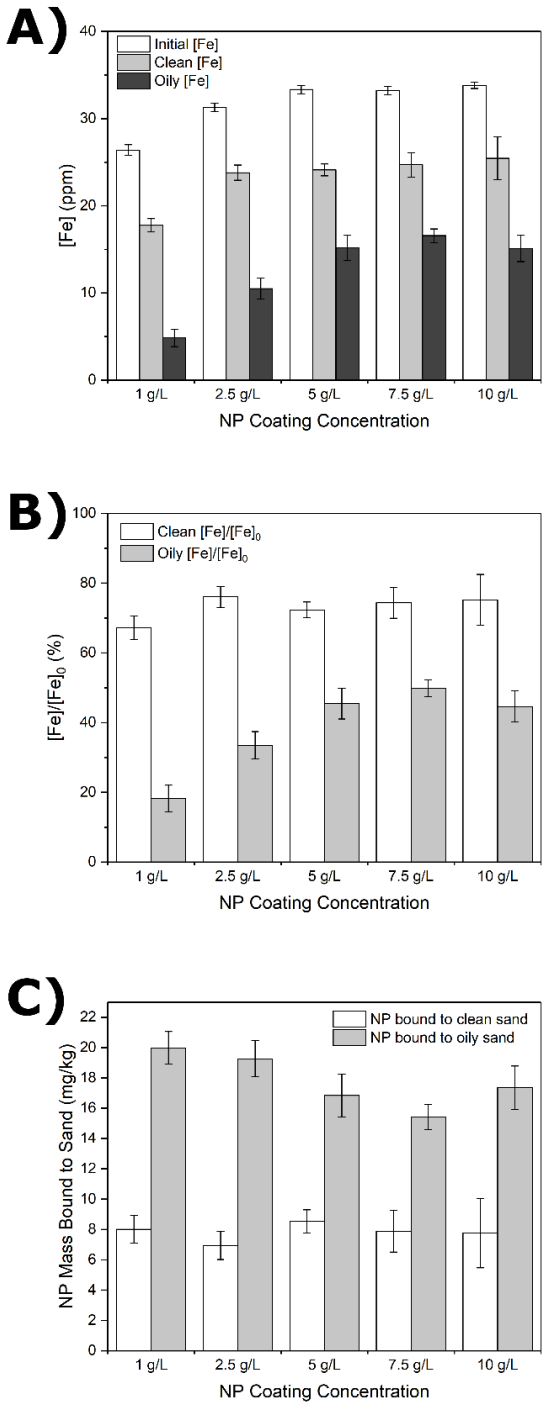

Figure 21. Effect of Pluronic NP coating concentration on binding to PHC-impacted sediments: **A)** concentration of iron in NP suspension initially, and after contact with clean sand or crude oil-impacted sand; **B)** normalized concentration of iron in NP suspension after contact with clean sand or crude oil-

impacted sand; **C)** estimated mass of NP bound to sand after contact with clean sand or crude oil-impacted sand.

Pluronic coating concentration of NPs was found to influence their binding behaviour in the binding batch tests. As the coating concentration decreased, the mass of NPs bound to oil-impacted sand increased, reaching a maximum of 20.0 ± 1.1 mg/kg for a coating concentration of 1 g/L, and a minimum of 15.4 ± 0.8 mg/kg for a coating concentration of 7.5 g/L. The average mass of NPs bound to clean sand for these trials was 7.8 ± 1.4 mg/kg and was not influenced by coating concentration (**Figure 21**). This is particularly evident when normalizing by the initial NP concentration, or mass bound per mass of sand (**Figure 21 B & C**). Previous work by Wang and Acosta indicates that charge disruption of the oleic acid layer surrounding similar particles allowed easier interaction of the hydrophobic phases[122]. We suspect that at the Pluronic concentrations explored, there was enough surface coverage to disrupt the oleic acid layer and promote hydrophobic interactions, but not enough to completely cover the oleic acid layer. This disrupted layer uses interactions from oleic acid and Pluronic to target the crude oil. NPs prepared with a 1 g/L coating concentration were selected for use in all subsequent binding batch experiments to maximize NP binding contrast between clean and oil-impacted sand.

5.4.2 Effect of Oil Concentration and Oil Type

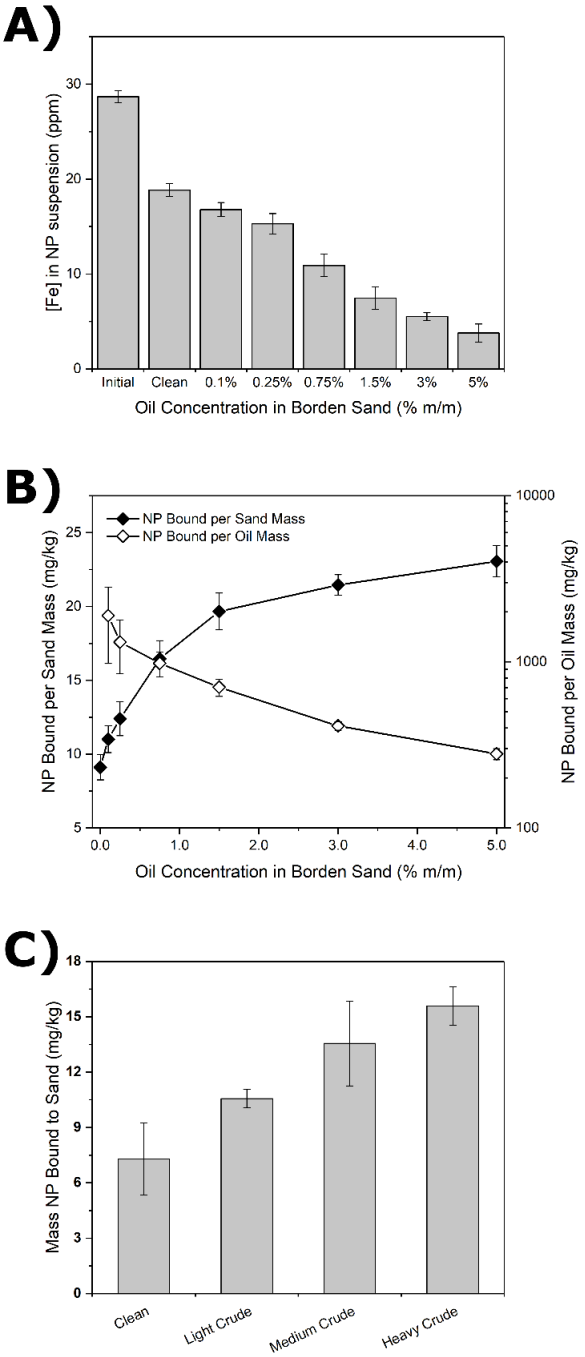

Figure 22. Influence of oil concentration **(A, B)** and type **(C)** on nanoparticle binding. **A)** NP binding to oil-impacted sand increases as oil concentration in the sand increases. **B)** Estimated NP binding normalized by mass of sand or mass of oil. As the oil concentration in the sand increases, NP increases but reaches a threshold point. This is also demonstrated by the decreasing mass of NP bound per mass of oil present in the sand. **C)** NP binding increases as the gravity and hydrocarbon chain length of the oil increases.

Oil concentration was found to substantially influence NP binding, resulting in an increase from 9.1 ± 0.8 mg/kg in 0.1% m/m oil-impacted sand to 23.0 ± 1.0 mg/kg in 5.0% m/m oil-impacted sand (**Figure 22**). As the concentration of oil in an impacted sand increases, so does the number of potential binding sites. In **Figure 22 B**, the mass of NPs bound in the oil-impacted sand normalized by the mass of oil present in the sample decreases from 1900 ± 920 mg/kg to 280 ± 21 mg/kg as the oil concentration increases. Assuming the oil coated the sand homogeneously, adding more oil would only contribute to greater thickness of the oil layer surrounding the sand grains without increasing the surface area. The flattening of the slope of the mass of NPs bound per mass of sand at ~1.5% crude oil m/m, suggests that this oil concentration may be close to the NP binding threshold.

The type of crude oil used was also found to have an influence on the binding behaviour of NPs. Three different types of crude oil were used in this study; a light crude with average carbon-number of 22.8, a medium crude oil with average carbon-number of 23.4, and a heavy crude oil with average carbon-number of 25.1. As the carbon-number of the oil increased, so did the NP binding response (**Figure 22 C**). Previous studies on Pluronic adsorption to hydrophobic surfaces indicated that adsorption is strongly dependent on the hydrophobicity of the underlying surface[194,218]. Without considering the influence of functional groups or non-linear hydrocarbons in the different oil samples, an increasing average carbon length may produce a more hydrophobic interface, promoting Pluronic interaction with the surface, resulting in increased NP binding.

To investigate the combined influence of oil type and oil content on NP binding behaviour, a surface response experimental study was used, blending oils in specific ratios to achieve a linearly-scaled average C-number from heavy to light oils, and varying the oil concentration from 1-3% m/m. Details of the experimental design and selection of data can be found in **Table 8**.

Table 8. Selection of variables for surface response plot showing effect of oil concentration and oil type on Nanoparticle binding to Borden Sand.

Sample	Coded Variable		Actual Variable	
	Concentration	Type	Concentration (m/m %)	Type
1	-1	-1	1	Blend: 70% ‘light’, 30% ‘medium’
2	1	-1	3	Blend: 70% ‘light’, 30% ‘medium’
3	-1	1	1	Blend: 70% ‘heavy’, 30% ‘medium’
4	1	1	3	Blend: 70% ‘heavy’, 30% ‘medium’
5	0	-√2	2	100% ‘light’
6	0	√2	2	100% ‘heavy’
7	-√2	0	2 - √2	100% ‘medium’
8	√2	0	2 + √2	100% ‘medium’

9	0	0	2	100% 'medium'
10	0	0	2	100% 'medium'
11	0	0	2	100% 'medium'
12	0	0	2	100% 'medium'

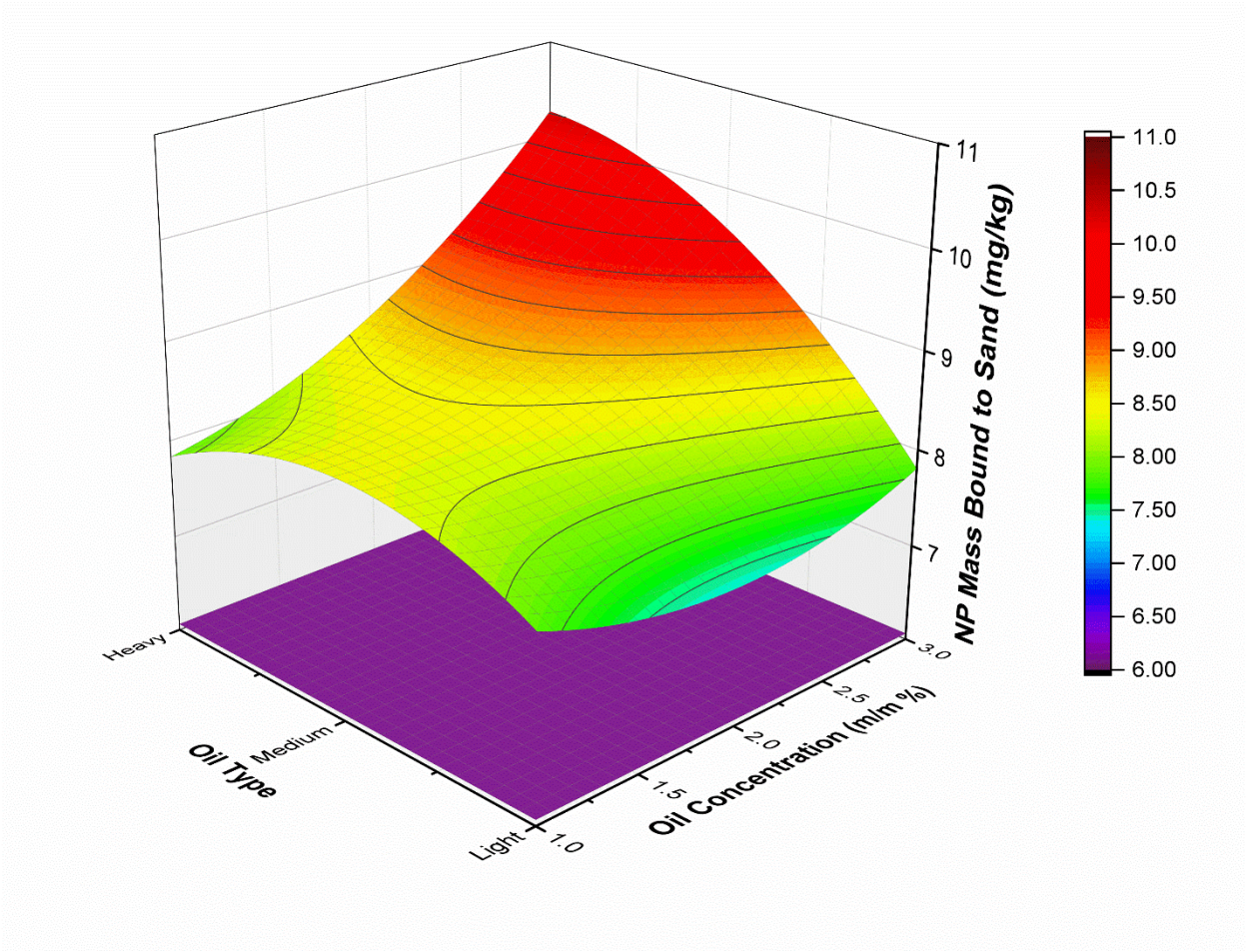

Figure 23. Surface response plot showing how NP binding is influenced by crude oil concentration and oil type. At high oil concentrations, binding significantly increases as oils increase in gravity and hydrocarbon chain length. For high gravity oils, binding significantly increases as oil concentration increases. The horizontal plane at the bottom of the figure represents nanoparticle binding to clean Borden Sand under identical test conditions.

The results of this study are presented in **Figure 23** and supports the type/concentration independent observations shown in **Figure 22**, where increasing oil concentration results in increased NP binding and that heavier oil elicits greater NP binding response. This oil type and concentration dependent study also indicates that at low concentrations or when using lighter oils, the influence of the other factor is greatly diminished. For example, changing the concentration of a heavy oil significantly influences NP binding behaviour as clearly shown in **Figure 22A**, but changing the concentration of a light oil has a much less pronounced effect (see the 'light' edge of **Figure 23**). Likewise, at higher oil concentrations,

changing the oil type from light to heavy results in a marked increase in NP binding, but at lower oil concentrations, the type of oil present has little to no effect. These results indicate that targeting may be more efficient in porous media containing high concentrations of a highly hydrophobic LNAPL. All samples containing oil resulted in greater NP binding than NP binding to this trial's clean sand control (6.1 ± 0.1 mg/kg) shown as the horizontal plane at the bottom of **Figure 23**.

5.4.3 Effect of Temperature and pH

Conducting binding batch tests at temperatures ranging from room temperature (22 ºC) to 60 ºC revealed that temperature has a significant effect on NP binding behaviour. As temperature increased, NP binding to clean sand increased from 3.5 ± 0.9 mg/kg at room temperature to 8.1 ± 2.6 mg/kg at 50 ºC while NP binding to oily sand increased from 10.5 ± 0.7 mg/kg to 25.4 ± 0.9 mg/kg under the same conditions (**Figure 24A**).

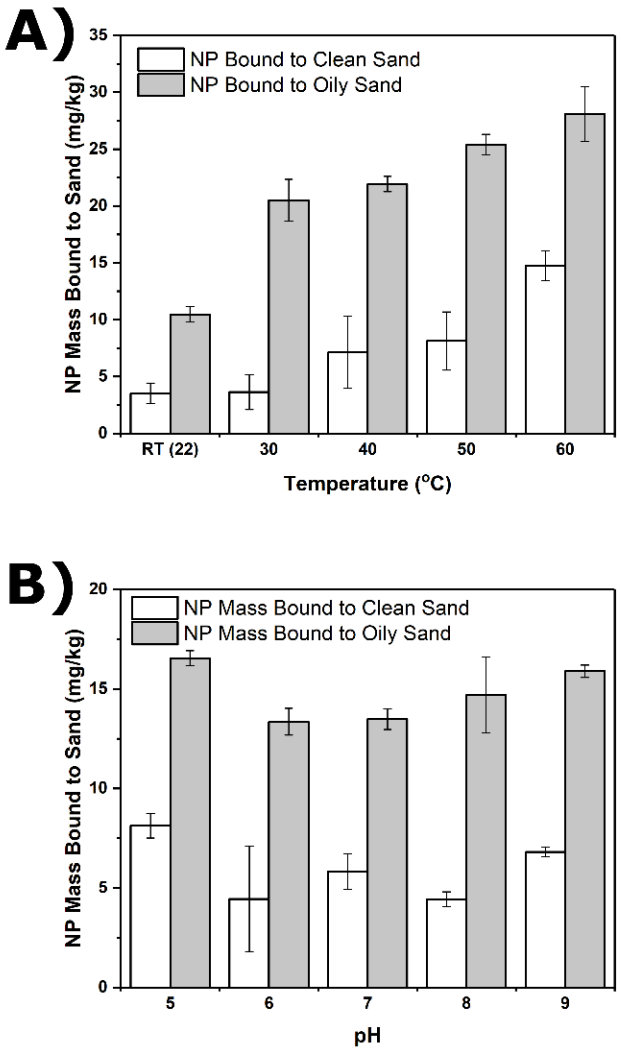

Figure 24. Effect of temperature **(A)** and pH **(B)** on NP binding to oil-impacted sand. As temperature increases, approaching the LCST of Pluronic, binding of NP to oil-impacted sand increases. Over the pH range of 5 to 9, pH was not found to significantly influence NP binding to oil-impacted sand.

Even at a moderate temperature increase to 30 °C, NP binding to clean sand demonstrated no appreciable change from 3.5 ± 0.9 mg/kg to 3.6 ± 1.5 mg/kg while NP binding to oily sand almost doubled from 10.5 ± 0.7 mg/kg to 20.5 ± 1.8 mg/kg. At temperatures ≥30°C, the difference in observed binding between clean and oily sand was maintained at 15.6 ± 1.8 mg/kg, approximately double the 6.9 mg/kg difference observed at room temperature. Pluronic exhibits a Lower Critical Solution Temperature (LCST) whereby the entropy of mixing becomes more unfavourable at higher temperature, eventually leading to phase separation (the cloud point) at ~32 °C for L62 and ~81 °C for P104. As water structures formed around hydrophobic moieties are disrupted at higher temperatures, it becomes more energetically favourable for hydrophobic phases to coalesce, leading to an effective increase in the hydrophobic forces

experienced by the Pluronic coating. The increased hydrophobic characteristic of the NPs results in more NP binding. This phenomenon has been harnessed in previous work to engineer functional NPs, such as crosslinked Pluronic micelles or Pluronic coating NPs which swell and contract with lower or higher temperature[219–221]. As the temperature increases further, water structures around the hydrophilic PEO moieties are disrupted and the PEO may hydrogen bond with silanol groups on the grain surface to reduce their energy[171], leading to the increase in binding to clean sand observed at 60 °C.

The effect of pH on NP binding was also investigated over a range of pH 5 to 9, and it was observed that pH changes within this range had no appreciable effect on NP binding (**Figure 24B**). The pH ranges investigated here are within typical pH ranges for a subsurface system, indicating that application of the NP coating investigated in this work should not be limited by pH under typical field conditions. This observation is significant as oleic-acid stabilized NPs demonstrate susceptibility to pH changes as protonation disrupts the bilayer, and such particles only become lipophilic at low pH[122,222]. With the addition of a neutral surfactant coating unaffected by pH, the application range of the material becomes more versatile. It should be noted that the pH adjustments performed in this work do not represent the typical acids and bases which contribute to natural pH variations. Furthermore, this observation indicates that NP binding is not dependent on DLVO interactions which are affected by solution ionic strength[223,224]. Specific mineral materials or dissolved species may influence NP stability and binding behaviour, although prior studies using pluronic-coated NPs in physiological environments note good stability in saline aqueous conditions[208]. Lowering the pH to <5 may result in increased NP binding by protonating the oleate later, allowing easier disruption of the oleate surface or easier interaction between the oleic acid and the oil/water interface[122]. It should also be noted that corrosive, low pH conditions may also cause dissolution of the iron oxide core of this NP, prohibiting application in low pH environments.

5.4.4 Nanoparticle Transport and Binding in Stop-Flow Systems

NP transport and binding using 2.5 g/L-coated particles was demonstrated in triplicate using columns packed with either BS or OBS. A 2.5 g/L coating concentration was selected for comparison to previous work which investigated NP transport and binding under similar conditions at room temperature (22 °C) in BS (**Chapter 4.4.2** Nanoparticle Transport and Binding in Clean and Oil-Impacted Porous Media; **Figure 18**). These experiments were conducted at 50 °C to take advantage of the improved NP binding observed at higher temperature. It was observed that for the BS packed columns the average NP recovery (defined as the fraction of total injected NP mass observed in column effluent) under these conditions was 54.0 ± 8.6%, while for the OBS packed columns the average recovery was 0.4 ± 0.1% (**Figure 25**).

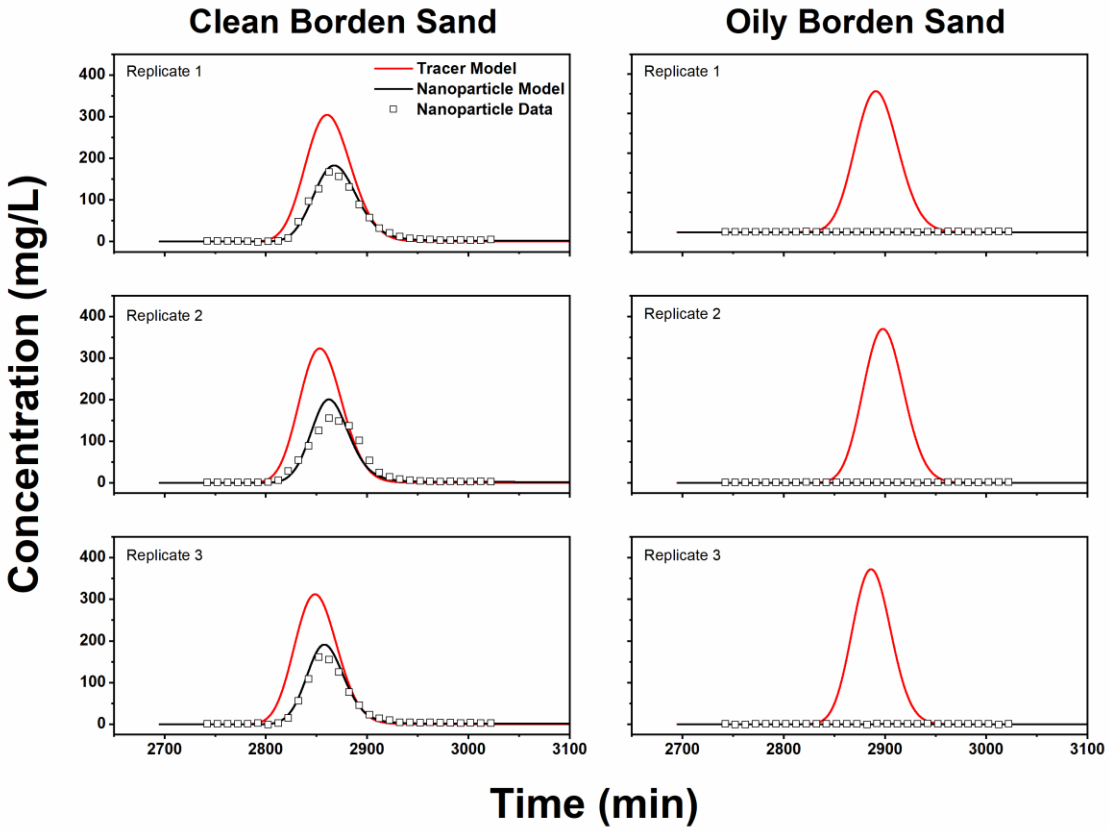

Figure 25. Observed (symbols) and simulated (black line) nanoparticle BTCs in clean (left panels) and oil-impacted (right panels) Borden Sand packed columns. For comparison, the tracer BTCs (red line) are shown for simulations using the column specific porosity, dispersivity and stop-flow conditions.

These results demonstrate affinity for the NPs to bind to this oil-impacted porous medium relative to the clean porous medium. Compared to our previous work, NP recovery through BS was moderately decreased from 72.6% at room temperature to 54.0% at 50 °C while NP recovery through OBS was drastically decreased from 59.4% at room temperature to 0.4% at 50 °C. The average calibrated effective porosity for the BS columns (0.36 ± 0.01) and OBS columns (0.38 ± 0.01) were nearly identical (**Table 9** and **Figure 26**).

Table 9. Calibrated effective porosity and dispersivity values for each column trial.

Trial	Clean Borden Sand (BS)		Oily Borden Sand (OBS)	
	Porosity (-)	**Dispersivity (cm)**	**Porosity (-)**	**Dispersivity (cm)**
1	0.360	0.0579	0.390	0.0388
2	0.362	0.0450	0.379	0.0277
3	0.345	0.0454	0.372	0.0264

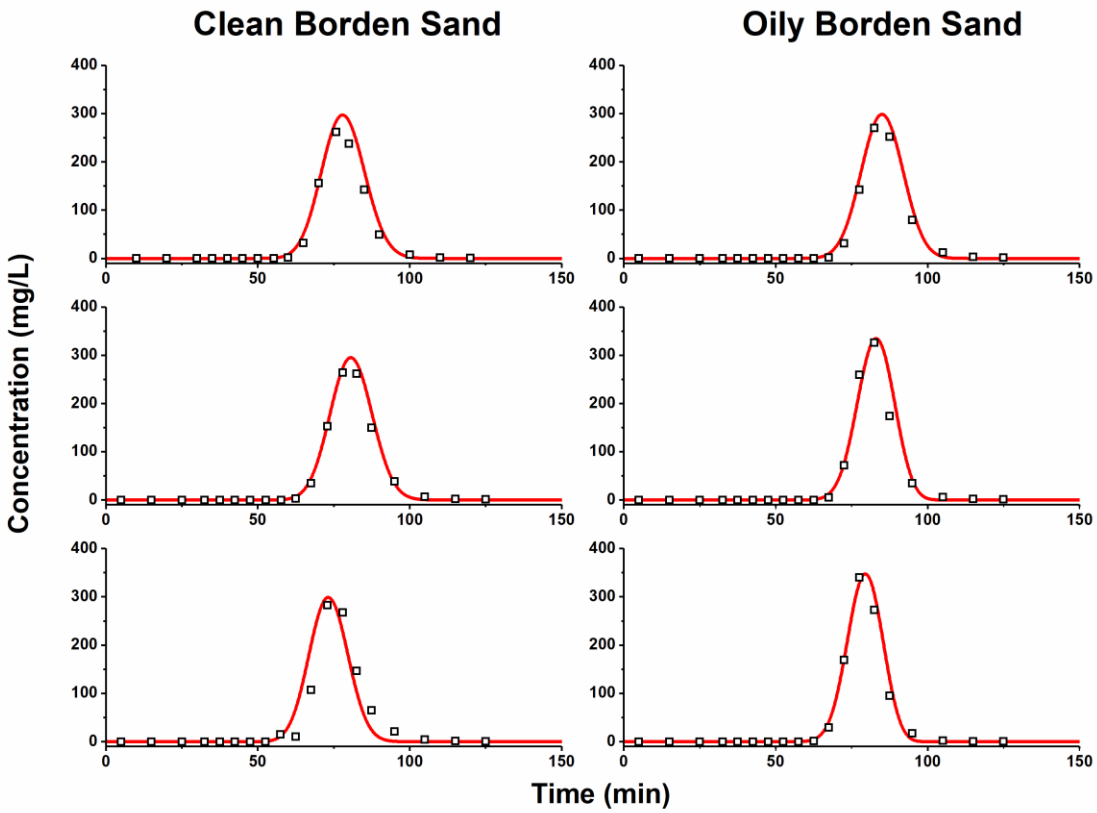

Figure 26. Comparison of observed (symbols) and simulated (lines) bromide breakthrough curves for the columns packed with clean Borden sand (left panels) and oil-impacted Borden sand (right panels). Each experimental system was performed in triplicate (vertically descending from trial 1 to 3).

In contrast, the average estimated dispersivity for the BS columns (4.9±0.7 x 10^{-4} m) was larger than that for the OBS columns (3.1±0.7 x 10^{-4} m) indicating that the presence of the oil reduced the variations in pore velocity. The average M_{attach}^{max} from batch binding tests performed at 50ºC was 8.1 ± 2.6 x 10^{-3} g kg^{-1} for the BS, and 25.4 ± 0.9 x 10^{-3} g kg^{-1} for the OBS (**Figure 24**). For the BS columns, the average k_{attach} (2.10 ± 0.66 x 10^{-4} s^{-1}) was estimated to be two-orders of magnitude larger than the average k_{detach} (4.56 ± 1.26 x 10^{-6} s^{-1}) (Table 2). The magnitude of k_{attach} compares closely to values reported for iron oxide nanoparticles under equivalent experimental conditions. In work by Carstens et al., it was found that k_{att} values between 6.0 x10^{-4} and 1.4 x 10^{-5} were sufficient to describe iron oxide nanoparticle deposition in quartz sand during stop-flow periods in 12 cm packed columns[223]. Since the NP BTCs for the OBS packed columns are essentially flat at the MDL, we assumed k_{detach} to be zero as there is no evidence of NP detachment and estimated the minimum k_{attach} required to achieve a maximum NP concentration in the effluent equal to the MDL. The required k_{attach} for this BTC condition to be satisfied was 8.86±0.43 x 10^{-4} s^{-1} (**Table 10**); approximately 4 times larger than the average k_{attach} estimated for the BS columns.

Table 10. Estimated attachment-detachment kinetic model parameters from equation (23). M_{attach}^{max} values were adopted from the binding batch tests (**Figure 24**, 50°C). Minimum k_{attach} values were estimated for the OBS packed columns.

Column Type	Replicate	M_{attach}^{max} (mg·kg^{-1})*	k_{attach} (s^{-1}) x 10^4	k_{detach} (s^{-1}) x 10^6	RMSE
BS	1	8.1 ± 2.6	1.34	5.56	4.03
	2		2.39	4.97	16.43
	3		2.58	3.15	9.02
OBS	1	25.4 ± 0.9	>9.32	0†	-
	2		>8.48	0†	-
	3		>8.78	0†	-

†assumed since no NPs observed in column effluent

Establishing these parameters for nanoparticle transport and binding in BS or OBS at 50 °C allows us to make some predictions regarding how environmental factors such as oil concentration or oil type influence the attachment profile, as well as injection parameters such as flow rate. **Figure 27** presents 1D-USAT predicted attached mass profiles along the length of OBS columns used in this study under difference conditions.

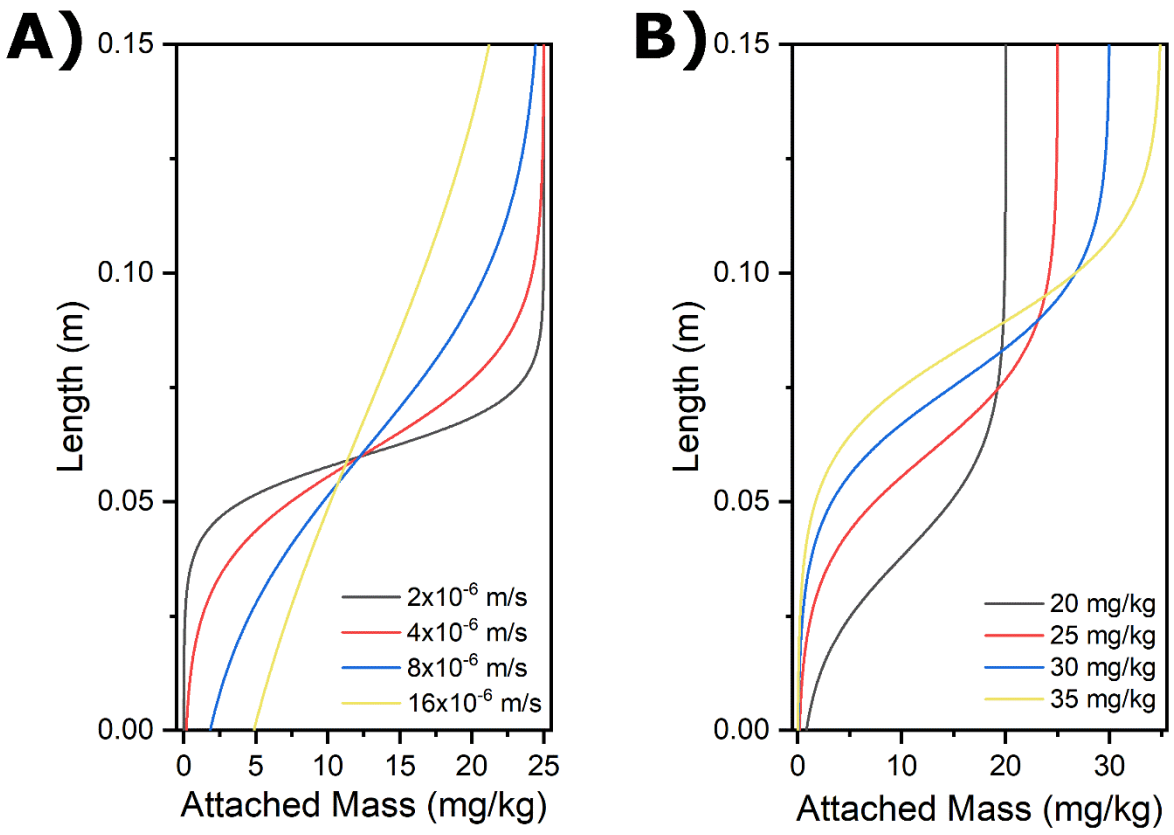

Figure 27. 1D-USAT simulations of NP attached mass profiles over a 15 cm column under **A)** different flow rates and **B)** different M_{attach}^{max}. Different M_{attach}^{max} values are representative of how NP binding changes with different oil type and concentration.

For this predictive modelling, a continuous flow scenario was investigated with k_{attach} = 8.86 x 10^{-4} s^{-1} based on the modelling results from **Table 10**. Porosity and dispersivity values were selected as 0.38 and 3.1 x 10^{-4} m, reflecting the average column parameters for OBS columns (**Table 9**). Injected NP concentration was set to 500 mg/L and total injected particle mass was maintained at a constant 4.0 mg for all trials. By varying the injection velocity in **Figure 27 A)**, the NP distribution at 8 h along the column length is affected. Higher injection velocities result in a NP distribution that penetrates further in the column however the bound concentration is below M_{attach}^{max}. This observation suggests that to achieve greater NP distribution at bound concentrations below the M_{attach}^{max}, higher injection velocities or flow rates may be used. The influence of oil type and concentration on NP binding appears related to the M_{attach}^{max}; in **Figure 22** and **Figure 23** it is clear that by using higher oil concentrations or longer hydrocarbon chains, a higher M_{attach}^{max} is achieved. **Figure 27 B)** demonstrates how the attached mass profile responds to different M_{attach}^{max} values, and that variation in the parameter by amounts as small as 5 mg/kg – within the range of effect observed in **Figure 22** and **Figure 23** – can drastically affect the final profile. By using lower oil concentrations or lighter oil types, we can expect that the attached mass is

distributed more fully along the total length of the column while the amount of NP retained in the porous media closer to the inlet decreases. Factors such as temperature, oil concentration, and oil type have a significant effect on binding and transport behaviour of these NP and must be considered when attempting to achieve a desired spatial distribution of NP in porous media.

To investigate the binding behaviour for a spatial scale representative of a potential field application where NPs would be injected into a saturated porous medium, a 1.0 m long one-dimensional system was simulated (**Figure 28**).

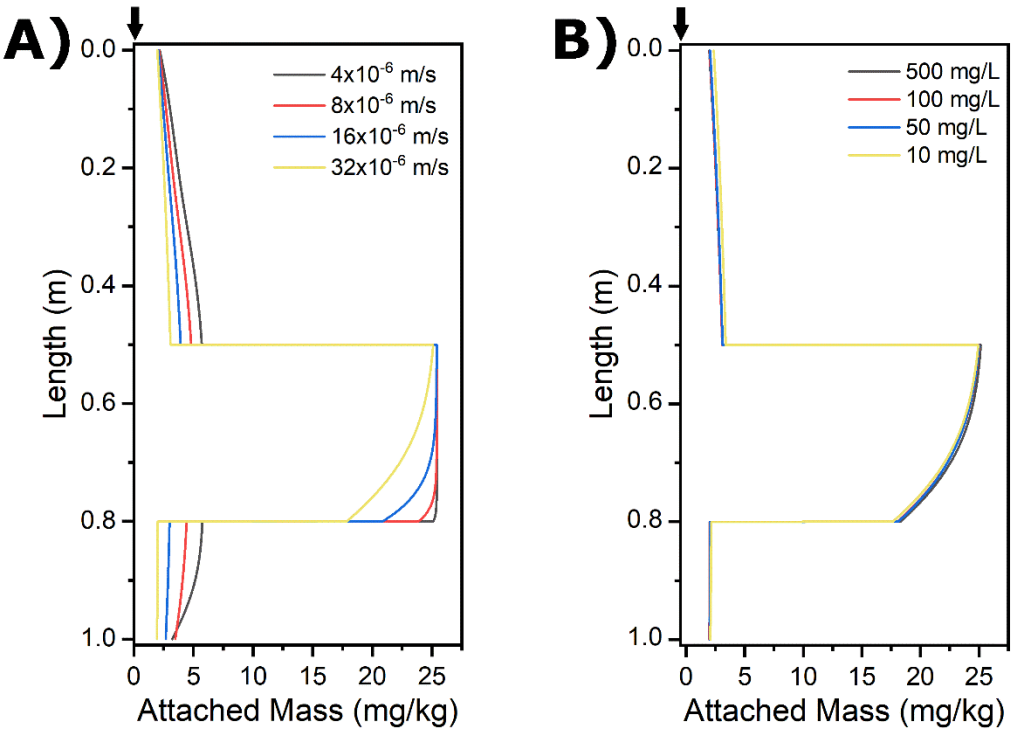

Figure 28. 1D-USAT simulations of NP attached mass profiles in a 1 m column containing an impacted zone under continuous flow conditions. The column geometry consists, from top to bottom, of a 50 cm zone of BS, a 30 cm zone of OBS, and a final 20 cm zone of BS. M_{attach}^{max} and k_{attach}/k_{detach} values were selected for each zone according to the average values from **Table 10**. Panel **A)** shows how attached mass profile changes with flow rate (constant injection concentration = 400 mg/L) and panel **B)** shows how attached mass profile changes with input concentration (constant flow rate = 4 x 10^{-6} m/s).

Between 0.5 and 0.8 m from the NP injection location (z = 0.0 m) a 0.3 m long oil impacted zone was specified representing the NP binding target. In this impacted zone k_{attach} of 8.86 x 10^{-4} s^{-1}, k_{detach} of zero, M_{attach}^{max} of 25.4 x 10^{-3} g kg^{-1}, porosity of 0.38, and dispersivity of 3.1 x 10^{-4} m were assigned. The remainder of the system (z = 0.0 to 0.5 m, and z = 0.8 to 1.0 m) was assumed to be comprised of clean sand and thus assigned k_{attach} of 2.10 x 10^{-4} s^{-1}, k_{detach} of 4.56 x 10^{-6} s^{-1}, M_{attach}^{max} of 8.1 x 10^{-3} g kg^{-1}, porosity of 0.36, and dispersivity of 4.9 x 10^{-4} m consistent with the average values estimated for the BS

column experiments. **Figure 28 A)** shows the attached NP mass distribution at a time of approximately 80 h for a range of injection velocities using a NP injection concentration of 400 mg/L and total NP injection mass of 20 mg. As the injection velocity is increased from $4x10^{-6}$ m/s to $3.2x10^{-5}$ m/s, a smaller fraction of the NPs are retained in the system, with the total deposited mass decreasing from 10.6 mg to 8.5 mg. At higher flow rates, the mass of NP bound in the target region accounts for a greater fraction of the retained mass – 71.5% of the 10.6 mg retained at the injection velocity of $4x10^{-6}$ m/s is bound in the oil-impacted zone compared to 80.2% of the 8.5 mg retained in the system at $32x10^{-6}$ m/s (Table S3). In contrast for a constant injection velocity of 4×10^{-6} m/s, **Figure 28 B)** shows the impact of variations of the NP injection concentration (from 10 to 500 mg/L) on the distribution of NP mass attached in the oil impacted zone while maintaining the injected NP mass constant. It was found that attachment was not greatly affected by NP concentration, with only a slight increase in attached mass with increasing concentration. We attribute this behaviour to the high attachment rate constant which overwhelms any effect concentration may have on the attachment rate. Overall, we find that increasing the flow rate will maximize NP retention in the target zone and reduce NP retention in the clean zone to produce greater contrast in NP concentration between clean and target impacted porous media.

5.5 Conclusions

NP targeted binding to viscous LNAPL in porous media can be achieved through the use of amphiphilic polymer coatings, and the degree of binding is further affected by environmental parameters. It was determined that by increasing the application temperature from room temperature to 50 ºC, NP binding in 1.5% m/m heavy crude oil-impacted sand was increased from 7.6 to 18.6 mg/kg, while binding in clean sand at the same temperatures experienced only a 3.4 mg/kg increase. NP coating concentration was also found to influence binding – lower coating concentrations resulted in more aggregated particles and greater NP binding. Oil concentration and oil type also played a role in promoting NP binding. It was observed that higher oil concentrations and longer-chain hydrocarbons resulted in greater NP binding. NP attachment to 0.1% m/m heavy crude oil-impacted sand was found to be 9.1 mg/kg and increased to 23.0 mg/kg at a heavy crude oil content of 5.0% m/m. When the mass of NPs bound was normalized by the mass of sand or oil present, an apparent binding threshold emerged, likely due to NP saturation of interfacial surface area as the overall volume of oil increased. NP transport and binding was demonstrated in packed columns under high temperature conditions corresponding to an environmental factor that favoured NP binding. NP transport simulation results compared well with the observed NP BTCs for columns packed with BS. The estimated attachment rate coefficient was $2.10 \pm 0.66 \times 10^{-4}$ s^{-1} for the BS columns; however, for the OBS columns a minimum attachment rate coefficient of $8.86 \pm 0.43 \times 10^{-4}$ s^{-1} was determined.

Using this attachment rate coefficient combined with knowledge of how M_{attach}^{max} changes with oil type and concentration, simulations may be used to predict how nanoparticle attached mass is distributed through porous media, an important consideration when attempting to deliver reactive NP to a contaminated zone.

Iron oxide NP deposition under stop-flow conditions in clean sand has been reported to result from colloid-dependent aggregation and straining as well as gravitational settling, by surface-particle dependent attractive DLVO interactions, and by non-DLVO interactions[223,224]. Owing to Pluronic coated iron oxide NP reported stability in saline media[208] as well as the independent nature of NP binding to pH in this chapter, the binding mechanism is likely a non-DLVO interaction, suspected to be hydrophobic forces. This is supported by the NP binding response to varying temperatures, oil concentrations, and oil types. Overall, NP targeted binding to crude oil was demonstrated to be responsive to environmental factors, and this finding was applied in a hydrodynamic one-dimensional porous medium environment. Simulation of one-dimensional system under continuous flow conditions predicted preferential accumulation of NPs in the impacted zone of a heterogeneously impacted column. Furthermore, the results showed that NP retention in the target oil-impacted zone could be increased by choosing appropriate injection concentrations and injection velocities. Taken together, these findings indicate the application potential for *in situ* targeted NP binding as a technique that may enhance nanotechnology enabled remediation and characterization efforts.

Chapter 6

Pluronic as a Universal Nanoparticle Coating for Targeted Delivery of Nanoparticles to PHC-Impacted Porous Media†

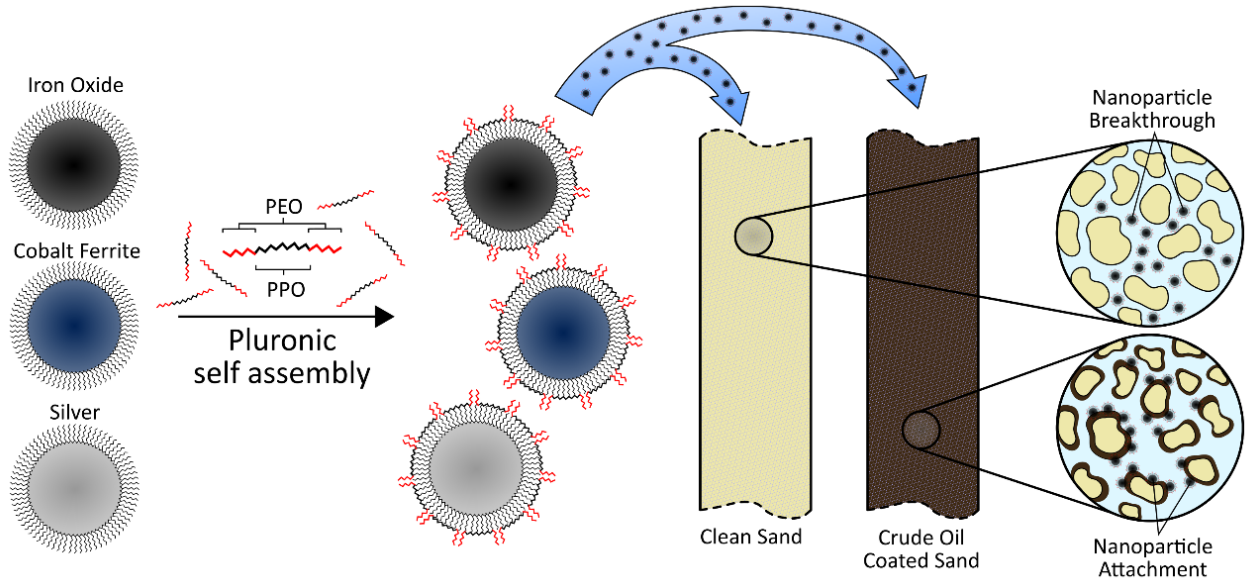

Figure 29. Schematic illustrating Pluronic self-assembly onto various oleic acid-coated nanoparticles and subsequent targeted binding behaviour toward PHC-impacted porous media; NP attach to crude oil coated sand and transport through clean sand.

6.1 Summary

In situ nanoremediation is a promising alternative to traditional remediation techniques which has raised serious questions regarding the unintended consequences of nanoparticle application in subsurface environments. A targeted nanoparticle binding strategy using amphiphilic polymer surface coatings caused more nanoparticles to be retained in oily versus clean sand. The versatility of this technique was demonstrated through identical coating application to three distinct types of nanoparticles produced using different synthetic methods (**Figure 29**). Preferential nanoparticle attachment to crude-oil impacted sands was confirmed for all three types of nanoparticles. Optimized model nanoparticle breakthrough curves were generated using a modified advection-dispersion equation in 1D-USAT and it was found that

† This chapter is adapted from a drafted manuscript: Linley, S.; Phann, D.; Thomson, N.R..; McVey, K.; Sra, K.; Gu, F. X. Pluronic as a Universal Nanoparticle Coating for Targeted Delivery of Nanoparticle to PHC-Impacted Porous Media. Not yet submitted.

nanoparticles exhibited higher solid phase concentrations and attachment rate coefficients in oily sand compared to clean sand. Detachment rate coefficients were largely unchanged. This work demonstrates a coating which confers targeted binding properties and may be applied to various types of nanoparticles, indicating that targeted binding is a strategy that may be adopted for many subsurface nanoparticle applications such as remediation or sensing.

6.2 Introduction

For the last two decades, remediation practitioners and regulators have advocated for *in situ* remediation strategies for contaminated sites as an alternative to *ex situ* treatment methods which are considered to be more expensive, less efficient, and highly energy intensive[225–227]. Within the portfolio of *in situ* remediation strategies, the concept of nanoremediation has gained recognition for its potential to reduce costs and time for site cleanup[228,229], and is expected to be a major player in the remediation market by 2025[230]. The merits of nanoremediation manifest in two key ways: first, and most importantly, that higher specific surface area materials provide greater treatment efficiency due to greater availability of reactive and adsorptive sites[64]; and second, that nanoparticles can be made mobile in porous media, allowing access to a larger treatment volume from a single injection site[63]. In recent years, bench-scale implementation of nanoremediation processes has demonstrated that suitable treatment approaches exists for many of the environmentally relevant contaminants including chlorinated hydrocarbons[231,232], toxic metals and metalloids[92,233,234], and polycyclic aromatic hydrocarbons[235,236]. By far the nanomaterial of greatest interest has been nano-Zero Valent Iron (nZVI)[63], which is notable for its innate reactivity towards various organic compounds, including highly toxic and prevalent chlorinated and polycyclic aromatic hydrocarbons[237,238]. Other nanoremediation materials of interest include iron oxide and various ferrites for their adsorptive properties[92], capacity to catalyze Fenton oxidation reactions[239,240] and influence on microbial remediation[241,242], as well as carbonaceous nanomaterials[235,243–245].

Much of the research concerning mobility of nanoparticles in subsurface environments has been focused improving mobility of particles and examining the fate and transport dynamics of engineered nanoparticles. It has been shown that the mobility of nanomaterials can be greatly improved by application of polymeric surface coatings such as carboxymethyl cellulose[246,247], polysulfonates[248], xanthan gum[249], and guar gum[250,251]. Furthermore, certain surface coatings reportedly have little influence on the treatment reaction kinetics between nZVI and the target contaminants[64,252], and some surface coatings have shown improved treatment rates[253,254]. With this technology growing in popularity[23,255,256], questions surrounding the use of mobile nanoparticles in the subsurface typically focus on the unintended migration of particles to the wider environment and their potential adverse effects. The toxicological effects of the nanoparticles themselves have been examined in assays of particle exposure to plants[257–259],

animals[260], and microorganisms[261–263], while the mobility of particles are usually examined in laboratory-scale experiments to allow prediction of their environmental fate in a given porous medium. Characterization of nanoparticle transport dynamics is typically undertaken by applying a modified advection-dispersion equation with consideration for particle attachment and detachment to experimental data[264]. Attachment/detachment rate coefficients for nanoparticles are strongly dependent on a wide range of factors, including nanoparticle shape, size, concentration and surface properties, as well as porous medium type, surface properties, and grain size[265]. Thus, transport parameters for a given nanoparticle are only comparable within a given porous medium type.

Controlling the mobility of nanoparticles in porous media and developing 'smarter' engineered nanomaterials is a necessary requirement as nanoremediation technologies gain widespread implementation[266,267]. To this end, several methods, including two-stage injection strategies to destabilize particles[268], functional coatings to promote attachment to impacted zones[67–70,269], and nanoparticles that become benign when the treatment process is complete have been investigated. In this study, we seek to address the problem of unintended nanoparticle environmental release directly through the application of an amphiphilic polymeric coating designed to produce a mobile nanoparticle which will preferentially attach to light non-aqueous phase liquid (LNAPL) presence in porous media. Previous research in this field has demonstrated that nanoparticle binding to non-aqueous phase contaminants can be achieved by selecting a surface coating, which facilitates energetically favourable interactions between the nanoparticle and the contaminant. Our previous research has demonstrated that Pluronic coatings provide mobility and preferential attachment to crude oil in porous media[71]. These findings have shown that nanoparticle attachment is a function of the surface coating, and for this reason we anticipated that the transport dynamics and binding to target crude oil should be similar for any type of nanoparticle having a similar coating. Herein, we investigate the transport and binding of three different types of nanoparticles produced using completely different synthetic methods, but coated with identical polymer surface coatings.

6.3 Materials and Methods

6.3.1 Materials

Iron (II) sulfate heptahydrate ($FeSO_4 \cdot 7H_2O$, ACS grade, > 99.0%), iron (III) chloride hexahydrate ($FeCl_3 \cdot 6H_2O$, > 99%), ammonium hydroxide (NH_4OH, ACS grade, 28-30% NH_3 basis in water), silver nitrate ($AgNO_3$, ACS grade, > 99.0%), sodium borohydride ($NaBH_4$, 99.99% trace metals basis), sodium oleate (> 90% fatty acids (as oleic acid) basis), phosphoric acid (H_3PO_4, ACS grade, 85 wt.% in water), iron (III) nitrate nonahydrate ($Fe(NO_3)_3 \cdot 9H_2O$, ACS grade, > 98%), cobalt (II) nitrate ($Co(NO_3)_2 \cdot 6H_2O$, ACS grade, > 98%), sodium hydroxide (NaOH, ACS grade, > 98%), 1-pentanol (ReagentPlus® grade, >

99%), oleic acid (OA, technical grade, 90%), dichloromethane (DCM, > 99.9%, contains 50-150 ppm amylene), hydrochloric acid (HCl, ACS grade, 37%), nitric acid (HNO_3, ACS grade, 70%), and potassium bromide (KBr, >99%) were purchased from Sigma Aldrich. Ethanol (ACS grade, 99%, anhydrous) and hexane (ACS Grade, >98.5%) were purchased from Fisher Scientific. Pluronic co-polymers P104 and L62 were gifted by Brenntag Canada and BASF Canada. Borden sand (d_{50} = 0.19 mm) was gathered from CFB Borden, Ontario (see Appendix B for soil characterization). Crude oil (heavy, sour crude, API gravity 13.3 (ρ = 0.977 g/cm^3), kinematic viscosity 4.745 x 10^{-4} m^2/s @ 40 °C) was provided by Chevron Energy Technology Company. All materials were used as received except the Borden Sand which was oven-treated at 90°C for 8 h prior to use.

6.3.2 Nanoparticle Synthesis

Synthesis of various types of nanoparticles was adapted from several methods previously reported[163–165,270–272].

6.3.2.1 Iron Oxide Nanoparticles

$FeSO_4 \cdot 7H_2O$ and $FeCl_3 \cdot 6H_2O$ were added to deoxygenated Millipore DI water (Millipore Elix 5) at a molar ratio of 2:3 ($FeSO_4$:$FeCl_3$). This solution was heated to 70 °C. Once the temperature equilibrated, sufficient NH_4OH and oleic acid were added to achieve final concentrations of 4 M and 0.2 M, respectively. This solution was stirred for 1h, then stirred at 90 °C under flowing N_2 for 1 h to purge evolved NH_3 gas. After cooling to room temperature, the black, magnetic precipitate was recovered by magnetic decantation and washed 3x by Millipore DI water, and then 3x by ethanol before being dried under flowing N_2.

6.3.2.2 Silver Nanoparticles

$AgNO_3$ was added to ice cold Millipore DI water to produce a 0.01M solution. Another ice-cold solution of 0.04 M $NaBH_4$ and 0.003 M sodium oleate was prepared the same way. An equal volume of each solution was added to each other and the resulting solution was stirred vigorously for 2 h in an ice-water bath. Stock H_3PO_4 was diluted to 10 M, then added to the silver nanoparticle suspension to achieve a final concentration of 0.024 M. The volume of the silver nanoparticle suspension was doubled with hexane and the resulting emulsion was stirred vigorously for 1 h to transfer the silver nanoparticles to the organic phase. The organic phase was decanted, and then the hexane was evaporated using a rotary evaporator (IKA RV 10 basic).

6.3.2.3 Cobalt Ferrite Nanoparticles

A 0.96 g/mL solution of oleic acid dissolved in ethanol was added to a 6.6 M solution of NaOH dissolved in Millipore DI water at a volumetric ratio of 2:1 (oleic acid:NaOH) to produce a sodium oleate solution. A solution of $Fe(NO_3)_3 \cdot 9H_2O$ and $Co(NO_3)_2 \cdot 6H_2O$ dissolved in Millipore DI water was added to

the sodium oleate solution to achieve final concentrations of 0.4 M and 0.2 M, respectively. Hexane was added to the cobalt-iron-oleate solution at a volumetric ratio of 1:2 (hexane:cobalt-iron-oleate solution) and the mixture was refluxed for 1 h at 85 °C, with occasional stirring. After cooling, the aqueous phase was removed by pipette. The organic phase was washed twice by adding 4:1:1 Millipore DI water:ethanol:hexane and refluxing for 30 minutes at 85 °C. The aqueous phase was removed after every wash. 1-pentanol was added such that final estimated concentrations of 1 M cobalt oleate and 2 M iron oleate would be achieved after boiling the solution at 100 °C for 2 h to evaporate hexane, ethanol and water.

A mixture consisting of 3 parts Co-Fe oleate, 11 parts 1-pentanol, and 7 parts Millipore DI water was purged with N_2 gas for 30 mins, and then heated at 180 °C for 10 h in a Teflon-lined stainless steel autoclave. After cooling, the liquid phases were discarded by magnetic decantation. The precipitate was suspended with hexane, and then precipitated with ethanol, and then the liquid phase was discarded by magnetic decantation. This step was performed twice. The precipitate was dried under flowing N_2 gas.

6.3.2.4 Nanoparticle Phase Transfer

Dried nanoparticles produced in the previous syntheses were suspended in hexane at a concentration of 90 g/L and sonicated for 10 min (VWR "Symphony" 1.9 L Ultrasonic Cleaner). In the case of silver nanoparticles, 1 % (v/v) oleic acid was added as well. The resulting suspension was added to an aqueous solution of 8 g/L L62 and 2 g/L P104 Pluronic co-polymers at a concentration of 10 % (v/v) and probe sonicated for 10 min to emulsify the water and hexane phases (Fisher Scientific FB505 Sonic Dismembrator, 200 W). The emulsified nanoparticle sample was transferred to a separatory funnel and separated over 48 h. The resulting aqueous nanoparticle suspension (typically 7-8 g/L) was stored refrigerated until used.

6.3.3 Binding Batch Studies

1.5 % (m/m) crude oil added to Borden sand (OBS) was prepared by dissolving crude oil in excess DCM, pouring the solution over clean Borden sand (BS), then letting the DCM fully evaporate while physically mixed until a homogenous coating was achieved. 15 g of OBS was added to 20 mL scintillation vials, followed by 10 mL of aqueous nanoparticle suspension diluted by a factor of 100 with Millipore DI water. The vials were left to sit at either room temperature or at 50 °C for 48 h. The same process was repeated with clean and dried Borden sand (BS). The nanoparticle suspension was then collected by filtration (Whatman glass microfiber filter, Grade 934-AH). All samples were performed in triplicate.

6.3.4 Column Transport and Binding Studies

15 cm long Plexiglas columns with an inner diameter of 3.8 cm were packed with either ~300 g of BS or OBS in a way to prevent air pockets and stratification. For BS, the columns were wet packed using Millipore DI water, and for OBS, the columns were dry packed then flushed with CO_2 gas for 15 minutes before being saturated from bottom-to-top with Millipore DI water by peristaltic pump (Cole Parmer MasterFlex 7535-04). Once packed, all columns were preheated to 50 °C in an oven (Binder ED53). Aqueous suspension of nanoparticles, diluted by a factor of 10 (20 for silver nanoparticles) with Millipore DI water were injected into the columns from top-to-bottom by peristaltic pump for 30 min at a rate of 0.34 mL/min, after which Millipore DI water was injected at the same rate for 1 h 5 min. The nanoparticles were held in the column for 44 h at 50 °C, after which the injection of Millipore water resumed until a total of ~1.5 pore volumes were eluted. Elution was collected every 30 minutes for 5 minutes prior to the stop-flow period and every 10 minutes upon resuming water injection. The mass of nanoparticles injected, flow rate and pore volume were monitored throughout the experiment. All column tests were performed in triplicate. Tracer tests of each column were performed immediately following nanoparticle transport studies. Briefly, 500 ppm bromide tracer solution was injected into the columns from top-to-bottom at a rate of 1 mL/min for 10 minutes, after which Millipore DI water was injected at the same rate for 2 h. Elution was continuously sampled, and mass of bromide tracer solution and flow rate were monitored throughout the experiment. Tracer concentration was measured using ion chromatography after a 5x dilution (Dionex ICS-1100).

6.3.5 Analyses

Prior to analysis by Inductively Coupled Plasma Optical Emission Spectrometry (ICP-OES, Prodigy) to quantify total metal ion concentration (method detection limit (MDL) of 4 µg/L), samples from the batch binding studies were digested with 12.1 M HCl (15.7 M HNO_3 for silver nanoparticles) at a concentration of 9 % (v/v). For the column transport and binding studies, samples were digested with 12.1 M HCl (15.7 M HNO_3 for silver nanoparticles) at a concentration of 20 % (v/v), then diluted by a factor of 10 with 0.1 M HCl (0.047 M HNO_3 for silver nanoparticles). Standards and check solutions were prepared from Fe, Ag and ICP 20 stock standards purchased from Inorganic Ventures and High Purity Standards.

Solid-phase adsorbed CoFe nanoparticles were analyzed by ICP after acid digestion of the collected sediments. The BS or OBS from the batch tests was collected after filtration and washed with 100 mL Millipore DI water, then oven dried at 70°C. 1 g of each dried sample was weighed out in a 50 mL plastic digestion tube followed by 5 mL of 70% Nitric Acid. The samples were heated to reflux temperature and boiled for 30 minutes after which an additional 5 mL of nitric acid was added. This process was repeated until a total of 15 mL nitric acid had been added to the samples. The samples were

then boiled down to a total volume of 5 mL and cooled to ~50ºC, after which 3 mL 30% H_2O_2 was added and gentle heat was applied until effervescence appeared and subsided. This step was repeated an additional two times, and then samples were boiled down to a total volume of 5 mL. Finally, 5 mL 12.1 mol/L HCl was added to each sample, and samples were boiled down to a total volume of 5 mL. Samples were diluted to a total volume of 10 mL with Millipore DI water prior to filtration using 0.45 µm PTFE filters (Digitube). Cobalt concentration in the final digestant solution was assessed using ICP-OES.
High Resolution Transmission Electron Microscopy (HR-TEM) analysis was performed using a Philips CM10 with an acceleration voltage of 80 keV. The nanoparticles were dispersed in water (for Pluronic coatings) or hexane (for oleic acid coatings), then placed dropwise on a holey Carbon-coated copper TEM grid and allowed to dry prior to analysis.

6.3.6 Nanoparticle Transport Modelling

Kinetic model parameters to describe the observed binding behaviour during stop-flow column experiments were determined assuming a single-site attachment model with nonlinear Langmuirian blocking[214] and advective-dispersive NP transport in the aqueous phase (**Chapter 5**; equations **(22) - (24)**). 1D-USAT[215], an unsaturated flow and solute transport model, provided a numerical solution to equations (22) - (24) and was used in conjunction with the dynamically dimensioned search (DDS)[216] algorithm within the OSTRICH toolkit[217] to identify optimal model parameters. Br^- tracer experimental data from each column was used to determine the porosity (ϕ) and dispersivity (α) by using equation (22) without attachment/detachment. The Br^- breakthrough curve (BTC) data were chosen as calibration targets using a Root Mean Square Error (RMSE) objective function.
The optimal ϕ and α_l values for each column were then used to fit the nanoparticle experimental BTCs in which k_{attach}, k_{detach}, and s_{max} were iteratively determined to produce a model of best fit with an RMSE objective function. For experimental column systems with no observable BTC, s_{max} was assigned a value from the corresponding binding batch test, which was assumed representative of binding saturation, and k_d was assigned a value of zero as no nanoparticle detachment was evident. The DDS algorithm was then used to estimate a k_a value so that the peak of the simulated BTC was equal to the associated nanoparticle concentration detection limit. This k_a value was assumed the minimum attachment rate coefficient necessary to achieve the observed experimental result. Stop-flow conditions consistent with NP experiments were employed in these simulations.6.4 Results and Discussion

6.4.1 Silver Nanoparticle Synthesis

In the case of iron oxide and cobalt ferrite particles, previously established synthesis protocols were sufficient to produce the quantity of nanoparticles necessary for transport and binding application experiments. In the case of silver nanoparticles, existing protocols from the literature had to be scaled up.

To understand the influence of synthesis parameters on the final concentration and yield of the silver nanoparticle synthesis, a 2-factor surface response optimization was performed. The silver synthesis procedure occurs in three steps, first the silver nanoparticle are produced via sodium borohydride-mediated reduction of silver nitrate. Second, sodium oleate is added which adsorbs to the silver surface through the electron-rich double bond in the centre of its tail. Finally, phosphoric acid induces a conformational change in the adsorption of the oleate when in the presence of hexane, causing its protonated carboxylic acid head to adsorb to the silver surface and its hydrophobic tail to extend into solution, allowing phase transfer from water to hexane[270]. By tuning the concentrations of oleate and phosphoric acid, the degree of oleate coating and efficiency of phase transfer to hexane can be optimized.

A two-trial surface response optimization was performed to maximize oleate coating and final Ag nanoparticle concentration in hexane. Initially, phosphoric acid and sodium oleate concentrations recommended by the literature for lower silver concentrations were tested: H_3PO_4 ranging from 4 to 16 mmol/L and Na oleate ranging from 2.5 to 12.5 mmol/L (**Table C-1**). The concentration of silver nanoparticle in hexane after phase transfer was observed via visible light absorbance at 410 nm (y-response in **Table C-1**) – the peak absorbance for the silver nanoparticles. These data were used to construct a surface response plot **Figure C-1** which shows that increasing phosphoric acid concentration significantly increases silver nanoparticle concentration in hexane while sodium oleate concentration seems to reach an optimal point around 5 mmol/L. This was used to inform parameter selection for the second optimization trial. Higher H_3PO_4 concentrations ranging from 18 to 30 mmol/L and lower Na oleate concentrations ranging from 1 to 5 mmol/L were selected (**Table C-2**). The resulting surface response plot produces a 3-D parabola indicating an optimal concentration for each parameter within the range tested (**Figure C-2**). For the silver nanoparticle synthesis investigated here, an optimal H_3PO_4 concentration of 24 mmol/L and an optimal Na oleate concentration of 3 mmol/L were selected. The findings here indicate that silver nanoparticles may be synthesized efficiently at higher concentrations, but that phase transfer efficiency must be carefully controlled by selecting the proper amounts of H_3PO_4 and Na oleate.

6.4.2 Nanoparticle Characterization

Nanoparticle cores composed of iron oxide, silver, or cobalt ferrite were characterized by TEM immediately after synthesis, after coating with 1 g/L Pluronic solution, and after coating with 10 g/L Pluronic solution (**Figure 30**). Nanoparticle morphology was found to vary with coating rather than material composition.

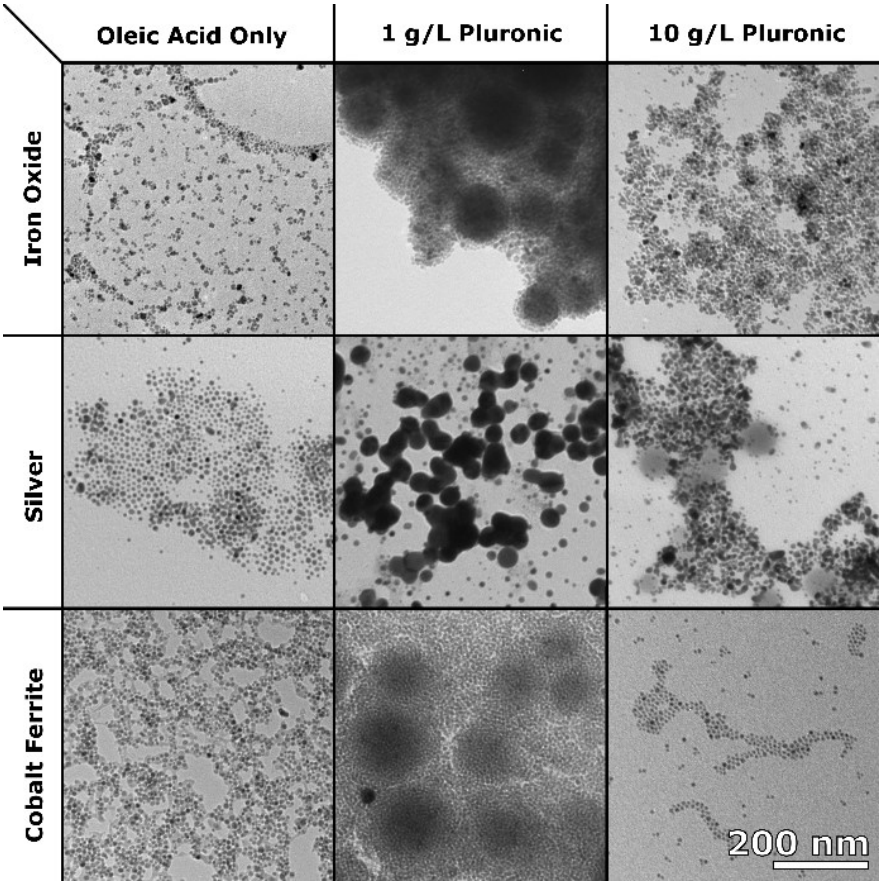

Figure 30. TEM characterization of nanoparticle samples composed of different materials (**Top Row:** iron oxide, **Middle Row:** silver, **Bottom Row:** cobalt ferrite) and different coatings (**Left Column:** oleic acid, **Middle Column:** 1 g/L Pluronic solution, **Right Column:** 10 g/L Pluronic solution). Nanoparticle morphology was strongly dependent on coating rather than material composition.

When coated by oleic acid, all nanoparticle samples exhibited a uniform spherical morphology with particle diameter <10 nm (7.4 ± 1.8 nm, 7.0 ± 1.4 nm, 7.8 ± 1.6 nm for Fe_3O_4, Ag, and $CoFe_2O_4$ particles, respectively). This morphology was maintained after a coating procedure using a high concentration (10 g/L) of Pluronic coating, but a low concentration Pluronic coating resulted in the formation of aggregates of nanoparticles with diameters of 89.7 ± 28.2 nm, 38.0 ± 7.8 nm, and 127.8 ± 32.3 nm for Fe_3O_4, Ag, and $CoFe_2O_4$ particles, respectively. This aggregate structure was maintained in the case of iron oxide and cobalt ferrite, but the silver nanoparticles appear to coalesce into solid particles. In previous work, we attributed the formation of aggregates to insufficient concentrations of Pluronic to fully coat all available surface area of the particles[71]. Silver nanoparticles coated with Pluronic have been found to Ostwald ripen and produce larger particles when surface coating is insufficient[273], supporting this theory. In the case where Pluronic concentration is high enough to maintain a coating around individual particles (10 g/L), their morphology and size is preserved, with diameters of 7.6 ± 1.8 nm, 8.2 ± 1.7 nm,

and 5.9 ± 1.2 nm for Fe_3O_4, Ag, and $CoFe_2O_4$ particles, respectively. Thus, the morphology of the various nanoparticle types can be controlled through application of the Pluronic surface coating.

6.4.3 Effect of Temperature on Nanoparticle Binding

Nanoparticle preferential binding to 1.5 % crude oil-coated Borden Sand was demonstrated through binding batch experiments. It was found that the ion concentration of the aqueous phase after acid digestion was consistently lower for samples exposed to oily sand (**Figure 31**).

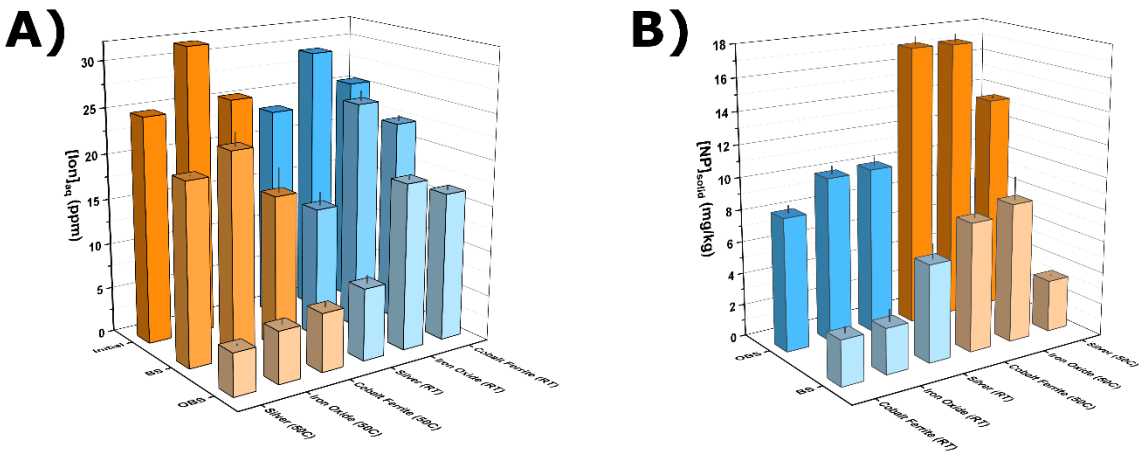

Figure 31. Batch binding trials demonstrating 1g/L Pluronic-coated nanoparticles preferentially binding to 1.5% m/m crude oil-coated Borden sand (OBS) at room temperature and at 50 ºC. **A)** ion concentration in the aqueous phase as measured by ICP, **B)** estimated solid-phase NP concentration from $[ion]_{aq}$ measurements. Increased temperature increases nanoparticle attachment to both clean and oily sand.

This indicates that the concentration of nanoparticles in water decreased more substantially when exposed to oily sand, an effect attributed to nanoparticle binding. This was the case for all 3 types of nanoparticles tested. At room temperature (~22 ºC), nanoparticle solid phase concentration was an average of 5.3 ± 1.0 mg/kg higher on oily Borden Sand (OBS) than on clean borden sand (BS). At 50 ºC, binding was increased to both clean and oily sand, and the solid phase concentration difference between clean and oily sand rose to an average of 11.6 ± 3.2 mg/kg. The cause of increased binding at elevated temperatures is hypothesized to be due to a mechanism suggested by Saleh et al., whereby hydrophobic forces between the NAPL phase and the amphiphilic nanoparticle coating causes attachment[67,68]. It is well known that Pluronic exhibits temperature dependent interactions with solvents – at low temperatures, solvent solute interactions are favourable and at higher temperatures, these interactions become unfavourable, driving micellization[274]. The consistent increase in attachment for all particle types at higher temperature indicates that attachment is due to interactions between the solid phase and the nanoparticle coating as solvent-particle interactions become less favourable. In the absence of crude oil, some amount of nanoparticle binding still occurs, and this binding is also increased with temperature.

This is thought to be due to van der Waals interactions between polar groups in the ethylene oxide segment of the coating and acidic metal oxide groups on the surface of the sand[275]. Similarly, water solvation of ethylene oxide is decreased at higher temperature as less polar conformations dominate[274], and the ethylene oxide groups seek to lower their potential energy by associating with other materials such as the NAPL.

The capability of estimating nanoparticle solid phase concentration from aqueous phase ion concentrations was verified through direct solid-phase analysis of sand from the binding batch tests when using $CoFe_2O_4$ nanoparticles. The sand from binding batch tests was recovered, washed, and acid digested to test the concentration of adsorbed cobalt after exposure to Pluronic-coated nanoparticles. This method was not viable for Fe_3O_4 or Ag nanoparticles due to the high background Fe concentration in Borden Sand and the difficulty of digesting and accurately measuring silver, respectively. It was found that all estimations from aqueous phase ion concentration measurements corresponded closely with the direct measurements from acid digestion of the sand except for the room temperature OBS measurements (**Figure 32**).

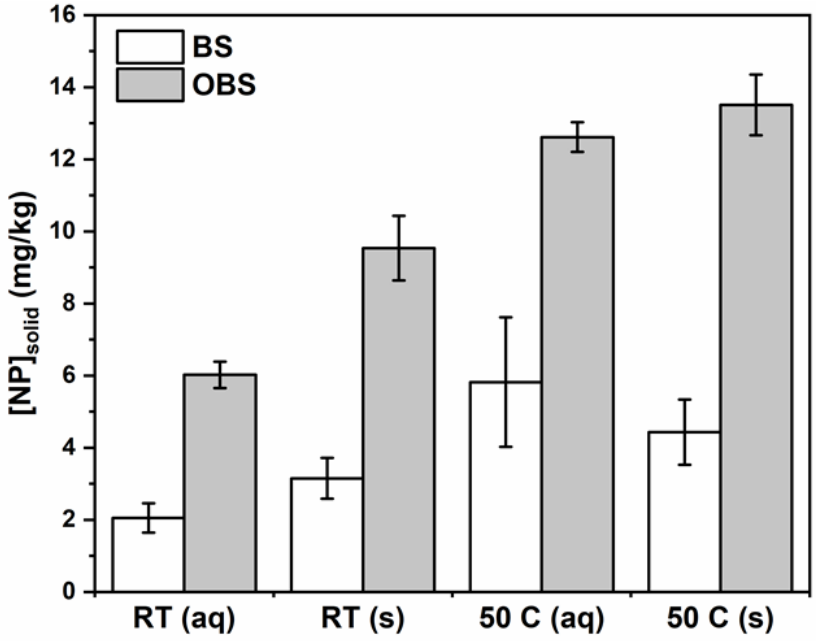

Figure 32. NP binding to clean (BS) or 1.5% crude oil-coated Borden Sand (OBS) at room temperature (RT; ~22 ºC) and 50 ºC determined by indirect (aq) and direct (s) methods to estimate NP solid-phase concentration. Both methods (e.g., RT BS (aq) and RT BS (s)) are equal within one standard deviation except for RT OBS.

Overall, this was taken as an indication that estimating solid-phase concentration from aqueous-phase ion concentrations was an accurate technique, corroborating our previous findings where

nanoparticle concentration was directly assessed by measuring magnetic moment of samples before and after nanoparticle binding[71] (**Chapter 3**).

Previous work has demonstrated that nanoparticle transport through sand and binding to crude oil-coated sand is dependent on the Pluronic coating concentration used in synthesis. These results showed that lower coating concentrations produced higher nanoparticle binding at room temperature. Before proceeding with transport and binding experiments at high temperature (50 °C), it was desirable confirm the dependence of nanoparticle binding on formulation coating concentration under these conditions. It was found that at elevated temperatures, there was little influence from coating concentration on nanoparticle binding for both Fe_3O_4 and Ag nanoparticles, with an increase in binding concentration only observed for the 10 g/L Pluronic-coated Fe_3O_4 sample (**Figure 33**). Based on this observation and previous work that demonstrated nanoparticle transport in sands was improved with higher Pluronic coating concentrations, 10 g/L Pluronic coatings were selected for all nanoparticles for the transport and binding experimental work.

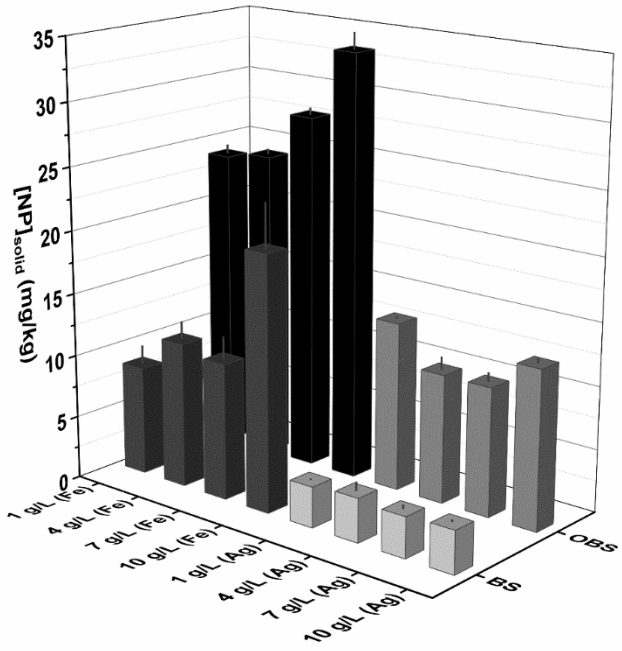

Figure 33. Effect of Pluronic coating concentration on Iron Oxide (Fe) and Silver (Ag) nanoparticle binding to clean (BS) and 1.5% crude oil-coated (OBS) Borden Sand at 50 °C. It appeared that binding of iron oxide particles to both BS and OBS increased with coating concentration while binding of silver

particles was completely unaffected. Overall, it appeared that coating concentration had little influence on nanoparticle binding at 50 °C.

6.4.4 Nanoparticle Transport and Binding in Column Tests

Iron oxide nanoparticles (**Figure 34**), silver nanoparticles (**Figure 35**), and cobalt ferrite nanoparticles (**Figure 36**) were all detected in the effluent of all columns packed with BS.

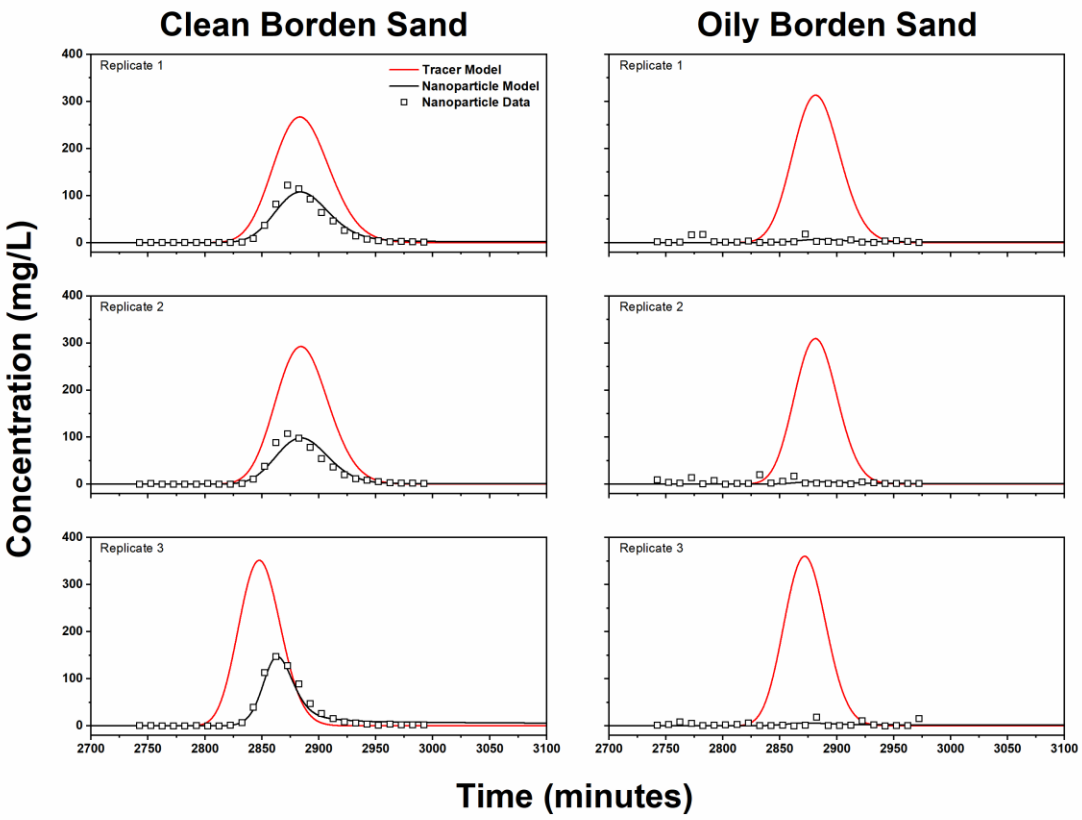

Figure 34. Iron oxide nanoparticle (10 g/L Pluronic coated) breakthrough curves (BTCs) from the transport and binding experiments (open square symbols) in columns (L = 15 cm, Q = 0.3 mL/min, stop flow from 95 min to 2740 min) packed with either clean sand (BS) or oily Borden Sand (OBS). Nanoparticle elution is clearly observed in all BS packed columns, while nanoparticle retention is observed in all OBS packed columns. The simulated nanoparticle BTC (solid black line) (see **Table 12** and **Table 13** for parameters) and simulated conservative tracer BTC (red solid line) are also shown.

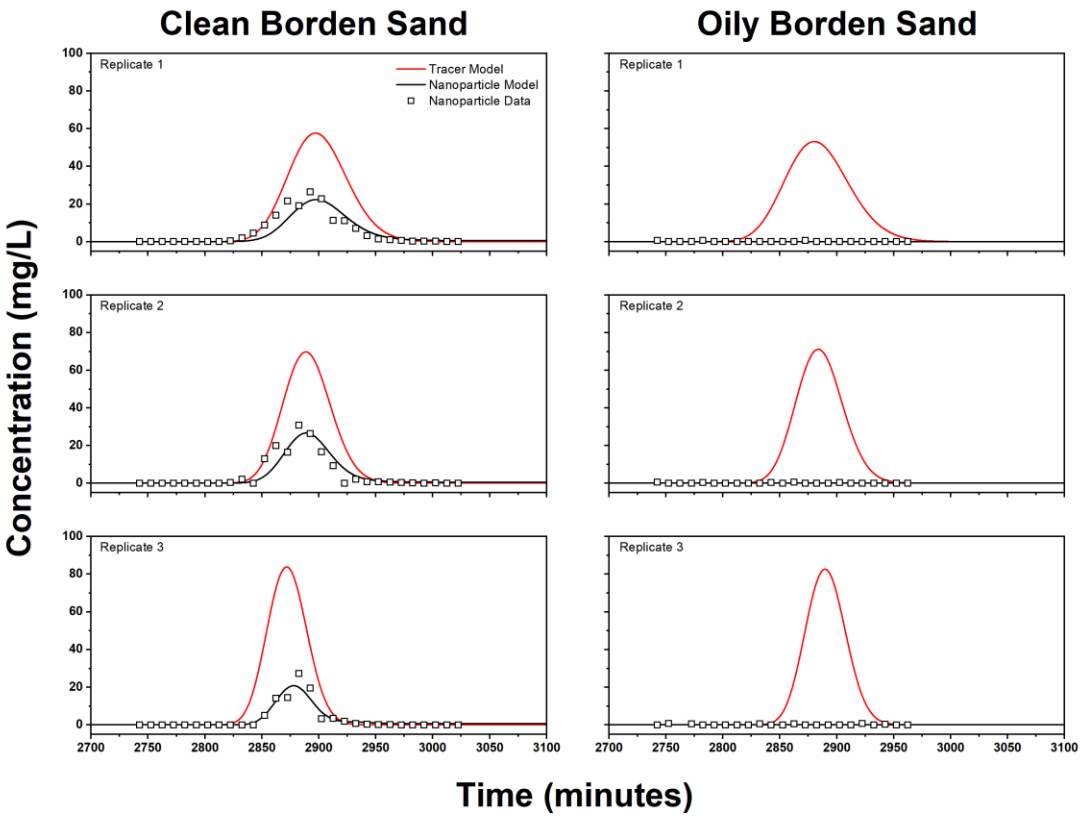

Figure 35. Silver nanoparticle (10 g/L Pluronic coated) breakthrough curves (BTCs) from the transport and binding experiments (open square symbols) in columns (L = 15 cm, Q = 0.3 mL/min, stop flow from 95 min to 2740 min) packed with either clean sand (BS) or oily Borden Sand (OBS). Nanoparticle elution is clearly observed in all BS packed columns, while nanoparticle retention is observed in all OBS packed columns. The simulated nanoparticle BTC (solid black line) (see **Table 12** and **Table 13** for parameters) and simulated conservative tracer BTC (red solid line) are also shown.

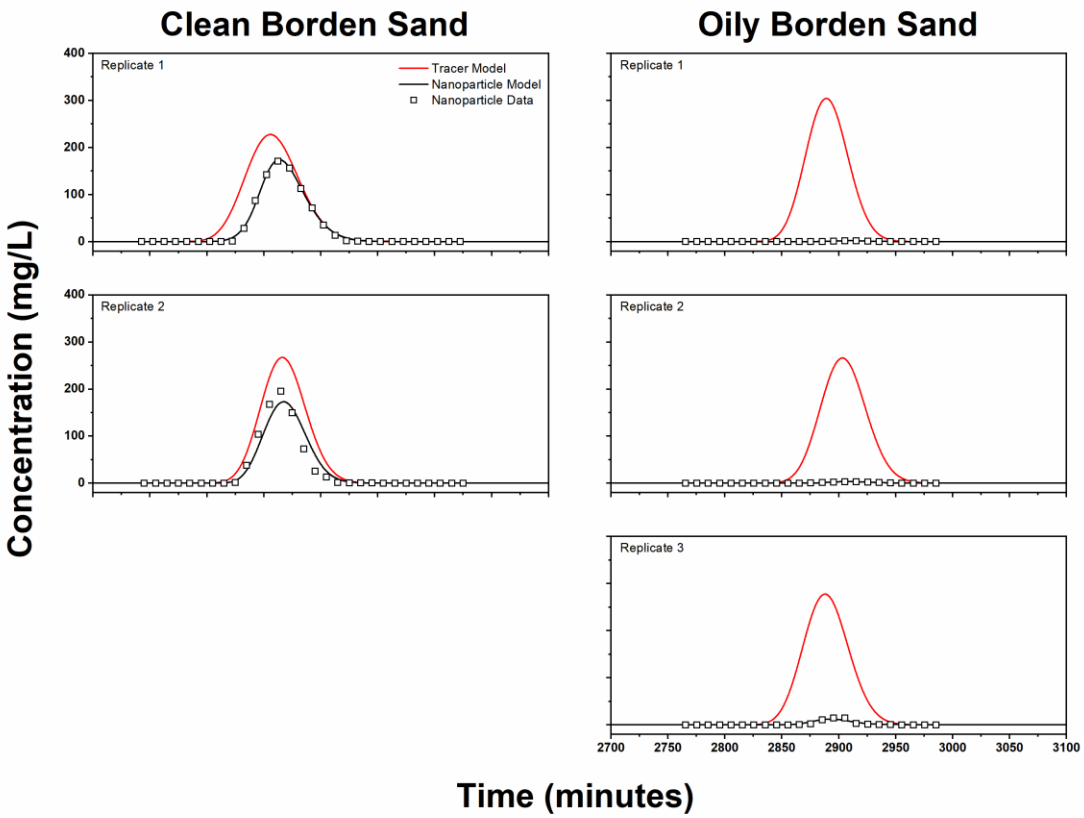

Figure 36. Cobalt ferrite nanoparticle (10 g/L Pluronic coated) breakthrough curves (BTCs) from the transport and binding experiments (open square symbols) in columns (L = 15 cm, Q = 0.3 mL/min, stop flow from 95 min to 2740 min) packed with either clean sand (BS) or oily Borden Sand (OBS). Nanoparticle elution is clearly observed in all BS packed columns, while nanoparticle retention is observed in all OBS packed columns. Some nanoparticle breakthrough is evident in the OBS columns from cobalt ion analysis. The simulated nanoparticle BTC (solid black line) (see **Table 12** and **Table 13** for parameters) and simulated conservative tracer BTC (red solid line) are also shown.

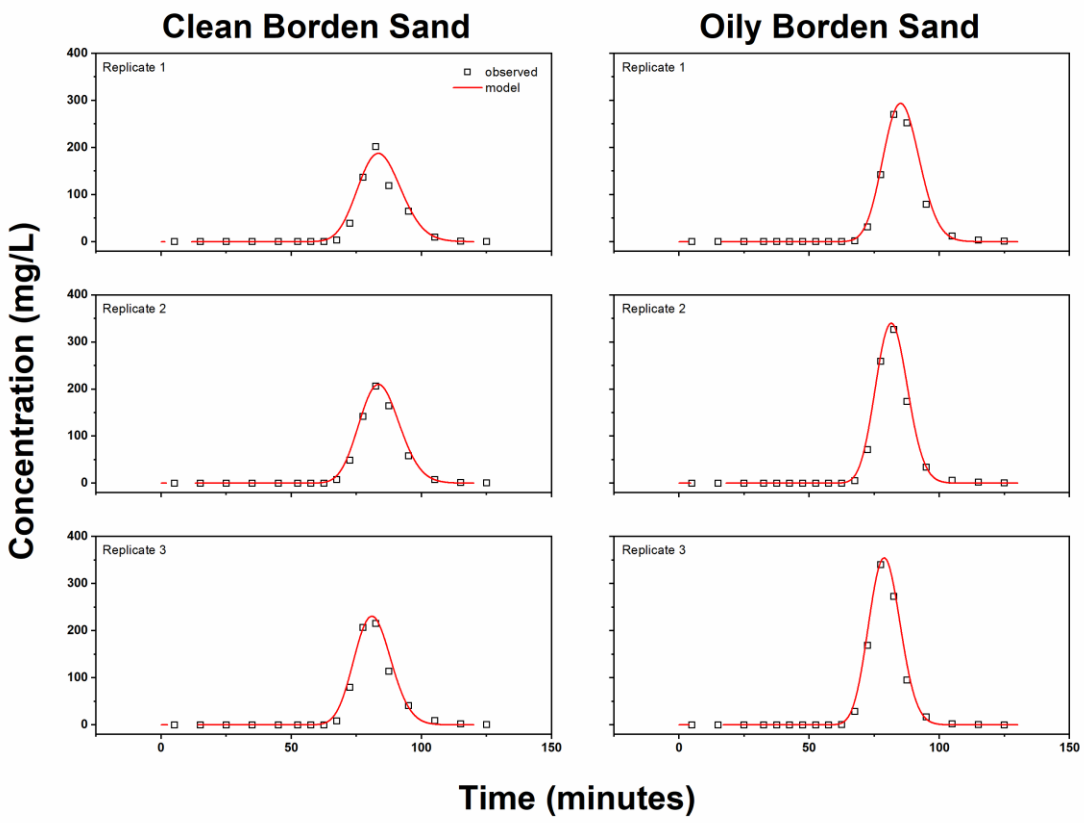

Figure 37. Comparison of observed (symbols) and simulated (lines) bromide breakthrough curves for the columns packed with clean Borden sand (left panels) and oil-impacted Borden sand (right panels) used for transport and binding experiments using iron oxide nanoparticles. Each experimental system was performed in triplicate (vertically descending from trial 1 to 3).

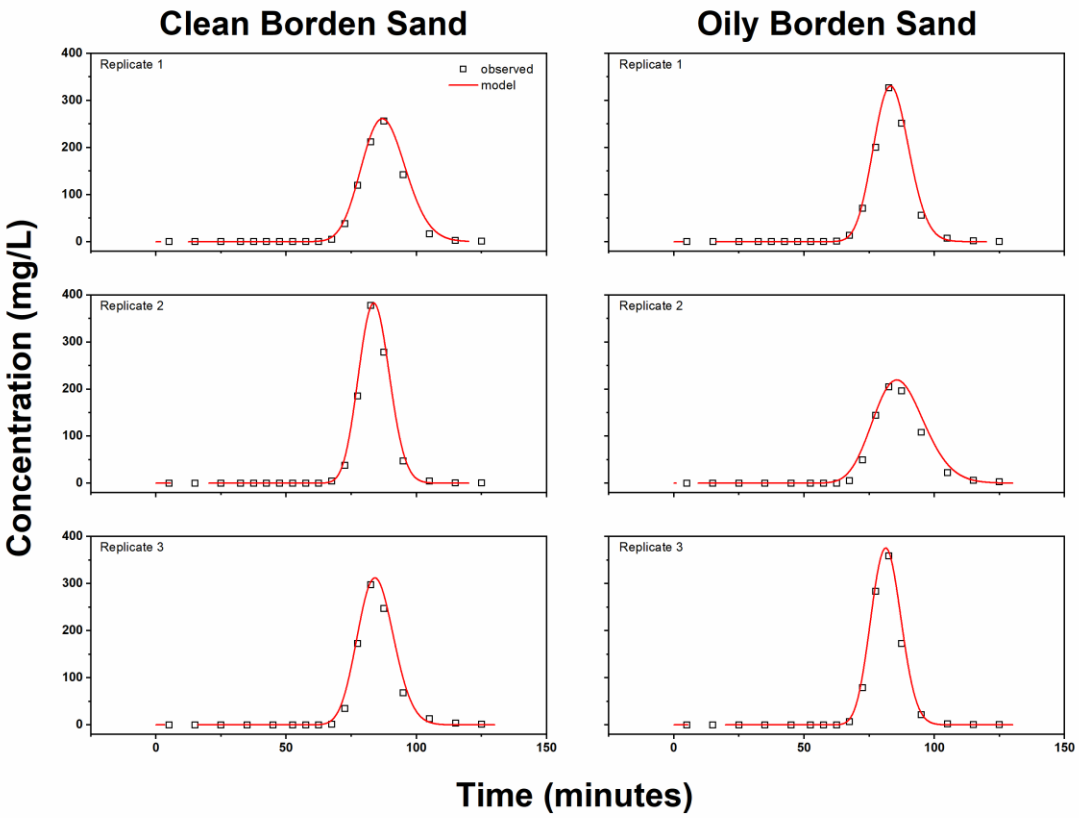

Figure 38. Comparison of observed (symbols) and simulated (lines) bromide breakthrough curves for the columns packed with clean Borden sand (left panels) and oil-impacted Borden sand (right panels) used for transport and binding experiments using silver nanoparticles. Each experimental system was performed in triplicate (vertically descending from trial 1 to 3).

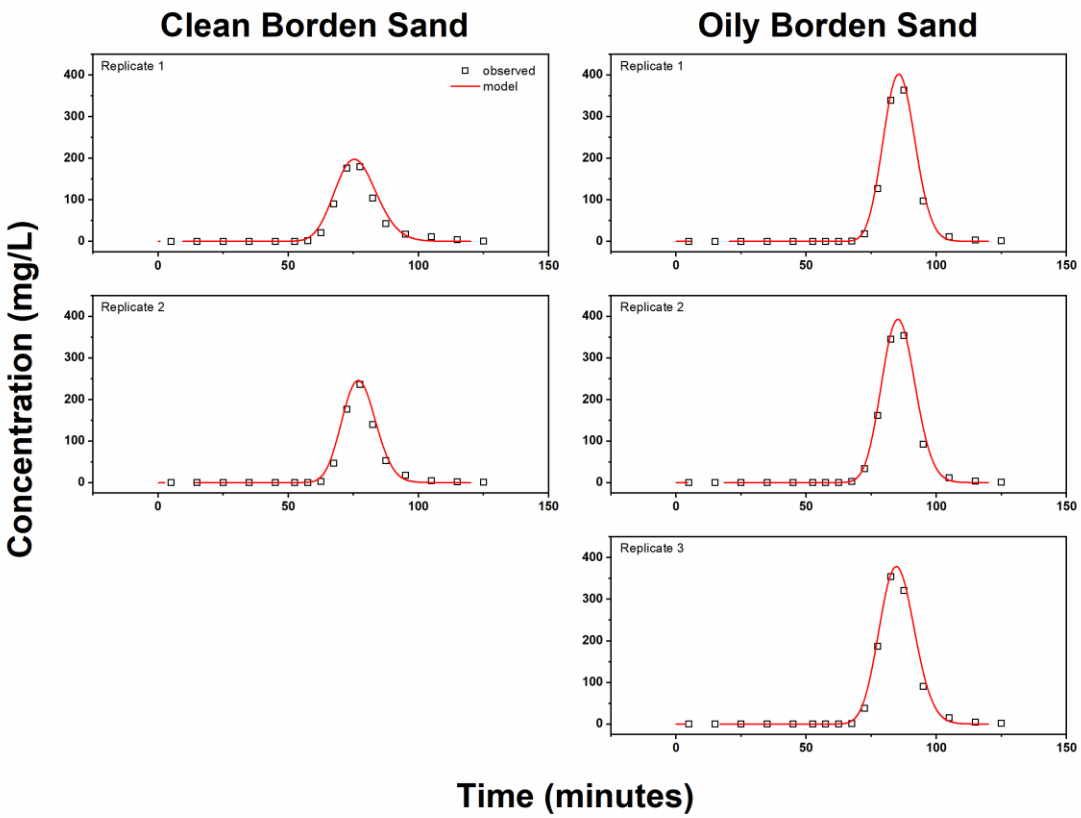

Figure 39. Comparison of observed (symbols) and simulated (lines) bromide breakthrough curves for the columns packed with clean Borden sand (left panels) and oil-impacted Borden sand (right panels) used for transport and binding experiments using cobalt ferrite nanoparticles. The clean sand experimental system was performed in duplicate owing to a leak in one of the columns (vertically descending from trial 1 to 2). The oily sand experimental system was performed in triplicate (vertically descending from trial 1 to 3).

Table 11. Column physical parameters for all transport & binding experiments

Nanoparticle	Replicate	Clean Borden Sand		Oily Borden Sand	
		Porosity	Dispersivity (m^{-1})	Porosity	Dispersivity (m^{-1})
Iron Oxide	1	0.3778	7.21E-04	0.3681	4.63E-04
	2	0.3718	5.11E-04	0.3745	3.58E-04
	3	0.3721	5.47E-04	0.3736	3.66E-04
Cobalt Ferrite	1	0.3403	8.30E-04	0.3847	3.16E-04
	2	0.3557	4.75E-04	0.3963	3.71E-04
	3	-	-	0.3903	4.20E-04
Silver	1	0.3954	7.02E-04	0.3598	9.94E-04
	2	0.3839	4.45E-04	0.3883	4.73E-04
	3	0.3963	3.05E-04	0.3881	3.03E-04

Table 12. Attachment parameters estimated from 1D-USAT/DDS fitting of experimental data for various nanoparticle samples to clean Borden Sand (BS).

Nanoparticle	Replicate	M_{attach}^{max} (mg/kg)	k_{att} (s^{-1})	k_{det} (s^{-1})	RMSE
Iron Oxide	1	35.8	3.95E-05	2.55E-06	7.86
	2	126.2*	3.74E-05	1.28E-06	9.99
	3	13.1	6.71E-04	1.81E-05	7.27
	Average	**58.3**	**2.49E-04**	**7.32E-06**	**8.38**
Cobalt Ferrite	1	5.18	3.82E-04	7.64E-07	3.75
	2	17.9	1.73E-05	1.98E-06	15.2
	Average	**11.5**	**1.20E-04**	**1.37E-06**	**9.46**
Silver	1	8.55	3.16E-05	3.35E-06	3.08
	2	10.5	3.61E-05	3.18E-06	3.29
	3	15.9	8.07E-05	6.62E-06	2.68
	Average	**11.6**	**4.945E-05**	**4.385E-06**	**3.02**

*significant outlier

Table 13. Attachment parameters estimated from 1D-USAT/DDS fitting of experimental data for various nanoparticle samples to oily Borden Sand (OBS).

Nanoparticle	Replicate	M_{attach}^{max} (mg/kg)	k_{att} (s^{-1})	k_{det} (s^{-1})	RMSE
Iron Oxide	1	33.7*	>5.13E-04	0†	2.12E-02
	2	33.7*	>4.63E-04	0†	8.06E-03
	3	33.7*	>5.26E-04	0†	4.33E-03
	Average	**33.7***	**>5.01E-04**	**0†**	**1.12E-02**
Cobalt Ferrite	1	18.9	8.85E-04	1.88E-06	0.056
	2	34.5	2.95E-04	1.38E-06	0.081
	3	45.0	1.61E-04	1.74E-06	1.85
	Average	**32.8**	**4.47E-04**	**1.67E-06**	**0.66**
Silver	1	12.7*	>9.04E-05	0†	5.43E-02
	2	12.7*	>1.68E-04	0†	1.75E-03
	3	12.7*	>2.36E-05	0†	9.06E-02
	Average	**12.7***	**>9.40E-05**	**0†**	**4.89E-02**

*M_{attach}^{max} value taken from binding batch test
†k_{det} assumed to be 0 due to no observable attachment

For the columns packed with OBS, the concentration of iron oxide nanoparticles and silver nanoparticles was <MDL, while the concentration of cobalt ferrite nanoparticles reached a peak of 14.6 mg/L (3.2% of injection concentration) in one of the replicates. These results clearly demonstrate that Pluronic-coated nanoparticles are capable of transporting through clean sands and are preferentially retained in oily sands. Tracer breakthrough data (**Figure 37** to **Figure 39**; **Table 11**) were used to determine the porosity and dispersivity of the respective columns. It was found that BS had an average

porosity of 0.374±0.019 and an average dispersivity of (5.67±1.72) x 10^{-4} m^{-1}, while OBS had an average porosity of 0.380±0.012 and an average dispersivity of (4.52±2.12) x 10^{-4} m^{-1}. These findings are consistent with our previous studies in Borden sand (**Chapter 5**) which found nearly identical porosity and lower dispersivity in OBS, indicating that the presence of oil reduces variations in pore velocity. The optimal model parameters determined are listed in **Table 12** & **Table 13** for the BS and OBS column systems, and were used to produce the simulated BTCs (black lines) on **Figure 34** to **Figure 36**. The majority of the estimated M_{attach}^{max} values for the BS systems (from 5.2 to 17.9 mg/kg) match closely with values expected based on the batch test results presented in Figures 2 and 4 (from 4 to 20 mg/kg). Some outliers were observed in the iron oxide estimates, most notably for the second column replicate. For all BS column systems, the detachment rate coefficient was estimated to be on the order of 10^{-6} s^{-1} which agrees closely with our previous findings. The minimum attachment rate coefficient, k_{attach}, was consistently found to be between 2 and 4 times greater for the OBS systems than for the BS systems, a finding consistent with previous work which indicates preferential NP attachment in oil-impacted sands. Furthermore, the M_{attach}^{max} values for cobalt ferrite nanoparticles in the OBS system (from 18.9 to 45.0 mg/kg), which were estimated from observed BTC data, agree closely with the values from the batch binding experiments (17.3 to 33.7 mg/kg). For the cobalt ferrite nanoparticles in the OBS system, the detachment rate coefficient was estimated to be on the same order as detachment in the BS systems. Considering only cobalt ferrite nanoparticles, the maximum solid-phase concentration (M_{attach}^{max}) triples from 11.5 to 32.8 mg/kg, the attachment rate coefficient (k_{attach}) nearly quadruples from 1.20 x 10^{-4} s^{-1} to 4.47 x 10^{-4} s^{-1}, and detachment rate coefficient (k_{detach}) remains approximately the same (increasing slightly from 1.37 x 10^{-6} s^{-1} to 1.67 x 10^{-6} s^{-1}) between the OBS and BS systems.

6.5 Conclusions

For the past 20 years, research in the field of pharmaceuticals and therapeutics, particularly in oncology, has recognized nanotechnology-enabled targeted delivery as a significant part of cancer detection, diagnosis, and therapy[276]. The improved delivery methods rely on drugs encapsulated in micellar nanoparticles which enable specific targeting of diseased tissue. Concentrating the drug in areas of the body where it can perform its intended function increases efficiency of use, thereby decreasing the cost and frequency of application[277,278]. In addition to this, unwanted side effects, such as the drug acting on healthy tissue, is avoided[276]. Chemotherapeutic treatment of cancer bears many similarities to nanoremediation of impacted soil. In both cases, there is a zone requiring treatment that has distinct physical and chemical properties differentiating it from the surrounding material. The factors that make targeted therapeutics a successful improvement to traditional chemotherapy have direct applicability in

the field of nanoremediation and consideration should be made for the deployment of remediation agents early in their development.

In this work we have demonstrated that targeted delivery of various nanoparticles, produced using varied synthetic methods, can be achieved by using the same amphiphilic coating on each. It was demonstrated that under heated deployment conditions, nanoparticle attachment to impacted zones could be doubled compared to their performance in clean sand. While the temperature employed in this study was rather high (50 ^{o}C), previous work has demonstrated that a moderate temperature increase from ~22 ^{o}C to 30 ^{o}C results in a significant improvement to binding behaviour (**Chapter 5**), indicating that final application conditions may not need to be to be as great as demonstrated in this effort.

The implementation of successful targeted remediation of impacted soils requires three goals to be met: 1) the remediation agent must be able to transport through porous media, 2) the remediation agent must preferentially accumulate in an area with target physical and/or chemical properties (i.e. an impacted zone), and 3) the remediation agent must impart a treatment effect on the contaminant in the target zone. In this work, we have demonstrated successful implementation of the first two goals which address the 'targeted' aspect of targeted remediation. Iron oxide, silver, and cobalt ferrite could be targeted to preferentially accumulate on sands coated with viscous LNAPL. Iron oxide is already known as a remediation agent – in particular magnetite is known to be an activator for oxidants such as persulfate, giving one potential remediation pathway using the materials demonstrated here. It is also understood that the surface of nZVI is coated in a thin iron-oxide passivated layer which could likely support the coating strategy discussed in this work. The targeted delivery behaviour shown here is a result of the nanoparticle coating rather than the core material, and that such a coating may be applied to various materials, giving versatility to choose the best remediation agent for a specific site. Targeted delivery has great potential to improve current remediation technology and this work demonstrates how it can be applied in the case of viscous LNAPLs.

Chapter 7

Conclusions and Future Work

7.1 Summary

This thesis presents the development of a nanoparticle coating strategy which endows particles with aqueous stability, mobility in natural porous media, and targeted adsorption to crude oil-impacted porous media. A two-step coating technique comprising coating the nanoparticles with hydrophobic oleic acid followed by amphiphilic Pluronic block co-polymers produced a surface which facilitated the previously stated design requirements. Nanoparticle transport and binding was evaluated through binding batch tests as well as flow-through experiments in packed columns containing clean or oil-impacted natural aquifer sediments which confirmed preferential nanoparticle adsorption to oil-impacted sands when compared to clean sands. Various factors influencing nanoparticle mobility and binding to porous media were evaluated, and it was found that design parameters such as coating type and coating concentration influenced the nanoparticles' transport and binding behaviour. In addition to this, environmental parameters including oil concentration, oil type, and temperature were found to increase nanoparticle binding to oil-impacted sands. Simulation of experimental data using a solute transport modelling software enabled estimation of kinetic parameters defining nanoparticle transport and binding behaviour and allowed some prediction of how flow rate and different oil types or concentration would impact nanoparticle distribution within a porous medium. Finally, the coating strategy was applied to different types of nanoparticle core materials, including iron oxide, silver, and cobalt ferrite, all produced using different synthetic methods, to evaluate the versatility of coating application. It was found that all nanoparticles coated with the Pluronic formulation exhibited preferential binding to oil-impacted sands as well as mobility through natural aquifer sediment.

7.2 Conclusions

A nanoparticle coating enabling aqueous nanoparticle stability, mobility in natural porous media, and preferential adsorption to oil-impacted porous media was developed. The coating relied on a two-step method whereby nanoparticle cores were first made hydrophobic by the addition of oleic acid, then made amphiphilic by the addition of a blend of Pluronic block co-polymers. The morphology of the coated nanoparticles was dependent on the concentration of the coating, ranging from ~100 nm aggregated clusters of nanoparticles at Pluronic coating concentrations of 1 g/L to ~7 nm individually stabilized nanoparticles at Pluronic coating concentration of 10 g/L. It was also found that coating concentration and coating hydrophobicity played a significant role in the preferential attachment of nanoparticles to crude oil at room temperature, with lower coating concentrations and more hydrophobic polymer molecules

resulting in higher observed binding. It was also found that nanoparticle coating formulation influenced the mobility of nanoparticles in porous media, with higher coating concentrations and more hydrophobic molecules resulting in increased nanoparticle recovery through columns packed with unmodified natural aquifer sediment. To this end, the nanoparticle coating formulation may be tuned to produce nanoparticles with higher mobility or increased attachment as necessary.

The nanoparticles demonstrated maximum attachment to clean sand in the range of 2 – 13 mg/kg and maximum attachment to oily sand in the range of 8 – 32 mg/kg, dependent on the nanoparticle formulation and environmental factors selected. Experimental data were used to estimate kinetic attachment and detachment parameters in clean and oil-impacted sands under nanoparticle flow-through conditions, and it was found that typically the attachment rate (k_{attach}) for nanoparticles in oil-impacted sand exceeds the k_{attach} for nanoparticles in clean sand by approximately one order of magnitude (10x). The attachment rates varied on the order of 10^{-5} - 10^{-4} s^{-1} in clean sand, while attachment rates varied on the order of 10^{-4} - 10^{-3} s^{-1} in oily sand. Detachment rates (k_{detach}) in clean sand flowthrough were found to be on the order of 10^{-6} s^{-1}. Detachment rates were estimated to be ~0 for most experiments in oil-impacted sand packed columns due to the absence of detectable nanoparticles in the effluent, but results using CoFe nanoparticles revealed that the k_{detach} may be on the same order of magnitude as calculated in clean sand experiments – approximately 10^{-6} s^{-1}. These results indicate that nanoparticle transport and binding can be described using current colloid filtration theory and allow us to predict nanoparticle behaviour under various conditions such as increased flow rate or higher contaminant concentration.

Most of this work was carried out using iron oxide nanoparticles as a core material due to its inexpensiveness and ease of synthesis, but the targeted delivery coating strategy should ideally be able to be applied to any nanomaterial relevant for environmental remediation purposes. To this end, we investigated two additional nanoparticle core materials: silver and cobalt ferrite. Each of the nanoparticles selected for evaluation in this thesis were produced using different synthetic methods: coprecipitation (iron oxide), chemical reduction (silver), and thermal decomposition (cobalt ferrite). In each case, oleic acid-coated hydrophobic nanoparticles were produced which were amenable to the Pluronic coated process. The resulting Pluronic-coated nanoparticles all exhibited mobility through clean sand-packed columns and preferential retention in oil-impacted sand-packed columns, and we conclude that this behaviour is a result of the surface coating properties.

An important consideration for this work is anticipating how the developed coating strategy may be applied to enhance subsurface deployment of nanoparticle agents. To this end, X-Ray computed tomography was investigated as a detection mechanism for identifying sands with a higher nanoparticle content. It was found that the preferential nanoparticle binding toward oil-impacted sand was sufficient to produce a significant contrast between samples exposed to nanoparticles and un-exposed control sand.

The same was not true for clean sands under the same conditions. Therefore, we envision a possible use-case for targeted nanoparticle attachment to oil-impacted porous media, and subsequent detection of heterogenous contaminated zones delineated by bound nanoparticle contrast agents. Furthermore, recent work using the nanoparticles discussed in this thesis as contrast agents in spectral induced polarization processes indicates that these nanoparticles may be detected in porous media by monitoring electrical signals from emplaced probes and that the signal is concentration dependent[279]. Combined with the particles' targeted binding capabilities, we anticipate the possibility of nanoparticle binding and subsequent delineation of impacted vs. unimpacted porous media.

7.3 Recommendations for Future Work

Based on the conclusions presented in this thesis, several tasks to further advance this work are proposed herein:

1. Application of the nanoparticle coating nZVI to investigate nanoparticle targeted binding and subsequent remediation of the target contaminant. The Pluronic coating applied to iron oxide in this thesis is anchored to the nanoparticle through carboxylate-Fe chelation interactions. nZVI forms a natural iron oxide shell on exposure to atmospheric oxygen and it is expected that the oleic acid and subsequent Pluronic coating may be applied to produce an nZVI particle with targeted delivery and remedial properties. This future work would investigate targeted binding of Pluronic-coated nZVI to crude oil, how the treatment rate of such particles may be influenced by the coating strategy, and what amendments may be required to facilitate remediation. It is well understood that nZVI-activated persulfate can enhance the oxidation rate of organic contaminants[19], but recent research has indicated that electromagnetic induction can improve nZVI reaction rates and increase local temperatures[280]. Critically, the threshold concentration of nanoparticles in soil required to initiate remediation under various activation conditions should be determined. Furthermore, local nanoparticle heating via electromagnetic induction may introduce an efficient mechanism for increasing nanoparticle temperature, thereby enhancing targeted binding interactions as seen in this work.

2. Integration of nanoparticle targeted delivery with electrooxidation-based treatment methods. The iron oxide particles investigated in this work may act as a source of iron ions for Fenton oxidation processes accelerated by the application of electrical bias. It may be possible to deliver nanoparticles to a target treatment zone, then apply voltage across this zone to initiate an oxidative process to degrade the target contaminant. This work must begin with proof of concept studies using nanoparticles spiked into artificially impacted soil to determine the experimental

parameters required for remediation, including contaminant type, contaminant concentration, nanoparticle concentration, electrolyte concentration, electrode type, electrode geometry, and applied voltage. Following proof of concept, batch-scale targeted binding experiments should seek to inform what experimental conditions are required to achieve the necessary nanoparticle loading. Subsequent application of electrooxidation to nanoparticles bound in batch experiments should seek to demonstrate the possibility of such a two-step treatment. Pending positive results from the aforementioned experiments, the final stage of this work should involve a column apparatus allowing nanoparticle transport and binding to be combined with subsequent electrode application for oxidation.

3. Investigate the attachment and detachment kinetics of Pluronic-coated nanoparticles in continuous-flow packed columns at varying flow rates, temperatures, and oil concentrations. This work is important to validate the predictions made by 1D-USAT simulations in this thesis, generate data more relevant to field application of these nanoparticles, as well as provide a way to better evaluate the effect of temperature on the binding interaction. Calculating k_{attach} and k_{detach} at multiple temperatures may relate changes in attachment and detachment to temperature through an Arrhenius relationship, allowing calculation of the energies associated with the binding process. This is important for confirming the nature of the binding interactions through comparison of the binding energies with literature values for hydrophobic interactions.

4. Investigate bound nanoparticle detection by sensing techniques such as X-Ray CT and Spectral Induced Polarization (SIP) in flow-through packed column studies. Work presented in Chapter 3 of this thesis, as well as a recently published manuscript using the nanoparticles developed for this project[279] has confirmed the capability for Pluronic-coated iron oxide particles to be detected in sands by both techniques. The next stages of this work should focus on analysis of porous media which has undergone transport and binding experiments to determine the contrast between nanoparticles bound to impacted regions and clean sand. This next step will elucidate the potential application of targeted nanoparticle subsurface delivery as a detection method for monitoring heterogeneously impacted sites.

5. Investigate the binding mechanism in more detail using quartz crystal microbalance (QCM) experiments to examine nanoparticle binding to pristine hydrophobic surfaces. Real time measurement of binding processes would provide insight regarding the rate of attachment and detachment as well as how these processes are affected by coating formulation and environmental factors such as temperature. This represents another method by which the nature of the binding

mechanism may be confirmed through measuring the binding energy of the nanoparticles to hydrophobic surfaces. Combined with the suggestions from next steps item 3, this should provide conclusive evidence for nature of binding interactions. Some preliminary QCM binding trials have already been attempted and a brief summary of this work is discussed in Appendix D: Quartz Crystal Microbalance (QCM) Preliminary Investigation

6. Investigate the stability of nanoparticle formulations during storage over time, in relation to aggregation and settling as well as transport and binding performance. Determine the nature of stability degradation, if any, is it due to oxidation or biological processes? Determine whether the addition of natural antioxidants such as ascorbic acid or vitamin E, or packaging conditions such as an anoxic environment, may prolong nanoparticle stability in suspension.

7.5 Preparations for Field Deployment

The work discussed in this thesis outlines the development and validation strategy for nanoparticle coatings which allow targeted delivery to crude oil in a subsurface environment. While this represents a good first step towards improving nanoremediation and site characterization technologies, several knowledge gaps must be addressed before this new technology can be usefully applied at scale. The critical issues to address include the following: 1. understanding how variations in nanoparticle coating formulation responds to a variety of different contaminants within the same class (i.e. crude oil vs. gasoline, vs. jet fuel, etc.); 2. Understanding how nanoparticle attachment behaviour is affected by site heterogeneity; 3. Understanding how nanoparticle transport and binding is affected by site-specific variations porous media make-up. Answering these questions will allow for a reasonable starting point or educated guess when determining the application conditions for this technology each time a new site is faced.

This work addressed how variations in oil type and oil concentration influence nanoparticle binding in Chapter 5, but it remains unclear on how the nanoparticle coating formulation may be adjusted to tune binding behaviour to be appropriate to the characteristics of a given site. For example, when addressing a different aliphatic hydrocarbon contaminant, would a different Pluronic coating formulation provide improved binding characteristics? To provide a good starting point for selecting a best educated guess for the appropriate Pluronic formulation, it would be advantageous to conduct a batch binding factorial analysis investigating both coating formulation and contaminant characteristics. This factorial analysis can be used to identify the importance of interactions between coating formulation and contaminant type or concentration. With this information, when approaching a new site with a known type of contaminant, the best coating formulation can be applied to achieve the desired binding response.

This work addressed homogenous transport and binding environments, composed of either clean sand or oil-impacted sand. Furthermore, transport and binding were investigated in essentially 1-dimensional environments where the nanoparticle slug was forced to interact uniformly with the porous media. In real environments, crude-oil impaction is not uniformly distributed across an entire site and the injected solution will not necessarily transport through the impacted area, but may follow preferential flow pathways around lower porosity regions. To better understand the movement and binding of injected nanoparticles, lab-scale investigations of heterogeneous environments should be performed. These may include column experiments containing layers or pockets of crude oil-impacted soil or 2-dimensional experiments using "sand boxes" with built-in pockets of crude oil-impacted soil. Such conditions can verify the predictions from Chapter 5 of this work which shows that nanoparticles should accumulate in the oil-impacted regions as well as use tracers and nanoparticle analysis to determine the movement of nanoparticle suspension around heterogenous pockets of impacted porous media.

Finally, the way nanoparticles respond to different types of porous media is critical to predicting performance of this technology at field scale. The most realistic way to gather this information is to perform many lab-scale transport and binding tests in real soils with well-characterized profiles. The soils should be selected to address a variety of factors including grain size distribution, mineral constituents, and presence of naturally occurring organic matter (NOM). Previous literature has indicated that the presence of NOM can facilitate enhanced nanoparticle mobility and that NOM molecules, such as humic acids, have a wide range of functional moieties, including aliphatic hydrocarbons, polyaromatic hydrocarbons, anionic, cationic, and zwitterionic groups. The effect of such NOM may enhance or decrease both particle mobility and binding behaviour according to the structure of the adsorbed NOM. Similar concerns exist for different mineral constituents which may exhibit increased or decreased adsorption affinity for Pluronic-coated nanoparticles. Porous media surface area, influenced by grain size distribution, may influence adsorption behaviour as well.

Appendix A: Description of Variables in Advection/Dispersion Equation

φ	Porosity of medium
c	Concentration of NP in suspension
D	Hydrodynamic dispersion coefficient
ρ_b	Density of porous medium
s_1, s_2	Mass of NP deposited per mass of porous medium. 1 = adsorption, 2= filtration
$k_{a,1}$, $k_{a,2}$	Deposition rate of NP. 1= adsorption, 2=filtration
$k_{d,1}$, $k_{d,2}$	Release rate of NP. 1=adsorption, 2=filtration
β_1, β_2	Exponential coefficient describing interaction dynamics. 1=adsorption, 2=filtration
A_1	Multiplier constant describing interaction dynamics for adsorption
d_{50}	Mean pore diameter of porous medium

Appendix B: Borden Sand Soil Characterization

All data reported in this appendix is copied from Ball et al., "Characterization of a sandy aquifer material at the grain scale"[281].

Table B-1. Grain composition in Borden size fractions[281]

U.S. Standard mesh size	Particles counted (%)[a]							
	-4 +12	-12 +20	-20 +40	-40 +60	-60 +80	-80 +120	-120 +200	-200
Single mineral grains:								
Quartz	3	12	36	33	45	39	48	30
Plagioclase	1	11	15	16	13	25	10	8
K-Feldspar	1	3	6	22	19	20	6	3
Hornblende	-	-	-	3	-	1	6	15
Garnet	-	-	-	-	-	1	5	5
Calcite	-	-	2	5	4	2	9	5
Opaque minerals[b]	-	-	-	-	-	-	5	20
Zircon	-	-	-	-	-	-	-	5
Pyroxenes[c]	-	-	-	-	-	-	-	5
Chloritized-biotite	-	-	1	-	-	-	5	-
Rock fragments:								
Micrite/Biomicrite	31	26	19	6	6	7	6	8
Sparite/Biosparite	52	35	10	8	5	2	-	-
Schist[d]	1	3	4	3	2	2	-	-
Sandstone[e]	9	6	4	2	4	1	-	-
Plutonics[f]	3	4	3	2	1	-	-	-

[a]thin sections (0.030 mm) of each size fraction were examined under a petrographic microscope. 100 randomly selected particles (falling on a grid line) in each size fraction were identified and counted by type.
[b]Primarily magnetite and ilmenite.
[c]Believed to be primarily augite and hypersthene.
[d]Believed to be primarily quartz-plagioclase, quartz-chlorite, and quartz-sericite.
[e]Some fragments in the -1 to +12 fraction were very fine grained (siltstone); most sandstones and siltstones contained significant amounts of calcite cement.
[f]Medium- to coarse-grained rock fragments of granitoid texture and igneous origin.

Table B-2. Mass distribution by size fraction for Borden bulk solids – dry sieving results[281]

U.S. Standard mesh size	Size range (mm)	Nominal diameter[a] (mm)	Mass fraction	No. of assays	Rel. error
-4 +12	4.75 – 1.7	2.8	0.0058	6	0.168
-12 +20	1.7 – 0.85	1.2	0.0091	6	0.033
-20 +40	0.85 – 0.42	0.6	0.0524	6	0.034
-40 +60	0.42 – 0.25	0.33	0.163	4	0.039
-60 +80	0.25 – 0.18	0.21	0.257	4	0.018
-80 +120	0.18 – 0.125	0.15	0.315	4	0.015
-120 +200	0.125 – 0.075	0.097	0.165	4	0.032
-200	< 0.075		0.0341	4	0.049

[a]Geometric mean of sieve sizes

Appendix C: Silver Nanoparticle Synthesis Optimization

Table C-1. Silver nanoparticle synthesis optimization response surface trial 1 variable selection

	Actual Variables		Coded Variables		Response
Observation	[H3PO4]	[Na Oleate]	x1	x2	y
1	16	2.5	1	-1	0.8145
2	16	12.5	1	1	0.2235
3	4	12.5	-1	1	0.044
4	4	2.5	-1	-1	0.098
5	18.5	7.5	1.414214	0	3.597
6	1.5	7.5	-1.41421	0	0.044
7	10	14.57	0	1.414214	0.046
8	10	0.429	0	-1.41421	0.043
9	10	7.5	0	0	0.103
10	10	7.5	0	0	0.119
11	10	7.5	0	0	0.1405
12	10	7.5	0	0	0.105

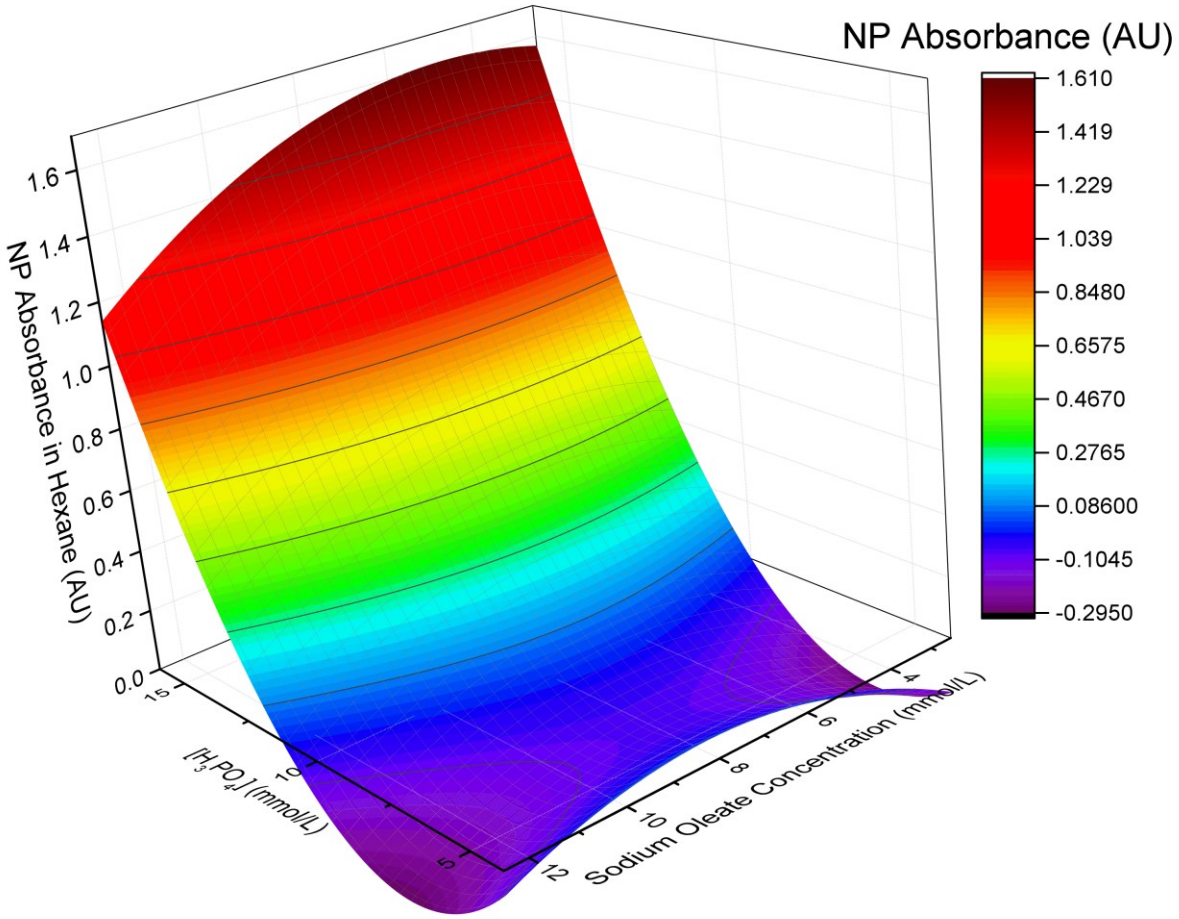

Figure C-1. Trial 1 of a surface response optimization examining the influence of phosphoric acid (H_3PO_4) and sodium oleate concentration on silver nanoparticle synthesis yield. Higher absorbance reflects a higher yield of oleate-coated silver nanoparticles transferred to hexane. Under the conditions tested, higher [H_3PO_4] resulted in significant increases in Ag NP yield while sodium oleate appeared to exhibit an optimal concentration around 5 mmol/L.

Table C-2. Silver nanoparticle synthesis optimization response surface trial 2 variable selection

	Actual Variables		Coded Variables		Response
Observation	[H3PO4]	[Na Oleate]	x1	x2	y
1	30	5	1	1	1.831262
2	30	1	1	-1	0.551791
3	18	1	-1	-1	0.848223
4	18	5	-1	1	2.220635
5	32.5	3	1.414214	0	2.619727
6	15.5	3	-1.41421	0	2.17134
7	24	5.8284	0	1.414214	1.569631
8	24	0.1716	0	-1.41421	2.310695
9	24	3	0	0	2.616898
10	24	3	0	0	2.810008
11	24	3	0	0	2.568611
12	24	3	0	0	2.654118

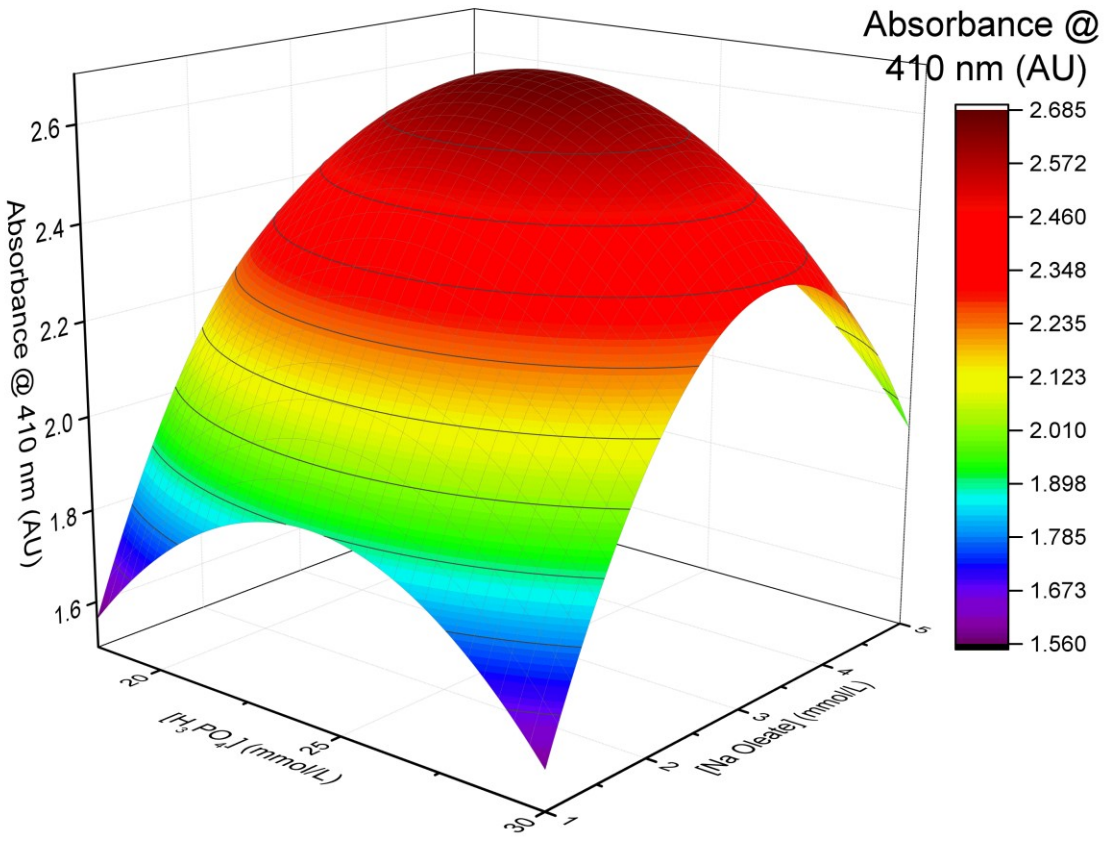

Figure C-2. Trial 2 of a surface response optimization examining the influence of phosphoric acid (H_3PO_4) and sodium oleate concentration on silver nanoparticle synthesis yield. Higher absorbance reflects a higher yield of oleate-coated silver nanoparticles transferred to hexane. Trial 1 was used to inform parameter range selection for trial 2. Under the conditions tested, an optimal [H_3PO_4] of 25 mmol/L and an oprimal [Na Oleate] of 3 mmol/L were determined.

Appendix D: Quartz Crystal Microbalance (QCM) Preliminary Investigation

D.1 Purpose & Introduction

Quartz Crystal Microbalance (QCM) is an analytical technique for measuring the mass quantity adsorbed onto the surface of a vibrating quartz crystal. The crystal is electrically biased, and the vibration may be detected through an electrical signal which oscillates at a specific frequency. This frequency is dampened as the oscillation frequency of the quartz crystal is dampened by adsorbed mass. This change in frequency can be correlated to adsorbed mass through the Saurbrey equation:

$$\Delta m = -\frac{A\sqrt{\rho_q \mu_q}}{2{f_0}^2}\Delta f \qquad \text{(D-1)}$$

Where Δm is the change in areal mass (ng/cm^2), A is the area of the sensor (cm^2), ρ_q is the density of quartz (g/cm^3), μ_q is the shear modulus of quartz (g cm^{-1} s^{-1}) f_0 is the resonant frequency of the quartz (Hz), and Δf is the observed change in frequency (Hz).

The binding of Pluronic-coated nanoparticles to a pristine hydrophobic surface from aqueous medium may be observed by recording the areal mass change on the surface of a QCM sensor in the presence of nanoparticles or free Pluronic. The set of experiments presented here sought to confirm nanoparticle preferential binding to hydrophobic surfaces, as well as determine how much, if at all, free Pluronic may influence nanoparticle binding.

D.2 Materials & Methods

D.2.1 Materials

Ethanol (ACS grade, 99%) was purchased from Fisher Scientific and 1-octadecanethiol (1-ODT; 98%) was purchased from Sigma Aldrich and used as received. Pluronic P104 and Pluronic L62 were gifted from BASF Canada via Brenntag Canada and used as received. Pluronic-coated iron oxide nanoparticles and oleic acid-coated iron oxide nanoparticles were produced as described in Chapter 3 and used at concentrations suspended in water of ~500 mg/L.

D.2.2 QCM Experiments

QCM experiments were performed using a Q-Sense QCM-D instrument and Q-Sense Au-coated QSensors. For binding experiments to pristine gold sensors, Milli-Q water was injected into the QCM cell at a constant flow rate of 0.3 mL/min. After a steady state frequency had been reached, injection was

swapped to Pluronic-coated nanoparticles, oleic acid-coated nanoparticles, or Pluronic solution (1 g/L). After 30 minutes, injection was swapped back to Milli-Q water. In the case of binding experiments on hydrophobized surfaces, ethanol was injected into the QCM cell until steady state was reached. Injection was then swapped to 0.02 mol/L 1-ODT in ethanol to allow the thiol group to react and attach to the gold surface. The cell was then injected with ethanol once again to wash out any unbound 1-ODT. Following this, Milli-Q water was injected into the QCM cell until steady state frequency was reached, and the experiment proceeded identically to the binding experiments using a pristine gold surface.

Analysis used the frequency change reported by the Q-Sense instrument coupled with the Saurbrey equation to produce an areal mass change for each sample. Frequency changes were calculated from the minimum value at steady state to the maximum value after introduction of the sample.

D.3 Results & Discussion

Binding of four samples were assessed using the QCM; two replicates of Pluronic coated nanoparticles (80L62-P104 1 g/L coating; see formulation B-80 from **Table 3**), oleic acid-only coated nanoparticles, and 1 g/L Pluronic solution (80% L62, 20% P104). The results of the Pluronic-coated nanoparticle binding experiments are seen in **Figures D-1** and **D-2.** The first notable observation is the confirmation of 1-ODT deposition on the gold sensor, evidenced by the small decrease in areal mass observed at △ compared to the large increase observed at ○. After introduction of the Pluronic-coated nanoparticles in water, an increase in areal mass is observed on all sensors, however it is much more significant on the hydrophobic surfaces, with increases of 259.7 ng/cm^2 and 245.9 ng/cm^2 in the respective replicates compared to 71.6 ng/cm^2 and 57.6 ng/cm^2 on the pristine gold surfaces (**Table D-1**).

Table D-1. QCM areal mass changes upon introduction of binding species

Sample	**Δm on pristine gold (ng/cm^2)**	**Δm on hydrophobic gold (ng/cm^2)**
Pluronic-NP 1	71.6	259.7
Pluronic-NP 2	57.6	245.9
OA-NP	8.4	78.3
Pluronic Solution	177.7	382.4

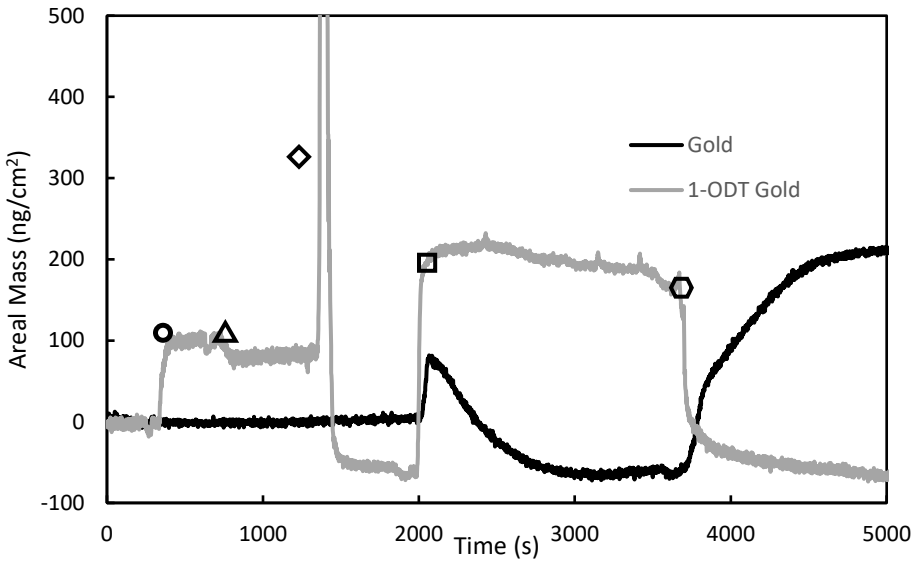

Figure D-1. Quartz Crystal Microbalance data for Pluronic-coated nanoparticle binding replicate 1 at room temperature to two different sensors: unmodified gold (**black**) and gold modified with 1-octadecanethiol (1-ODT; **grey**), a hydrophobic material. The various symbols indicate different stages of the QCM experiment: ○ 0.02 mol/L 1-ODT in ethanol is injected into one of the QCM cells, △ ethanol is injected in to wash out any excess 1-ODT, ◇ water is injected to replace ethanol, □ Pluronic-coated nanoparticles suspended in water (~500 mg/L) are injected into each cell, ⬡ water is injected into each cell. Results clearly demonstrate that nanoparticles preferentially attach to the hydrophobic surface as evidenced by the step increase in areal mass in the grey line at 2000 s. Note the irregular downward trend for the pristine gold surface observed at 2000 s and the severe increase at ~4000 s. This is attributed to instrument error.

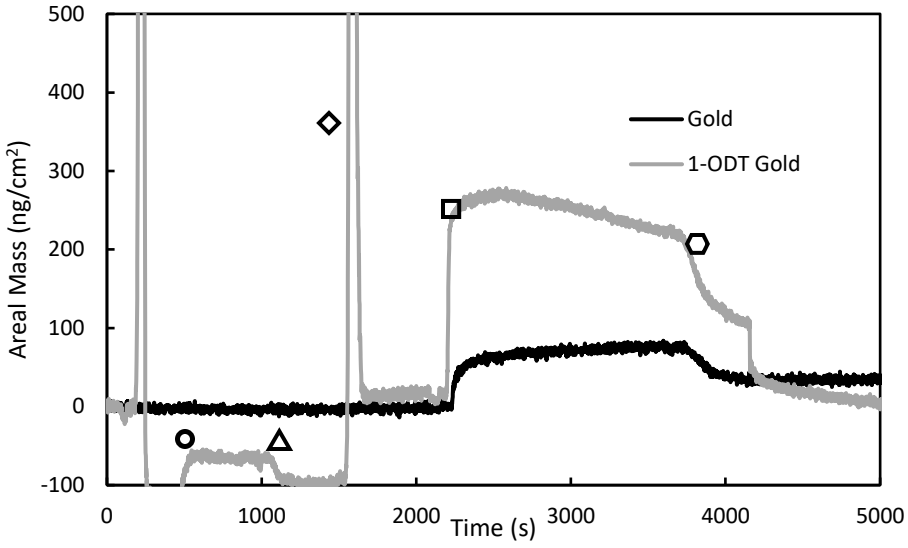

Figure D-2. Quartz Crystal Microbalance data for Pluronic-coated nanoparticle binding replicate 2 at room temperature to two different sensors: unmodified gold (**black**) and gold modified with 1-octadecanethiol (1-ODT; **grey**), a hydrophobic material. The various symbols indicate different stages of the QCM experiment: ○ 0.02 mol/L 1-ODT in ethanol is injected into one of the QCM cells, △ ethanol is injected in to wash out any excess 1-ODT, ◇ water is injected to replace ethanol, □ Pluronic-coated nanoparticles suspended in water (~500 mg/L) are injected into each cell, ⬡ water is injected into each cell. Results clearly demonstrate that nanoparticles preferentially attach to the hydrophobic surface as evidenced by the step increase in areal mass in the grey line at 2200 s.

Upon introduction of water at 4000 s, the frequency of the QCM sensors for both pristine and hydrophobized gold was returned to the resonant frequency of the sensor, indicating that nanoparticles had been flushed from these surfaces.

To investigate the importance of the Pluronic coating on nanoparticle binding, oleic acid-coated iron oxide nanoparticle binding was investigated, as shown in **Figure D-3**. Similar results to Pluronic-coated nanoparticle binding were observed, however the magnitude of the areal mass changes were reduced. Where a moderate increase in areal mass of ~70 ng/cm^2 was observed for Pluronic-NP nanoparticles on pristine gold, an increase of only 8.4 ng/cm^2 was observed when using OA-NP. Similarly, binding to the hydrophobized gold surface was calculated to be 78.3 ng/cm^2 for OA-NP compared to the ~250 ng/cm^2 of Pluronic-NP. Note that some equipment error hindered analytical capabilities for this sample and the values reported here may be somewhat inaccurate for the hydrophobic surface. The pristine surface, however, clearly shows a much lower binding affinity. Following the final flush with water, it was impossible to confirm from this data whether the nanoparticles were removed from the sensor surface. Based on these observations, it is reasonable to conclude that the presence of Pluronic improves the binding capability of the particles.

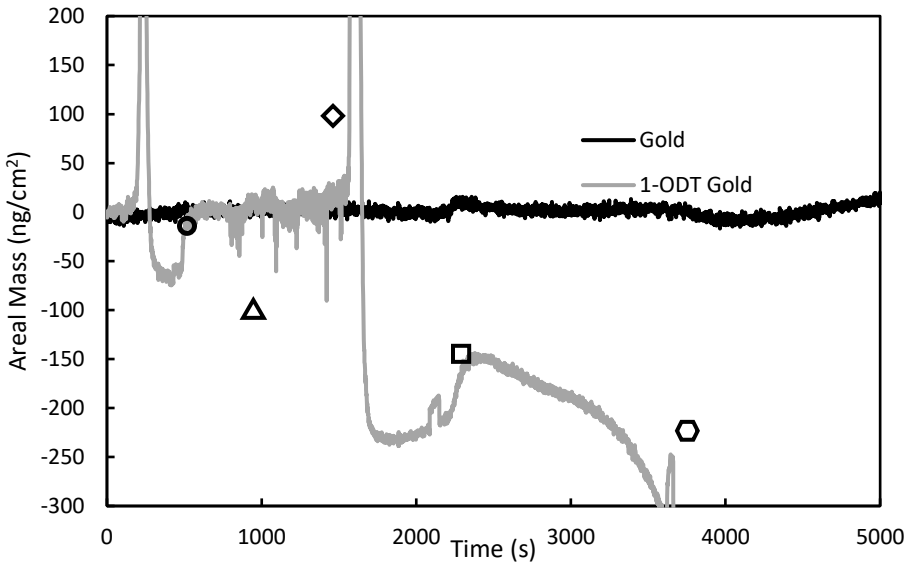

Figure D-3. Quartz Crystal Microbalance data for oleic acid-coated nanoparticle binding (no pluronic coating) at room temperature to two different sensors: unmodified gold (**black**) and gold modified with 1-octadecanethiol (1-ODT; **grey**), a hydrophobic material. The various symbols indicate different stages of the QCM experiment: ○ 0.02 mol/L 1-ODT in ethanol is injected into one of the QCM cells, △ ethanol is injected in to wash out any excess 1-ODT, ◇ water is injected to replace ethanol, □ oleic acid-coated nanoparticles suspended in water (~500 mg/L) are injected into each cell, ⬡ water is injected into each cell. Results clearly demonstrate that nanoparticles preferentially attach to the hydrophobic surface as evidenced by the step increase in areal mass in the grey line at ~2300 s, however the areal mass change observed is not as great as for Pluronic-coated nanoparticles. Note the irregular downward drift in the areal mass signal which is attributed to instrument error.

As a final experiment, binding of free Pluronic block co-polymer in aqueous solution to the QCM sensors was investigated. This was done to predict the effect that free Pluronic might have on nanoparticle binding as well as observe any differences between Pluronic versus Pluronic-NP binding behaviour. The results of Pluronic binding are shown in **Figure D-4**.

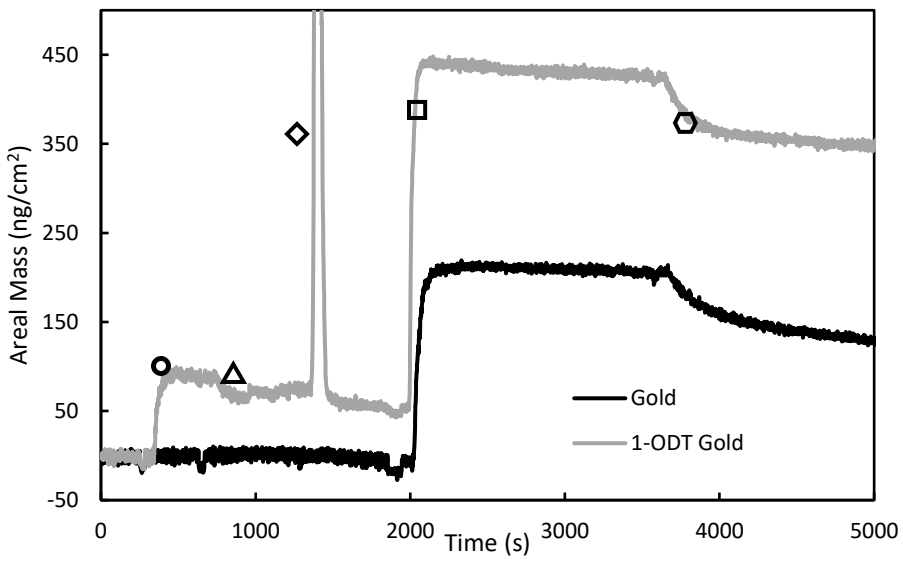

Figure D-4. Quartz Crystal Microbalance data for Pluronic binding at room temperature to two different sensors: unmodified gold (**black**) and gold modified with 1-octadecanethiol (1-ODT; **grey**), a hydrophobic material. The various symbols indicate different stages of the QCM experiment: ○ 0.02 mol/L 1-ODT in ethanol is injected into one of the QCM cells, △ ethanol is injected in to wash out any excess 1-ODT, ◇ water is injected to replace ethanol, □ Pluronic-coated nanoparticles suspended in water (~500 mg/L) are injected into each cell, ⬡ water is injected into each cell. Results clearly demonstrate that Pluronic preferentially attaches to the hydrophobic surface as evidenced by the step increase in areal mass in the grey line at 2000 s. Notably, the areal mass increase for Pluronic on unmodified gold exceeds the attachment

Pluronic was found to bind preferentially to the hydrophobized surface, an expected result given prior literature investigating Pluronic attachment to hydrophobic surfaces[282]. It was found that the magnitude of areal mass change for Pluronic exceeded that observed for Pluronic-NP, with 177.7 ng/cm^2 adsorbed to the pristine gold surface and 382.4 ng/cm^2 adsorbed to the hydrophobic gold surface. This is possibly due to multi-layer adsorption of Pluronic on the gold surface compared with nanoparticle adsorption, which is expected to be Langmuirian in nature. Notably for this sample, upon flushing with water at ~4000 s, the majority of the Pluronic remains adsorbed to the surface of the sensor, a significant difference from the Pluronic-NP samples. Based on this observation, it appears that the amount of free Pluronic present in the nanoparticle samples is minimal, otherwise it would be expected that residual areal mass would remain on the sensor after flushing with water. Based on this, it should not be expected that Pluronic will significantly compete for binding during a nanoparticle transport and binding experiment when using nanoparticles as prepared in this work.

D.4 Conclusions and Next Steps

Based on the QCM experiments shown here, two significant conclusions can be made about the binding behaviour of Pluronic-coated nanoparticles. First, the presence of the Pluronic coating is critical to the binding behaviour of the particle. In previous chapters 3 and 5, it was speculated based on the literature that Pluronic provided disruption to the anionic oleic acid bilayer which forms around the particle when coated solely with oleic acid, leading to increased hydrophobic forces, and this theory also supports the QCM data shown here. Second, based on the QCM binding profiles for Pluronic-NP and Pluronic polymer, it appears that the concentration of free Pluronic present in the NP samples is minimal and should not produce any interference with transport and binding experiments. Finally, based on experimental observation, it appears that the adsorption of Pluronic-NP to both the hydrophobic and pristine gold surfaces was rapid, and thus this process is likely diffusion limited, rather than adsorption-rate limited. It should be noted that the crude oil used in the remainder of this work does not necessarily behave as a single thin layer, and over time the surface may change, leading to more complicated adsorption behaviour.

Recommended next steps for QCM experimentation are to repeat Pluronic-coated nanoparticle binding experiments at increased temperatures in order to confirm the type of influence temperature has on nanoparticle binding, whether it is a further increase in areal mass, or an observed binding rate increase. Based on this information, it may be possible to determine the nature of nanoparticle binding based on calculated binding energy.

Bibliography

(1) Ivshina, I. B.; Kuyukina, M. S.; Krivoruchko, A. V.; Elkin, A. A.; Makarov, S. O.; Cunningham, C. J.; Peshkur, T. A.; Atlas, R. M.; Philp, J. C. Oil Spill Problems and Sustainable Response Strategies through New Technologies. *Environ. Sci.: Processes Impacts* **2015**, *17* (7), 1201–1219. https://doi.org/10.1039/C5EM00070J.

(2) Canada-Wide Standard for Petroleum Hydrocarbons in Soil 2014 Progress Report PN 1516 - PN 1516_PHC CWS 2014 Progress Rpt 1.0_e.pdf http://www.ccme.ca/files/Resources/csm/phc_cws/PN%201516_PHC%20CWS%202014%20Progress%20Rpt%201.0_e.pdf (accessed Feb 12, 2016).

(3) Franco, I.; Contin, M.; Bragato, G.; De Nobili, M. Microbiological Resilience of Soils Contaminated with Crude Oil. *Geoderma* **2004**, *121* (1–2), 17–30. https://doi.org/10.1016/j.geoderma.2003.10.002.

(4) Erdogan, E. (Eraydin); Karaca, A. Bioremediation of Crude Oil Polluted Soils. *Asian Journal of Biotechnology* **2011**, *3* (3), 206–213. https://doi.org/10.3923/ajbkr.2011.206.213.

(5) Yavari, S.; Malakahmad, A.; Sapari, N. B. A Review on Phytoremediation of Crude Oil Spills. *Water Air Soil Pollut* **2015**, *226* (8), 1–18. https://doi.org/10.1007/s11270-015-2550-z.

(6) Gomes, H. I.; Dias-Ferreira, C.; Ribeiro, A. B. Overview of in Situ and Ex Situ Remediation Technologies for PCB-Contaminated Soils and Sediments and Obstacles for Full-Scale Application. *Science of The Total Environment* **2013**, *445–446*, 237–260. https://doi.org/10.1016/j.scitotenv.2012.11.098.

(7) CHAPTER 6 OF THE CONTAMINATED SEDIMENT REMEDIATION GUIDANCE FOR HAZARDOUS WASTE SITES: DREDGING AND EXCAVATION - 174460.pdf https://semspub.epa.gov/work/11/174460.pdf (accessed Feb 16, 2016).

(8) Agarwal, S.; Al-Abed, S. R.; Dionysiou, D. D. In Situ Technologies for Reclamation of PCB-Contaminated Sediments: Current Challenges and Research Thrust Areas. *Journal of Environmental Engineering* **2007**, *133* (12), 1075–1078. https://doi.org/10.1061/(ASCE)0733-9372(2007)133:12(1075).

(9) Agarwal, A.; Liu, Y. Remediation Technologies for Oil-Contaminated Sediments. *Marine Pollution Bulletin* **2015**, *101* (2), 483–490. https://doi.org/10.1016/j.marpolbul.2015.09.010.

(10) Chien, Y.-C. Field Study of in Situ Remediation of Petroleum Hydrocarbon Contaminated Soil on Site Using Microwave Energy. *Journal of Hazardous Materials* **2012**, *199–200*, 457–461. https://doi.org/10.1016/j.jhazmat.2011.11.012.

(11) Do, S.-H.; Kwon, Y.-J.; Kong, S.-H. Effect of Metal Oxides on the Reactivity of Persulfate/Fe(II) in the Remediation of Diesel-Contaminated Soil and Sand. *Journal of Hazardous Materials* **2010**, *182* (1–3), 933–936. https://doi.org/10.1016/j.jhazmat.2010.06.068.

(12) Zhou, H.; Hu, L.; Wan, J.; Yang, R.; Yu, X.; Li, H.; Chen, J.; Wang, L.; Lu, X. Microwave-Enhanced Catalytic Degradation of p-Nitrophenol in Soil Using MgFe2O4. *Chemical Engineering Journal* **2016**, *284*, 54–60. https://doi.org/10.1016/j.cej.2015.08.103.

(13) Li, X.; Elliott, D. W.; Zhang, W. Zero-Valent Iron Nanoparticles for Abatement of Environmental Pollutants: Materials and Engineering Aspects. *Critical Reviews in Solid State and Materials Sciences* **2006**, *31* (4), 111–122. https://doi.org/10.1080/10408430601057611.

(14) Cantrell, K. J.; Kaplan, D. I.; Wietsma, T. W. Zero-Valent Iron for the in Situ Remediation of Selected Metals in Groundwater. *Journal of Hazardous Materials* **1995**, *42* (2), 201–212. https://doi.org/10.1016/0304-3894(95)00016-N.

(15) Gillham, R. W.; O'Hannesin, S. F. Enhanced Degradation of Halogenated Aliphatics by Zero-Valent Iron. *Groundwater* **1994**, *32* (6), 958–967. https://doi.org/10.1111/j.1745-6584.1994.tb00935.x.

(16) Morkin, M.; Devlin, J. F.; Barker, J. F.; Butler, B. J. In Situ Sequential Treatment of a Mixed Contaminant Plume. *Journal of Contaminant Hydrology* **2000**, *45* (3), 283–302. https://doi.org/10.1016/S0169-7722(00)00111-X.

(17) Han, Y.; Yan, W. Reductive Dechlorination of Trichloroethene by Zero-Valent Iron Nanoparticles: Reactivity Enhancement through Sulfidation Treatment. *Environ. Sci. Technol.* **2016**, *50* (23), 12992–13001. https://doi.org/10.1021/acs.est.6b03997.
(18) Kang, Y.-G.; Yoon, H.; Lee, W.; Kim, E.; Chang, Y.-S. Comparative Study of Peroxide Oxidants Activated by NZVI: Removal of 1,4-Dioxane and Arsenic(III) in Contaminated Waters. *Chemical Engineering Journal* **2018**, *334*, 2511–2519. https://doi.org/10.1016/j.cej.2017.11.076.
(19) Al-Shamsi, M. A.; Thomson, N. R. Treatment of Organic Compounds by Activated Persulfate Using Nanoscale Zerovalent Iron. *Industrial & Engineering Chemistry Research* **2013**, *52* (38), 13564–13571. https://doi.org/10.1021/ie400387p.
(20) Al-Shamsi, M. A.; Thomson, N. R. Treatment of a Trichloroethylene Source Zone Using Persulfate Activated by an Emplaced Nano-Pd–Fe<Superscript>0</Superscript> Zone. *Water Air Soil Pollut* **2013**, *224* (11), 1780. https://doi.org/10.1007/s11270-013-1780-1.
(21) Liang, C.; Wang, Z.-S.; Bruell, C. J. Influence of PH on Persulfate Oxidation of TCE at Ambient Temperatures. *Chemosphere* **2007**, *66* (1), 106–113. https://doi.org/10.1016/j.chemosphere.2006.05.026.
(22) Wu, S.; He, H.; Li, X.; Yang, C.; Zeng, G.; Wu, B.; He, S.; Lu, L. Insights into Atrazine Degradation by Persulfate Activation Using Composite of Nanoscale Zero-Valent Iron and Graphene: Performances and Mechanisms. *Chemical Engineering Journal* **2018**, *341*, 126–136. https://doi.org/10.1016/j.cej.2018.01.136.
(23) Song, Y.; Fang, G.; Zhu, C.; Zhu, F.; Wu, S.; Chen, N.; Wu, T.; Wang, Y.; Gao, J.; Zhou, D. Zero-Valent Iron Activated Persulfate Remediation of Polycyclic Aromatic Hydrocarbon-Contaminated Soils: An in Situ Pilot-Scale Study. *Chemical Engineering Journal* **2019**, *355*, 65–75. https://doi.org/10.1016/j.cej.2018.08.126.
(24) Dong, H.; He, Q.; Zeng, G.; Tang, L.; Zhang, L.; Xie, Y.; Zeng, Y.; Zhao, F. Degradation of Trichloroethene by Nanoscale Zero-Valent Iron (NZVI) and NZVI Activated Persulfate in the Absence and Presence of EDTA. *Chemical Engineering Journal* **2017**, *316*, 410–418. https://doi.org/10.1016/j.cej.2017.01.118.
(25) Mu, Y.; Jia, F.; Ai, Z.; Zhang, L. Iron Oxide Shell Mediated Environmental Remediation Properties of Nano Zero-Valent Iron. *Environmental Science: Nano* **2017**, *4* (1), 27–45. https://doi.org/10.1039/C6EN00398B.
(26) Crane, R. A.; Scott, T. B. Nanoscale Zero-Valent Iron: Future Prospects for an Emerging Water Treatment Technology. *Journal of Hazardous Materials* **2012**, *211–212*, 112–125. https://doi.org/10.1016/j.jhazmat.2011.11.073.
(27) Tang, C.; Huang, Y. H.; Zeng, H.; Zhang, Z. Reductive Removal of Selenate by Zero-Valent Iron: The Roles of Aqueous Fe2+ and Corrosion Products, and Selenate Removal Mechanisms. *Water Research* **2014**, *67*, 166–174. https://doi.org/10.1016/j.watres.2014.09.016.
(28) Gheju, M. Hexavalent Chromium Reduction with Zero-Valent Iron (ZVI) in Aquatic Systems. *Water Air Soil Pollut* **2011**, *222* (1), 103–148. https://doi.org/10.1007/s11270-011-0812-y.
(29) Tuček, J.; Prucek, R.; Kolařík, J.; Zoppellaro, G.; Petr, M.; Filip, J.; Sharma, V. K.; Zbořil, R. Zero-Valent Iron Nanoparticles Reduce Arsenites and Arsenates to As(0) Firmly Embedded in Core–Shell Superstructure: Challenging Strategy of Arsenic Treatment under Anoxic Conditions. *ACS Sustainable Chemistry & Engineering* **2017**, *5* (4), 3027–3038. https://doi.org/10.1021/acssuschemeng.6b02698.
(30) Gu, M.; Sui, Q.; Farooq, U.; Zhang, X.; Qiu, Z.; Lyu, S. Degradation of Phenanthrene in Sulfate Radical Based Oxidative Environment by NZVI-PDA Functionalized RGO Catalyst. *Chemical Engineering Journal* **2018**, *354*, 541–552. https://doi.org/10.1016/j.cej.2018.08.039.
(31) Gu, M.; Sui, Q.; Farooq, U.; Zhang, X.; Qiu, Z.; Lyu, S. Enhanced Degradation of Trichloroethylene in Oxidative Environment by NZVI/PDA Functionalized RGO Catalyst. *Journal of Hazardous Materials* **2018**, *359*, 157–165. https://doi.org/10.1016/j.jhazmat.2018.07.013.

(32) Zhu, K.; Chen, C.; Xu, M.; Chen, K.; Tan, X.; Wakeel, M.; Alharbi, N. S. In Situ Carbothermal Reduction Synthesis of Fe Nanocrystals Embedded into N-Doped Carbon Nanospheres for Highly Efficient U(VI) Adsorption and Reduction. *Chemical Engineering Journal* **2018**, *331*, 395–405. https://doi.org/10.1016/j.cej.2017.08.126.

(33) Ahmed, M. B.; Zhou, J. L.; Ngo, H. H.; Guo, W.; Johir, M. A. H.; Sornalingam, K.; Belhaj, D.; Kallel, M. Nano-Fe 0 Immobilized onto Functionalized Biochar Gaining Excellent Stability during Sorption and Reduction of Chloramphenicol via Transforming to Reusable Magnetic Composite. *Chemical Engineering Journal* **2017**, *322*, 571–581. https://doi.org/10.1016/j.cej.2017.04.063.

(34) Yi, Y.; Wu, J.; Wei, Y.; Fang, Z.; Tsang, E. P. The Key Role of Biochar in the Rapid Removal of Decabromodiphenyl Ether from Aqueous Solution by Biochar-Supported Ni/Fe Bimetallic Nanoparticles. *Journal of Nanoparticle Research* **2017**, *19* (7). https://doi.org/10.1007/s11051-017-3927-2.

(35) Jiang, X.; Guo, Y.; Zhang, L.; Jiang, W.; Xie, R. Catalytic Degradation of Tetracycline Hydrochloride by Persulfate Activated with Nano Fe0 Immobilized Mesoporous Carbon. *Chemical Engineering Journal* **2018**, *341*, 392–401. https://doi.org/10.1016/j.cej.2018.02.034.

(36) Cohen, M.; Weisbrod, N. Field Scale Mobility and Transport Manipulation of Carbon-Supported Nanoscale Zerovalent Iron in Fractured Media. *Environ. Sci. Technol.* **2018**, *52* (14), 7849–7858. https://doi.org/10.1021/acs.est.8b01226.

(37) Su, H.; Fang, Z.; Tsang, P. E.; Fang, J.; Zhao, D. Stabilisation of Nanoscale Zero-Valent Iron with Biochar for Enhanced Transport and in-Situ Remediation of Hexavalent Chromium in Soil. *Environmental Pollution* **2016**, *214*, 94–100. https://doi.org/10.1016/j.envpol.2016.03.072.

(38) Xu, J.; Dozier, A.; Bhattacharyya, D. Synthesis of Nanoscale Bimetallic Particles in Polyelectrolyte Membrane Matrix for Reductive Transformation of Halogenated Organic Compounds. *J Nanopart Res* **2005**, *7* (4), 449–467. https://doi.org/10.1007/s11051-005-4273-3.

(39) Zhu, B.-W.; Lim, T.-T.; Feng, J. Reductive Dechlorination of 1,2,4-Trichlorobenzene with Palladized Nanoscale Fe0 Particles Supported on Chitosan and Silica. *Chemosphere* **2006**, *65* (7), 1137–1145. https://doi.org/10.1016/j.chemosphere.2006.04.012.

(40) Kumar, M. A.; Bae, S.; Han, S.; Chang, Y.; Lee, W. Reductive Dechlorination of Trichloroethylene by Polyvinylpyrrolidone Stabilized Nanoscale Zerovalent Iron Particles with Ni. *Journal of Hazardous Materials* **2017**, *340*, 399–406. https://doi.org/10.1016/j.jhazmat.2017.07.030.

(41) Kim, E.-J.; Kim, J.-H.; Azad, A.-M.; Chang, Y.-S. Facile Synthesis and Characterization of Fe/FeS Nanoparticles for Environmental Applications. *ACS Appl. Mater. Interfaces* **2011**, *3* (5), 1457–1462. https://doi.org/10.1021/am200016v.

(42) Su, Y.; Adeleye, A. S.; Keller, A. A.; Huang, Y.; Dai, C.; Zhou, X.; Zhang, Y. Magnetic Sulfide-Modified Nanoscale Zerovalent Iron (S-NZVI) for Dissolved Metal Ion Removal. *Water Research* **2015**, *74*, 47–57. https://doi.org/10.1016/j.watres.2015.02.004.

(43) Su, Y.; Jassby, D.; Song, S.; Zhou, X.; Zhao, H.; Filip, J.; Petala, E.; Zhang, Y. Enhanced Oxidative and Adsorptive Removal of Diclofenac in Heterogeneous Fenton-like Reaction with Sulfide Modified Nanoscale Zerovalent Iron. *Environmental Science & Technology* **2018**, *52* (11), 6466–6475. https://doi.org/10.1021/acs.est.8b00231.

(44) Fan, D.; O'Brien Johnson, G.; Tratnyek, P. G.; Johnson, R. L. Sulfidation of Nano Zerovalent Iron (NZVI) for Improved Selectivity During In-Situ Chemical Reduction (ISCR). *Environmental Science & Technology* **2016**, *50* (17), 9558–9565. https://doi.org/10.1021/acs.est.6b02170.

(45) He, F.; Li, Z.; Shi, S.; Xu, W.; Sheng, H.; Gu, Y.; Jiang, Y.; Xi, B. Dechlorination of Excess Trichloroethene by Bimetallic and Sulfidated Nanoscale Zero-Valent Iron. *Environmental Science & Technology* **2018**, *52* (15), 8627–8637. https://doi.org/10.1021/acs.est.8b01735.

(46) Bhattacharjee, S.; Ghoshal, S. Optimal Design of Sulfidated Nanoscale Zerovalent Iron for Enhanced Trichloroethene Degradation. *Environmental Science & Technology* **2018**, *52* (19), 11078–11086. https://doi.org/10.1021/acs.est.8b02399.
(47) Phenrat, T.; Saleh, N.; Sirk, K.; Tilton, R. D.; Lowry, G. V. Aggregation and Sedimentation of Aqueous Nanoscale Zerovalent Iron Dispersions. *Environ. Sci. Technol.* **2007**, *41* (1), 284–290. https://doi.org/10.1021/es061349a.
(48) Schrick, B.; Hydutsky, B. W.; Blough, J. L.; Mallouk, T. E. Delivery Vehicles for Zerovalent Metal Nanoparticles in Soil and Groundwater. *Chem. Mater.* **2004**, *16* (11), 2187–2193. https://doi.org/10.1021/cm0218108.
(49) Mondal, P. K.; Furbacher, P. D.; Cui, Z.; Krol, M. M.; Sleep, B. E. Transport of Polymer Stabilized Nano-Scale Zero-Valent Iron in Porous Media. *Journal of Contaminant Hydrology* **2018**, *212*, 65–77. https://doi.org/10.1016/j.jconhyd.2017.11.004.
(50) Kumar, N.; Labille, J.; Bossa, N.; Auffan, M.; Doumenq, P.; Rose, J.; Bottero, J.-Y. Enhanced Transportability of Zero Valent Iron Nanoparticles in Aquifer Sediments: Surface Modifications, Reactivity, and Particle Traveling Distances. *Environ Sci Pollut Res* **2017**, *24* (10), 9269–9277. https://doi.org/10.1007/s11356-017-8597-1.
(51) Liu, J.; Liu, A.; Zhang, W. The Influence of Polyelectrolyte Modification on Nanoscale Zero-Valent Iron (NZVI): Aggregation, Sedimentation, and Reactivity with Ni(II) in Water. *Chemical Engineering Journal* **2016**, *303*, 268–274. https://doi.org/10.1016/j.cej.2016.05.132.
(52) He, F.; Zhao, D.; Liu, J.; Roberts, C. B. Stabilization of Fe−Pd Nanoparticles with Sodium Carboxymethyl Cellulose for Enhanced Transport and Dechlorination of Trichloroethylene in Soil and Groundwater. *Ind. Eng. Chem. Res.* **2007**, *46* (1), 29–34. https://doi.org/10.1021/ie0610896.
(53) Laumann, S.; Micić, V.; Hofmann, T. Mobility Enhancement of Nanoscale Zero-Valent Iron in Carbonate Porous Media through Co-Injection of Polyelectrolytes. *Water Research* **2014**, *50*, 70–79. https://doi.org/10.1016/j.watres.2013.11.040.
(54) Kim, H.-J.; Phenrat, T.; Tilton, R. D.; Lowry, G. V. Fe0 Nanoparticles Remain Mobile in Porous Media after Aging Due to Slow Desorption of Polymeric Surface Modifiers. *Environ. Sci. Technol.* **2009**, *43* (10), 3824–3830. https://doi.org/10.1021/es802978s.
(55) Xin, J.; Tang, F.; Zheng, X.; Shao, H.; Kolditz, O. Transport and Retention of Xanthan Gum-Stabilized Microscale Zero-Valent Iron Particles in Saturated Porous Media. *Water Research* **2016**, *88*, 199–206. https://doi.org/10.1016/j.watres.2015.10.005.
(56) Comba, S.; Dalmazzo, D.; Santagata, E.; Sethi, R. Rheological Characterization of Xanthan Suspensions of Nanoscale Iron for Injection in Porous Media. *Journal of Hazardous Materials* **2011**, *185* (2), 598–605. https://doi.org/10.1016/j.jhazmat.2010.09.060.
(57) López-Cruz, A.; López, G. E. Formation of an Iron Oxide Bond in Iron Carboxylate Complexes: A Density Functional Theory Study. *Molecular Physics* **2009**, *107* (17), 1799–1804. https://doi.org/10.1080/00268970903078567.
(58) Lu, H.; Wen, C.; Gao, S.; Dong, Y.; Zhang, M.; Li, B.; Hu, W.; Dong, J. Incorporation of Nanoscale Zero-Valent Iron Particles in Monodisperse Mesoporous Silica Nanospheres: Characterization, Reactivity, Transport in Porous Media. *Colloids and Surfaces A: Physicochemical and Engineering Aspects* **2018**, *553*, 28–34. https://doi.org/10.1016/j.colsurfa.2018.05.038.
(59) Doong, R.; Saha, S.; Lee, C.; Lin, H. Mesoporous Silica Supported Bimetallic Pd/Fe for Enhanced Dechlorination of Tetrachloroethylene. *RSC Adv.* **2015**, *5* (110), 90797–90805. https://doi.org/10.1039/C5RA15070A.
(60) Yang, Z.; Qiu, X.; Fang, Z.; Pokeung, T. Transport of Nano Zero-Valent Iron Supported by Mesoporous Silica Microspheres in Porous Media. *Water Science & Technology* **2015**, *71* (12), 1800. https://doi.org/10.2166/wst.2015.158.
(61) Lv, X.; Zhang, Y.; Fu, W.; Cao, J.; Zhang, J.; Ma, H.; Jiang, G. Zero-Valent Iron Nanoparticles Embedded into Reduced Graphene Oxide-Alginate Beads for Efficient Chromium (VI) Removal.

Journal of Colloid and Interface Science **2017**, *506*, 633–643. https://doi.org/10.1016/j.jcis.2017.07.024.

(62) HonetschlÄgerová, L.; Janouškovcová, P.; Kubal, M. Enhanced Transport of Si-Coated Nanoscale Zero-Valent Iron Particles in Porous Media. *Environmental Technology* **2016**, *37* (12), 1530–1538. https://doi.org/10.1080/09593330.2015.1120784.

(63) Karn, B.; Kuiken, T.; Otto, M. Nanotechnology and in Situ Remediation: A Review of the Benefits and Potential Risks. *Environmental Health Perspectives* **2009**, *117* (12), 1823–1831.

(64) Xue, W.; Huang, D.; Zeng, G.; Wan, J.; Cheng, M.; Zhang, C.; Hu, C.; Li, J. Performance and Toxicity Assessment of Nanoscale Zero Valent Iron Particles in the Remediation of Contaminated Soil: A Review. *Chemosphere* **2018**, *210*, 1145–1156. https://doi.org/10.1016/j.chemosphere.2018.07.118.

(65) Lei, C.; Sun, Y.; Tsang, D. C. W.; Lin, D. Environmental Transformations and Ecological Effects of Iron-Based Nanoparticles. *Environmental Pollution* **2018**, *232*, 10–30. https://doi.org/10.1016/j.envpol.2017.09.052.

(66) Louie, S. M.; Tilton, R. D.; Lowry, G. V. Critical Review: Impacts of Macromolecular Coatings on Critical Physicochemical Processes Controlling Environmental Fate of Nanomaterials. *Environ. Sci.: Nano* **2016**, *3* (2), 283–310. https://doi.org/10.1039/C5EN00104H.

(67) Saleh, N.; Sirk, K.; Liu, Y.; Phenrat, T.; Dufour, B.; Matyjaszewski, K.; Tilton, R. D.; Lowry, G. V. Surface Modifications Enhance Nanoiron Transport and NAPL Targeting in Saturated Porous Media. *Environmental Engineering Science* **2006**, *24* (1), 45–57. https://doi.org/10.1089/ees.2007.24.45.

(68) Saleh, N.; Phenrat, T.; Sirk, K.; Dufour, B.; Ok, J.; Sarbu, T.; Matyjaszewski, K.; Tilton, R. D.; Lowry, G. V. Adsorbed Triblock Copolymers Deliver Reactive Iron Nanoparticles to the Oil/Water Interface. *Nano Lett.* **2005**, *5* (12), 2489–2494. https://doi.org/10.1021/nl0518268.

(69) Song, J. E.; Phenrat, T.; Marinakos, S.; Xiao, Y.; Liu, J.; Wiesner, M. R.; Tilton, R. D.; Lowry, G. V. Hydrophobic Interactions Increase Attachment of Gum Arabic- and PVP-Coated Ag Nanoparticles to Hydrophobic Surfaces. *Environ. Sci. Technol.* **2011**, *45* (14), 5988–5995. https://doi.org/10.1021/es200547c.

(70) Phenrat, T.; Fagerlund, F.; Illangasekare, T.; Lowry, G. V.; Tilton, R. D. Polymer-Modified Fe0 Nanoparticles Target Entrapped NAPL in Two Dimensional Porous Media: Effect of Particle Concentration, NAPL Saturation, and Injection Strategy. *Environ. Sci. Technol.* **2011**, *45* (14), 6102–6109. https://doi.org/10.1021/es200577n.

(71) Linley, S.; Holmes, A.; Leshuk, T.; Nafo, W.; Thomson, N. R.; Al-Mayah, A.; McVey, K.; Sra, K.; Gu, F. X. Targeted Nanoparticle Binding & Detection in Petroleum Hydrocarbon Impacted Porous Media. *Chemosphere* **2018**. https://doi.org/10.1016/j.chemosphere.2018.10.046.

(72) Hu, Y.; Zhang, M.; Qiu, R.; Li, X. Encapsulating Nanoscale Zero-Valent Iron with a Soluble Mg(OH)2 Shell for Improved Mobility and Controlled Reactivity Release. *J. Mater. Chem. A* **2018**, *6* (6), 2517–2526. https://doi.org/10.1039/C7TA08605A.

(73) Gong, Y.; Liu, Y.; Xiong, Z.; Zhao, D. Immobilization of Mercury by Carboxymethyl Cellulose Stabilized Iron Sulfide Nanoparticles: Reaction Mechanisms and Effects of Stabilizer and Water Chemistry. *Environ. Sci. Technol.* **2014**, *48* (7), 3986–3994. https://doi.org/10.1021/es404418a.

(74) Morse, J. W.; Arakaki, T. Adsorption and Coprecipitation of Divalent Metals with Mackinawite (FeS). *Geochimica et Cosmochimica Acta* **1993**, *57* (15), 3635–3640. https://doi.org/10.1016/0016-7037(93)90145-M.

(75) Gong, Y.; Liu, Y.; Xiong, Z.; Kaback, D.; Zhao, D. Immobilization of Mercury in Field Soil and Sediment Using Carboxymethyl Cellulose Stabilized Iron Sulfide Nanoparticles. *Nanotechnology* **2012**, *23* (29), 294007. https://doi.org/10.1088/0957-4484/23/29/294007.

(76) Sun, Y.; Liu, Y.; Lou, Z.; Yang, K.; Lv, D.; Zhou, J.; Baig, S. A.; Xu, X. Enhanced Performance for Hg(II) Removal Using Biomaterial (CMC/Gelatin/Starch) Stabilized FeS Nanoparticles: Stabilization Effects and Removal Mechanism. *Chemical Engineering Journal* **2018**, *344*, 616–624. https://doi.org/10.1016/j.cej.2018.03.126.

(77) Sun, M.; Cheng, G.; Ge, X.; Chen, M.; Wang, C.; Lou, L.; Xu, X. Aqueous Hg(II) Immobilization by Chitosan Stabilized Magnetic Iron Sulfide Nanoparticles. *Science of The Total Environment* **2018**, *621*, 1074–1083. https://doi.org/10.1016/j.scitotenv.2017.10.119.
(78) Sheng, G.; Huang, C.; Chen, G.; Sheng, J.; Ren, X.; Hu, B.; Ma, J.; Wang, X.; Huang, Y.; Alsaedi, A.; et al. Adsorption and Co-Adsorption of Graphene Oxide and Ni(II) on Iron Oxides: A Spectroscopic and Microscopic Investigation. *Environmental Pollution* **2018**, *233*, 125–131. https://doi.org/10.1016/j.envpol.2017.10.047.
(79) Ghasemi, E.; Heydari, A.; Sillanpaa, M. Superparamagnetic Fe3O4@EDTA Nanoparticles as an Efficient Adsorbent for Simultaneous Removal of Ag(I), Hg(II), Mn(II), Zn(II), Pb(II) and Cd(II) from Water and Soil Environmental Samples. *Microchem J.* **2017**, *131*, 51–56. https://doi.org/10.1016/j.microc.2016.11.011.
(80) Hu, Q.; Liu, Y.; Gu, X.; Zhao, Y. Adsorption Behavior and Mechanism of Different Arsenic Species on Mesoporous MnFe2O4 Magnetic Nanoparticles. *Chemosphere* **2017**, *181*, 328–336. https://doi.org/10.1016/j.chemosphere.2017.04.049.
(81) Zhang, Y.; Yang, M.; Dou, X.-M.; He, H.; Wang, D.-S. Arsenate Adsorption on an Fe−Ce Bimetal Oxide Adsorbent: Role of Surface Properties. *Environ. Sci. Technol.* **2005**, *39* (18), 7246–7253. https://doi.org/10.1021/es050775d.
(82) Zhang, Y.; Yang, M.; Huang, X. Arsenic(V) Removal with a Ce(IV)-Doped Iron Oxide Adsorbent. *Chemosphere* **2003**, *51* (9), 945–952. https://doi.org/10.1016/S0045-6535(02)00850-0.
(83) Zhang, Y.; Dou, X.; Zhao, B.; Yang, M.; Takayama, T.; Kato, S. Removal of Arsenic by a Granular Fe–Ce Oxide Adsorbent: Fabrication Conditions and Performance. *Chemical Engineering Journal* **2010**, *162* (1), 164–170. https://doi.org/10.1016/j.cej.2010.05.021.
(84) Soo Lee, S.; Li, W.; Kim, C.; Cho, M.; J. Lafferty, B.; D. Fortner, J. Surface Functionalized Manganese Ferrite Nanocrystals for Enhanced Uranium Sorption and Separation in Water. *Journal of Materials Chemistry A* **2015**, *3* (43), 21930–21939. https://doi.org/10.1039/C5TA04406E.
(85) Lin, L.; Yan, X.; Liao, X.; Wang, Z. Migration and Arsenic Adsorption Study of Starch-Modified Fe-Ce Oxide on a Silicon-Based Micromodel Observation Platform. *Journal of Hazardous Materials* **2017**, *338*, 202–207. https://doi.org/10.1016/j.jhazmat.2017.05.027.
(86) Huong, P. T. L.; Tu, N.; Lan, H.; Thang, L. H.; Quy, N. V.; Tuan, P. A.; Dinh, N. X.; Phan, V. N.; Le, A.-T. Functional Manganese Ferrite/Graphene Oxide Nanocomposites: Effects of Graphene Oxide on the Adsorption Mechanisms of Organic MB Dye and Inorganic As(V) Ions from Aqueous Solution. *RSC Adv.* **2018**, *8* (22), 12376–12389. https://doi.org/10.1039/c8ra00270c.
(87) Kumar, S.; Nair, R. R.; Pillai, P. B.; Gupta, S. N.; Iyengar, M. a. R.; Sood, A. K. Graphene Oxide-MnFe2O4 Magnetic Nanohybrids for Efficient Removal of Lead and Arsenic from Water. *ACS Appl. Mater. Interfaces* **2014**, *6* (20), 17426–17436. https://doi.org/10.1021/am504826q.
(88) Xiang, B.; Ling, D.; Lou, H.; Gu, H. 3D Hierarchical Flower-like Nickel Ferrite/Manganese Dioxide toward Lead (II) Removal from Aqueous Water. *J. Hazard. Mater.* **2017**, *325*, 178–188. https://doi.org/10.1016/j.jhazmat.2016.11.011.
(89) Martinez-Vargas, S.; Martínez, A. I.; Hernández-Beteta, E. E.; Mijangos-Ricardez, O. F.; Vázquez-Hipólito, V.; Patiño-Carachure, C.; Hernandez-Flores, H.; López-Luna, J. Arsenic Adsorption on Cobalt and Manganese Ferrite Nanoparticles. *J Mater Sci* **2017**, *52* (11), 6205–6215. https://doi.org/10.1007/s10853-017-0852-9.
(90) Penke, Y. K.; Anantharaman, G.; Ramkumar, J.; Kar, K. K. Aluminum Substituted Cobalt Ferrite (Co-Al-Fe) Nano Adsorbent for Arsenic Adsorption in Aqueous Systems and Detailed Redox Behavior Study with XPS. *ACS Appl. Mater. Interfaces* **2017**, *9* (13), 11587–11598. https://doi.org/10.1021/acsami.6b16414.

(91) Penke, Y. K.; Anantharaman, G.; Ramkumar, J.; Kar, K. K. Aluminum Substituted Nickel Ferrite (Ni-Al-Fe): A Ternary Metal Oxide Adsorbent for Arsenic Adsorption in Aqueous Medium. *RSC Adv.* **2016**, *6* (60), 55608–55617. https://doi.org/10.1039/c6ra06332b.
(92) Hughes, D. L.; Afsar, A.; Laventine, D. M.; Shaw, E. J.; Harwood, L. M.; Hodson, M. E. Metal Removal from Soil Leachates Using DTPA-Functionalised Maghemite Nanoparticles, a Potential Soil Washing Technology. *Chemosphere* **2018**, *209*, 480–488. https://doi.org/10.1016/j.chemosphere.2018.06.121.
(93) Smedley, P. L.; Kinniburgh, D. G. A Review of the Source, Behaviour and Distribution of Arsenic in Natural Waters. *Applied Geochemistry* **2002**, *17* (5), 517–568. https://doi.org/10.1016/S0883-2927(02)00018-5.
(94) Shen, X.; Zhao, L.; Ding, Y.; Liu, B.; Zeng, H.; Zhong, L.; Li, X. Foam, a Promising Vehicle to Deliver Nanoparticles for Vadose Zone Remediation. *Journal of Hazardous Materials* **2011**, *186* (2–3), 1773–1780. https://doi.org/10.1016/j.jhazmat.2010.12.071.
(95) Ding, Y.; Liu, B.; Shen, X.; Zhong, L.; Li, X. Foam-Assisted Delivery of Nanoscale Zero Valent Iron in Porous Media. *J. Environ. Eng.* **2013**, *139* (9), 1206–1212. https://doi.org/10.1061/(ASCE)EE.1943-7870.0000727.
(96) Luna, M. Pressure-Controlled Injection of Guar Gum Stabilized Microscale Zerovalent Iron for Groundwater Remediation. *181* (Complete), 46–58.
(97) Christiansen, C. M.; Damgaard, I.; Broholm, M.; Kessler, T.; Klint, K. E.; Nilsson, B.; Bjerg, P. L. Comparison of Delivery Methods for Enhanced In Situ Remediation in Clay Till. *Ground Water Monitoring & Remediation* **2010**, *30* (4), 107–122. https://doi.org/10.1111/j.1745-6592.2010.01314.x.
(98) ShamsiJazeyi, H.; Miller, C. A.; Wong, M. S.; Tour, J. M.; Verduzco, R. Polymer-Coated Nanoparticles for Enhanced Oil Recovery. *J. Appl. Polym. Sci.* **2014**, *131* (15), n/a-n/a. https://doi.org/10.1002/app.40576.
(99) Crane, R. A.; Scott, T. B. Nanoscale Zero-Valent Iron: Future Prospects for an Emerging Water Treatment Technology. *Journal of Hazardous Materials* **2012**, *211–212*, 112–125. https://doi.org/10.1016/j.jhazmat.2011.11.073.
(100) Tosco, T.; Petrangeli Papini, M.; Cruz Viggi, C.; Sethi, R. Nanoscale Zerovalent Iron Particles for Groundwater Remediation: A Review. *Journal of Cleaner Production* **2014**, *77*, 10–21. https://doi.org/10.1016/j.jclepro.2013.12.026.
(101) Tosco, T.; Sethi, R. Transport of Non-Newtonian Suspensions of Highly Concentrated Micro- And Nanoscale Iron Particles in Porous Media: A Modeling Approach. *Environ. Sci. Technol.* **2010**, *44* (23), 9062–9068. https://doi.org/10.1021/es100868n.
(102) Tosco, T.; Sethi, R. MNM1D: A Numerical Code for Colloid Transport in Porous Media: Implementation and Validation. *American Journal of Environmental Sciences* **2009**, *5* (4), 517–525. https://doi.org/10.3844/ajessp.2009.517.525.
(103) Yao, K.-M.; Habibian, M. T.; O'Melia, C. R. Water and Waste Water Filtration. Concepts and Applications. *Environ. Sci. Technol.* **1971**, *5* (11), 1105–1112. https://doi.org/10.1021/es60058a005.
(104) Petosa, A. R.; Jaisi, D. P.; Quevedo, I. R.; Elimelech, M.; Tufenkji, N. Aggregation and Deposition of Engineered Nanomaterials in Aquatic Environments: Role of Physicochemical Interactions. *Environ. Sci. Technol.* **2010**, *44* (17), 6532–6549. https://doi.org/10.1021/es100598h.
(105) Zhulina, E. B.; Borisov, O. V.; Priamitsyn, V. A. Theory of Steric Stabilization of Colloid Dispersions by Grafted Polymers. *Journal of Colloid and Interface Science* **1990**, *137* (2), 495–511. https://doi.org/10.1016/0021-9797(90)90423-L.
(106) Yan, W.; Lien, H.-L.; Koel, B. E.; Zhang, W. Iron Nanoparticles for Environmental Clean-up: Recent Developments and Future Outlook. *Environ. Sci.: Processes Impacts* **2012**, *15* (1), 63–77. https://doi.org/10.1039/C2EM30691C.

(107) Saleh, N.; Kim, H.-J.; Phenrat, T.; Matyjaszewski, K.; Tilton, R. D.; Lowry, G. V. Ionic Strength and Composition Affect the Mobility of Surface-Modified Fe0 Nanoparticles in Water-Saturated Sand Columns. *Environ. Sci. Technol.* **2008**, *42* (9), 3349–3355. https://doi.org/10.1021/es071936b.

(108) Bagaria, H. G.; Neilson, B. M.; Worthen, A. J.; Xue, Z.; Yoon, K. Y.; Cheng, V.; Lee, J. H.; Velagala, S.; Huh, C.; Bryant, S. L.; et al. Adsorption of Iron Oxide Nanoclusters Stabilized with Sulfonated Copolymers on Silica in Concentrated NaCl and CaCl2 Brine. *Journal of Colloid and Interface Science* **2013**, *398*, 217–226. https://doi.org/10.1016/j.jcis.2013.01.056.

(109) Kim, H.-J.; Phenrat, T.; Tilton, R. D.; Lowry, G. V. Effect of Kaolinite, Silica Fines and PH on Transport of Polymer-Modified Zero Valent Iron Nano-Particles in Heterogeneous Porous Media. *Journal of Colloid and Interface Science* **2012**, *370* (1), 1–10. https://doi.org/10.1016/j.jcis.2011.12.059.

(110) Kharisov, B. I.; Dias, H. V. R.; Kharissova, O. V.; Jiménez-Pérez, V. M.; Pérez, B. O.; Flores, B. M. Iron-Containing Nanomaterials: Synthesis, Properties, and Environmental Applications. *RSC Adv.* **2012**, *2* (25), 9325–9358. https://doi.org/10.1039/C2RA20812A.

(111) Sheng-Nan, S.; Chao, W.; Zan-Zan, Z.; Yang-Long, H.; Venkatraman, S. S.; Zhi-Chuan, X. Magnetic Iron Oxide Nanoparticles: Synthesis and Surface Coating Techniques for Biomedical Applications. *Chinese Phys. B* **2014**, *23* (3), 037503. https://doi.org/10.1088/1674-1056/23/3/037503.

(112) Hua, M.; Zhang, S.; Pan, B.; Zhang, W.; Lv, L.; Zhang, Q. Heavy Metal Removal from Water/Wastewater by Nanosized Metal Oxides: A Review. *Journal of Hazardous Materials* **2012**, *211–212*, 317–331. https://doi.org/10.1016/j.jhazmat.2011.10.016.

(113) Maity, D.; Agrawal, D. C. Synthesis of Iron Oxide Nanoparticles under Oxidizing Environment and Their Stabilization in Aqueous and Non-Aqueous Media. *Journal of Magnetism and Magnetic Materials* **2007**, *308* (1), 46–55. https://doi.org/10.1016/j.jmmm.2006.05.001.

(114) Ju-Nam, Y.; Lead, J. R. Manufactured Nanoparticles: An Overview of Their Chemistry, Interactions and Potential Environmental Implications. *Sci. Total Environ.* **2008**, *400* (1–3), 396–414. https://doi.org/10.1016/j.scitotenv.2008.06.042.

(115) Xie, J.; Xu, C.; Kohler, N.; Hou, Y.; Sun, S. Controlled PEGylation of Monodisperse Fe3O4 Nanoparticles for Reduced Non-Specific Uptake by Macrophage Cells. *Adv. Mater.* **2007**, *19* (20), 3163–3166. https://doi.org/10.1002/adma.200701975.

(116) Qin, J.; Laurent, S.; Jo, Y. S.; Roch, A.; Mikhaylova, M.; Bhujwalla, Z. M.; Muller, R. N.; Muhammed, M. A High-Performance Magnetic Resonance ImagingT2 Contrast Agent. *Advanced Materials* **2007**, *19* (14), 1874–1878. https://doi.org/10.1002/adma.200602326.

(117) Dehvari, K.; Lin, K.-S.; Wang, S. S.-S. Structural Characterization and Adsorption Properties of Pluronic F127 Onto Iron Oxides Magnetic Nanoparticles. *Journal of Nanoscience and Nanotechnology* **2014**, *14* (3), 2361–2367. https://doi.org/10.1166/jnn.2014.8537.

(118) Saleh, N.; Phenrat, T.; Sirk, K.; Dufour, B.; Ok, J.; Sarbu, T.; Matyjaszewski, K.; Tilton, R. D.; Lowry, G. V. Adsorbed Triblock Copolymers Deliver Reactive Iron Nanoparticles to the Oil/Water Interface. *Nano Lett.* **2005**, *5* (12), 2489–2494. https://doi.org/10.1021/nl0518268.

(119) Saleh, N.; Sirk, K.; Liu, Y.; Phenrat, T.; Dufour, B.; Matyjaszewski, K.; Tilton, R. D.; Lowry, G. V. Surface Modifications Enhance Nanoiron Transport and NAPL Targeting in Saturated Porous Media. *Environmental Engineering Science* **2006**, *24* (1), 45–57. https://doi.org/10.1089/ees.2007.24.45.

(120) Petros, R. A.; DeSimone, J. M. Strategies in the Design of Nanoparticles for Therapeutic Applications. *Nat Rev Drug Discov* **2010**, *9* (8), 615–627. https://doi.org/10.1038/nrd2591.

(121) Ganta, S.; Devalapally, H.; Shahiwala, A.; Amiji, M. A Review of Stimuli-Responsive Nanocarriers for Drug and Gene Delivery. *Journal of Controlled Release* **2008**, *126* (3), 187–204. https://doi.org/10.1016/j.jconrel.2007.12.017.

(122) Wang, Z.; Acosta, E. Formulation Design for Target Delivery of Iron Nanoparticles to TCE Zones. *Journal of Contaminant Hydrology* **2013**, *155*, 9–19. https://doi.org/10.1016/j.jconhyd.2013.08.005.
(123) Davis, M. E.; Chen, Z. (Georgia); Shin, D. M. Nanoparticle Therapeutics: An Emerging Treatment Modality for Cancer. *Nature Reviews Drug Discovery* **2008**, *7* (9), 771–782. https://doi.org/10.1038/nrd2614.
(124) Srinivasarao, M.; Galliford, C. V.; Low, P. S. Principles in the Design of Ligand-Targeted Cancer Therapeutics and Imaging Agents. *Nature Reviews Drug Discovery* **2015**, *14* (3), 203–219. https://doi.org/10.1038/nrd4519.
(125) Gupta, A. K.; Gupta, M. Synthesis and Surface Engineering of Iron Oxide Nanoparticles for Biomedical Applications. *Biomaterials* **2005**, *26* (18), 3995–4021. https://doi.org/10.1016/j.biomaterials.2004.10.012.
(126) Rosen, J. E.; Chan, L.; Shieh, D.-B.; Gu, F. X. Iron Oxide Nanoparticles for Targeted Cancer Imaging and Diagnostics. *Nanomedicine: Nanotechnology, Biology and Medicine* **2012**, *8* (3), 275–290. https://doi.org/10.1016/j.nano.2011.08.017.
(127) Chang, K.; Li, X.; Liao, Q.; Hu, B.; Hu, J.; Sheng, G.; Linghu, W.; Huang, Y.; Asiri, A. M.; Alamry, K. A. Molecular Insights into the Role of Fulvic Acid in Cobalt Sorption onto Graphene Oxide and Reduced Graphene Oxide. *Chemical Engineering Journal* **2017**, *327*, 320–327. https://doi.org/10.1016/j.cej.2017.06.100.
(128) Hu, B.; Chen, G.; Jin, C.; Hu, J.; Huang, C.; Sheng, J.; Sheng, G.; Ma, J.; Huang, Y. Macroscopic and Spectroscopic Studies of the Enhanced Scavenging of Cr(VI) and Se(VI) from Water by Titanate Nanotube Anchored Nanoscale Zero-Valent Iron. *Journal of Hazardous Materials* **2017**, *336*, 214–221. https://doi.org/10.1016/j.jhazmat.2017.04.069.
(129) Hu, B.; Qiu, M.; Hu, Q.; Sun, Y.; Sheng, G.; Hu, J.; Ma, J. Decontamination of Sr(II) on Magnetic Polyaniline/Graphene Oxide Composites: Evidence from Experimental, Spectroscopic, and Modeling Investigation. *ACS Sustainable Chem. Eng.* **2017**, *5* (8), 6924–6931. https://doi.org/10.1021/acssuschemeng.7b01126.
(130) Linghu, W.; Yang, H.; Sun, Y.; Sheng, G.; Huang, Y. One-Pot Synthesis of LDH/GO Composites as Highly Effective Adsorbents for Decontamination of U(VI). *ACS Sustainable Chem. Eng.* **2017**, *5* (6), 5608–5616. https://doi.org/10.1021/acssuschemeng.7b01303.
(131) Chang, K.; Sun, Y.; Ye, F.; Li, X.; Sheng, G.; Zhao, D.; Linghu, W.; Li, H.; Liu, J. Macroscopic and Molecular Study of the Sorption and Co-Sorption of Graphene Oxide and Eu(III) onto Layered Double Hydroxides. *Chemical Engineering Journal* **2017**, *325*, 665–671. https://doi.org/10.1016/j.cej.2017.05.122.
(132) Hu, B.; Huang, C.; Li, X.; Sheng, G.; Li, H.; Ren, X.; Ma, J.; Wang, J.; Huang, Y. Macroscopic and Spectroscopic Insights into the Mutual Interaction of Graphene Oxide, Cu(II), and Mg/Al Layered Double Hydroxides. *Chemical Engineering Journal* **2017**, *313*, 527–534. https://doi.org/10.1016/j.cej.2016.12.102.
(133) Sheng, G.; Huang, C.; Chen, G.; Sheng, J.; Ren, X.; Hu, B.; Ma, J.; Wang, X.; Huang, Y.; Alsaedi, A.; et al. Adsorption and Co-Adsorption of Graphene Oxide and Ni(II) on Iron Oxides: A Spectroscopic and Microscopic Investigation. *Environmental Pollution* **2018**, *233*, 125–131. https://doi.org/10.1016/j.envpol.2017.10.047.
(134) Jawitz, J. W.; Annable, M. D.; Rao, P. S. C.; Rhue, R. D. Field Implementation of a Winsor Type I Surfactant/Alcohol Mixture for in Situ Solubilization of a Complex LNAPL as a Single-Phase Microemulsion. *Environmental Science & Technology* **1998**, *32* (4), 523–530. https://doi.org/10.1021/es970507i.
(135) Salanitro, J. P.; Johnson, P. C.; Spinnler, G. E.; Maner, P. M.; Wisniewski, H. L.; Bruce, C. Field-Scale Demonstration of Enhanced MTBE Bioremediation through Aquifer Bioaugmentation and Oxygenation. *Environmental Science & Technology* **2000**, *34* (19), 4152–4162. https://doi.org/10.1021/es000925e.

(136) Sra, K. S.; Thomson, N. R.; Barker, J. F. Persulfate Injection into a Gasoline Source Zone. *Journal of Contaminant Hydrology* **2013**, *150*, 35–44. https://doi.org/10.1016/j.jconhyd.2013.03.007.
(137) Kuppusamy, S.; Palanisami, T.; Megharaj, M.; Venkateswarlu, K.; Naidu, R. Ex-Situ Remediation Technologies for Environmental Pollutants: A Critical Perspective. In *Reviews of Environmental Contamination and Toxicology Volume 236*; de Voogt, P., Ed.; Springer International Publishing: Cham, 2016; Vol. 236, pp 117–192.
(138) Karn, B.; Kuiken, T.; Otto, M. Nanotechnology and in Situ Remediation: A Review of the Benefits and Potential Risks. *Environmental Health Perspectives* **2009**, *117* (12), 1823–1831.
(139) Pardo, F.; Rosas, J. M.; Santos, A.; Romero, A. Remediation of a Biodiesel Blend-Contaminated Soil with Activated Persulfate by Different Sources of Iron. *Water Air Soil Pollut* **2015**, *226* (2), 1–12. https://doi.org/10.1007/s11270-014-2267-4.
(140) Al-Shamsi, M. A.; Thomson, N. R. Treatment of Organic Compounds by Activated Persulfate Using Nanoscale Zerovalent Iron. *Industrial & Engineering Chemistry Research* **2013**, *52* (38), 13564–13571. https://doi.org/10.1021/ie400387p.
(141) Luna, M.; Gastone, F.; Tosco, T.; Sethi, R.; Velimirovic, M.; Gemoets, J.; Muyshondt, R.; Sapion, H.; Klaas, N.; Bastiaens, L. Pressure-Controlled Injection of Guar Gum Stabilized Microscale Zerovalent Iron for Groundwater Remediation. *Journal of Contaminant Hydrology* **2015**, *181*, 46–58. https://doi.org/10.1016/j.jconhyd.2015.04.007.
(142) Braun, A.; Klumpp, E.; Azzam, R.; Neukum, C. Transport and Deposition of Stabilized Engineered Silver Nanoparticles in Water Saturated Loamy Sand and Silty Loam. *Science of The Total Environment* **2015**, *535*, 102–112. https://doi.org/10.1016/j.scitotenv.2014.12.023.
(143) Su, Y.; Zhao, Y.-S.; Li, L.-L.; Qin, C.-Y. Enhanced Delivery of Nanoscale Zero-Valent Iron in Porous Media by Sodium Dodecyl Sulfate Solution and Foam. *Environmental Engineering Science* **2015**, *32* (8), 684–693. https://doi.org/10.1089/ees.2014.0529.
(144) Johnson, R. L.; Nurmi, J. T.; O'Brien Johnson, G. S.; Fan, D.; O'Brien Johnson, R. L.; Shi, Z.; Salter-Blanc, A. J.; Tratnyek, P. G.; Lowry, G. V. Field-Scale Transport and Transformation of Carboxymethylcellulose-Stabilized Nano Zero-Valent Iron. *Environ. Sci. Technol.* **2013**, *47* (3), 1573–1580. https://doi.org/10.1021/es304564q.
(145) Li, J.; Bhattacharjee, S.; Ghoshal, S. The Effects of Viscosity of Carboxymethyl Cellulose on Aggregation and Transport of Nanoscale Zerovalent Iron. *Colloids and Surfaces A: Physicochemical and Engineering Aspects* **2015**, *481*, 451–459. https://doi.org/10.1016/j.colsurfa.2015.05.023.
(146) Höss, S.; Fritzsche, A.; Meyer, C.; Bosch, J.; Meckenstock, R. U.; Totsche, K. U. Size- and Composition-Dependent Toxicity of Synthetic and Soil-Derived Fe Oxide Colloids for the Nematode *Caenorhabditis Elegans*. *Environmental Science & Technology* **2015**, *49* (1), 544–552. https://doi.org/10.1021/es503559n.
(147) Bertrand, N.; Wu, J.; Xu, X.; Kamaly, N.; Farokhzad, O. C. Cancer Nanotechnology: The Impact of Passive and Active Targeting in the Era of Modern Cancer Biology. *Advanced Drug Delivery Reviews* **2014**, *66*, 2–25. https://doi.org/10.1016/j.addr.2013.11.009.
(148) Elkhodiry, M. A.; Momah, C. C.; Suwaidi, S. R.; Gadalla, D.; Martins, A. M.; Vitor, R. F.; Husseini, G. A. Synergistic Nanomedicine: Passive, Active, and Ultrasound-Triggered Drug Delivery in Cancer Treatment. *Journal of Nanoscience and Nanotechnology* **2016**, *16* (1), 1–18. https://doi.org/10.1166/jnn.2016.11124.
(149) Singh-Joy, S. D.; McLain, V. C. Safety Assessment of Poloxamers 101, 105, 108, 122, 123, 124, 181, 182, 183, 184, 185, 188, 212, 215, 217, 231, 234, 235, 237, 238, 282, 284, 288, 331, 333, 334, 335, 338, 401, 402, 403, and 407, Poloxamer 105 Benzoate, and Poloxamer 182 Dibenzoate as Used in Cosmetics. *International Journal of Toxicology* **2016**. https://doi.org/10.1080/10915810802244595.

(150) Usman, M.; Faure, P.; Hanna, K.; Abdelmoula, M.; Ruby, C. Application of Magnetite Catalyzed Chemical Oxidation (Fenton-like and Persulfate) for the Remediation of Oil Hydrocarbon Contamination. *Fuel* **2012**, *96*, 270–276. https://doi.org/10.1016/j.fuel.2012.01.017.
(151) Chien, Y.-C. Field Study of in Situ Remediation of Petroleum Hydrocarbon Contaminated Soil on Site Using Microwave Energy. *Journal of Hazardous Materials* **2012**, *199–200*, 457–461. https://doi.org/10.1016/j.jhazmat.2011.11.012.
(152) Kharisov, B. I.; Dias, H. V. R.; Kharissova, O. V.; Jiménez-Pérez, V. M.; Pérez, B. O.; Flores, B. M. Iron-Containing Nanomaterials: Synthesis, Properties, and Environmental Applications. *RSC Adv.* **2012**, *2* (25), 9325–9358. https://doi.org/10.1039/C2RA20812A.
(153) Maehara, T.; Konishi, K.; Kamimori, T.; Aono, H.; Hirazawa, H.; Naohara, T.; Nomura, S.; Kikkawa, H.; Watanabe, Y.; Kawachi, K. Selection of Ferrite Powder for Thermal Coagulation Therapy with Alternating Magnetic Field. *J Mater Sci* **2005**, *40* (1), 135–138. https://doi.org/10.1007/s10853-005-5698-x.
(154) Zhou, H.; Hu, L.; Wan, J.; Yang, R.; Yu, X.; Li, H.; Chen, J.; Wang, L.; Lu, X. Microwave-Enhanced Catalytic Degradation of p-Nitrophenol in Soil Using MgFe2O4. *Chemical Engineering Journal* **2016**, *284*, 54–60. https://doi.org/10.1016/j.cej.2015.08.103.
(155) Zeng, G.; Zhu, Y.; Zhang, Y.; Zhang, C.; Tang, L.; Guo, P.; Zhang, L.; Yuan, Y.; Cheng, M.; Yang, C. Electrochemical DNA Sensing Strategy Based on Strengthening Electronic Conduction and a Signal Amplifier Carrier of NanoAu/MCN Composited Nanomaterials for Sensitive Lead Detection. *Environ. Sci.: Nano* **2016**, *3* (6), 1504–1509. https://doi.org/10.1039/C6EN00323K.
(156) Zhu, Y.; Zeng, G.; Zhang, Y.; Tang, L.; Chen, J.; Cheng, M.; Zhang, L.; He, L.; Guo, Y.; He, X.; et al. Highly Sensitive Electrochemical Sensor Using a MWCNTs/GNPs-Modified Electrode for Lead (II) Detection Based on Pb2+-Induced G-Rich DNA Conformation. *Analyst* **2014**, *139* (19), 5014–5020. https://doi.org/10.1039/C4AN00874J.
(157) Cnudde, V.; Masschaele, B.; Dierick, M.; Vlassenbroeck, J.; Hoorebeke, L. V.; Jacobs, P. Recent Progress in X-Ray CT as a Geosciences Tool. *Applied Geochemistry* **2006**, *21* (5), 826–832. https://doi.org/10.1016/j.apgeochem.2006.02.010.
(158) Liu, J.; Luo, X.; Wang, J.; Xiao, T.; Yin, M.; Belshaw, N. S.; Lippold, H.; Kong, L.; Xiao, E.; Bao, Z.; et al. Provenance of Uranium in a Sediment Core from a Natural Reservoir, South China: Application of Pb Stable Isotope Analysis. *Chemosphere* **2018**, *193*, 1172–1180. https://doi.org/10.1016/j.chemosphere.2017.11.131.
(159) Liu, J.; Luo, X.; Wang, J.; Xiao, T.; Chen, D.; Sheng, G.; Yin, M.; Lippold, H.; Wang, C.; Chen, Y. Thallium Contamination in Arable Soils and Vegetables around a Steel Plant—A Newly-Found Significant Source of Tl Pollution in South China. *Environmental Pollution* **2017**, *224*, 445–453. https://doi.org/10.1016/j.envpol.2017.02.025.
(160) Senesi, G. S.; Dell'Aglio, M.; Gaudiuso, R.; De Giacomo, A.; Zaccone, C.; De Pascale, O.; Miano, T. M.; Capitelli, M. Heavy Metal Concentrations in Soils as Determined by Laser-Induced Breakdown Spectroscopy (LIBS), with Special Emphasis on Chromium. *Environmental Research* **2009**, *109* (4), 413–420. https://doi.org/10.1016/j.envres.2009.02.005.
(161) Kaveh, F.; Beauchemin, D. Improvement of the Capabilities of Solid Sampling ETV-ICP-OES by Coupling ETV to a Nebulisation/Pre-Evaporation System. *Journal of Analytical Atomic Spectrometry* **2014**, *29* (8), 1371–1377. https://doi.org/10.1039/C4JA00041B.
(162) Russo, R. E.; Mao, X.; Liu, H.; Gonzalez, J.; Mao, S. S. Laser Ablation in Analytical Chemistry—a Review. *Talanta* **2002**, *57* (3), 425–451. https://doi.org/10.1016/S0039-9140(02)00053-X.
(163) Chan, T.; Gu, F. Development of a Colorimetric, Superparamagnetic Biosensor for the Capture and Detection of Biomolecules. *Biosensors and Bioelectronics* **2013**, *42*, 12–16. https://doi.org/10.1016/j.bios.2012.10.008.
(164) Cui, L.; Xu, H.; He, P.; Sumitomo, K.; Yamaguchi, Y.; Gu, H. Developing a Hybrid Emulsion Polymerization System to Synthesize Fe3O4/Polystyrene Latexes with Narrow Size Distribution

and High Magnetite Content. *J. Polym. Sci. A Polym. Chem.* **2007**, *45* (22), 5285–5295. https://doi.org/10.1002/pola.22273.
(165) Xu, H.; Cui, L.; Tong, N.; Gu, H. Development of High Magnetization Fe3O4/Polystyrene/Silica Nanospheres via Combined Miniemulsion/Emulsion Polymerization. *J. Am. Chem. Soc.* **2006**, *128* (49), 15582–15583. https://doi.org/10.1021/ja066165a.
(166) Wilson, D.; Langell, M. A. XPS Analysis of Oleylamine/Oleic Acid Capped Fe3O4 Nanoparticles as a Function of Temperature. *Applied Surface Science* **2014**, *303* (Supplement C), 6–13. https://doi.org/10.1016/j.apsusc.2014.02.006.
(167) Lin, J.-J.; Chen, J.-S.; Huang, S.-J.; Ko, J.-H.; Wang, Y.-M.; Chen, T.-L.; Wang, L.-F. Folic Acid–Pluronic F127 Magnetic Nanoparticle Clusters for Combined Targeting, Diagnosis, and Therapy Applications. *Biomaterials* **2009**, *30* (28), 5114–5124. https://doi.org/10.1016/j.biomaterials.2009.06.004.
(168) Landfester, K. Recent Developments in Miniemulsions ― Formation and Stability Mechanisms. *Macromol. Symp.* **2000**, *150* (1), 171–178. https://doi.org/10.1002/1521-3900(200002)150:1<171::AID-MASY171>3.0.CO;2-D.
(169) Brandani, P.; Stroeve, P. Adsorption and Desorption of PEO−PPO−PEO Triblock Copolymers on a Self-Assembled Hydrophobic Surface. *Macromolecules* **2003**, *36* (25), 9492–9501. https://doi.org/10.1021/ma0342675.
(170) Hotze, E. M.; Louie, S. M.; Lin, S.; Wiesner, M. R.; Lowry, G. V. Nanoparticle Core Properties Affect Attachment of Macromolecule-Coated Nanoparticles to Silica Surfaces. *Environmental Chemistry* **2014**, *11* (3), 257. https://doi.org/10.1071/EN13191.
(171) Addai-Mensah, J. Enhanced Flocculation and Dewatering of Clay Mineral Dispersions. *Powder Technology* **2007**, *179* (1–2), 73–78. https://doi.org/10.1016/j.powtec.2006.11.008.
(172) Jain, T. K.; Foy, S. P.; Erokwu, B.; Dimitrijevic, S.; Flask, C. A.; Labhasetwar, V. Magnetic Resonance Imaging of Multifunctional Pluronic Stabilized Iron-Oxide Nanoparticles in Tumor-Bearing Mice. *Biomaterials* **2009**, *30* (35), 6748–6756. https://doi.org/10.1016/j.biomaterials.2009.08.042.
(173) Feldkamp, L. A.; Davis, L. C.; Kress, J. W. Practical Cone-Beam Algorithm. *J. Opt. Soc. Am.* **1984**, *1* (6), 612–619. https://doi.org/10.1364/JOSAA.1.000612.
(174) Gusenbauer, C.; Reiter, M.; Kastner, J.; Kloesch, G. Detection of Non-Metallic Inclusions in Quenched and Tempered Steel Bars by XCT and after Fatigue Life Testing. *Steel Research Int.* **2016**, *87* (3), 386–393. https://doi.org/10.1002/srin.201500083.
(175) Louie, S. M.; Tilton, R. D.; Lowry, G. V. Critical Review: Impacts of Macromolecular Coatings on Critical Physicochemical Processes Controlling Environmental Fate of Nanomaterials. *Environ. Sci.: Nano* **2016**, *3* (2), 283–310. https://doi.org/10.1039/C5EN00104H.
(176) Li, Q.; Chen, X.; Zhuang, J.; Chen, X. Decontaminating Soil Organic Pollutants with Manufactured Nanoparticles. *Environ Sci Pollut Res* **2016**, *23* (12), 11533–11548. https://doi.org/10.1007/s11356-016-6255-7.
(177) Mylon, S. E.; Sun, Q.; Waite, T. D. Process Optimization in Use of Zero Valent Iron Nanoparticles for Oxidative Transformations. *Chemosphere* **2010**, *81* (1), 127–131. https://doi.org/10.1016/j.chemosphere.2010.06.045.
(178) Lefevre, E.; Bossa, N.; Wiesner, M. R.; Gunsch, C. K. A Review of the Environmental Implications of in Situ Remediation by Nanoscale Zero Valent Iron (NZVI): Behavior, Transport and Impacts on Microbial Communities. *Science of The Total Environment* **2016**, *565*, 889–901. https://doi.org/10.1016/j.scitotenv.2016.02.003.
(179) Al-Shamsi, M. A.; Thomson, N. R. Treatment of a Trichloroethylene Source Zone Using Persulfate Activated by an Emplaced Nano-Pd–Fe<Superscript>0</Superscript> Zone. *Water Air Soil Pollut* **2013**, *224* (11), 1780. https://doi.org/10.1007/s11270-013-1780-1.
(180) Dien, N. T.; De Windt, W.; Buekens, A.; Chang, M. B. Application of Bimetallic Iron (BioCAT Slurry) for Pentachlorophenol Removal from Sandy Soil. *Journal of Hazardous Materials* **2013**, *252–253*, 83–90. https://doi.org/10.1016/j.jhazmat.2013.02.029.

(181) Al-Shamsi, M. A.; Thomson, N. R.; Forsey, S. P. Iron Based Bimetallic Nanoparticles to Activate Peroxygens. *Chemical Engineering Journal* **2013**, *232*, 555–563. https://doi.org/10.1016/j.cej.2013.07.109.
(182) Braunschweig, J.; Bosch, J.; Meckenstock, R. U. Iron Oxide Nanoparticles in Geomicrobiology: From Biogeochemistry to Bioremediation. *New Biotechnology* **2013**, *30* (6), 793–802. https://doi.org/10.1016/j.nbt.2013.03.008.
(183) Su, C. Environmental Implications and Applications of Engineered Nanoscale Magnetite and Its Hybrid Nanocomposites: A Review of Recent Literature. *Journal of Hazardous Materials* **2017**, *322*, 48–84. https://doi.org/10.1016/j.jhazmat.2016.06.060.
(184) Apul, O. G.; Delgado, A. G.; Kidd, J.; Alam, F.; Dahlen, P.; Westerhoff, P. Carbonaceous Nano-Additives Augment Microwave-Enabled Thermal Remediation of Soils Containing Petroleum Hydrocarbons. *Environ. Sci.: Nano* **2016**, *3* (5), 997–1002. https://doi.org/10.1039/C6EN00261G.
(185) Li, S.; Turaga, U.; Shrestha, B.; Anderson, T. A.; Ramkumar, S. S.; Green, M. J.; Das, S.; Cañas-Carrell, J. E. Mobility of Polyaromatic Hydrocarbons (PAHs) in Soil in the Presence of Carbon Nanotubes. *Ecotoxicology and Environmental Safety* **2013**, *96*, 168–174. https://doi.org/10.1016/j.ecoenv.2013.07.005.
(186) Zhang, L.; Wang, L.; Zhang, P.; Kan, A. T.; Chen, W.; Tomson, M. B. Facilitated Transport of 2,2′,5,5′-Polychlorinated Biphenyl and Phenanthrene by Fullerene Nanoparticles through Sandy Soil Columns. *Environ. Sci. Technol.* **2011**, *45* (4), 1341–1348. https://doi.org/10.1021/es102316m.
(187) Zhao, X.; Liu, W.; Cai, Z.; Han, B.; Qian, T.; Zhao, D. An Overview of Preparation and Applications of Stabilized Zero-Valent Iron Nanoparticles for Soil and Groundwater Remediation. *Water Research* **2016**, *100*, 245–266. https://doi.org/10.1016/j.watres.2016.05.019.
(188) Bossa, N.; Carpenter, A. W.; Kumar, N.; Lannoy, C.-F. de; Wiesner, M. Cellulose Nanocrystal Zero-Valent Iron Nanocomposites for Groundwater Remediation. *Environ. Sci.: Nano* **2017**, *4* (6), 1294–1303. https://doi.org/10.1039/C6EN00572A.
(189) Bishop, E. J.; Fowler, D. E.; Skluzacek, J. M.; Seibel, E.; Mallouk, T. E. Anionic Homopolymers Efficiently Target Zerovalent Iron Particles to Hydrophobic Contaminants in Sand Columns. *Environ. Sci. Technol.* **2010**, *44* (23), 9069–9074. https://doi.org/10.1021/es1017398.
(190) Irvine, D. J. Drug Delivery: One Nanoparticle, One Kill. *Nature Materials* **2011**, *10* (5), 342–343. https://doi.org/10.1038/nmat3014.
(191) Liu, S.; Jones, L.; Gu, F. X. Nanomaterials for Ocular Drug Delivery. *Macromol. Biosci.* **2012**, *12* (5), 608–620. https://doi.org/10.1002/mabi.201100419.
(192) Gonzales, M.; Krishnan, K. M. Phase Transfer of Highly Monodisperse Iron Oxide Nanocrystals with Pluronic F127 for Biomedical Applications. *Journal of Magnetism and Magnetic Materials* **2007**, *311* (1), 59–62. https://doi.org/10.1016/j.jmmm.2006.10.1150.
(193) Dehvari, K.; Lin, K.-S.; Wang, S. S.-S. Structural Characterization and Adsorption Properties of Pluronic F127 Onto Iron Oxides Magnetic Nanoparticles. *Journal of Nanoscience and Nanotechnology* **2014**, *14* (3), 2361–2367. https://doi.org/10.1166/jnn.2014.8537.
(194) Nejadnik, M. R.; Olsson, A. L. J.; Sharma, P. K.; van der Mei, H. C.; Norde, W.; Busscher, H. J. Adsorption of Pluronic F-127 on Surfaces with Different Hydrophobicities Probed by Quartz Crystal Microbalance with Dissipation. *Langmuir* **2009**, *25* (11), 6245–6249. https://doi.org/10.1021/la9001169.
(195) Linley, S.; Holmes, A.; Leshuk, T.; Nafo, W.; Thomson, N. R.; Al-Mayah, A.; McVey, K.; Sra, K.; Gu, F. X. Targeted Nanoparticle Binding & Detection in Petroleum Hydrocarbon Impacted Porous Media. *Chemosphere* **2019**, *215*, 353–361. https://doi.org/10.1016/j.chemosphere.2018.10.046.
(196) Das, S.; Sen, B.; Debnath, N. Recent Trends in Nanomaterials Applications in Environmental Monitoring and Remediation. *Environ Sci Pollut Res* **2015**, *22* (23), 18333–18344. https://doi.org/10.1007/s11356-015-5491-6.

(197) He, F.; Zhao, D. Manipulating the Size and Dispersibility of Zerovalent Iron Nanoparticles by Use of Carboxymethyl Cellulose Stabilizers. *Environ. Sci. Technol.* **2007**, *41* (17), 6216–6221. https://doi.org/10.1021/es0705543.
(198) Raychoudhury, T.; Naja, G.; Ghoshal, S. Assessment of Transport of Two Polyelectrolyte-Stabilized Zero-Valent Iron Nanoparticles in Porous Media. *Journal of Contaminant Hydrology* **2010**, *118* (3), 143–151. https://doi.org/10.1016/j.jconhyd.2010.09.005.
(199) Sharma, V. K.; Siskova, K. M.; Zboril, R.; Gardea-Torresdey, J. L. Organic-Coated Silver Nanoparticles in Biological and Environmental Conditions: Fate, Stability and Toxicity. *Advances in Colloid and Interface Science* **2014**, *204*, 15–34. https://doi.org/10.1016/j.cis.2013.12.002.
(200) Zhang, M.; He, F.; Zhao, D.; Hao, X. Transport of Stabilized Iron Nanoparticles in Porous Media: Effects of Surface and Solution Chemistry and Role of Adsorption. *Journal of Hazardous Materials* **2017**, *322*, 284–291. https://doi.org/10.1016/j.jhazmat.2015.12.071.
(201) Reith, F.; Cornelis, G. Effect of Soil Properties on Gold- and Platinum Nanoparticle Mobility. *Chemical Geology* **2017**, *466*, 446–453. https://doi.org/10.1016/j.chemgeo.2017.06.033.
(202) Hou, J.; Zhang, M.; Wang, P.; Wang, C.; Miao, L.; Xu, Y.; You, G.; Lv, B.; Yang, Y.; Liu, Z. Transport, Retention, and Long-Term Release Behavior of Polymer-Coated Silver Nanoparticles in Saturated Quartz Sand: The Impact of Natural Organic Matters and Electrolyte. *Environmental Pollution* **2017**, *229*, 49–59. https://doi.org/10.1016/j.envpol.2017.05.059.
(203) Wang, D.; Jaisi, D. P.; Yan, J.; Jin, Y.; Zhou, D. Transport and Retention of Polyvinylpyrrolidone-Coated Silver Nanoparticles in Natural Soils. *Vadose Zone Journal* **2015**, *14* (7). https://doi.org/10.2136/vzj2015.01.0007.
(204) Makselon, J.; Zhou, D.; Engelhardt, I.; Jacques, D.; Klumpp, E. Experimental and Numerical Investigations of Silver Nanoparticle Transport under Variable Flow and Ionic Strength in Soil. *Environ. Sci. Technol.* **2017**, *51* (4), 2096–2104. https://doi.org/10.1021/acs.est.6b04882.
(205) Prédélus, D.; Lassabatere, L.; Louis, C.; Gehan, H.; Brichart, T.; Winiarski, T.; Angulo-Jaramillo, R. Nanoparticle Transport in Water-Unsaturated Porous Media: Effects of Solution Ionic Strength and Flow Rate. *J Nanopart Res* **2017**, *19* (3), 104. https://doi.org/10.1007/s11051-017-3755-4.
(206) Phenrat, T.; Fagerlund, F.; Illangasekare, T.; Lowry, G. V.; Tilton, R. D. Polymer-Modified Fe0 Nanoparticles Target Entrapped NAPL in Two Dimensional Porous Media: Effect of Particle Concentration, NAPL Saturation, and Injection Strategy. *Environ. Sci. Technol.* **2011**, *45* (14), 6102–6109. https://doi.org/10.1021/es200577n.
(207) Wang, A. Z.; Gu, F.; Zhang, L.; Chan, J. M.; Radovic-Moreno, A.; Shaikh, M. R.; Farokhzad, O. C. Biofunctionalized Targeted Nanoparticles for Therapeutic Applications. *Expert Opinion on Biological Therapy* **2008**, *8* (8), 1063–1070. https://doi.org/10.1517/14712598.8.8.1063.
(208) Park, J.; Kyung Yu, M.; Yeon Jeong, Y.; Woong Kim, J.; Lee, K.; Ngoc Phan, V.; Jon, S. Antibiofouling Amphiphilic Polymer -Coated Superparamagnetic Iron Oxide Nanoparticles : Synthesis, Characterization, and Use in Cancer Imaging in Vivo. *Journal of Materials Chemistry* **2009**, *19* (35), 6412–6417. https://doi.org/10.1039/B902445J.
(209) Alexandridis, P.; Holzwarth, J. F.; Hatton, T. A. Micellization of Poly(Ethylene Oxide)-Poly(Propylene Oxide)-Poly(Ethylene Oxide) Triblock Copolymers in Aqueous Solutions: Thermodynamics of Copolymer Association. *Macromolecules* **1994**, *27* (9), 2414–2425. https://doi.org/10.1021/ma00087a009.
(210) Lin, Y.; Alexandridis, P. Temperature-Dependent Adsorption of Pluronic F127 Block Copolymers onto Carbon Black Particles Dispersed in Aqueous Media. *J. Phys. Chem. B* **2002**, *106* (42), 10834–10844. https://doi.org/10.1021/jp014221i.
(211) Bodratti, A. M.; Wu, J.; Jahan, R.; Sarkar, B.; Tsianou, M.; Alexandridis, P. Mono- and Di-Valent Salts as Modifiers of PEO-PPO-PEO Block Copolymer Interactions with Silica Nanoparticles in Aqueous Dispersions. *Journal of Dispersion Science and Technology* **2015**, *36* (12), 1806–1815. https://doi.org/10.1080/01932691.2015.1011273.

(212) Sasidharan, S.; Torkzaban, S.; Bradford, S. A.; Cook, P. G.; Gupta, V. V. S. R. Temperature Dependency of Virus and Nanoparticle Transport and Retention in Saturated Porous Media. *Journal of Contaminant Hydrology* **2017**, *196*, 10–20. https://doi.org/10.1016/j.jconhyd.2016.11.004.
(213) Xu, X.; Thomson, N. R. Estimation of the Maximum Consumption of Permanganate by Aquifer Solids Using a Modified Chemical Oxygen Demand Test. *Journal of Environmental Engineering* **2008**, *134* (5), 353–361. https://doi.org/10.1061/(ASCE)0733-9372(2008)134:5(353).
(214) Adamczyk, Z.; Siwek, B.; Zembala, M.; Belouschek, P. Kinetics of Localized Adsorption of Colloid Particles. *Advances in Colloid and Interface Science* **1994**, *48*, 151–280. https://doi.org/10.1016/0001-8686(94)80008-1.
(215) Thomson, N. R. *1DUSAT: A Flexible One-Dimensional Unsaturated Flow and Solute Transport Model*; University of Waterloo, 2018.
(216) Tolson, B. A.; Shoemaker, C. A. Dynamically Dimensioned Search Algorithm for Computationally Efficient Watershed Model Calibration. *Water Resources Research* **2007**, *43* (1). https://doi.org/10.1029/2005WR004723.
(217) Matott, L. *OSTRICH: An Optimization Software Tool, Documentation and User's Guide*; University at Buffalo Center for Computational Research, 2017.
(218) Liu, X.; Wu, D.; Turgman-Cohen, S.; Genzer, J.; Theyson, T. W.; Rojas, O. J. Adsorption of a Nonionic Symmetric Triblock Copolymer on Surfaces with Different Hydrophobicity. *Langmuir* **2010**, *26* (12), 9565–9574. https://doi.org/10.1021/la100156a.
(219) Bae, K. H.; Choi, S. H.; Park, S. Y.; Lee, Y.; Park, T. G. Thermosensitive Pluronic Micelles Stabilized by Shell Cross-Linking with Gold Nanoparticles. *Langmuir* **2006**, *22* (14), 6380–6384. https://doi.org/10.1021/la0606704.
(220) Rapoport, N. Stabilization and Activation of Pluronic Micelles for Tumor-Targeted Drug Delivery. *Colloids and Surfaces B: Biointerfaces* **1999**, *16* (1), 93–111. https://doi.org/10.1016/S0927-7765(99)00063-6.
(221) Chen, S.; Li, Y.; Guo, C.; Wang, J.; Ma, J.; Liang, X.; Yang, L.-R.; Liu, H.-Z. Temperature-Responsive Magnetite/PEO−PPO−PEO Block Copolymer Nanoparticles for Controlled Drug Targeting Delivery. *Langmuir* **2007**, *23* (25), 12669–12676. https://doi.org/10.1021/la702049d.
(222) Kanicky, J. R.; Shah, D. O. Effect of Premicellar Aggregation on the PKa of Fatty Acid Soap Solutions. *Langmuir* **2003**, *19* (6), 2034–2038. https://doi.org/10.1021/la020672y.
(223) Carstens, J. F.; Bachmann, J.; Neuweiler, I. Effects of Flow Interruption on Transport and Retention of Iron Oxide Colloids in Quartz Sand. *Colloids and Surfaces A: Physicochemical and Engineering Aspects* **2017**, *520*, 532–543. https://doi.org/10.1016/j.colsurfa.2017.02.003.
(224) Carstens, J. F.; Bachmann, J.; Neuweiler, I. A New Approach to Determine the Relative Importance of DLVO and Non-DLVO Colloid Retention Mechanisms in Porous Media. *Colloids and Surfaces A: Physicochemical and Engineering Aspects* **2019**, *560*, 330–335. https://doi.org/10.1016/j.colsurfa.2018.10.013.
(225) Song, B.; Zeng, G.; Gong, J.; Liang, J.; Xu, P.; Liu, Z.; Zhang, Y.; Zhang, C.; Cheng, M.; Liu, Y.; et al. Evaluation Methods for Assessing Effectiveness of in Situ Remediation of Soil and Sediment Contaminated with Organic Pollutants and Heavy Metals. *Environment International* **2017**, *105*, 43–55. https://doi.org/10.1016/j.envint.2017.05.001.
(226) Kuppusamy, S.; Palanisami, T.; Megharaj, M.; Venkateswarlu, K.; Naidu, R. In-Situ Remediation Approaches for the Management of Contaminated Sites: A Comprehensive Overview. In *Reviews of Environmental Contamination and Toxicology Volume 236*; de Voogt, P., Ed.; Springer International Publishing: Cham, 2016; Vol. 236, pp 1–115.
(227) Agarwal, A.; Liu, Y. Remediation Technologies for Oil-Contaminated Sediments. *Marine Pollution Bulletin* **2015**, *101* (2), 483–490. https://doi.org/10.1016/j.marpolbul.2015.09.010.
(228) Kuppusamy, S.; Thavamani, P.; Venkateswarlu, K.; Lee, Y. B.; Naidu, R.; Megharaj, M. Remediation Approaches for Polycyclic Aromatic Hydrocarbons (PAHs) Contaminated Soils:

Technological Constraints, Emerging Trends and Future Directions. *Chemosphere* **2017**, *168*, 944–968. https://doi.org/10.1016/j.chemosphere.2016.10.115.
(229) Tratnyek, P. G.; Johnson, R. L. Nanotechnologies for Environmental Cleanup. *Nano Today* **2006**, *1* (2), 44–48. https://doi.org/10.1016/S1748-0132(06)70048-2.
(230) Bartke, S.; Hagemann, N.; Harries, N.; Hauck, J.; Bardos, P. Market Potential of Nanoremediation in Europe – Market Drivers and Interventions Identified in a Deliberative Scenario Approach. *Science of The Total Environment* **2018**, *619–620*, 1040–1048. https://doi.org/10.1016/j.scitotenv.2017.11.215.
(231) Kuang, Y.; Du, J.; Zhou, R.; Chen, Z.; Megharaj, M.; Naidu, R. Calcium Alginate Encapsulated Ni/Fe Nanoparticles Beads for Simultaneous Removal of Cu (II) and Monochlorobenzene. *Journal of Colloid and Interface Science* **2015**, *447*, 85–91. https://doi.org/10.1016/j.jcis.2015.01.080.
(232) Kim, H.-J.; Leitch, M.; Naknakorn, B.; Tilton, R. D.; Lowry, G. V. Effect of Emplaced NZVI Mass and Groundwater Velocity on PCE Dechlorination and Hydrogen Evolution in Water-Saturated Sand. *Journal of Hazardous Materials* **2017**, *322* (Part A), 136–144. https://doi.org/10.1016/j.jhazmat.2016.04.037.
(233) Gil-Díaz, M.; Alonso, J.; Rodríguez-Valdés, E.; Gallego, J. R.; Lobo, M. C. Comparing Different Commercial Zero Valent Iron Nanoparticles to Immobilize As and Hg in Brownfield Soil. *Science of The Total Environment* **2017**, *584–585*, 1324–1332. https://doi.org/10.1016/j.scitotenv.2017.02.011.
(234) Gil-Díaz, M.; Pinilla, P.; Alonso, J.; Lobo, M. C. Viability of a Nanoremediation Process in Single or Multi-Metal(Loid) Contaminated Soils. *Journal of Hazardous Materials* **2017**, *321*, 812–819. https://doi.org/10.1016/j.jhazmat.2016.09.071.
(235) Qiu, C.; He, Y.; Brookes, P.; Xu, J. The Systematic Characterization of Nanoscale Bamboo Charcoal and Its Sorption on Phenanthrene:A Comparison with Microscale. *Science of the Total Environment* **2017**, *578*, 691–693. https://doi.org/10.1016/j.scitotenv.2016.10.196.
(236) Pardo, F.; Peluffo, M.; Santos, A.; Romero, A. Optimization of the Application of the Fenton Chemistry for the Remediation of a Contaminated Soil with Polycyclic Aromatic Hydrocarbons. *Journal of Chemical Technology and Biotechnology* **2016**, *91* (6), 1763–1772. https://doi.org/10.1002/jctb.4767.
(237) Lefevre, E.; Bossa, N.; Wiesner, M. R.; Gunsch, C. K. A Review of the Environmental Implications of in Situ Remediation by Nanoscale Zero Valent Iron (NZVI): Behavior, Transport and Impacts on Microbial Communities. *Science of The Total Environment* **2016**, *565*, 889–901. https://doi.org/10.1016/j.scitotenv.2016.02.003.
(238) Tian, H.; Liang, Y.; Zhu, T.; Zeng, X.; Sun, Y. Surfactant-Enhanced PEG-4000-NZVI for Remediating Trichloroethylene-Contaminated Soil. *Chemosphere* **2018**, *195*, 585–593. https://doi.org/10.1016/j.chemosphere.2017.12.070.
(239) Poza-Nogueiras, V.; Rosales, E.; Pazos, M.; Sanromán, M. Á. Current Advances and Trends in Electro-Fenton Process Using Heterogeneous Catalysts – A Review. *Chemosphere* **2018**, *201*, 399–416. https://doi.org/10.1016/j.chemosphere.2018.03.002.
(240) Mirzaee, E.; Gitipour, S.; Mousavi, M.; Amini, S. Optimization of Total Petroleum Hydrocarbons Removal from Mahshahr Contaminated Soil Using Magnetite Nanoparticle Catalyzed Fenton-like Oxidation. *Environ Earth Sci* **2017**, *76* (4), 165. https://doi.org/10.1007/s12665-017-6484-1.
(241) Leitão, P.; Aulenta, F.; Rossetti, S.; Nouws, H. P. A.; Danko, A. S. Impact of Magnetite Nanoparticles on the Syntrophic Dechlorination of 1,2-Dichloroethane. *Science of The Total Environment* **2018**, *624*, 17–23. https://doi.org/10.1016/j.scitotenv.2017.12.110.
(242) Jorfi, S.; Samaei, M. R.; Darvishi Cheshmeh Soltani, R.; Talaie Khozani, A.; Ahmadi, M.; Barzegar, G.; Reshadatian, N.; Mehrabi, N. Enhancement of the Bioremediation of Pyrene-Contaminated Soils Using a Hematite Nanoparticle-Based Modified Fenton Oxidation in a Sequenced Approach. *Soil and Sediment Contamination: An International Journal* **2017**, *26* (2), 141–156. https://doi.org/10.1080/15320383.2017.1255875.

(243) Matos, M. P. S. R.; Correia, A. A. S.; Rasteiro, M. G. Application of Carbon Nanotubes to Immobilize Heavy Metals in Contaminated Soils. *J Nanopart Res* **2017**, *19* (4), 126. https://doi.org/10.1007/s11051-017-3830-x.
(244) Zhang, J.; Gong, J.-L.; Zeng, G.-M.; Yang, H.-C.; Zhang, P. Carbon Nanotube Amendment for Treating Dichlorodiphenyltrichloroethane and Hexachlorocyclohexane Remaining in Dong-Ting Lake Sediment — An Implication for in-Situ Remediation. *Science of The Total Environment* **2017**, *579*, 283–291. https://doi.org/10.1016/j.scitotenv.2016.11.105.
(245) Apul, O. G.; Delgado, A. G.; Kidd, J.; Alam, F.; Dahlen, P.; Westerhoff, P. Carbonaceous Nano-Additives Augment Microwave-Enabled Thermal Remediation of Soils Containing Petroleum Hydrocarbons. *Environ. Sci.: Nano* **2016**, *3* (5), 997–1002. https://doi.org/10.1039/C6EN00261G.
(246) Wang, D.; Park, C. M.; Masud, A.; Aich, N.; Su, C. Carboxymethylcellulose Mediates the Transport of Carbon Nanotube—Magnetite Nanohybrid Aggregates in Water-Saturated Porous Media. *Environmental Science & Technology* **2017**, *51* (21), 12405–12415. https://doi.org/10.1021/acs.est.7b04037.
(247) Zhang, M.; He, F.; Zhao, D.; Hao, X. Transport of Stabilized Iron Nanoparticles in Porous Media: Effects of Surface and Solution Chemistry and Role of Adsorption. *Journal of Hazardous Materials* **2017**, *322*, 284–291. https://doi.org/10.1016/j.jhazmat.2015.12.071.
(248) Sirk, K. M.; Saleh, N. B.; Phenrat, T.; Kim, H.-J.; Dufour, B.; Ok, J.; Golas, P. L.; Matyjaszewsk, K.; Lowry, G. V.; Tilton, R. D. Effect of Adsorbed Polyelectrolytes on Nanoscale Zero Valent Iron Particle Attachment to Soil Surface Models. *Environmental Science and Technology* **2009**, *43* (10), 3803–3808. https://doi.org/10.1021/es803589t.
(249) Fan, G.; Cang, L.; Qin, W.; Zhou, C.; Gomes, H. I.; Zhou, D. Surfactants-Enhanced Electrokinetic Transport of Xanthan Gum Stabilized NanoPd/Fe for the Remediation of PCBs Contaminated Soils. *Separation and Purification Technology* **2013**, *114*, 64–72. https://doi.org/10.1016/j.seppur.2013.04.030.
(250) Velimirovic, M.; Tosco, T.; Uyttebroek, M.; Luna, M.; Gastone, F.; De Boer, C.; Klaas, N.; Sapion, H.; Eisenmann, H.; Larsson, P.-O.; et al. Field Assessment of Guar Gum Stabilized Microscale Zerovalent Iron Particles for In-Situ Remediation of 1,1,1-Trichloroethane. *Journal of Contaminant Hydrology* **2014**, *164*, 88–99. https://doi.org/10.1016/j.jconhyd.2014.05.009.
(251) Tiraferri, A.; Sethi, R. Enhanced Transport of Zerovalent Iron Nanoparticles in Saturated Porous Media by Guar Gum. *Journal of Nanoparticle Research* **2009**, *11* (3), 635–645. https://doi.org/10.1007/s11051-008-9405-0.
(252) Wang, W.; Zhou, M.; Jin, Z.; Li, T. Reactivity Characteristics of Poly(Methyl Methacrylate) Coated Nanoscale Iron Particles for Trichloroethylene Remediation. *Journal of Hazardous Materials* **2010**, *173* (1), 724–730. https://doi.org/10.1016/j.jhazmat.2009.08.145.
(253) Wang, Z.; Choi, F.; Acosta, E. Effect of Surfactants on Zero-Valent Iron Nanoparticles (NZVI) Reactivity. *Journal of Surfactants and Detergents* **2017**, *20* (3), 577–588. https://doi.org/10.1007/s11743-017-1941-0.
(254) Wacławek, S.; Chronopoulou, L.; Petrangeli Papini, M.; Vinod, V. T. P.; Palocci, C.; Kupčík, J.; Černík, M. Enhancement of Stability and Reactivity of Nanosized Zero-Valent Iron with Polyhydroxybutyrate. *Desalination and Water Treatment* **2017**, *69*, 302–307. https://doi.org/10.5004/dwt.2017.0704.
(255) Chowdhury, A. I. A.; Krol, M. M.; Kocur, C. M.; Boparai, H. K.; Weber, K. P.; Sleep, B. E.; O'Carroll, D. M. NZVI Injection into Variably Saturated Soils: Field and Modeling Study. *Journal of Contaminant Hydrology* **2015**, *183*, 16–28. https://doi.org/10.1016/j.jconhyd.2015.10.003.
(256) Kocur, C. M. D.; Lomheim, L.; Molenda, O.; Weber, K. P.; Austrins, L. M.; Sleep, B. E.; Boparai, H. K.; Edwards, E. A.; O'Carroll, D. M. Long-Term Field Study of Microbial Community and Dechlorinating Activity Following Carboxymethyl Cellulose-Stabilized

Nanoscale Zero-Valent Iron Injection. *Environmental Science and Technology* **2016**, *50* (14), 7658–7670. https://doi.org/10.1021/acs.est.6b01745.
(257) Ghosh, I.; Mukherjee, A.; Mukherjee, A. In Planta Genotoxicity of NZVI: Influence of Colloidal Stability on Uptake, DNA Damage, Oxidative Stress and Cell Death. *Mutagenesis* **2017**, *32* (3), 371–387. https://doi.org/10.1093/mutage/gex006.
(258) Rede, D.; Santos, L. H. M. L. M.; Ramos, S.; Oliva-Teles, F.; Antão, C.; Sousa, S. R.; Delerue-Matos, C. Ecotoxicological Impact of Two Soil Remediation Treatments in Lactuca Sativa Seeds. *Chemosphere* **2016**, *159*, 193–198. https://doi.org/10.1016/j.chemosphere.2016.06.002.
(259) Libralato, G.; Costa Devoti, A.; Zanella, M.; Sabbioni, E.; Mičetić, I.; Manodori, L.; Pigozzo, A.; Manenti, S.; Groppi, F.; Volpi Ghirardini, A. Phytotoxicity of Ionic, Micro- and Nano-Sized Iron in Three Plant Species. *Ecotoxicology and Environmental Safety* **2016**, *123* (Complete), 81–88. https://doi.org/10.1016/j.ecoenv.2015.07.024.
(260) Qualhato, G.; Rocha, T. L.; de Oliveira Lima, E. C.; e Silva, D. M.; Cardoso, J. R.; Koppe Grisolia, C.; de Sabóia-Morais, S. M. T. Genotoxic and Mutagenic Assessment of Iron Oxide (Maghemite-γ-Fe2O3) Nanoparticle in the Guppy Poecilia Reticulata. *Chemosphere* **2017**, *183*, 305–314. https://doi.org/10.1016/j.chemosphere.2017.05.061.
(261) Hjorth, R.; Coutris, C.; Nguyen, N. H. A.; Sevcu, A.; Gallego-Urrea, J. A.; Baun, A.; Joner, E. J. Ecotoxicity Testing and Environmental Risk Assessment of Iron Nanomaterials for Sub-Surface Remediation – Recommendations from the FP7 Project NanoRem. *Chemosphere* **2017**, *182*, 525–531. https://doi.org/10.1016/j.chemosphere.2017.05.060.
(262) Schiwy, A.; Maes, H. M.; Koske, D.; Flecken, M.; Schmidt, K. R.; Schell, H.; Tiehm, A.; Kamptner, A.; Thümmler, S.; Stanjek, H.; et al. The Ecotoxic Potential of a New Zero-Valent Iron Nanomaterial, Designed for the Elimination of Halogenated Pollutants, and Its Effect on Reductive Dechlorinating Microbial Communities. *Environmental Pollution* **2016**, *216*, 419–427. https://doi.org/10.1016/j.envpol.2016.05.051.
(263) Nguyen, N. H. A.; Špánek, R.; Kasalický, V.; Ribas, D.; Vlková, D.; Řeháková, H.; Kejzlar, P.; Ševců, A. Different Effects of Nano-Scale and Micro-Scale Zero-Valent Iron Particles on Planktonic Microorganisms from Natural Reservoir Water. *Environ. Sci.: Nano* **2018**, *5* (5), 1117–1129. https://doi.org/10.1039/C7EN01120B.
(264) Molnar, I. L.; Johnson, W. P.; Gerhard, J. I.; Willson, C. S.; O'Carroll, D. M. Predicting Colloid Transport through Saturated Porous Media: A Critical Review. *Water Resour. Res.* **2015**, *51* (9), 6804–6845. https://doi.org/10.1002/2015WR017318.
(265) Wang, M.; Gao, B.; Tang, D. Review of Key Factors Controlling Engineered Nanoparticle Transport in Porous Media. *Journal of Hazardous Materials* **2016**, *318*, 233–246. https://doi.org/10.1016/j.jhazmat.2016.06.065.
(266) Patil, S. S.; Shedbalkar, U. U.; Truskewycz, A.; Chopade, B. A.; Ball, A. S. Nanoparticles for Environmental Clean-up: A Review of Potential Risks and Emerging Solutions. *Environmental Technology & Innovation* **2016**, *5*, 10–21. https://doi.org/10.1016/j.eti.2015.11.001.
(267) Thatai, S.; Khurana, P.; Boken, J.; Prasad, S.; Kumar, D. Nanoparticles and Core–Shell Nanocomposite Based New Generation Water Remediation Materials and Analytical Techniques: A Review. *Microchemical Journal* **2014**, *116*, 62–76. https://doi.org/10.1016/j.microc.2014.04.001.
(268) Bianco, C.; Patiño Higuita, J. E.; Tosco, T.; Tiraferri, A.; Sethi, R. Controlled Deposition of Particles in Porous Media for Effective Aquifer Nanoremediation. *Scientific Reports* **2017**, *7*. https://doi.org/10.1038/s41598-017-13423-y.
(269) Wang, Z.; Acosta, E. Formulation Design for Target Delivery of Iron Nanoparticles to TCE Zones. *Journal of Contaminant Hydrology* **2013**, *155*, 9–19. https://doi.org/10.1016/j.jconhyd.2013.08.005.
(270) Li, D.-G.; Chen, S.-H.; Zhao, S.-Y.; Hou, X.-M.; Ma, H.-Y.; Yang, X.-G. A Study of Phase Transfer Processes of Ag Nanoparticles. *Applied Surface Science* **2002**, *200* (1), 62–67. https://doi.org/10.1016/S0169-4332(02)00606-2.

(271) Repko, A.; Nižňanský, D.; Poltierová-Vejpravová, J. A Study of Oleic Acid-Based Hydrothermal Preparation of CoFe2O4 Nanoparticles. *J Nanopart Res* **2011**, *13* (10), 5021. https://doi.org/10.1007/s11051-011-0483-z.
(272) Repko, A.; Vejpravová, J.; Vacková, T.; Zákutná, D.; Nižňanský, D. Oleate-Based Hydrothermal Preparation of CoFe2O4 Nanoparticles, and Their Magnetic Properties with Respect to Particle Size and Surface Coating. *Journal of Magnetism and Magnetic Materials* **2015**, *390* (Supplement C), 142–151. https://doi.org/10.1016/j.jmmm.2015.04.090.
(273) Angelescu, D. G.; Vasilescu, M.; Anastasescu, M.; Baratoiu, R.; Donescu, D.; Teodorescu, V. S. Synthesis and Association of Ag(0) Nanoparticles in Aqueous Pluronic F127 Triblock Copolymer Solutions. *Colloids and Surfaces A: Physicochemical and Engineering Aspects* **2012**, *394*, 57–66. https://doi.org/10.1016/j.colsurfa.2011.11.025.
(274) Linse, P.; Malmsten, M. Temperature-Dependent Micellization in Aqueous Block Copolymer Solutions. *Macromolecules* **1992**, *25* (20), 5434–5439. https://doi.org/10.1021/ma00046a048.
(275) Addai-Mensah, J. Enhanced Flocculation and Dewatering of Clay Mineral Dispersions. *Powder Technology* **2007**, *179* (1–2), 73–78. https://doi.org/10.1016/j.powtec.2006.11.008.
(276) Hema, S.; Thambiraj, S.; Shankaran, D. R. Nanoformulations for Targeted Drug Delivery to Prostate Cancer: An Overview. *Journal of Nanoscience and Nanotechnology* **2018**, *18* (8), 5171–5191. https://doi.org/10.1166/jnn.2018.15420.
(277) Petros, R. A.; DeSimone, J. M. Strategies in the Design of Nanoparticles for Therapeutic Applications. *Nat Rev Drug Discov* **2010**, *9* (8), 615–627. https://doi.org/10.1038/nrd2591.
(278) Srinivasarao, M.; Galliford, C. V.; Low, P. S. Principles in the Design of Ligand-Targeted Cancer Therapeutics and Imaging Agents. *Nature Reviews Drug Discovery* **2015**, *14* (3), 203–219. https://doi.org/10.1038/nrd4519.
(279) Mellage, A.; Holmes, A. B.; Linley, S.; Vallée, L.; Rezanezhad, F.; Thomson, N.; Gu, F.; Cappellen, P. V. Sensing Coated Iron-Oxide Nanoparticles with Spectral Induced Polarization (SIP): Experiments in Natural Sand Packed Flow-Through Columns. *Environmental Science & Technology* **2018**. https://doi.org/10.1021/acs.est.8b03686.
(280) Phenrat, T.; Thongboot, T.; Lowry, G. V. Electromagnetic Induction of Zerovalent Iron (ZVI) Powder and Nanoscale Zerovalent Iron (NZVI) Particles Enhances Dechlorination of Trichloroethylene in Contaminated Groundwater and Soil: Proof of Concept http://pubs.acs.org/doi/abs/10.1021/acs.est.5b04485 (accessed Feb 26, 2019). https://doi.org/10.1021/acs.est.5b04485.
(281) Ball, W. P.; Buehler, C.; Harmon, T. C.; Mackay, D. M.; Roberts, P. V. Characterization of a Sandy Aquifer Material at the Grain Scale. *Journal of Contaminant Hydrology* **1990**, *5* (3), 253–295. https://doi.org/10.1016/0169-7722(90)90040-N.
(282) Nejadnik, M. R.; Olsson, A. L. J.; Sharma, P. K.; van der Mei, H. C.; Norde, W.; Busscher, H. J. Adsorption of Pluronic F-127 on Surfaces with Different Hydrophobicities Probed by Quartz Crystal Microbalance with Dissipation. *Langmuir* **2009**, *25* (11), 6245–6249. https://doi.org/10.1021/la9001169.